UNIVERSITY OF CALIFORNIA,
IRVINE

New Dimensions in Time-Series Analysis for Exoplanet Detection

DISSERTATION

submitted in partial satisfaction of the requirements
for the degree of

DOCTOR OF PHILOSOPHY

in Physics

by

Jack Lubin

Dissertation Committee:
Assistant Professor Paul Robertson, Chair
Associate Professor Aomawa Shields
Assistant Professor Stephanie Sallum
Professor Aaron Barth

2023

DEDICATION

To Mom and Dad, for giving me the universe

TABLE OF CONTENTS

LIST OF FIGURES

LIST OF TABLES

ACKNOWLEDGMENTS

No one is an island. The work represented here is only the shining top of the pyramid, upon which many people have helped build the support structures. This dissertation would not be possible without those support structures and those people who helped build them and lift me up into the position I am in today.

First, I would like to thank a thousand times over my advisor, Paul Robertson, who has shown me through example not only how to do good science, but also how to be a good scientist.

Next, given that I have trained as an observational astronomer through this dissertation work, I would like to thank and acknowledge the people, institutions, and places that have helped train me as an observer and those who have collected data on my behalf. I gratefully recognize and acknowledge the cultural role and reverence that the summit of Maunakea has within the indigenous Hawaiian community. I am deeply grateful to have the opportunity to conduct observations from this mountain. I am further grateful for the efforts and dedication of the Keck Observatory staff for support of HIRES and remote observing. I thank the McDonald Observatory and staff for executing observations of Barnard's star on behalf of my efforts to characterize the system. Additionally, I am grateful to Lick Observatory and staff, particularly Elinor Gates and Paul Lynam, for helping train me to be an observer myself, and for support of the APF and ShaneAO systems.

Then, I am grateful for the many collaborations that I have been lucky enough to be a part of. These include the HPF and NEID science teams, and the TESS-Keck Survey team. I have learned so much about science, the process of performing science, working in large teams, and asking good questions through my work with these collaborations. I am also so grateful to the large groups of fellow graduate students I have come to know, work closely with, and call friends through these collaborations, many of which appear below in coauthor lists. Further, I want to specially thank my long time collaborator Nathan Hara for all the help and guidance he has given me throughout building `Lia`.

I want to thank the friends I've made through grad school at UC Irvine. A special shout out to Corey Beard and Rae Holcomb. The three of us formed the original core of Paul's first students and in many ways we have all learned together. Thank you for letting me bounce my most outlandish astro ideas off you! Additionally I give special added thanks to Corey Beard (and parents Carolyn and Mike Beard!) for hosting and caring for my remote server in your living room during the early days of Covid. I also want to thank the more recent members of Paul's group: Jacob Luhn, Te Han, and Pranav Premnath. I've learned so much from you all. We have a had a lot of fun all together, I firmly believe we are the most fun group in astronomy! I look forward to continuing to work with all of you in the future. Thank you to Francisco Mercado and Devontae Baxter, my two office mates who I may have subjected to lots of distractions! We have had so much fun together! I also want to thank rest of my 2018 UCI Astro cohort: Abby Bault, Alex Lazar, and José Flores Velázquez. José, I know you will be standing with me on the on the graduation stage. Thank you to all

of you for enriching my grad school experience!

I am grateful to the UCI Physics and Astronomy department for taking a chance on me. I was accepted to only one graduate program, and I'll never forget the joy and excitement of opening that letter. I recall visiting on accepted students day and meeting with the head of the admissions committee. They told me that my application stood out because I was so passionate about studying exoplanets and that the department was making a concerted effort to expand the exoplanet team and program. At the time there was one professor, one grad student, and one postdoc working in exoplanets, and Paul had just been hired weeks earlier (I met with him that day for the first time in his bare office, only a folding table and two folding chairs!). I was promised I would see a growth in the exoplanet team and that if I came to UCI, I would be a part of that growth and help shape the culture. Now as I graduate, there are three professors, 9 grad students, 4 postdocs, and a small army of undergrads all working in exoplanets at UCI. I've seen the wonderful growth of this sub-field within UCI and I know the best is yet to come.

Next, I want to thank my wonderful partner, Marlee Goldstein. You are the brightest star in my life and while I seek out other worlds, there is nothing I enjoy more than exploring this one with you. I cannot imagine completing graduate school without you and all your support. You make me feel like I can do anything and you've helped me grow in so many ways. I love you lots and lots!

Lastly, I wish to thank my family. My parents, Carol and Charles Lubin, to whom this dissertation is dedicated, for everything they have given me. Your support and love has propelled me to and through graduate school. Elizabeth, my sister, who teaches me as much as I could ever teach her. And my grandparents Doris and Joseph, Alma and Bernard, who are not here to see me graduate, but who also have given me all the opportunity to succeed. I love you all so much!

Finally, a few necessary acknowledgements.

Chapter 2 of this dissertation is a reprint of the material (excluding Foreward) as it appears in Lubin, J., Robertson, P., Stefansson, G., et al. *Stellar Activity Manifesting at a One Year Alias Explains Barnard b as a False Positive*, AJ, 162:61, August 2021. This work is used with permission from The Astronomical Journal and IOP Publishing under their authors' rights policies. The co-authors listed in this publication are, as they appear in the paper, Judah van Zandt, Rae Holcomb, Lauren M. Weiss, Erik A. Petigura, Paul Robertson, Joseph M. Akana Murphy, Nicholas Scarsdale, Konstantin Batygin, Alex S. Polanski, Natalie M. Batalha, Ian J. M. Crossfield, Courtney Dressing, Benjamin Fulton, Andrew W. Howard, Daniel Huber, Howard Isaacson, Stephen R. Kane, Arpita Roy, Corey Beard, Sarah Blunt, Ashley Chontos, Fei Dai, Paul A. Dalba, Kaz Gary, Steven Giacalone, Michelle L. Hill, Andrew Mayo, Teo Mocnik, Molly R. Kosiarek, Malena Rice, Ryan A. Rubenzahl, David W. Latham, S. Seager, and Joshua N. Winn.

The text of Chapter 3 of this dissertation is a reprint of the material as it appears in Lubin, J., van Zandt, J., Holcomb, R., et al. TESS-Keck Survey IX: Masses of Three Sub-Neptunes

Orbiting HD 191939 and the Discovery of a Warm Jovian Plus a Distant Sub-Stellar Companion, AJ, 163:101, February 2022. This work is ued with permission from The Astronomical Journal and IOP Publishing under their author's rights policies. The co-authors listed in this publication are, as they appear in the paper, Paul Robertson, Gudmundur Stefansson, Joe Ninan, Suvrath Mahadevan, Michael Endl, Eric Ford, Jason T. Wright, Corey Beard, Chad Bender, William D. Cochran, Scott A. Diddams, Connor Fredrick, Samuel Halverson, Shubham Kanodia, Andrew J. Metcalf, Lawrence Ramsey, Arpital Roy, Christian Schwab, and Ryan Terrien.

VITA

Jack Lubin

EDUCATION

Ph.D. Physics 2023
Thesis Advisor: Paul Robertson
University of California, Irvine

Masters of Science, Physics 2020
University of California, Irvine

Bachelors of Arts, Physics and Applied Mathematics 2016
Thesis Advisor: Keivan Stassun
Vanderbilt University

APPOINTMENTS

Teaching Assistant September 2018 - June 2023
University of California, Irvine

Associate Data Engineer June 2016 - September 2017
Capital One Financial

Physics Tutor September 2015 - June 2016
Vanderbilt, Athletics Department

Research Experience for Undergraduates (REU) Summer 2015
Hosted at Vanderbilt University

TEACHING EXPERIENCE

Teaching Assistant — September 2018 - June 2023
Department of Physics and Astronomy, UCI

- Phys 7E, Classical Physics: Fluids; oscillations; waves; and optics — Spring 2023
- Phys 215B, Graduate Quantum Mechanics — Winter 2023
- Phys 7D, Classical Physics: Electricity and Magnetism (2nd time) — Winter 2023
- Phys 213A, Graduate Electricity & Magnetism — Winter 2022
- Phys 20A, Introduction to Astronomy (3rd time) — Winter 2022
- Phys 139, Observational Astronomy Lab — Fall 2021
- Phys 52C, Experimental Physics Lab, Statistics (online) — Spring 2021
- Phys 138, Galactic Astrophysics (online, 2nd time) — Winter 2021
- Phys 20A, Introduction to Astronomy (online, 2nd time) — Winter 2021
- Phys 7C, Classical Physics: Kinematics/Energy/Gravity (online) — Spring 2020
- Phys 138, Galactic Astrophysics — Winter 2020
- Phys 18, How Things Work — Winter 2020
- Phys 20A, Introduction to Astronomy — Fall 2019
- Phys 51A, Modern Physics — Spring 2019
- Phys 7D, Classical Physics: Electricity and Magnetism — Winter 2019
- Phys 52A, Experimental Physics Lab, Wave Theory — Fall 2018

HONORS, AWARDS & FELLOWSHIPS

Astronomical Society of the Pacific (ASP) Junior Board Fellow 2023

UCI Grad Slam Finalist 2023

CSU PREPP, Fellow 2023

Astrobites, Contributor 2023

NASA ExoExplorer, Fellow 2023

ARCS Foundation Scholar, Fellow 2023

National Osterbrock Leadership Program (NOLP), Fellow 2022

UCI Diversity Fellow - Funding to lead the PACE program (see below), Fellow 2022

Highest Honors in Astronomy – For successful defense of undergrad honors thesis 2016

Larry Ross Cathey Award – For best undergrad honors thesis in astronomy 2016

Sigma Pi Sigma – Member 2016

OBSERVING EXPERIENCE

Keck/HIRES - 51 nights

Lick/ShaneAO - 36 nights

WIYN/NEID - 29 hours

HET/HPF - 8 hours

COMMUNITY SERVICE AND OUTREACH

AAS 241 Splinter Session, Lead Organizer - I led the design and implementation of a splinter session at the AAS241 conference in Seattle where we held a community discussion on how to improve Astro PhD education and programs. Jan 11, 2023

Physics & Astronomy Community Excellence (PACE), Co-Leader. A UCI graduate student led organization providing a peer-mentoring program and career-building workshops for graduate students. Helped organize the program and run workshops. Academic years 2020-2023.

Physics Graduate Caucus (PGC), Treasurer. The student-run government representing graduate student interests to the department. Served for 4 academic years, 2019-2023.

Intro2Astro Summer Course, Grad student mentor. A 10 week free introduction to astronomy research for aspiring students/researchers/enthusiasts. Helped organize and run weekly seminars (recorded to YouTube) including fully leading two lessons per year. Summers 2021 and 2022

Osterbrock Sierra Conference Campus Leader. Helped plan, organize, and implement the annual camping conference/retreat for astro grad students across the UC system. Summer 2020 (entirely planned, but then cancelled due to Covid) and Summer 2021.

Science Olympiad Test Writer, Orange County Regional. Authored, proctored, and scored the *Astronomy B* and *Astronomy C* tests for local 5th and 6th graders. Hosted at UCI, February 15, 2020.

Referee for AAS Journals, I have been asked, and accepted, the role of referee for an academic paper in review. The paper was ultimately accepted for publication in The Astrophysical Journal.

MENTORING

Antony Rozic 2022
UCI Undergrad. Assisted in getting set up with software tools for Radial Velocity fitting as well as project design.

Adam Hagen 2022
High School student. Helped both in getting set up with the best software tools for working with TESS light curves and with applying new knowledge to search for transits.

Simon Olshan-Cantin 2022
High School student. Helped them with the software skills needed for searching archival radio data sets for Fast Radio Bursts (FRB)

David Zhou 2021
High School student. Helped both in getting set up with the best software tools for working with TESS light curves and with applying new knowledge to search for transits.

PRESENTATIONS

"Is Our Solar System Unique?", UCI Grad Slam Finals, Public Talk, March 09, 2023.

"Exploring New Dimensions in Time Series Analysis", AAS 241, Talk, Seattle, January 11, 2022.

"The Lives and Deaths of Barnard b", Astronomy on Tap, Seattle. Public Talk, In-Person. January 11, 2023

"Exploring New Dimensions in Time Series Analysis", Invited Talk, Ohio State Exoplanet Group, September 30, 2022.

"Stellar Activity Manifesting at a One Year Alias Explains Barnard b as a False Positive", AAS 240, Talk, Pasadena, June 14, 2022.

"Stellar Activity Manifesting at a One Year Alias Explains Barnard b as a False Positive", Exoplanets IV, Talk, Las Vegas, May 5, 2022.

Cal-Bridge Graduate Student Workshop, Cal-Bridge Program, Panel Member. In-person, April 24, 2022.

'Trends and Biases in the Now 5000 Strong Exoplanet Population", UCI Undergraduate Astronomy Club, Talk. In-person, April 13, 2022.

"TKS IX: HD 191939 Hosts a Multi-Planet System", Keck Science Meeting. Poster, Virtual. Sepember 9, 2021

"The Lives and Deaths of Barnard b", Astronomy on Tap, Penn State University. Public Talk, Virtual. June 21, 2021

"TKS IX: HD 191939 Hosts a Multi-Planet System", Emerging Researchers in Exoplanet Science (ERES) 2021, Talk. Virtual, May 24, 2021.

"My Research in Exoplanets", UCI Undergraduate Astronomy Club, Talk. Virtual, February 3, 2021.

"TKS V: HD 191939 Hosts a 5 Planet System", American Astronomical Society (AAS) 237th Meeting Oral Session 117, Talk. Virtual, January 11, 2021.

Teaching Assistant Professional Development Training, Panel Member. Virtual, November 5, 2020

The Search for M-M Eclipsing Binaries, Vanderbilt University Science Fair, Poster. September 17, 2015.

PROFESSIONAL DEVELOPMENT

CodeAstro - An astronomy-focused workshop teaching best coding practices for software development, testing, and publishing. June 21-24, 2022

Farmer-Trimble Graduate Observational Astronomy Workshop - A program designed for UC astronomy graduate students on observational techniques. Hosted at Lick Observatory over 5 nights. Learned telescope setup, observational strategies and limitations, and data reduction techniques. October 10-16, 2019

PRESS COVERAGE

"Planet Around Barnard's Star Probably Doesn't Exist At All", Scientias.nl (Dutch language science news website), May 26, 2021

"Astronomers Challenge Claim of Planet Around Barnard's Star", Sky & Telescope, May 21, 2021

"Astronomers Nix Idea Of Super-Earth Around Barnard's Star", Forbes, May 18, 2021

"A very stealthy alias: the impostor planet of Barnard's star", HPF Blog, May 17, 2021

"Astronomers use new technology developed with help from UC Irvine professor to look for habitable planets", LA Times, March 11, 2019

PUBLICATIONS

As of July 2023
Count = 42
h-Index = 15
460 total citations

First Author

Lubin, J., van Zandt, J., Holcomb, R., et al. *TESS-Keck Survey IX: Masses of Three Sub-Neptunes Orbiting HD 191939 and the Discovery of a Warm Jovian Plus a Distant Sub-Stellar Companion*, AJ, 163:101, February 2022.

Lubin, J., Robertson, P., Stefansson, G., et al. *Stellar Activity Manifesting at a One Year Alias Explains Barnard b as a False Positive*, AJ, 162:61, August 2021

Lubin, J., Rodriguez, J., Zhou, G., et al. *A Bright Short Period M-M Eclipsing Binary from the KELT Survey: Magnetic Activity and the Mass-Radius Relationship for M-dwarfs*, ApJ, 844:134, August 2017.

N Author

Murphy, J., Batalha, N., Scarsdale, N. et al. The TESS-Keck Survey. XVI. Mass Measurements for 12 Planets in Eight Systems, arXiv, June 2023

Hon, M., Huber, D., Rui, N. et al. A close-in giant planet escapes engulfment by its star, arXiv, June 2023

Dai, F., Schlaufman, K., Reggiani, H. et al. A Mini-Neptune Orbiting the Metal-poor K Dwarf BD+29 2654, arXiv, June 2023

Blunt, S., Carvalho, A., David, T. et al. Overfitting Affects the Reliability of Radial Velocity Mass Estimates of the V1298 Tau Planets, arXiv, June 2023

MacDougall, M., Petigura, E., Gilbert, G. et al. The TESS-Keck Survey. XV. Precise Properties of 108 TESS Planets and Their Host Stars, arXiv, June 2023

Zink, J., Hardegree-Ullman, K., Christiansen, J., et al. *Scaling K2. VI. Reduced Small Planet Occurrence in High Galactic Amplitude Stars*, arXiv, May 2023

Grunblatt, S., Saunders, N., Chontos, A., et al. *TESS Giants Transiting Giants III: An eccentric warm Jupiter supports a period-eccentricity relation for giant planets transiting evolved stars*, arXiv, November 2022

Yee, S., Winn, J., Hartman, J., et al. *The TESS Grand Unified Hot Jupiter Survey. II. Twenty New Giant Planets*, arXiv, October 2022

Dai, F., Masuda, M., Beard, C., et al. TOI-1136 is a Young, Coplanar, Aligned Planetary System in a Pristine Resonant Chain, arXiv, October 2022

Brinkman, C., Weiss, L., Dai, F., et al. *TOI-561 b: A Low Density Ultra-Short Period "Rocky" Planet around a Metal-Poor Star*, arXiv, October 2022

van Zandt, J., Petigura, E., MacDougall, M., Gregory, G., Lubin, J., et al. *TESS-Keck Survey XIV: 2 giant exoplanets from the Distant Giants Survey*, arXiv, September 2022

Beard, C., Robertson, P., Kanodia, S., et al. *GJ 3929: High Precision Photometric and Doppler Characterization of an Exo-Venus and its Hot, Mini-Neptune-mass Companion*, ApJ, 936:55, September 2022

MacDougall, M., Petigura, E., Fetherolf, T., Beard, C., Lubin, J., et al. *The TESS-Keck Survey. XIII. An Eccentric Hot Neptune with a Similar-Mass Outer Companion around TOI-1272*, AJ, 164:97, September 2022

Yee, S., Winn, J., Hartman, J., et al. *The TESS Grand Unified Hot Jupiter Survey. I. Ten TESS Planets*, AJ, 164:70, August 2022

Turtelboom, E., Weiss, L., Dressing, C., et al. *The TESS-Keck Survey. XI. Mass Measurements for Four Transiting sub-Neptunes orbiting K dwarf TOI-1246*, AJ, 163:293, June 2022

Beard, C., Robertson, P., Kanodia, S., et al., *TOI-1696 and TOI-2136: Constraining the Masses of Two Mini-Neptunes with HPF*, AJ, 163:286, April 2022

Reefe, M., Luque, R., Gaidos, E., et al. *A close-in puffy Neptune with hidden friends: The enigma of TOI 620*, AJ, 163:269, June 2022

Terrien, R., Keen, A., Oda, K. et al. *Rotational modulation of spectroscopic Zeeman signatures in low-mass stars*, ApJL, 927:L11, March 2022

Grunblatt, S., Saunders, N., Sun, M., et al. *TESS Giants Transiting Giants II: The hottest Jupiters orbiting evolved stars*, AJ, 163:120, March 2022

Canas, C., Mahadevan, S., Bender, C., et al. *An eccentric Brown Dwarf eclipsing an M dwarf*, AJ 163:89, February 2022

Dalba, P., Kane, S., Dragomir, D., et al. *The TESS-Keck Survey. VIII. Confirmation of a Transiting Giant Planet on an Eccentric 261 day Orbit with the Automated Planet Finder Telescope*, ApJ, 163:61, February 2022

El Mufti, M., Plavchan, P., Isaacson, H., et al. *TOI 560 : Two Transiting Planets Orbiting*

a K Dwarf Validated with iSHELL, PFS and HIRES RVs, arXiv December 2021

Wang, X., Rice, M., Wang, S., et al. *SOLES II: The Aligned Orbit of WASP-148b, the Only Known Hot Jupiter with a Nearby Warm Jupiter Companion, from NEID and HIRES*, ApJL: 926:L8, February 2022

Heidari, N., Boisse, I., Orell-Miquel, J., et al. *HD207897 b: A dense sub-Neptune transiting a nearby and bright K-type star*, MNRAS, 658:A176, February 2022

MacDougall, M., Petigura, E., Angelo, I., Lubin, J. et al. *The TESS-Keck Survey. VI. Two Eccentric sub-Neptunes Orbiting HIP-97166*, AJ, 162:265, December 2021

Scarsdale, N., Murphy, J., Batalha, N., et al. *TKS V. Twin sub-Neptunes Transiting the Nearby G Star HD 63935*, AJ, 162:215, November 2021

Kanodia, S., Stefannson, G., Canas, C., et al. *TOI-532b: The Habitable-zone Planet Finder confirms a Large Super Neptune in the Neptune Desert orbiting a metal-rich M dwarf host*, AJ, 162:135, October 2021

Llop-Sayson, J., Wang, J., Ruffio, J., et al. *Constraining the Orbit and Mass of ϵ Eridani b with Radial Velocities, Hipparcos IAD-Gaia DR2 Astrometry, and Multi-epoch Vortex Coronagraphy Upper Limits*, AJ, 162:61, August 2021

Chontos, A., Murphy, J., MacDougall, M., et al. *The TESS-Keck Survey: Science Goals and Target Selection*, AJ, 163:297, June 2022

Dai, F., Howard, A., Batalha, N., et al. *TKS X: Confirmation of TOI-1444b and a Comparative Analysis of the Ultra-short-period Planets with Hot Neptunes*, May 2021

Winters, J., Cloutier, R., Medina, A., et al. *A Second Planet Transiting LTT 1445A and a Determination of the Masses of Both Worlds*, AJ, 163:168, April 2022

Rubenzahl, R., Dai, F., Howard, A., et al. *The TESS-Keck Survey IV: A Retrograde, Polar Orbit for the Ultra-Low-Density, Hot Super-Neptune WASP-107b*, AJ, 161:119, March 2021

Weiss, L., Dai, F., Huber, D., et al. *The TESS-Keck Survey II: An Ultra-Short Period Rocky Planet and its Siblings Transiting the Galactic Thick-Disk Star TOI-561*, AJ, 161:56, February 2021

Dai, F., Roy, A., Fulton, B., et al. *TKS III: A Stellar Obliquity Measurement of TOI-1726 c*, AJ, 160:193, October 2020

Canas, C., Stefannson, G., Kanodia, S., et al. *A warm Jupiter transiting an M dwarf: A TESS single transit event confirmed with the Habitable-zone Planet Finder*, AJ, 160:147, September 2020

Carleo, I., Gandolfi, D., Barragan, O., et al. *The multi-planet system TOI-421 – A warm*

Neptune and a super puffy mini-Neptune transiting a G9 V star in a visual binary AJ, 160:114, September 2020

Robertson, P., Stefansson, G., Mahadevan, S., et al. *Persistent starspot signals on M dwarfs: multi-wavelength Doppler observations with the Habitable-zone Planet Finder and Keck/HIRES*, ApJ, 897:125, July 2020

Cloutier, R., Rodriguez, J., Irwin, J., et al. *TOI-1235 b: a keystone super-Earth for testing radius valley emergence models around early M dwarfs*, 160:22, July 2020

Dalba, P., Gupta, A., Rodriguez, J., et al. *The TESS-Keck Survey I: A Warm Sub-Saturn-mass Planet and a Caution about Stray Light in TESS Cameras*, AJ, 159:241, May 2020

ABSTRACT OF THE DISSERTATION

New Dimensions in Time-Series Analysis for Exoplanet Detection

By

Jack Lubin

Doctor of Philosophy in Physics

University of California, Irvine, 2023

Assistant Professor Paul Robertson, Chair

As one of the ultimate goals of the field of exoplanet science — discovering an Earth-mass planet orbiting a Sun-like star at 1 AU — begins to come into reach from the perspective of instrumentation, there are still many challenges in data analysis to overcome before such a discovery can be realized. The most promising method for discovering this Earth-twin, the radial velocity (RV) method, is one of the most successful ways of finding exoplanets. Through measuring the Doppler shift of light from a star due to the gravitational interaction between star and planet, the RV method looks for periodic signals in the changing velocity of the star. When a periodic signal is identified as planetary in origin, RVs also allow us to measure the mass of the planet.

In addition to a powerful discovery technique, the RV method is a powerful follow up tool. Planet mass, combined with radius as obtained from the transit method, allows us to compute the planet's bulk density. With density, it is possible to theorize what materials make up these planets and begin to ask questions concerning habitability. On this note, without a precise mass one cannot properly interpret transmission spectra and reveal insights into a planet's atmosphere. Planet mass also allows for investigations of planet formation and evolution. Lastly, without planet masses, one cannot investigate the dynamics of a system. Without a well-measured mass from RVs, a planet and its greater system cannot be

characterized in detail.

While the new era of Extreme Precision Radial Velocity (EPRV) spectrographs is allowing us to reveal ever smaller RV signals in our data sets, not all of these signals are planetary in origin. We expect a planet's signal to be strictly periodic: the frequency, amplitude, and phase of the signal should be consistent across all time spans. But more and more we are learning that quasi-periodic stellar activity induced signals plague our data sets. These signals are not consistent in time, frequency, amplitude, or phase. They come and go, sometimes stronger or weaker, with or without phase shifts. But nonetheless, our current methods for detecting periodic signals have trouble distinguishing between a strictly periodic planetary signal and a quasi-periodic activity signal. Properly and consistently identifying and characterizing activity will be the prime inhibitor to small planet detection and, by extension, their mass measurements. In this dissertation, I address the issue of distinguishing between strictly and quasi periodic signals in RV data sets.

First, I demonstrate the challenge, importance of, and lessons learned from measuring small RV signals to determine precise masses of planets. I use the exciting 5+ planet system HD 191939 as a demonstration of the importance of detailed intra-system studies. This scaled-down Solar System hosts three inner transiting sub-Neptunes, a shepherding Saturn-mass planet, and a very long period super-Jupiter. Our precise mass measurements allow for a deep dive into the compositions, formation, evolution, and dynamics of this system in a way that many more systems will be treated in the future.

Second, I describe my work on identifying quasi-periodic signals in RV data sets. Using Barnard's star as a test case, I explore how the 145-day stellar rotation period signal was aliased at one year to create a 233-day false positive planet detection. In the process, I develop new techniques for isolating the localized activity signal in time. This example stresses the importance of understanding the lifetime of all signals in a RV data set.

Lastly, with the special case of Barnard's star as motivation, I design and build a new software package, the ℓ_1 Apodized Periodogram, or `Lia`, with the explicit goal of estimating the decay lifetime of periodic signals. `Lia` will help us better understand our RV data sets, providing a holistic picture of each signal which allows us to more confidently describe their astrophysical origins.

In all, the main effort of my dissertation is to develop new methods and techniques for consistently distinguishing between strictly and quasi periodic signals in RV data sets. This effort will help set us up for discovering small RV signals and more precisely measuring known planet masses. Both of these endeavors will be vital in the broader search for discovering a true Earth-twin planet.

Chapter 1

Introduction

1.1 Exoplanets

1.1.1 Overview of Relevant Detection Methods

Radial Velocity

The first exoplanet confirmed around a Sun-like star, 51 Pegasi b [148], was discovered using the radial velocity (RV) technique. This method takes advantage of the gravitational pull between the planet and the host star. The two bodies orbit their shared center of mass, with the planet sweeping a wide orbit and the star moving through a much smaller orbit. Looking down from above onto this orbital dance, both star and planet move through a two dimensional ellipse. If viewed as edge-on to the plane of this ellipse, the motion can be collapsed down to a one dimensional back and forth action. To an observer on Earth, this will appear as if the star is moving in and out of the plane of the sky, or the radial direction, see Figure 1.1. By measuring the velocity of the star at many different times and tracking

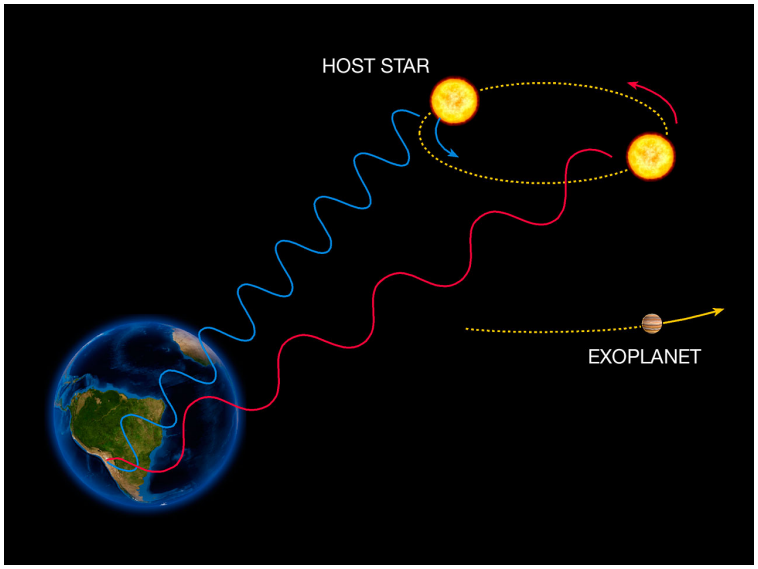

Figure 1.1: Artist's impression of the RV method in action. The Doppler-shifted light of the host star due to the unseen planet's motion is detectable with precise spectrographs. Image credit: ESO.

how the velocity changes, one can trace the motion of the star and infer the existence and properties of the unseen planet.

The velocity of the star is calculated from the Doppler shift of the light in the stellar spectrum. As the star moves towards and away from Earth observers, absorption lines in the spectra are shifted in wavelength space. The direction of the shift in wavelength space determines the direction of the star's motion: shifts to longer wavelengths (to the red side of the spectrum) indicate the star is moving away from us and shifts to shorter wavelengths (to the blue side of the spectrum) indicate the star is moving towards us. In effect for calculating RVs, this sets the plus/minus sign on the velocity magnitude. That magnitude is determined from the size of the shift in wavelength space, with larger shifts, as measured from the rest frame of the star or from a stellar template, corresponding to larger velocity magnitudes. For the constant and consistent signal that a planet imparts, one expects for all absorption lines to shift linearly in wavelength space by the same amount. By obtaining many stellar spectra over many nights and using them to calculate the RV at those timestamps, one hopes to sample the strictly periodic motion of the star due to an unseen planet.

Once RVs are computed, the primary observables of the RV method are the stellar orbital period, or how long it takes for the star to complete one orbit around the center of mass, and the RV semi-amplitude, or the magnitude of the variation in the star's velocity across one orbit. These observables correspond to parameters of the associated planet. First, the orbital period of the planet will match that of the star exactly one to one. Next, the semi-amplitude relates to the mass of the planet via a Newtonian gravitational effect [163]:

$$K = \left(\frac{2\pi G}{P}\right)^{\frac{1}{3}} \frac{M_p \sin i}{(M_* + M_p)^{\frac{2}{3}}} \frac{1}{(1-e^2)^{\frac{1}{2}}} \tag{1.1}$$

where P is the orbital period in units of seconds (to match the units of the gravitational constant) and masses are given in a shared unit of choice. The e term represents the orbital eccentricity, see below. This framework can be further extended to a more general estimate and simplified to only circular orbits (and assuming planet mass is much smaller than host star mass) via:

$$K = 28.4 \text{ m/s} \left(\frac{P}{1\,\text{yr}}\right)^{-\frac{1}{3}} \left(\frac{M_p \sin i}{M_J}\right) \left(\frac{M_*}{M_\odot}\right)^{-\frac{2}{3}} \tag{1.2}$$

where P is now the orbital period in years, M_p is the planet mass in units of Jupiter masses (M_J) and M_* is the stellar mass in unit of solar masses ($M_\odot$). All else equal, the larger the planetary mass, the larger the velocity semi-amplitude. Similarly, shorter orbital periods (corresponding to shorter semi-major axis of the orbit via Kepler's Second Law of Orbital Motion) and/or smaller stellar masses leads to larger velocity semi-amplitudes. Through this equation, we can plug in numbers of some Solar System planets to serve as a benchmark for exoplanet detection. For example, our Jupiter imparts a $\sim$12 m/s RV signal over its 12

year orbital period whereas our Saturn imparts only a 2.75 m/s RV signal. Lastly, to find a planet like our own Earth in terms of mass and orbital period requires measuring a 9 cm/s RV signal.

Eccentricity, or the deviation into an elliptical orbit from a pure circular orbit, is a further measurable directly traced by RVs. This parameter is coupled with another measurable, the argument of pericenter (ω) which represents the angle from an arbitrary, but defined, line of sight position to the point in the orbit where the planet is closest to its host star. Together, with the semi-major axis distance which can be estimated from Kepler's Second Law of Orbital Motion and the observed orbital period, they describe nearly (see below) the full orbital path of the planet around the star.

Finally, the last measurable from RVs is the time of periastron. This is a point in time in which the planet is positioned at the periapsis position. The periapsis position is the point of the orbit that places the planet closest to the host star. For circular orbits, all positions in the orbit are equally close and so this angle is arbitrary. The time of periastron merely sets a reference time from which we can track the position of the planet in its orbit at any past or future time.

These 5 measureable parameters, all discerned from fitting a Keplerian model to the RVs, fully describe the orbit of the planet in two dimensions. To ascertain the third dimension, one must measure two more parameters. First, as tempered by the $\sin i$ in the equations above, the mass measurement from RVs is actually a lower limit. Since the inclination of the orbit, or how edge-on it appears to us, is unknown, the component of the total velocity that is in the radial direction is unknown. The larger the system's inclination, the smaller the radial component is of the total velocity vector and so the observed planet mass will scaled down by a factor of the sine of the inclination angle, $\sin i$. Second, the longitude of the ascending node (Ω), which sets the angle between the observer's line of sight and the point in the orbit at which the planet's inclination takes it from below to above the reference

plane of the orbit. Unfortunately, neither of these parameters can be measured from RVs alone.

While the RV method is highly successful in planet discovery, there are two primary disadvantages it. First, there is no way to measure the planet radius from this method. Second, the method is slower than others. To measure an RV, one must observe a single star at a time. Additionally, it is very likely that confidently measuring the signal will require multiple orbital periods worth of time to conduct observations. The RV method is also subject to far more sources of error and noise, including stellar activity induced signals exhibiting in the data in the same way that true stellar motion signals are expected to exhibit; more on this in §1.2.

Despite these, there are two primary advantages of the RV method that make it more than worthwhile to continue RV observations. First, the method allows for a direct measurement of the mass of the planet. In the field of astronomy, mass is one of the most important characteristics of any object. For example, the stellar life cycle is almost exclusively determined by initial formation mass. Similarly, planetary mass informs us of possible formation history, helps us classify planets into categories, and provides insight into possible material make up. It also provides an invaluable data point for all kinds of dynamical studies of planetary systems which further informs the way systems evolve.

Second, the RV method is valid for nearly all inclination angles of the system (even though the inclination value itself cannot be estimated from the RVs themselves). While the RV signal of a planet is more easily measured for edge on systems ($i = 90°$), the method works for all inclinations except a true face-on orbit ($i = 0°$). This allows us to probe longer period planets, a whole population in itself (see §1.1.2) where the transit probability (see §1.1.1) is essentially zero.

For all these reasons, the RV method has been a standard detection and characterization

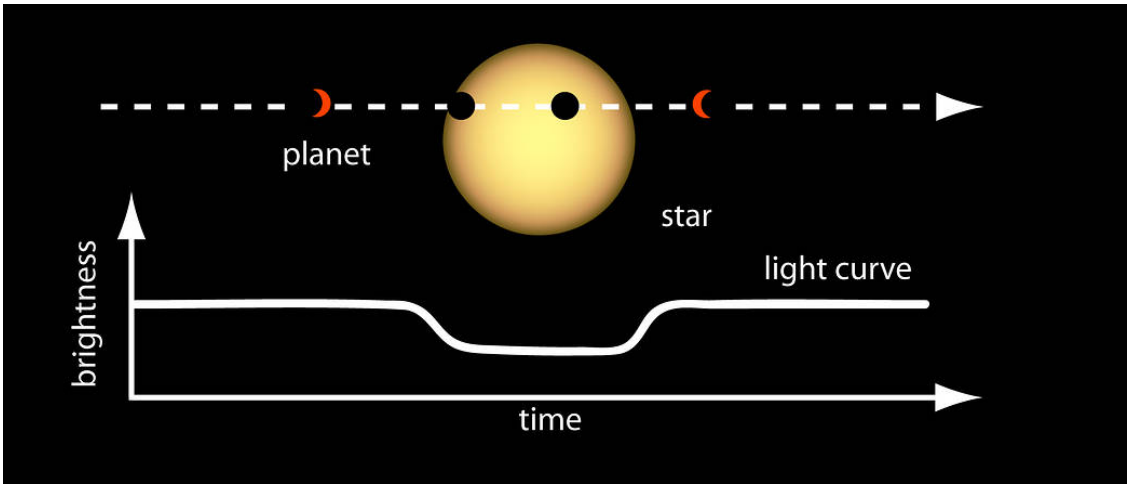

Figure 1.2: As a planet passes in front of its host star, it blocks a measurable amount of light. Credit: NASA Ames.

technique since the beginning of the field of exoplanet science.

Transit

The most successful method of planet detection in terms of raw number of planets discovered is by far the transit method. This technique takes advantage of the chance alignment of the host star, the planet, and observers on Earth. In such a scenario, once per orbit the planet passes directly between observers on Earth and its host star. At this time, the planet will physically block a small amount of the light from the star, decreasing the overall observed brightness of the star, see Figure 1.2. By the amount of the drop in flux, $\frac{\Delta \mathrm{F}}{\mathrm{F}}$, we can directly compute the radius of the planet, R_p:

$$\frac{\Delta F}{F} = \left(\frac{R_p}{R_*}\right)^2 \tag{1.3}$$

assuming the radius of the star, R_*, is known.

By observing multiple transits of the same planet, we can determine the orbital period very precisely by measuring the time between successive transits. Then through Kepler's Second Law, the orbital period is directly related to the semi-major axis of the planet's orbit (while also accounting for the star's mass and approximating that the planet mass is negligible). Through modeling the light curve, one can derive additional parameters including the inclination, which relates to the impact parameter, and is derived from the transit duration time. With a few assumptions, one can also make an estimate of the eccentricity.

Despite the thousands of planets discovered via transits, there are two primary disadvantages to the method. First, there is no way to directly measure planet mass. Second, the method heavily depends the precise geometric alignment of system with us on Earth. The probability of any planet having this precise alignment is given by:

$$P = \frac{R_*}{a} \tag{1.4}$$

where a is the semi-major axis and R_* is the stellar radius. For a given stellar radius, it is less likely a planet will transit as its semi-major axis increases. This heavily biases the detection of planets via the transit method to those with small semi-major axes (short orbital periods).

But the success of the transit method far outweighs its drawbacks and it has two primary advantages to other methods. First, the planet's radius is directly calculable from the transit depth, with error primarily limited by the uncertainty on the stellar radius. This is highly valuable, as radii can be very accurately and homogeneously measured. This provides a unique insight into planetary populations and hints at deeper astrophysics of planetary formation and system evolution, see §1.1.2 below. Second, transit surveys are fast. A single

telescope can observe a wide field of thousands of stars and monitor each one simultaneously for transit events [178, 34, 191].

Other

Beyond the two primary detection methods, there are a host of additional ways to discover exoplanets. Combined, these "other" methods have discovered only 304 planets (NASA Exoplanet Archive, access date June 15, 2023). Nonetheless, they are interesting methods in their own right, and will likely play larger roles in the future.

Astrometry works very similarly to the RV method in that it searches for the gravitational tug of the planet on the star. Rather than searching for the radial component of this interaction, astrometry searches within the plane of the sky. This is completely orthogonal to the radial motion. Astrometric signals are recovered in data of the precise position of a star relative to the background field of stars. Also like the RV method, astrometry is a time series measurement, requiring many observations over a long baseline. Astrometry preferentially discovers massive planets on long period orbits. For this reason, it could be a major contributor to our understanding of true Jupiter-analogs. The first spaced-based mission to study precision astrometry was Hipparcos [1], operating from 1989 to 1993. More recently, a successor mission, Gaia [88], was launched in 2013 and has been periodically releasing data batches which include astrometric measurements. To date, only a single planet has been discovered via astrometry (many known planets have been retroactively found in astrometric data), but with newer Gaia releases coming, more planets are expected to be revealed this way.

Direct Imaging is in some ways the ultimate pursuit of the exoplanet field. As the name suggests, it is the only method which *directly* measures the existence of the planet. The others merely infer the planet's existence from indirect methods. Direct Imaging is as simple

as taking a picture of the planet; but as simple as it seems it is very difficult to achieve. Stars are orders of magnitude brighter than their planets, so their light drowns out the light reflected off a planet as well as any thermal emission from the planet. Direct Imaging surveys employ coronagraphs, physical barriers placed in the light path of a telescope to block out the light from the star. These coronagraphs help to reveal the residual light from a system's planetary bodies. One of the long term goals of the field is to directly image an Earth-twin planet. This will likely be first attempted by the next generation large ground-based telescopes [242] and/or the next "Great Observatory", an effort defined by the 2020 Astronomy Decadal Survey [169] to build a space-based successor to Hubble, Spitzer, and JWST which will be capable of directly imaging Earth-twin planets.

Analysis of transit timing variations (TTVs) [3] is a technique that makes use of precise timing of transit events. In a single planet system, a transiting planet will always transit precisely on time and this timing is highly predictable. However, when multiple planets exist in the system, they will gravitationally interact, tugging on each other to speed up or slow down. This causes the precisely predicted transit times of each of the planets to occur slightly early or late. By measuring just how early/late a planet's transits occur over many transit events, one can infer the existence of non-transiting planets in the system and make an estimate of the mass and period ratios of the planets. Detecting TTVs requires high precision and high cadence photometry over many orbital periods of the transiting planet, sometimes requiring years of data.

The last notable detection method is microlensing [98], which leverages Einstein's general relativity. As a star passes between Earth and a more distant background star, it will act as a gravitational lens and magnify the light from that background star. If the foreground star additionally hosts a planet, that planet can further act as a secondary lens. The magnitude and time span of the planet's lensing effect will be smaller and shorter than the stellar lensing effect, but detectable as a deviation from the star-only lens scenario. Because this

method requires a chance alignments of two stars, microlensing is only practical for a large survey when observing towards the galactic bulge, where the density of stars is much higher than elsewhere in the galaxy. Furthermore, also due to the chance alignment, microlensing planets are nearly always single event detections, and are not able to be followed up by other means. Microlensing is particularly sensitive to planet populations that other methods are specifically insensitive to, namely small planets on 1-10 AU orbits. Microlensing will play a more prominent role in exoplanet detection in the coming years. Microlensing also requires high precision and high cadence photometry. The Nancy Grace Roman Space Telescope (NGRST) [217] is planning a microlensing survey of the galactic bulge and is expected to find many thousands of small, long period planets which will help us understand the statistics of this under-sampled population [176].

1.1.2 Populations

As the field of exoplanet science continues to flourish, the total population of exoplanets is exploding in size. To date of this dissertation, astronomers have collectively discovered 5445 exoplanets (NASA Exoplanet Archive, access date June 15, 2023), representing just about three decades of hard work from international teams of researchers. Figure 1.3 shows the explosion of discoveries in the short history of our field. As instrumentation and techniques have improved, new sub-populations within the known catalog of planets have begun to emerge. In this section, I provide an overview of some of these sub-populations.

Looking at Figure 1.4, plotting planet mass (left) and radius (right) vs. orbital period for all known planets (NASA Exoplanet Archive), one immediately sees the distinct populations and trends discovered to date. Most notably, there appears to be a few primary clusters of planets. Part of this clustering is an artifact of well understood biases. For example, looking at the radius vs. period diagram, there is a fairly hard vertical edge around $\sim$300

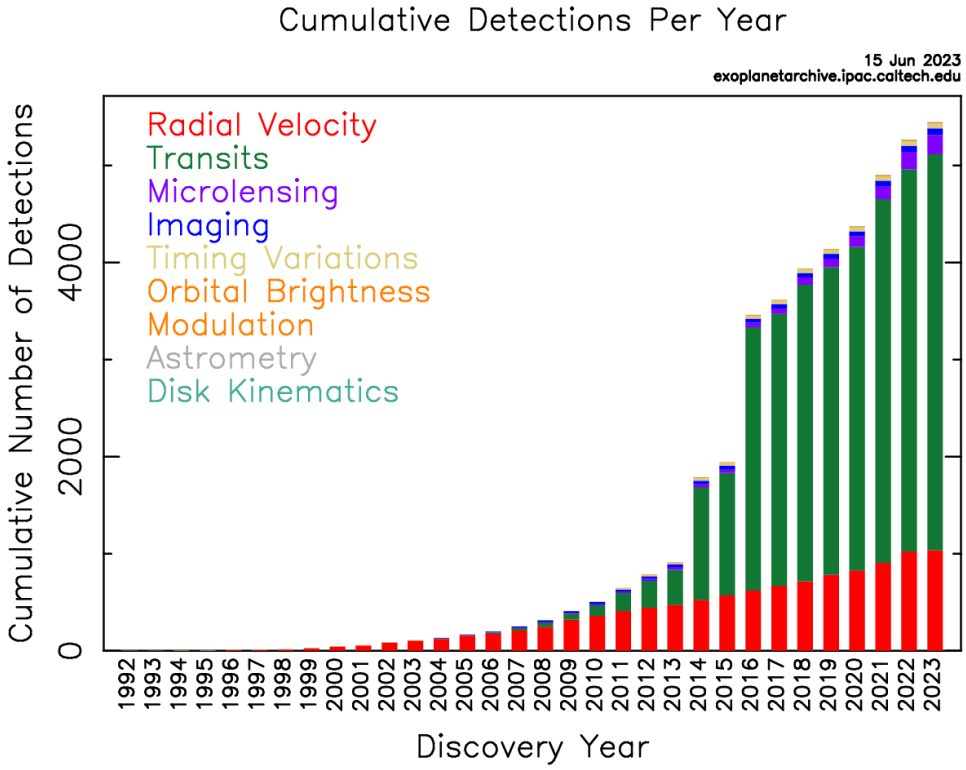

Figure 1.3: Cumulative exoplanet detections per year. The size of the known population initially grew very slowly. Then the known population dramatically increased in size after the Kepler Mission's first big result in 2014 [34] and has continued to grow exponentially. Colors are coordinated to detection method. From the NASA Exoplanet Archive.

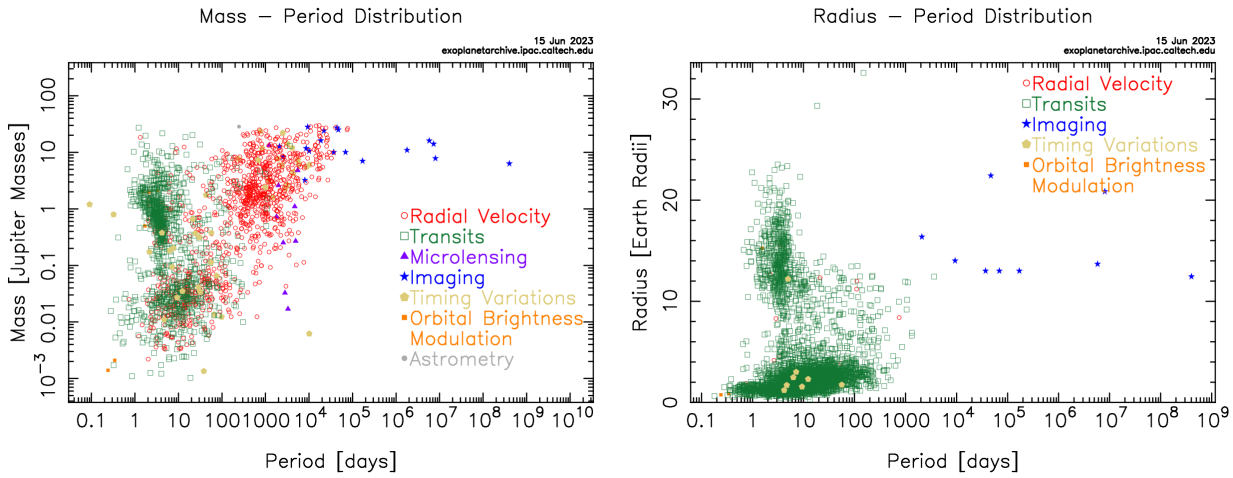

Figure 1.4: **Left:** The known population of planets with measured masses versus their orbital periods. **Right:** The known population of planets with measured radii versus their orbital periods. Colors are coordinated to detection method. From the NASA Exoplanet Archive.

days (excluding the imaging targets), but even then the vast majority of planets have orbital periods less than ∼100 days. This is an artificial trend in that the transit method struggles to discover planets beyond an orbital period of ∼100 days due to the extremely small transit probability at these separations (see §1.1.1 above). Additionally, the observing strategies most often employed by large surveys severely restrict detections beyond this soft boundary. Similarly, there is a hard lower limit on radius at about half an Earth radius from sub-day periods to about 30-day periods before the lower limit begins to turn upwards, creating a slant along the bottom right edge of the cluster. This minimum radius is not astrophysical (as far as we know), but rather instrumental. Our imperfect instruments are not capable of achieving the necessary SNR to measure smaller radii, at least not confidently. All orbital periods suffer, but longer periods suffer greater since fewer transit events equate to less certainty in ruling out false positive transit detections. Next there are clusters, or edges of clusters, that are set by seemingly truthful sampling of planets across the galaxy.

First are the Hot Jupiters that occupy the top left portion of both plots. The first confirmed planet around a Sun-like star, 51 Pegasi b [148], is a Hot Jupiter. This class of planet surprised astronomers, as we have nothing like it in our Solar System. Just how a Jupiter-

like planet finds itself in this short orbit position is still an open area of research. These planets are thought to form beyond the ice line of the system, the distance from the host star beyond which temperatures are cool enough for volitiles and ices to condense, and then the planet migrates into its current position through one of a variety of theoretical mechanisms stemming from the Kozai Mechanism [122], including descriptions from [251], [75], and[129]. These theories make predictions on the distribution of eccentricities among Hot Jupiters and they all but require Hot Jupiters to exist in single planet systems. They predict that as the migration occurs, the Jupiter's mass would gravitationally slingshot nearly all other planets out of the system. However, studies find that the Hot Jupiter companion occurrence rate varies with the Hot Jupiter's orbital period and that Hot Jupiters may not be as lonely as predicted [250]. Furthermore, despite our confirmed count in the hundreds, occurrence rate studies show that Hot Jupiters themselves are actually quite rare [109, 249]. There is also a gradient in occurrence rates based on stellar types [68].

Because the signals they produce in both transit and RV are so large, Hot Jupiters are fascinating first-test cases for all kinds of interesting planetary astrophysics. They are sometimes found to be inflated [90] by their extreme environments. Hot Jupiters have been used to make phase curves [12], measure transmission spectra [214], study orbital precession [174], make obliquity measurements [8], and more. In many ways, Hot Jupiters are the test subjects for many of the detailed characterization studies that astronomers eventually hope to perform on all types of planets.

The next major population is the Cold Jupiters, or Jupiter-analog planets. These are discovered nearly exclusively by the RV method (for now, until Gaia delivers astrometry discoveries) because their wide orbits make their transit probability essentially zero. Therefore, they are only seen in the mass-period diagram. Because these do not transit, less is known about them. We do know that they occur at low rates of 3-6% [202, 247], but note that this is higher than the Hot Jupiter rate of $\sim$1%. Interestingly, Jupiter-analogs appear to occur

far more frequently in systems that have small, interior planets, anywhere from 40-100% of such systems [41, 200]. The mass-period diagram also highlights the observed gap in Jovian planets at middle length periods between ∼10-200 days. Our instruments are more than capable of detecting Jupiter-sized transiting planets, and astronomers routinely detect the transits of smaller planets at these orbital periods. Therefore, this severe under-density of detections is surely a natural consequence rather than an observational bias.

Moving to smaller mass and radius regimes brings in the most common type of planet that we know of to date, those under 4 $R_\oplus$. Kepler statistics reveal these occur ubiquitously across the galaxy [180]. These planets are further found in high multiplicities within the same system [24] and there are further hints of a larger trend in architectures referred to as "peas-in-a-pod", where similar sized planets are found in similarly spaced orbits [245]. The small planet population is further bifurcated into two sub-populations, colloquially known as the sub-Neptunes and the super-Earths. The line between the two populations is blurred. Ideally, the difference would be that super-Earths are terrestrial with thin atmospheres while sub-Neptunes are thick gaseous atmospheres enveloping a solid core. However, at the present time it is rarely possible to make this distinction for a given planet with any confidence. Instead, we currently use the two terms to denote an observational discriminator: the radius gap. First predicted in works such as [171], the radius gap was described from observations in [84] as the bimodal distribution in radii of small planets. There exists a large pile up in the occurrence rate of planets with a radius near 1.3 $R_\oplus$, then a dearth of planets near 1.8 $R_\oplus$, and finally another peak in the distribution at 2.4 $R_\oplus$. The leading theory to explain the radius gap describes how these two populations are instead one: all sub-Neptune planets form with a large rocky core and a thick H/He atmosphere. Then, some planets have their atmospheres stripped through stellar wind. This mechanism leaves behind just the cores on the low side of the radius gap while the unstripped planets remain the high side of the gap. This theory is testable: younger planets should preferentially sit on the high side of the gap; and for a system with planets on each side of the gap, the small radius planet should always

exist interior to the large radius planet of the system [51].

Next, there are two notable regions of parameter space where there is a dearth of planets for reasons not associated with detection limits. The first is described as the Neptune Desert. This is the region of the radius-period diagram between $\sim$2 and $\sim$10 $R_\oplus$ planets at periods less than $\sim$4 days where there are very few planets confirmed. This scarcity does not appear to come from any instrumental or observational bias: we detect many Jovians and super-Earths at these short periods and therefore know our instruments are capable of detecting planets of Neptune sizes and of detecting planets at these orbital periods. One explanation for the Neptune Desert is that during migration from further out in the disk, strong stellar winds of young stars strip the atmospheres entirely [149], leaving only small radius super-Earths in hot orbits. Next there is a similar desert of Jovian planets between the Hot Jupiter population and the Jupiter-analog population, with a sharp drop off in transiting Jovians beyond 10 days, as discussed above. Similarly, at all orbital periods, there are very few planets with radii between 6 and 12 $R_\oplus$, representing planets potentially like our own Saturn at 9 $R_\oplus$. Both of these gaps are evident in the mass-period diagram as well, and therefore likely represent a true scarcity in this size planet, at least out to a few AU where we have been able to search.

Today's picture of the population and sub-populations of planets is only the beginning. We will continue to try to fill in and/or understand the gaps in these diagrams with more observations. Similarly, we will expand the boundaries and edges that define the current population as ever more precise instrumentation comes online. Eventually we will reveal the population of Earth-like planets and then smaller Mars-like planets. We will continue to probe longer timescales, finding Uranus and Neptune analogs as well. The more we find out there, the more we will be able to place our own Solar System in context with the underlying distribution of planetary systems across the galaxy.

1.2 Stellar Activity

Stellar activity is a catch-all term to describe a wide variety of phenomena originating from magnetic cycles and forces within stars. This activity can imprint Doppler shifts, or apparent shifts, in a stellar spectrum. These shifts are in opposition of what one hopes to measure when analyzing a stellar spectrum to search for planetary signals: a Doppler velocity shift from the reflex motion of the star due to the presence of an orbiting planet. Stellar activity shifts are by-catch in the stellar spectrum; they imprint into the calculation of the RVs as their own, unwanted signals. These signals can either mask true planetary signals, causing a false negative detection, or masquerade as planetary signals, causing a false positive detection.

The most distinctive observational difference between a planetary signal and a stellar activity induced signal is the signal's lifetime. True Keplerian planetary signals will be consistent across all observation times. Except in highly unique and rare scenarios, planetary signals will not vary in their frequency, phase, or amplitude. No matter what times the star's velocity is sampled, the same signal will persist. On the other hand, stellar activity signals are quasi-periodic. They will grow and decay, living over a characteristic timescale. They may come and go, returning with potential changes in frequency, and/or phase shifts, and/or amplitude variations. The difference in signal lifetimes is the primary lighthouse which will guide the exoplanet-searching astronomer to properly identify the astrophysical origin of a signal in question. The challenge of properly distinguishing a signal's origin will be a primary focus of this dissertation.

There are many varieties of stellar activity. Each manifests from a different stellar phenomenon and each plays out on its own timescale. Over the young history of exoplanet detection via the RV method, many strategies have been developed for mitigating contamination from each variety. For this dissertation, the most relevant variety is from starspots, faculae, and plage. Here I will detail these varieties of stellar activity and mitigation strate-

gies.

First is perhaps the most common from a historical perspective: star spots. The photosphere of a star is not a perfect, unblemished surface. Star spots form in the photosphere as a result of magnetic fields suppressing local convection [260, 261]. The suppressed region will cool relative to the surrounding regions as hot gas cannot be replenished to the surface. The cooler surface temperature of this area appears dark, hence the name of spot. For our Sun, sunspots generally form in the active latitudes within 30° of the equator [216].

As a starspot rotates from the limb to the face of a star, RV measurements are susceptible to contamination in two forms. First, a spot on or near the limb of the star breaks the symmetry of the face of the star. As the star rotates, the approaching limb is blue-shifted and the receding limb is red-shifted. When this symmetry is broken by a spot, net blue or red shifts can be pick up in the observed spectrum and imprinted in measured RV. Additionally, this breaks the symmetry of the Doppler broadening of all absorption lines, also due to the rotational velocity of the star. Secondly, the lower temperature of the starspot region affects the stellar spectrum as a whole.

Due to their intrinsic connection to the stellar rotation period, starspot signals most often present at the rotation period, or its harmonics [32], or as I will describe in detail later, at the associated aliases. For this reason, potential RV planetary signals at any of these periodicities must be treated with extreme care to determine the veracity of the signal's origin.

Spot lifetimes vary across stellar type. Sun-like G-dwarf stars are known to have spot lifetimes on the order ∼3 stellar rotations, depending on spot size [94]. For the typical stellar rotation period of G-dwarfs ranging from 10 to 30 days [164, 151, 107], this means a typical starspot will survive anywhere from 30 to ∼90 days. Similarly, while a single spot grows and decays, many other spots are similarly growing and decaying on similar timescales

but at time and/or phase offsets from one another. This leads to the inherent quasi-periodic nature of these kinds of signals: signal strength will come and go, often returning with a phase shift, or even a frequency shift depending on spot formation latitude and the degree of differential rotation of the star [216]. All this combined, it is not as easy as simply waiting out an active cycle of the star for a future quieter cycle where it would be more advantageous to observe the star.

Giles et al. 2017 [94] additionally note that spot lifetime and spot size as a percentage of the total stellar face both increase as the star's effective temperature decreases. This is in line with additional studies that show star spots on M dwarf stars can live for 10+ stellar rotations [196, 197, 62]. Through this long lifetime, coupled with potentially long rotation periods for these stars in excess of 100+ days [162, 223], means that spots can persist for over 1000 days on M dwarf stars. Timescales this long can begin to rival entire observing baselines of stars, and certainly persist for longer than a single observing season for any given star. When that is the case, it is easy to see how spot driven RV signals can appear to be robust across the entire observation window and therefore seem to be planetary in origin.

Two additional stellar activity phenomena related to starspots are faculae and plages. Both are, in some ways, the inverses of starspots in that they are bright regions in the photosphere and chromosphere, respectively. They very often accompany spots and are formed out of the same active regions of the star, driven by magnetic field lines that increase hot gas flow towards the surface [183]. They further break the symmetry of the blue and red shifted halves of the stellar face and suppress blueshifts from granulation.

While this kind of stellar activity can imprint into RV measurements, there are also separate features in the stellar spectrum which are known to be sensitive to activity, aptly named *activity tracers*. These are most often developed to measure the depth of a specific absorption line and/or any emission in the core of the line. One of the first developed activity tracers is the Mt. Wilson S-Index [246]. The S-Index traces heating in the chromosphere of a star by

measuring the ratio of emission in the cores of the Ca II H&K doublet lines to the nearby continuum [112, 74]. The S-Index is computed by measuring the the photon counts within a narrow, triangular bandpass centered around the H and K lines at 3968.469 Å and 3933.663 Å, respectively. The sum of counts is then divided by the counts in a nearby region of the continuum. An increase in chromospheric heating, which the S-Index traces, has been linked to an increase in magnetic activity [215], which further drives the creation of phenomena like starspots, faculae, and plages. A similar metric, the $\log R'_{HK}$, is a re-parametrization of the S-index where the value is normalized by bolometric luminosity and presented as a logarithm. The advantage of $\log R'_{HK}$ is that it is easier to compare values across stars [167]. Another tracer is the Hα line. By measuring variation in the depth of the line surrounding 6564.6 Å, magnetic activity can be traced [194, 188]. This tracer is especially suited for late type stars with more flux in the red portion of the visible spectrum, and almost no flux in the bluer regions where Ca II H&K resides. Furthermore, the Hα absorption line is generated at a different depth in the chromosphere from Ca II H&K and therefore can be valuable as a tracer of slightly different physics even when Ca II H&K have sufficient flux to make a measurement of the S-value.

Additional activity tracers come from diagnostics of the spectrum as a whole, particularly tracing the shape changes of a variety of absorption lines. These tracers include the bisector inverse span (BIS) metric, full width at half max (FWHM) measurements, and the differential line width measurements (dLW). Each of these are byproducts of the reduction from a spectrum to a RV measurement. The BIS, first introduced in [185], measures the wavelength center of an absorption line at many depths within the line. The average value from the top of the line, near the continuum, is subtracted from the value near the bottom of the line. Because the line bisector's shape, hence slope, should not change with true radial motion of the star, an activity metric is created. The other three metrics are tuned to similar logic: line shape variations can be tracked and be made distinct from line shift variations. The FWHM metric is constructed from fitting a Gaussian to the cross-correlation function (CCF) of a

Delta Function mask to the stellar spectrum and tracks the way in which the CCF flexes over time, in ways that a true velocity shift would not induce. Similarly, the dLW metric is computed from the second derivative of the spectrum to track shape changes [255].

In the early days of exoplanet searching, spot/plage/faculae-driven activity was mitigated by trying to avoid it. Large planet-searching surveys would simply pass over stars that were deemed to be sufficiently active based on computing the activity tracer levels in a reconnaissance spectrum. This strategy was very effective and these surveys were able to successfully search only the quietest stars for planets. To this day, a "quiet" star is one that exhibits activity signals with an amplitude of about the same order of magnitude as the single measurement precision of the spectrograph in use. When instruments were only capable of $\sim$10 m/s precision, many stars were sufficiently quiet and activity was more obviously diagnosed in a quick look. As instrumentation has gotten better, down to $\sim$1 m/s in the past decade, we learned that even the stars once thought to be quiet by the previous standards, are now quite noisy with activity. And now, in the Extreme Precision Radial Velocity (EPRV) era, where instruments capable of 30 cm/s precision are coming online, we are learning that there is, in fact, no such thing as a quiet star. All stars exhibit activity signals below the 1 m/s level. In cases where activity cannot be avoided, historically the first strategy for mitigation was detrending the computed RVs with the activity tracers. Now, more sophisticated techniques have been developed; see §1.4.1 below and throughout this dissertation.

A large effort of the exoplanet community has been spent on understanding stellar activity signals in RV data sets. We must be able to consistently and confidently identify, model, and then remove them from a time series if we hope to discover smaller planetary signals hiding underneath. My contribution to this effort will comprise a large portion of this dissertation.

1.3 Time Series Analysis

Any data set that consists of at least two measurements recorded at timestamps is a time series. In astronomy, and especially in the sub-field of exoplanet detection, we expect to find periodic patterns in our time series data. Therefore, determining the presence and periodicity of a signal in a time series is an important task in itself.

A periodogram is a measurement of the strength of a periodicity in a time series data set. For a given data set of timestamps, velocities, and error bars, a periodogram computes the strength of the periodicity in the data set at a large number of test periods. As I will demonstrate below, the result of the most commonly used periodogram in astronomy, the Generalized Lomb-Scargle Periodogram [132, 206, 252], is a plot of "power," a non-physical, statistical quantity, versus period. In a periodogram, at the periods where tall peaks appear there are most likely periodic signals. The taller the peak, or the greater the power, the stronger the fit of that test period to the data. See Figure 1.5 for an example of a time series data set and its resulting periodogram from the Generalized Lomb-Scargle construction (see below for details).

Here I will describe the theory and development of generalized periodograms used in exoplanet detection.

When the periodogram was first developed based on Fourier Analysis in [209], it was used to describe evenly sampled and evenly weighted weather data. A more modern version is called the Least Squares Periodogram. This periodogram is constructed by first taking the sum of the squares of the residuals of a sinusoidal fit to a data set:

$$S = \sum_{r=-n}^{n-1} w_r[y_r - A_\omega \sin(\omega t_r) - B_\omega \cos(\omega t_r)] \tag{1.5}$$

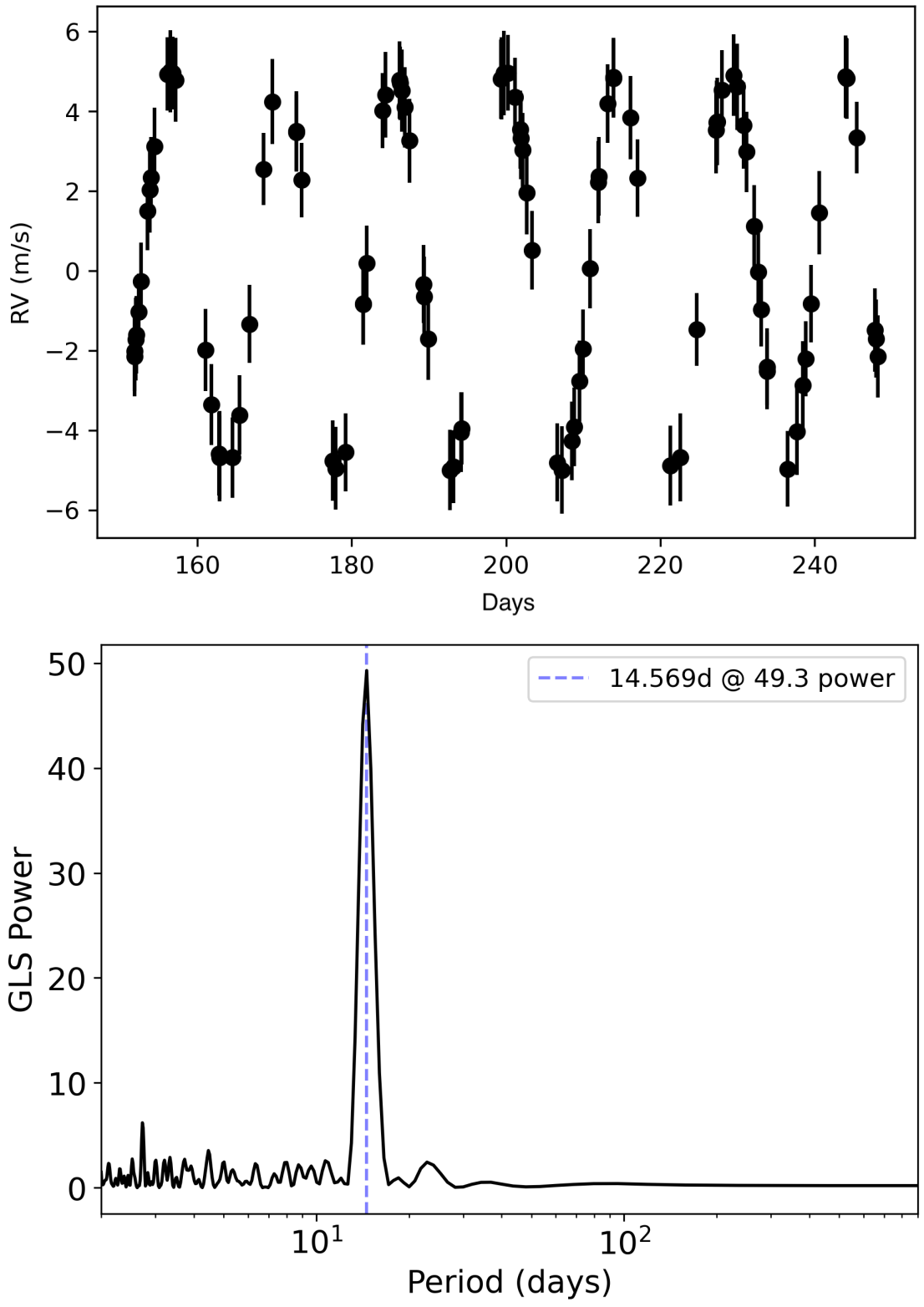

Figure 1.5: An example time series (top) and resulting GLS Periodogram (bottom). The tall peak at 14.5 days indicates a strong periodicity is recovered in the data set at this period.

where n is the number of observations, t are the timestamps of those observations with weight w_r (where $w_r = 1/\sigma$, with σ as the measurement error of all observations), and ω is a test frequency. Minimizing this sum S by taking partial derivatives with respect to A_ω and B_ω and setting equal to zero leads to orthogonal functions. Then, under the assumption of evenly spaced data where

$$\omega = \frac{2\pi mr}{N\Delta t} \tag{1.6}$$

with N equal to an oversampling factor and m is an integer (ranging from 1 to the number of frequencies to be tested) ensuring that frequencies are evenly spaced apart from one another. The orthogonal equations can be re-arranged to solve for the coefficients:

$$A_\omega = \frac{2}{N}\sum_{r=-n}^{n-1} y_r \sin\left(\frac{2\pi mr}{N}\right) \qquad B_\omega = \frac{2}{N}\sum_{r=-n}^{n-1} y_r \cos\left(\frac{2\pi mr}{N}\right) \tag{1.7}$$

from which the power of the spectrum for frequency ω is computed as

$$P_\omega = (A_\omega^2 + B_\omega^2)^{\frac{1}{2}}. \tag{1.8}$$

This procedure is identical to a Fourier transform. It is very easy to program and run, and carries many useful statistical properties. However, it is not all that applicable to astronomical data sets. In the field of astronomy, our data is hardly ever evenly sampled or evenly weighted. This is especially true for RV observations, where spectra are obtained sporadi-

cally throughout months to years, with large gaps in observations subject to human-designed scheduling of the telescope, and the natural seasonal rising and setting of a particular star of interest.

The requirement to be capable of finding periodicities in unevenly sampled (but still evenly weighted) data led to the development of what is now referred to as the Lomb-Scargle Periodogram (LSP) [132, 206]. The LSP is a procedure similar to the Least Squares Periodogram, but accounting for a zero point offset, τ, to re-align the data in time:

$$A_\omega \sum \sin^2(\omega[t_r - \tau]) + B_\omega \sum \sin(\omega[t_r - \tau]\cos(\omega[t_r - \tau]) = \sum y_r \sin(\omega[t_r - \tau]) \quad (1.9)$$

$$A_\omega \sum \sin(\omega[t_r - \tau])\cos(\omega[t_r - \tau]) + B_\omega \sum \cos^2(\omega[t_r - \tau]) = \sum y_r \cos(\omega[t_r - \tau]) \quad (1.10)$$

Then, τ is chosen so that off-diagonal elements in the matrix of orthogonal equations are equal to zero, the equations are re-arranged to give:

$$\tan(2\omega\tau) = \frac{\sum \sin(2\omega t_r)}{\sum \cos(2\omega t_r)} \quad (1.11)$$

so that τ depends on ω. Then the coefficients become

$$A_\omega = \frac{y_r \sum \sin(\omega[t_r - \tau_\omega])}{\sum \sin^2(\omega[t_r - \tau_\omega])} \qquad \text{and} \quad B_\omega = \frac{y_r \sum \cos(2\omega[t_r - \tau_\omega])}{\sum \cos^2(\omega[t_r - \tau_\omega])}. \quad (1.12)$$

However, because now the variances of A_ω and B_ω are no longer equal:

$$\sigma_{A_\omega} = \sigma^2 \Big[\sum \sin^2(\omega[t_r - \tau_\omega]) \Big]^{-1} \neq \sigma^2 \Big[\sum \cos^2(\omega[t_r - \tau_\omega]) \Big]^{-1} = \sigma_{B_\omega}, \tag{1.13}$$

the noise is no longer from a simple distribution. This can be circumvented by the Lomb-Scargle Power:

$$P_{LS} = \frac{1}{2} \frac{A_\omega^2}{\sigma_{A_\omega}^2} + \frac{1}{2} \frac{B_\omega^2}{\sigma_{B_\omega}^2}. \tag{1.14}$$

The LSP is a powerful tool but it still operates under the assumption that all data points have the same weight, i.e. the same error bar. This is almost never true when it comes to RV time series observations. For example, because the conditions across observing nights vary dramatically, different observations will have different SNRs (perhaps a cloud passes over the star one night while exposing), which leads to different error bars on a given observation's calculated RV. Similarly, different spectrographs have different noise properties and precision limits. To account for this, the LSP was extended further in [252] to become the *Generalized* Lomb-Scargle Periodogram (GLSP). This version is generalized in the sense that it allows for uneven error bars on the data and it does not assume that all frequencies tested have the same mean value of the independent variable.

It begins in the usual way by wanting to minimize the equation

$$S = \sum_{r=-n}^{n-1} w_r [y_r - A_\omega \sin(\omega t_r) - B_\omega \cos(\omega t_r) - c_\omega] \tag{1.15}$$

but now with an extra offset term c_ω unique to each frequency. Additionally, now weights are determined by $w_r = \sigma_r^{-2}$, with σ_r as the measurement error for the rth observation. By setting the partial derivatives equal to zero, orthogonal equations similar to earlier results can be derived. But now there is a third partial derivative with respect to c_ω which can be used to eliminate the variable from the other two partials. Then, we must choose a displacement in time dependent on frequency, τ_ω, to eliminate the off diagonal elements of the matrix. This allows us to solve for A_ω and B_ω, which combine to represent the power of the GLSP, P_{GLS}, via the same form as Eqn 1.14. But now the variances of each A_ω and B_ω are described differently:

$$A_\omega = \frac{\sigma^2}{\sum w_r \cos^2(\omega[t_r - \tau_r]) - \sum w_r \cos(\omega[t_r - \tau_r])} \tag{1.16}$$

and

$$B_\omega = \frac{\sigma^2}{\sum w_r \sin^2(\omega[t_r - \tau_r]) - \sum w_r \sin(\omega[t_r - \tau_r])} \tag{1.17}$$

where

$$\sigma^2 = \frac{1}{n-1} \sum w_r (y_r - \langle y \rangle)^2. \tag{1.18}$$

The third partial derivative, as well as this treatment of the noise, both allow for the GLSP to be the most general of periodograms, suitable for application to RV time series data sets.

Beyond the GLSP, many other periodograms have been proposed and developed. I summarize a few of the most notable and relevant to my research here, in chronological order.

Bretthorst 2001 [38] developed what they referred to as a generalized Lomb-Scagle periodogram (not to be confused with what I denote as the GLSP from [252]). They applied a Bayesian approach to the LSP and included a function that weights the sinusoidal fit, effectively allowing for it to be modulated by a Gaussian wrapper apodization function. However, this technique requires uniformly spaced data points, otherwise it reduces down to the LSP. Furthermore it does not fit for the variables that comprise $Z(t)$, defined within as a function describing the signal, rather it assumes they are known.

Next, [160] builds upon this idea and develops a fully Bayesian periodogram, the Bayesian generalised Lomb-Scargle periodogram (BGLSP). The motivating goal is that the GLSP power metric is purely statistical and therefore it is not possible to compare peaks in the GLSP. Under their Bayesian treatment, they derive $P(f|D, I)$, the probability finding a sinusoid with frequency, f, given the data, D, and our prior knowledge, I. Then, peaks can be directly compared to one another and model comparison is straightforward. That said, this sort of model assumes a periodicity is in the data, so it is only effective in comparing models which include different numbers of planets.

As part of a community data challenge, [97] developed the Apodized Keplerian Periodogram (AKP). By wrapping Keplerian functions in Gaussian apodization envelopes, these functions more accurately model stellar activity induced signals. The apodization timescale becomes a free parameter to fit. Then signals can be better categorized based on their apodization timescale: signals with apodization timescales longer than the baseline of observations are most likely to be planetary in origin. Signals with short apodization timescales, where they grow and decay within the baseline of observations, are most likely to be due to stellar activity. The AKP fits for periodicity and timescale using MCMC sampling to calculate likelihoods, which are used to produce a Bayesian periodogram.

In [77], the authors describe `Agatha`, a Bayes Factor periodogram built on a moving average algorithm. The moving average effectively smooths the data with respect to a red noise correlation timescale, τ. The result is that non-white noise models are included in the computation of the likelihood, which is ultimately used to determine the significance of peaks in the periodogram.

Next, as a modification to the GLSP, [159] describes the Stacked Bayesian GLSP. It attempts to identify non-coherent signals in RV data sets. They start with a continuous subset of the data starting from the first observation and the subsequent N observations, where N is enough data points to compute a meaningful GLSP. Then they add the next subsequent observation in time to the subset and recompute the GLSP, continuing this method until the entire time series is included. They track the power of all peaks as data is added. Signals that are coherent should monotonically increase in power while incoherent signals will flatten out or fall in power.

Lastly, in [100], the authors develop the L1 Periodogram built on a compressed sensing algorithm that leverages an L1 minimization penalty. As this is the framework upon which I've built a substantial portion of my dissertation via my software package, `Lia`, I will only briefly introduce the concepts behind the L1 Periodogram and defer details to §4. Compressed sensing algorithms generate a "dictionary" of functions, evaluated at the timestamps of the real observations. The intention is that a small number of these functions, when linearly combined, recreate the observed data to within an allowed tolerance. The L1 minimization enforces the idea that only a small number of functions should be selected out of the dictionary (sparsity) by penalizing choosing additional functions.

1.4 A History of Exoplanets by RV Detection

From my academic lineage, I have been passed down a saying, "In Astronomy, we do two things: collect stamps and physics." That is to say, there is a strong urge within astronomy of simply finding new objects and attempting to classify and categorize them. This is the stamp collecting phase, and it is somewhat unique to the field of astronomy for the simple reason that astronomy is perhaps the only field of physical sciences that cannot perform an in situ experiment on its subject matter. We cannot split open a rock from an exoplanet and run a mass spectroscopy analysis to determine its chemical composition. We cannot set up a collider experiment to smash stars together and reveal what comes out of the collisions. We cannot poke and prod a galaxy, subject it to extreme environments of heat or pressure or more, in hopes of revealing its secrets. The only experiment an astronomer can perform is to observe; to catch a few photons from a subject of interest and then cleverly squeeze out as much information as possible. For this inherently observational aspect of the field, discovering truths only wherever we happen to look, one can compare astronomy to stamp collecting.

For the longest time, the field of exoplanets was firmly in this stamp collecting phase. We sought out new discoveries primarily for the sake of discovery and the sense of wonder for what else was out there. We began to classify them in the same way that one would classify stamps. Big vs. small, hot vs. cold, this or that host star, etc and we were enamored by superlatives of the hottest or the biggest or the the place it rains liquid iron or the first binary host system.

Driving this stamp-collecting phase was simply that we did not have enough information to understand the physics behind exoplanets. This is where stage two comes in. In astronomy, once a large enough population of objects is discovered (a large enough collection of stamps), and their properties measured to a sufficient precision, the physics begins. When statistically

significant sample sizes are known, and known to good precisions on relevant parameters, that is when we are ready to take our analysis tools deeper to reveal and understand trends, to uncover truths and begin to ask even deeper, more insightful questions. Now we have begun to understand different populations of planets, how they form, how often they form, what they are made up of, and what forces shape planetary systems as a whole. With a sufficiently large collection of exoplanets within any given area of parameter space, we can truly explore deeper questions and reveal a greater understanding of our subject.

1.4.1 Past

The exoplanet era jump-started in 1995 with the discovery of 51 Pegasi b [148], the first exoplanet confirmed around a Sun-like star, for which authors Michel Mayor and Didier Queloz shared the 2019 Nobel Prize in Physics. This strange discovery of what we now call a Hot Jupiter was completely unexpected and set the tone for our field: the galaxy is full of strange worlds. This discovery was made using the ELODIE spectrograph [18] at Haute-Provence Observatory in France. At the time, they boasted that their instrument was capable of 13 m/s single measurement precision. Soon, more exoplanet teams began announcing discoveries; see [43, 168] and many more. Meanwhile, RV precision took a huge leap to as little as 3 m/s precision through the development of the iodine cell technique [44]. By passing the starlight through a cell of iodine gas, the absorption spectrum of the molecular iodine gas becomes overlaid onto the stellar spectrum. These iodine absorption lines, with precisely known wavelengths, act as a measurement stick for all of the stellar absorption line features in the spectrum, as well as tracking variations on the instrument profile for calibration purposes. This greatly increases the precision to which the lines can be measured in wavelength space, and therefore increases the precision of the resulting RV. That said, there is a trade-off: the total amount of starlight reaching the detector in a given exposure time is reduced. Given that at the time no spectrographs were purpose-built for

precision RV detection of exoplanets, another huge advantage to the iodine cell technique was that it was cheap: it was possible turn almost any high resolution spectrograph into a planet searching machine by sticking this tube of iodine gas in the light path.

With these new capabilities, RV teams continued to monitor the brightest stars in the sky, but chose their targets strategically. They purposefully tried to avoid stars that were deemed to be active. Armed with $\sim$3 m/s precision and all the bright stars in the sky to be explored, many Jupiter-analog planets were discovered [57, 45] and more. Between 1996 and 2010, of 414 total planets discovered, 227 were Jovian planets on orbits longer than 100 days. This would be the last time that distant giant planets would overtake close in small planets in terms of raw number of discoveries in a time frame, at least for now.

The entire reason for this shift in the type of planet most commonly discovered is the Kepler mission [34]. Launched in 2009, the mission was designed to search for exoplanet transits by staring, nearly unblinkingly, for 4 years into a small patch of sky in the space between the constellations Cygnus and Lyra. The primary goal of this mission was to build up statistics of exoplanet populations. In this regard, and many more, the mission was a massive success. In seminal works, [68] showed the occurrence rate of small planets in M dwarf systems, [180] estimated the general occurrence rate of planets, and [42] related stellar metallicity to planet occurrence. Suddenly, multi-planetary systems were becoming the norm, not the exciting exception. Now the exciting systems were the rare, strange, and/or unexpected: systems like Kepler-10 which hosts the first rocky exoplanet discovered [23], the first circumbinary "Tatooine" system [67], and the smallest radius planet about the size of our Moon [19].

Now the RV method had come to be seen more as a tool of mass measurement than one of pure discovery. All of the Kepler systems which were amenable to RV follow up were targeted by RV surveys. Masses were needed so that we could begin to probe the relationships between planet radius and planet mass, as well as calculate planet density to begin to infer what might make up these far-off worlds. Around the same time, as spectrographs were

being built for the sole dedicated purpose of exoplanet detection via the RV method, new techniques for calculating the RV from a spectrum began to emerge, including template matching [10, 255, 213]. In this technique, a template spectrum is obtained, either by high SNR observations of the star with the same instrument, or a synthetic spectrum is created, and the RV is computed by matching the observed spectra at different times to the reference template spectrum. Later, new techniques for computing RVs from spectra all under the umbrella term "Line-By-Line" emerged. These techniques evaluate the shift in wavelength space for each individual absorption line in the spectrum [69]. Generally, if an individual line's measured RV is far off from the average, it is thought to be a contaminated line and it can be discarded. Different methods of the line-by-line technique involve different line lists or changes in how the final RV is computed [56, 27, 13].

Along with better and novel reduction techniques, time series modeling and analysis has played a large role in addressing the challenge of stellar activity. Early efforts to identify stellar activity signals in RV data sets including fitting for a correlation between the RVs against one or more activity tracers [185, 102]. If a strong correlation was found, usually by simple linear regression, then that correlation could be removed from the RVs [72]. Activity identification and modeling have grown more creative and complex since then. In [187], the method of employing a Gaussian Process (GP) was first described. GPs are a highly flexible framework amenable to modeling unknown functional forms, like stellar activity. They generally model activity through the correlations of each single RV to all other single RVs in a data set through a pre-described covariance matrix. The application of GPs to RV data sets has been expanded due to enhancements in software from [78] and [79]. They have also been applied to identifying stellar rotation signals in [11] and to pull out planetary signals in activity-riddled data sets [103]. Next, GPs have been instrumental in studies showing how signals once thought to be planetary in nature are instead activity-driven signals [33]. Lastly, additional new activity modeling techniques have been developed. In [5], the authors describe a novel method for estimating the variation in RVs from observing

starspots in photometry.

With the new era of RV-dedicated instruments and new activity modeling underway, in 2018 NASA's Transiting Exoplanet Survey Satellite (TESS) [191] launched, providing us with thousands of new planetary systems to go after with our new techniques. The TESS mission is in many ways the spiritual successor to the Kepler mission. TESS is an all-sky survey where each hemisphere of the sky is partitioned into 13 "sectors". Each one of these sectors is observed for 28 days at a time so that throughout one year, TESS observes the entire hemisphere. At that point, it flips to the other hemisphere and continues. This survey design prioritizes discovering as many planets as possible around preferentially bright stars. This design also biases towards the detection of short period (<28 d) planets, with exceptions for the regions of overlap in the sectors towards the celestial poles where there is a continuous viewing zone. In its nominal two year mission, TESS discovered thousands of exoplanet candidates.

1.4.2 Present

At the present time, the sub-field of RV detection of exoplanets is entering a renaissance. TESS, beyond its nominal two year mission, is continuing to deliver many thousands of new transiting exoplanets candidates each year, each just waiting for their masses to be measured. The Kepler mission's survey of staring blankly into a small slice of the sky for four years was ideal for building up statistics of the planet population across the galaxy, and did so very successfully. However, this "deep" (at least for exoplanetary science standards) field design inherently included many stars that are relatively dim in apparent magnitude. So while thousands of exoplanets were discovered over the lifetime of the mission, the vast majority of these orbit stars that were too dim for meaningful follow up with RVs, and especially not suitable for large RV surveys to homogeneously measure masses. Now, TESS

is helping us make up for lost time. The survey design of TESS is strategic for large-scale discovery of exoplanets orbiting preferentially bright host stars, which are ideal for further characterization with RV follow up. TESS is delivering targets in line with our statistical understanding of the true population of exoplanets, but with the added bonus of stellar host brightness. Now, there are far more targets than there is telescope time available for the few dedicated ground-based RV teams across the globe. In this regard, RV teams can choose to dedicate their resources of personnel/team effort and telescope time to only the very best targets among a wide variety of science cases.

In this regard, RV teams have been choosing to provide invaluable follow up characterization to prepare for the coming golden age of atmospheric studies. With the launch of the long-awaited JWST having finally taken place on December 25, 2021, as well as its highly successful deployment and commissioning period, the field of exoplanet science is more than ready to take full advantage of this new observatory's capabilities. But JWST cannot perform transmission spectroscopy on just any target. In order to break degeneracies in the interpretation of transmission spectra, it is crucial to measure the planet mass to less than 20% uncertainty ($> 5\sigma$ precision) [21]. In today's hyper-competitive proposal environment, where the JWST Cycle 2 over-subscription rate was $\sim$7:1, it is a non-starter to ask to measure atmospheric properties for a planet if it does not already have a 5σ mass secured. For this reason, the primary focus for ground-based RV follow up teams has been to measure such precise masses as a stepping stone for eventual atmospheric characterization for JWST. In this effort, many new planets are achieving this mass result and therefore, almost as a bonus effect, the mass-radius diagram is tightening up. New trends and populations are emerging from these better mass measurements. For example [137] describe how the population of planets orbiting M Dwarfs may be cleanly bifurcated by density: water-rich worlds and rocky terrestrial worlds.

This effort is all greatly assisted by the dawn of the "Extreme" Precision Radial Velocity

(EPRV) era. Since the year 2020, four new spectrographs capable of ∼30 cm/s single measurement precision have seen first light: MAROON-X [211], EXPRES [116], NEID [210], and the Keck Planet Finder (KPF) [92]. These represent a huge leap in the technical abilities of our field. While KPF is currently still in commissioning as of the writing of this dissertation, the other three EPRV instruments are making good on their promises of stability, precision, and abilities to yield high impact science.

However, as discussed above in §1.2, even before these instruments came online, we expected that there would be no such thing as a quiet star anymore from an activity standpoint and this impacts the standard stars that instrument teams use. Standard stars are ideally stable stars observed during commissioning and engineering time to determine instrument stability and performance. Since they are standardized, all instrument teams use them and therefore it is easy to compare to other instruments' data. For two reasons, new spectrographs are increasingly using fewer standard stars. First, there are simply fewer stars where we understand all of the RV signals for that star and consider them "stable". Second, to understand a star more thoroughly, one must take more observations of that star with higher cadence than before, therefore there is less time to be spread out among more stars. It is better to have a smaller number of standards that can be observed more frequently. Additionally, instrument teams are becoming more clever with standard star selection. For example, all four of the above instruments have been observing HD 3651, a system with a highly eccentric Jovian believed to have dynamically cleaned out the inner system of any small planets [40]. Therefore, the only signal to model and remove is the planet, and all that remains in the residuals is any stellar noise and instrumental noise.

In the effort to understand stellar activity signals, instrument teams are increasingly collaborative. Teams are sharing standard star targets and producing public data nightly. Along this line, there is a strong push for an all-hands-on-deck approach to the activity problem. Recently, the EXPRES team led a public data challenge using some of their proprietary data.

The results were published in [258] where they invited teams to do their best in identifying and removing non-Keplerian signals from a few data sets. In all, 22 different techniques were applied to each of the sample data sets. They use the metric of residual RMS of the velocities to compare these techniques and determine best practices. Overall, they find that no one technique consistently performs better than the others.

There has also been a large push to include solar telescopes with all new EPRV instruments. Following the HARPS-N team's installation of a solar telescope [71] and publication of Solar RVs to the community [70], the value of Sun-as-a-Star observations with dedicated RV instruments was solidified. Next, the EXPRES team included a solar feed to the instrument and has been taking daily RVs. Then, the NEID team included a solar feed in their design and implementation [127]. Now, the KPF team has just installed their solar calibrator and will soon begin producing solar RVs. With solar feeds strategically spread out on the Earth across different longitudes, near continuous observation of the Sun from dedicated EPRV instruments is finally underway. These data sets, mostly public but at least periodically released in batches, are crucial in two ways. First, because the values of the RVs at nearly the same timestamps can be directly compared across instruments, they allow for greater understanding of the individual systematics for each instrument. And second, these data sets are invaluable for developing and training new techniques and methods for understanding stellar activity. Because the Sun is so close to us, it is an unparalleled opportunity to study it like no other star. The Solar Dynamics Observatory (SDO) [179] provides high resolution spatially-resolved spectra of the Sun as well as high definition imaging of the solar face. Therefore, at any time, we can compare our ground-based solar RVs to space-based observations and know for certain what activity features may be present on the solar face at a given time. All this combined with our historical knowledge of the Sun's various activity cycles, when we analyze the new ground-based RV solar data sets, it is like having the answers to the problem at the back of the book. We can use all this information to develop new strategies for identifying, characterizing, and mitigating the effects of stellar activity in

stellar data sets. In this dissertation, I will make use of the HARPS-N Solar data set as a common barometer to test new methods and techniques for identifying stellar activity in realistic RV data sets.

1.4.3 Future

What does the future of the field of exoplanets look like? Where will we be spending the majority of our efforts and our telescope time? While the answers to these questions are unknowable in certainty, there are a few trends at the current time that do not show signs of slowing. Here I will hypothesize how I see the near-term evolution of the field.

First, one cannot talk about the future of exoplanets without talking about JWST. The successful launch, deployment, and commissioning has the community very excited. Some early science from JWST transmission spectroscopy has returned mixed results. The Early Release Science of the Hot Jupiter WASP-39b data set was a huge success and fascinating atmospheric features are revealed [204, 9, 4, 76]. Then a totally featureless spectrum came through for observations of the 1 $R_\oplus$ planet LHS 475b [138]. I believe continuing to measure atmospheric features of exoplanets, and the supporting work required to make those observations possible like mass measurements via RVs, will dominate the efforts of exoplanet scientists for the next decade. As mentioned above in §1.4.2, dedicated mass measurement efforts from RV teams are needed to field suitable JWST targets. But before that, suitable RV targets will continue to be discovered by TESS. Meanwhile, as more transmission spectra are taken and analyzed across pre-selected bins of planet parameter space, theorists will enter a golden era of atmospheric data and will begin to build up a deeper understanding of the physics of planet formation. All through this effort, we will collectively hold our breath for a JWST transmission spectrum that definitively shows evidence for an oxygen and nitrogen-rich atmosphere of a rocky planet.

Beyond supplying 5σ masses for JWST atmospheric characterization, the RV method will continue to thrive as a detection tool in itself. In the quest to discover an Earth-twin planet, that is, an Earth-mass planet orbiting a Sun-like star at a distance of 1 AU, the RV method stands the best chance of discovering one that is also amenable to all kinds of follow-up characterization. The transit method via the Kepler mission has already delivered Earth-radius planets in 1 AU orbits. However, due to survey design, these planets all orbit very distant and therefore dim stars which are not amenable to detailed follow-up characterization, including even mass measurements with RVs. This creates a bottleneck. Discovering Earth-like planets is fastest and easiest with large transit surveys. However, combining the inherently small geometric transit probability of an Earth-like planet and the likelihood of that planet orbiting a bright host star amenable to direct imaging follow up is very small. This is where RVs will shine, as they eliminate both of these burdens: there is no geometric alignment of the planet required and RV surveys already preferentially target bright, nearby stars highly amenable to follow up characterization. It will be the RV method that supplies the target lists for future investigations of Earth-like planets, including future space-based direct imaging surveys.

On the horizon of the field is a new fleet of space-based "Great Observatories". First, and most importantly fully funded and built, is the Nancy Grace Roman Space Telescope (NGRST) [7], planned for launch in May 2027. NGRST will perform a microlensing survey of the galactic bulge as well as use a coronagraph to directly image planets while performing slitless spectroscopy. Looking further ahead, the 2020 Astronomy Decadal Survey [169] recommended a new flagship observatory, now referred to as the Habitable Worlds Observatory (HWO). While this mission is still unfunded and any suggestion of a launch date is nothing more than a guess, a primary science goal of this mission would be to directly image Earth-like planets. But neither of these missions will be *discovering* the Earth-like planets that they wish to directly image. It is far too expensive in telescope time to conduct a blind survey with a space-based observatory. Instead, they will be leveraging decades of

preparation to build their target lists, which will be defined before the observatories are even launched. These target lists will be filled with planets first discovered by the RV method. In order to be ready for these missions, RV surveys must be working now to build up data sets, extend observing baselines, and find these planets in time.

Next, it is my belief that in the near future we will begin to characterize exoplanet systems in the same way that we have characterized our own Solar System. The post-Kepler era was dominated by studies *between* systems. These include comparing planetary systems to each other and building up statistics in a broader sense. After all, statistics was the goal of the mission from the start and in that sense it was a highly successful mission. However, I believe the post-TESS era will be defined by studying *within* systems. TESS is delivering the same populations of planets that Kepler revealed, but with more amenable host stars to follow up. In the years after TESS's mission ends, we will finally begin to investigate deeper within single systems. For example, we will perform intra-system atmospheric characterizations by obtaining transmission spectra for multiple planets in the same system. In these efforts, we will start to really see exoplanet systems in the same way we see our own Solar System.

Lastly, the EPRV era will flourish in the next decade. The fleet of ground based spectrographs dedicated to RV measurements will deliver on their promises of stability and precision. We will continue to find smaller and smaller signals, measuring Earth-like masses with tighter error bars. We will measure smaller Rossiter-McLaughlin signals now that we have EPRV instruments on the largest aperture telescopes. We will leverage the new regime of precision to better understand the challenge of stellar activity. And we will continue to build ever more precise spectrographs. And someday we will wonder, what was so "extreme" about 30 cm/s precision RVs?

1.5 Dissertation Organization

My dissertation is organized into three main chapters. §2 concerns the discovery and characterization of the exciting 5+ planet system HD 191939. This work was first published in The Astronomical Journal, Volume 163, Number 2 as [135] and appears here unchanged. I have added a foreword beforehand to set the context for this paper. Next, in §3 I describe the stellar activity of Barnard's star and show how the proposed planet is instead a false positive detection. This work was first published in The Astronomical Journal, Volume 162, Number 2 as [134] and appears here unchanged. I have also included a foreword beforehand to set the context for this paper. Then §4 I describe a new software package I developed for identifying and characterizing quasi-periodic stellar activity signals in RV data sets, the ℓ_1 Apodized Periodogram, or `Lia`. This work will be submitted to The Astronomical Journal and appears here as a draft version. I have also included a foreword describing the greater context for this work. Lastly, in §5 I conclude by tying together all of this work.

Chapter 2

TESS-Keck Survey IX: Masses of Three Sub-Neptunes Orbiting HD 191939 and the Discovery of a Warm Jovian Plus a Distant Sub-Stellar Companion - Lubin et al. 2022

2.1 Foreword

NASA's *Transiting Exoplanet Survey Satellite* (TESS; [191]) is an all-sky photometric survey searching for new planetary systems. To cover the entire sky, TESS observes in "sectors", portions of the sky $24° \times 96°$ in size, for 28 days at a time. Over the course of a year, TESS observes 13 sectors in one hemisphere of the sky, then flips to the opposite hemisphere for another year of 13 new sectors. Due to this observing strategy, *TESS* is finding many

exoplanets in short period orbits (< 28 days), and it is increasing the number of known planets around bright stars. Through its 2-year nominal mission and the ongoing extended mission, TESS continues to discover many thousands of new planetary systems ripe for detailed investigation.

The TESS-Keck Survey (TKS) is a collaboration among exoplanet astronomers at Keck partner institutions. We combine telescope time and efforts to follow up TESS discoveries of transiting planets with precise RVs. Our primary goal is to measure the masses for 100 planets first identified by TESS. This will allow us to gain greater understanding of the relationship between planet mass and radius, to measure bulk densities to provide insight into possible planet compositions, and provide valuable mass measurements for future JWST targets. To date, we have published 12 individual system papers (see [60, 243, 59, 203, 207, 140, 61, 136, 58, 231, 141, 238]) with more on the way. Our survey is further concerned with the formation, evolution, and dynamics of various types of exoplanetary systems. The four sub-goals of TKS are characterizing systems with multiple planets, those with possible distant giant planets, planets orbiting evolved host stars, and those that show promise for high-quality atmospheric characterization [50].

This work concerns a system that crosses three of these goals. HD 191939 is a solar-like star (G9V) that hosts a multi planet system. TESS observed the star for 252 days in 9 non-consecutive sectors during its primary mission, allowing for a long baseline (326 days) of photometry and enabling discovery of longer-period planets. Badenas-Agusti et al. 2020 [14] had already announced three transiting planets, two of which would not have been discovered without multiple sectors of coverage. The following work includes the first mass measurements of the transiting planets as well as the discovery of an additional Jovian planet and a super-Jovian planet.

Bright systems with multiple planets like HD 191939 are invaluable to the exoplanet community. They are amenable to precise RV monitoring and are natural laboratories of planetary

astrophysics. With multiple planets forming from the same protoplanetary disk, such systems allow for comparative exoplanetology investigations, as we can assume a similar history of formation conditions for each planet.

We find that the transiting planets of HD 191939 fall into some of the patterns uncovered by statistics papers on the *Kepler* planets. They have nearly identical radii, as is typical of the Kepler planets [245], yet their spacing is irregular. They have similar masses, consistent with the pattern found in [157], but the planets have low masses for their sizes [244], implying lower than average densities. In all, HD 191939 will be a touchstone system studied for a long time.

2.2 Observations

2.2.1 TESS Photometry

Due to the star's high northern declination, *TESS* observed HD 191939 for a total of 9 sectors in Cycle 2. Data were obtained with a 2-minute cadence during sectors 15-19, 21-22, and 24-25, spanning a total baseline of 326 days from 2019-07-18 to 2020-06-08, though the star was not observed for the entirety of this time [219]. We downloaded data processed through the Science Processing Operations Center (SPOC) pipeline through the Mikulski Archive for Space Telescopes (MAST), and used the Pre-search Data Conditioning (PDC) light curves for our analysis. [114].

2.2.2 Radial Velocities

We acquired 73 RV observations with Keck/HIRES at the W.M. Keck Observatory on Maunakea, Hawaii between November 2019 and December 2020; see Table 2.3. We reduced the

spectra in the standard procedure of the California Planet Search [108]. We used a high SNR template from Keck/HIRES to generate a deconvolved stellar spectral template (DSST). We took all RV observations with a warm iodine cell in the light path for wavelength calibration [232, 44] with median SNR of ∼216 per pixel at the iodine wavelength region of ∼500 nm.

We also acquired 104 RV observations with the Automated Planet Finder telescope (APF) [240] at Lick Observatory in California between December 2019 and December 2020. At the beginning of the baseline, we observed twice per night and binned the two observations. After February 2020, we changed our observing strategy to obtain one spectrum per night due to time constraints within our survey. We used the same Keck/HIRES template to calculate the APF RVs because it produced a higher-quality DSST than the APF template. The median SNR for APF observations was ∼76 per pixel at the iodine wavelength region of ∼500 nm. To maintain only high-quality data points, we removed all (7) RVs from the APF time series that had SNR < 31, equivalent to an RV error of 9 m/s. We also removed 1 APF observation that was taken within 5 minutes of 12° twilight in the morning.

2.3 System Properties

2.3.1 Host Star

We analyzed our iodine-free HIRES spectrum with the `SpecMatch-Syn` code [181] to derive the $T_{\rm eff}$, $\log g$, and metallicity [Fe/H] of the host star, and we list our results in Table 2.1. We then derived stellar mass, radius, and age according to the approach described in [81]. We incorporated Gaia DR2 parallaxes [87], 2MASS apparent K magnitude, and the MIST models [48] using the `isoclassify` package [111, 30]. Following [226], we inflated the error bar on the stellar mass measurement by adding a systematic error term of 0.03 $M_{\odot}$ in quadrature. Given the limited spread in the HR diagram at HD 191939's $T_{\rm eff}$ (5348 ± 100

Table 2.1: HD 191939 System Parameters

Stellar Parameters					
Parameter	**Value**	**Source**			
General					
Other Names	TOI 1339, HIP 99175				
RA	20:08:06.15	[87]			
Dec	+66:51:01.08	[87]			
V mag	8.97	[14]			
Astrometry					
Parallax (mas)	18.71 ± 0.07	[14]			
Proper Motion in RA (mas)	150.26 ± 0.04	[14]			
Proper Motion in Dec (mas)	-63.91 ± 0.05	[14]			
Radial Velocity (km/s)	-9.5 ± 0.2	[87]			
SpecMatch Spectroscopy					
$T_{\rm eff}$ (K)	5348 ± 100	`SpecMatch-Synthetic`			
log g (cm s^{-2})	4.3 ± 0.1	`SpecMatch-Synthetic`			
[Fe/H] (dex)	-0.15 ± 0.06	`SpecMatch-Synthetic`			
$v \sin i$ (km/s)	<2.0	`SpecMatch-Synthetic`			
$logR'_{HK}$ (dex)	-5.11 ± 0.05	`SpecMatch-Synthetic`			
Spectral Type	G9V	[175]			
Isochrone Modelling					
Radius, $R_*(R_\odot)$	0.94 ± 0.02	`Isoclassify`			
Mass, $M_*(M_\odot)$	0.81 ± 0.04	`Isoclassify`	Before following Tayar et al. 2020, error was $\pm$ 0.03 [226]		
Luminosity, $L_*(L_\odot)$	0.65 ± 0.02	`Isoclassify`			
Age (Gyr)	>8.7	`Isoclassify`			
Stellar Abundances (Dex) from `KeckSpec`					
[C/H]	-0.12 ± 0.07		[N/H]	-0.17 ± 0.09	
[O/H]	0.09 ± 0.09		[Na/H]	-0.18 ± 0.07	
[Mg/H]	-0.09 ± 0.04		[Al/H]	-0.02 ± 0.08	
[Si/H]	-0.11 ± 0.06		[Ca/H]	-0.17 ± 0.07	
[Ti/H]	-0.07 ± 0.05		[V/H]	-0.12 ± 0.07	
[Cr/H]	-0.26 ± 0.05		[Mn/H]	-0.38 ± 0.07	
[Ni/H]	-0.21 ± 0.05		[Y/H]	-0.17 ± 0.09	

Planet Parameters					
Parameter	**Planet b**	**Planet c**	**Planet d**	**Planet e**	**Planet f**
Orbital Period (days)	8.88029 ± 0.00002	28.5805 ± 0.0002	38.3525 ± 0.0003	101.5 ± 0.4	1700-7200
Time of Conjunction (BJD)	2458715.3561 ± 0.0004	2458726.0534 ± 0.0006	2458743.5518 ± 0.0007	2459043.6 ± 0.3	–
Duration (hours)	3.1 ± 0.1	4.5 ± 0.2	5.5 ± 0.3	–	–
Impact Parameter	0.62 ± 0.02	0.63 ± 0.02	0.48 ± 0.04	–	–
Inclination (degrees)	88.06 ± 0.08	89.09 ± 0.03	89.43 ± 0.04	88.0-89.4	–
R_p/R_*	0.0336 ± 0.0007	0.0306 ± 0.0007	0.0302 ± 0.0007	–	–
Radius ($R_\oplus$)	3.39 ± 0.07	3.08 ± 0.07	3.04 ± 0.07	–	–
Semi-major axis (AU)	0.078 ± 0.001	0.170 ± 0.002	0.207 ± 0.003	0.397 ± 0.005	2.6-7.0
*Equilibrium temperature (K)	893 ± 36	605 ± 24	549 ± 22	397 ± 16	–
Eccentricity	0 (fixed)	0 (fixed)	0 (fixed)	0 (fixed)	0 (fixed)
RV semi-amplitude ()	3.8 ± 0.3	1.8 ± 0.3	0.6 ± 0.3	17.2 ± 0.4	>23.0
Mass ($M_\oplus$)	10.4 ± 0.9	7.2 ± 1.4	< 5.8 at 2σ	108 ± 3 / $\sin i$	630-3500
Density (g/cc)	1.5 ± 0.2	1.4 ± 0.3	0.5 ± 0.3	–	–

Model Parameters	
Parameter	**Value**
Linear Limb Coefficient, u_1	0.42 ± 0.06
Quadratic Limb Coefficient, u_2	0.05 ± 0.08
HIRES Zeropoint, $\gamma_{\rm HIRES}$ ()	-22.26
HIRES Jitter, $\sigma_{\rm HIRES}$ ()	1.7 ± 0.2
APF Zeropoint, $\gamma_{\rm APF}$ ()	-8.01
APF Jitter, $\sigma_{\rm APF}$ ()	3.7 ± 0.6
Trend, $\dot{\gamma}$ (d^{-1})	0.114 ± 0.006
Curve, $\ddot{\gamma}$ (d^{-2})	$(-6 \pm 2) \times 10^{-5}$

*Equilibrium Temperatures assume zero bond albedo

K, G9V), isochrone ages have large uncertainties. However, they indicate this star is older than 8.7 Gyr (2σ confidence).

We determined the abundances for 15 individual elements using `KeckSpec` [190] finding the composition of HD 191939 is generally sub-solar for most elements. We determine the Mg/Si ratio to be consistent with both the solar value and most local stars [39]. C/O, however, is found to be 0.34 ± 0.09; 2σ lower than the solar value implying the assumption of solar abundances for these elements may not be applicable to stellar atmospheric models. We obtain [Y/Mg] $= -0.08 \pm 0.1$ and use this with the abundance-age relation of [166] which

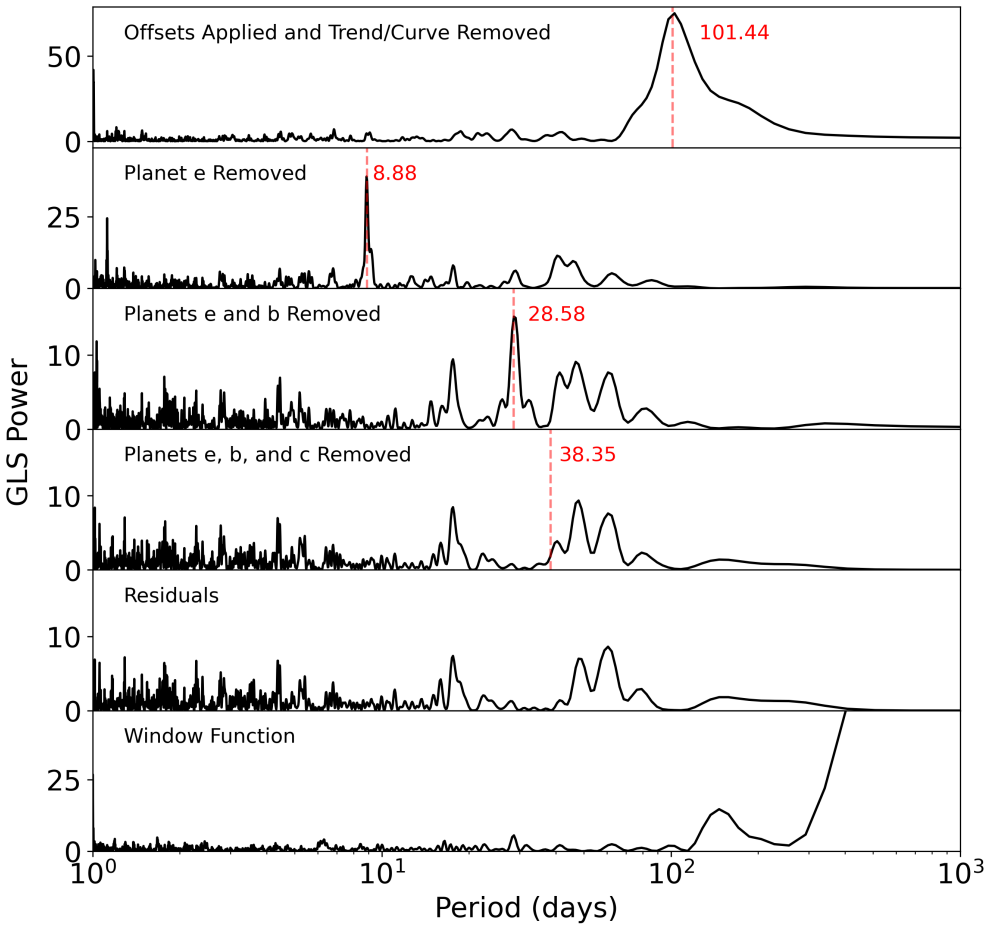

Figure 2.1: GLS periodograms of the combined time series of Keck/HIRES and APF data. The two data sets were first filtered by removing instrumental offsets as well as the trend and curvature according to the best fit parameters from our preferred model. In each descending panel, we have removed one planet at a time. The bottom panel shows the window function of the time series.

gives an age estimate of 7±3 Gyr. Although this is consistent with the lower bound obtained from an isochronal fit, HD 191939 is 400K cooler than the Sun-like stars used for this relation and should be treated with caution.

HD 191939 is a chromospherically inactive star with log R'_{HK} = -5.11 ± 0.05. We computed the Ca II H&K index (S_{HK}) as described in [113] for both our Keck/HIRES and APF time series, see Table 2.3. We find no significant correlations between the S_{HK} values and RVs. Additionally, we find no statistically significant periodicities in the S_{HK} time series.

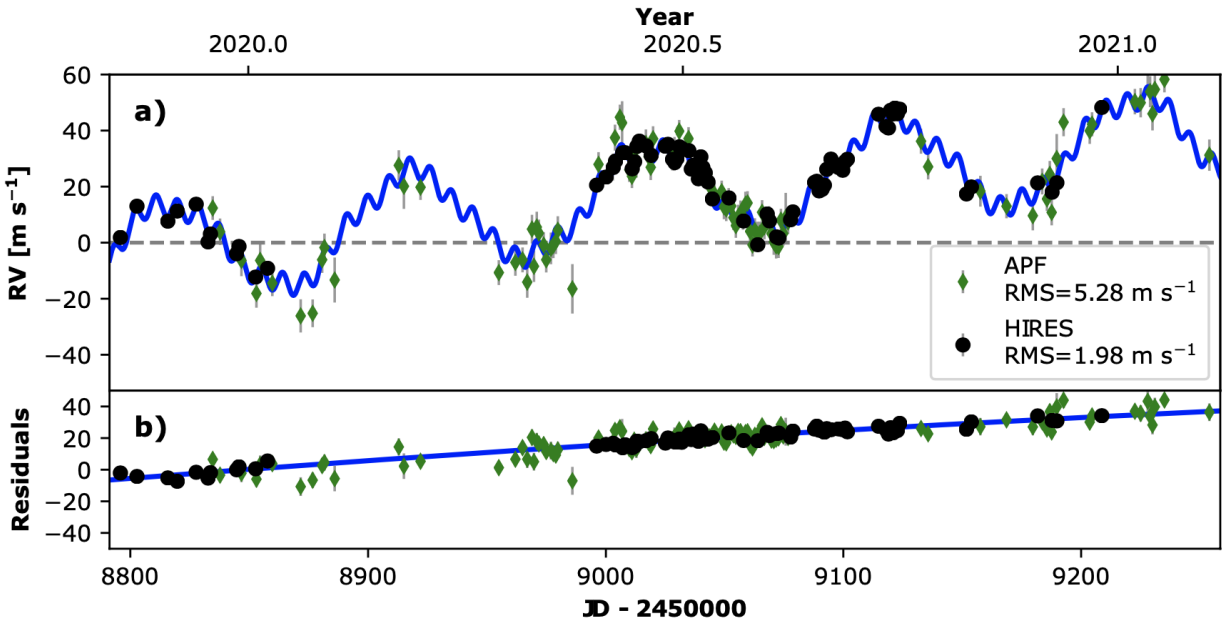

Figure 2.2: **a)** Our complete RV time series with our preferred model (blue) as well as **b)** residuals including trend and curvature. Data collected from Keck/HIRES are shown as black circles while data from the APF are shown by green diamonds.

2.3.2 RV Model

Soon after beginning our RV observations, we saw evidence of an additional planet beyond those identified by *TESS*, including observations which showed a ~ 40 m/s change in the RV, consistent with a massive planet. Continued observations further traced a large amplitude periodicity near ~ 100 days. The Generalized Lomb-Scargle (GLS) periodogram [253] of the RVs is dominated by this signal which we attribute to a fourth planet (e) (Figure 2.1, top panel).

To discern the architecture of the system, we performed a model comparison analysis. Using `RadVel` [82], we tested a variety of RV models: 3-5 total planets and either allowing eccentricity to vary for each or fixing it to zero, as well as allowing or prohibiting trend and/or curvature terms. We used Markov Chain Monte Carlo (MCMC) to explore the parameter space and estimate uncertainties; all planet models discussed here converged by the default

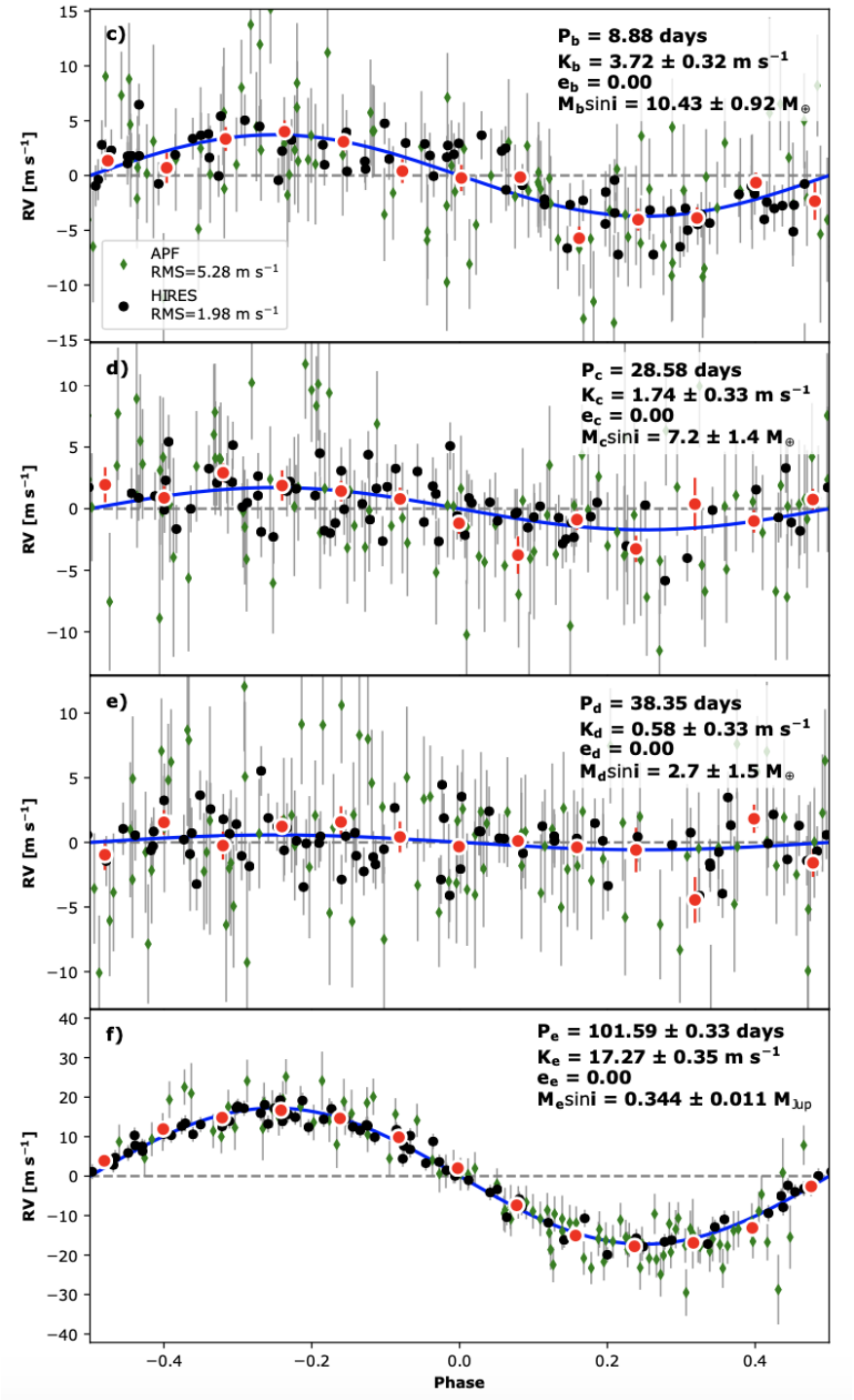

Figure 2.3: The phase folded RV time series for each planet with periods less than our baseline. Red circles are bins of size 0.08 phase.

`RadVel` criteria unless otherwise stated.

In all models, we fixed the periods and times of conjunction of the transiting planets to the values found from our *TESS* photometry model. We set uniform priors on the Doppler amplitudes $(-\infty, \infty)$, allowing negative values for all planets to avoid biasing the masses to higher values. We set a uniform prior from 1 to 1000 days on the period of planet e and a uniform prior on its time of conjunction (2459000, 2459100) BJD. For both instruments, we set a prior on the instrumental jitter as uniform (0, 10) m/s. Lastly we set a prior on the trend term uniform from $(-1, 1)$ m/s/d and on the curvature term uniform $(-0.1, 0.1)$ m/s/d^2.

Our preferred RV model has an Akaike Information Criterion (AIC) [6] of 858 and contains four planets on circular orbits, as well as both a trend and curvature term, which models a subset of a sinusoid as a quadratic to represent a 5th body in the system. The closest neighboring model, in terms of AIC, is one with 4 planets plus a trend but no curvature term (AIC = 866). Our preferred model is very strongly preferred over a model with 3 transiting planets (did not converge, AIC = 1332) and a 4-planet model with no trend and no curvature (AIC = 1202). Our full RV timeseries can be seen in Figure 3.1, and phase-folded RV time series for each planet can be seen in Figure 2.3. The orbital parameters and masses of all planets can be found in Table 2.1. We searched the residuals of our preferred model for additional planets but found no statistically significant signals.

2.3.3 Photometry Model

We pre-whitened the *TESS* photometry by using a Gaussian process model to subtract out low amplitude stellar and instrumental variability from the light curve. We then performed a blind transit search using `Transit Least Squares` (`TLS`; [106]). This recovered three transiting planets with period, depth, and duration values and errors consistent with the

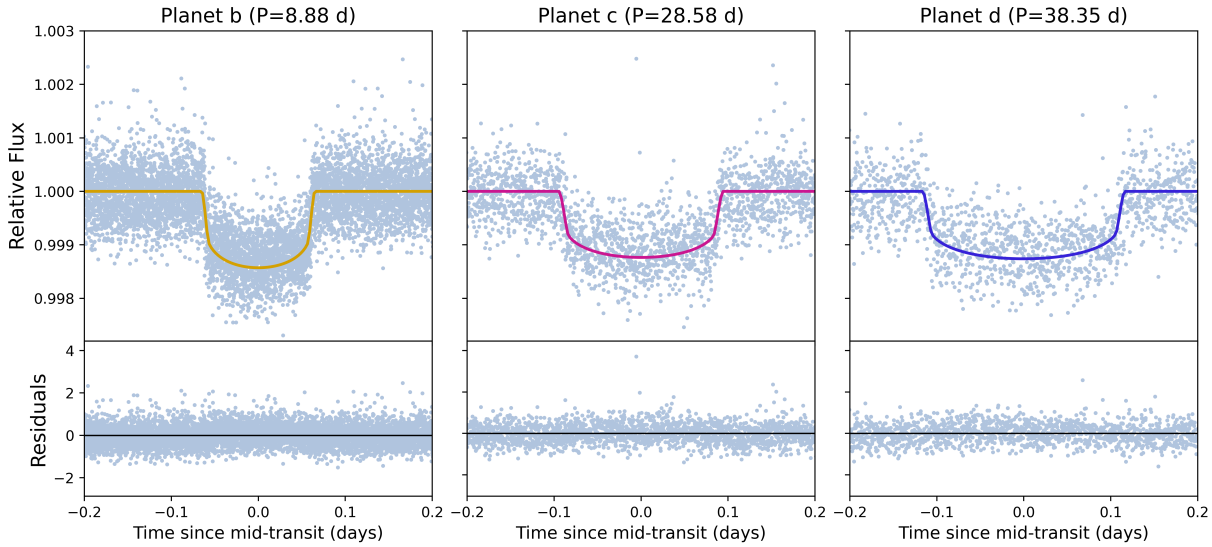

Figure 2.4: Phase folded light curves for each of the transiting planets with our best fit model overlaid and residuals below.

previously published values in [14]. We also performed a more targeted search with `TLS` for transits of planet e but found no evidence of any such events. We then modeled the transits of planets b, c, and d with the `Exoplanet` package [80] and re-derived planet parameters using our updated stellar parameters and the `TLS` output as priors (Table 2.1).

To calculate this model, we assumed circular orbits and fit for seventeen parameters: (1.) Orbital periods, with Gaussian priors informed by our `TLS` search values, (2.) Times of inferior conjunction, with Gaussian priors informed by our `TLS` search, (3.) Planet-to-star radius ratios, with a log-uniform prior from 0.01 to 0.1, (4.) Impact parameters, with a uniform prior from 0 to 1, (5.) Stellar radius, with Gaussian priors defined by the updated stellar parameters, (6.) Stellar mass, with Gaussian priors defined by the updated stellar parameters, (7.) Quadratic limb darkening parameters calculated using `Python Limb Darkening Toolkit` [173], and (8.) A white noise scaling term for the *TESS* light curve. `Exoplanet` implements MCMC algorithm, which we ran with 2000 iterations and a 500 step burn in and found that all chains converged. Additionally, we derived transit midpoints for each transit of each planet which is discussed further in §2.7 (see Appendix, Table 2.2). Figure 2.4 shows

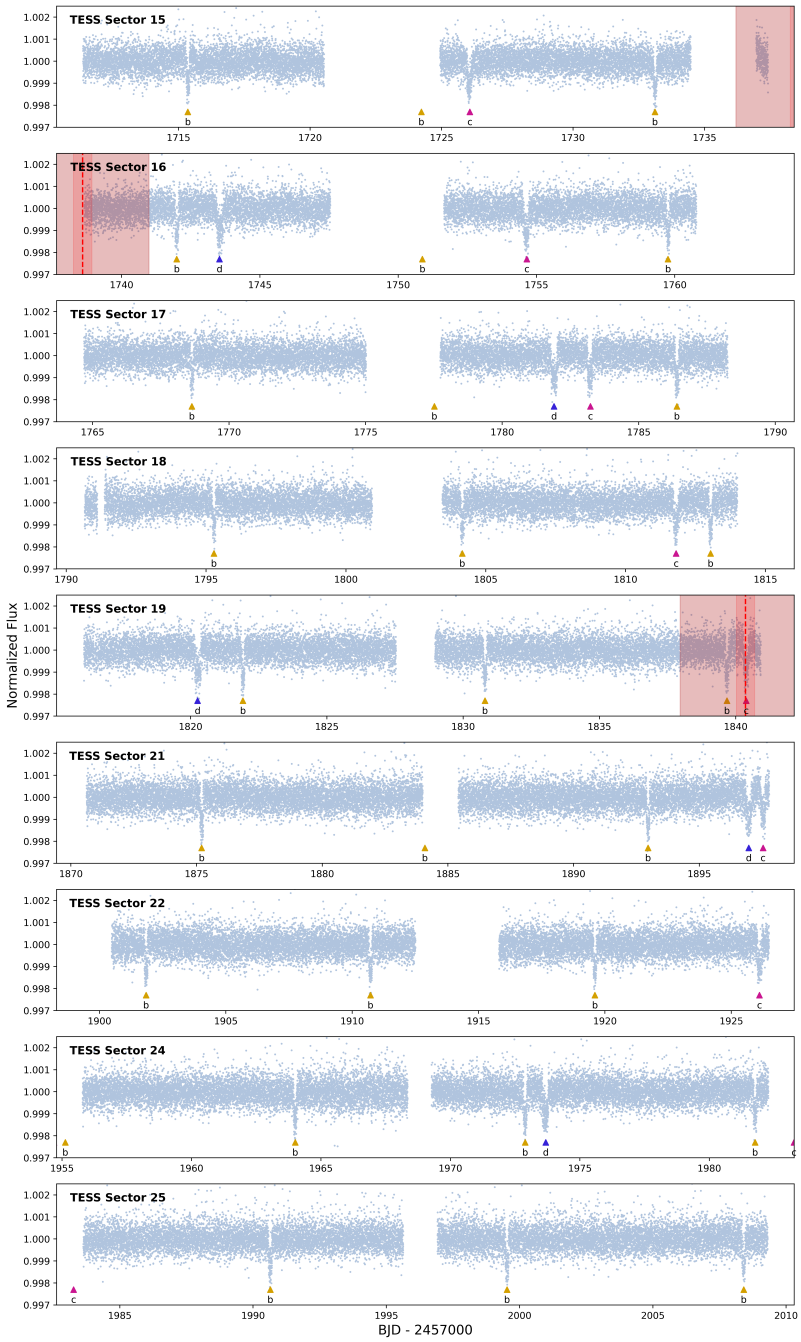

Figure 2.5: *TESS* photometry from sectors 15-19, 21, 22, 24, and 25 highlighting the transits of the three sub-Neptunes which are indicated by color-coded arrows. Our RV model's predicted transit midpoint times for planet e are shown by vertical dashed red lines along with 3σ error windows as light red shaded regions. The predicted ~ 8 hour transit duration (for a central transit) is shown by dark red shading. An additional transit window occurred in Sector 23 when the star was not visible in any *TESS* cameras.

our modeled phase-folded light curves for each planet and Figure 2.5 shows the full reduced *TESS* light curve of the star with transits color coded.

Given our weak detection of planet d in the RV time series, we returned to the photometry to confirm the period and transit times. Due to the positioning of data gaps in the light curve, there are 4 "odd" transits and 1 "even" transit of planet d. We considered the possibility that the single even transit, occurring at 2458781.89 BJD, comes from a different source than the four odd transits. In such a scenario, the orbital period of planet d would double to 76.7 days. However, comparing between the transits, including matching depths, durations, and ingress/egress shapes, we found no inconsistencies between the single transit and the other four. Furthermore, we find no evidence for a $\sim$76 day periodicity in our RV time series. Thus we conclude that all five transits do originate from a single planet with an orbital period of 38.4 days.

2.4 Composition of Transiting Planets

How do the transiting planets in this system compare to other known transiting planets? We find planet b imparts a Doppler semi-amplitude of 3.8 ± 0.3 ms^{-1}, corresponding to a mass of 10.4 ± 0.9 $M_{\oplus}$; planet c imparts 1.8 ± 0.3 ms^{-1}, corresponding to 7.2 ± 1.4 $M_{\oplus}$; and planet d imparts 0.6 ± 0.3 ms^{-1}, corresponding to 2.8 ± 1.5 $M_{\oplus}$. The placement of the three transiting planets on a mass-radius diagram reveals that they exist at the periphery of the known planet population (Figure 2.6). Planet b fits more consistently with previously known planets, while planet d is a low-mass outlier. The relatively low masses for their radii implies small densities. We find planet b has a bulk density of 1.5 ± 0.2 g/cc, planet c has 1.4 ± 0.3 g/cc, and planet d has 0.5 ± 0.3 g/cc.

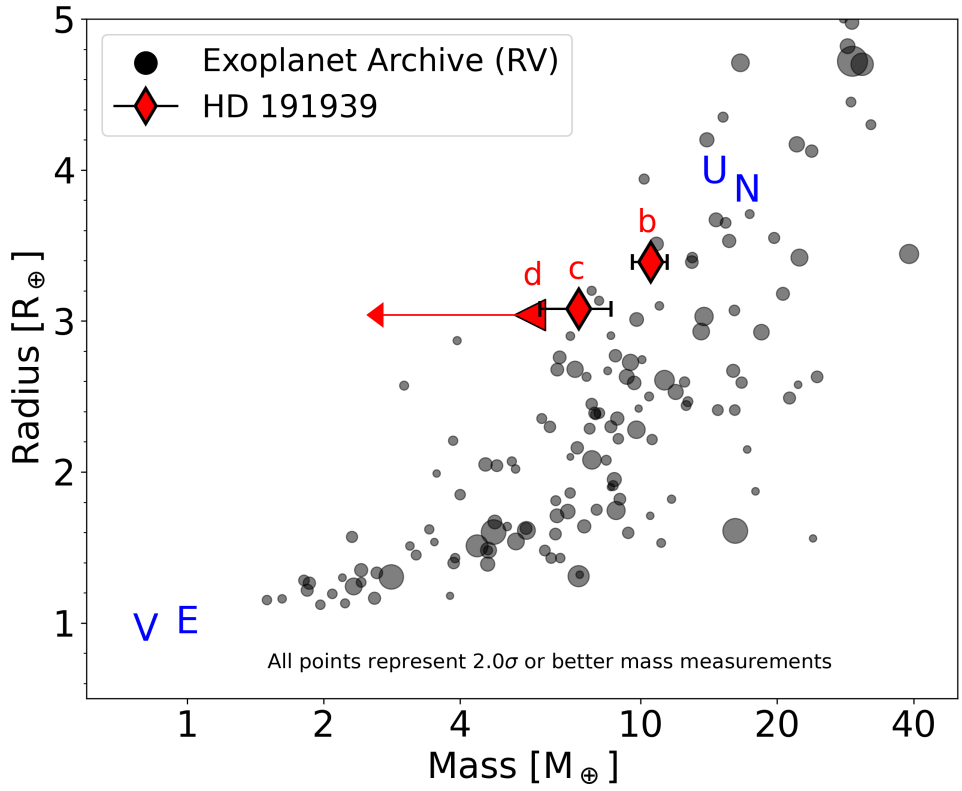

Figure 2.6: A Mass-Radius diagram highlighting the HD 191939 transiting planets. Larger marker sizes correspond to more precise mass measurements, excluding the HD 191939 planets. Planet d's marker represents the 2σ upper limit, and its arrow points back to the median value. Grey points are from the NASA Exoplanet Archive as of 2021-07-01, with cuts to include only 2σ masses or better.

[84] and [237] described the radius gap as a region of radius phase space from 1.5-2.0 $R_\oplus$ where relatively few planets are found. Studies have explained this gap as most likely due to a transitional phase between planets with and without extended H/He envelopes, which may be due to photoevaporation [133, 172]. Given that all three transiting planets in the HD 191939 system have radii above the gap, it is likely that the best description of their compositions is that of a volatile rich envelope surrounding a rocky core [244, 198, 84]. Employing `Smint` [182], which interpolates the model grids from [133] and [256] and samples posterior space with MCMC, we explored the possible fractions of H/He by mass for the three transiting planets assuming a dry, Earth-like, rock-iron core. Using a flat prior for the

age from 9 to 13 Gyr, we find H/He envelopes of $6.5 \pm 0.5\%$ for planet b, $5.7 \pm 0.6\%$ for planet c, and $6.4 \pm 0.5\%$ for planet d.

From our RV model, we place a 2σ upper limit on planet d's mass at 5.8 $M_\oplus$. This corresponds to 2σ upper limit on planet d's density of 1.1 g/cc. While this density upper limit places it within the range of planets b and c, the potential low density for planet d is noteworthy. In the literature, there is a population of low density planets: the Kepler-51 system [146], Kepler-79d [115], and Kepler-87c [170], which are collectively described as "super-puffs" for their inflated radii (4-8 $R_\oplus$) and low masses (2-5 $M_\oplus$), which implies densities of $\sim$0.1 g/cc. While HD 191939 d is not a super-puff since its radius is smaller (only 3 $R_\oplus$), it does share a notable characteristic with the super-puffs: they all exist in or near resonance with another planet in their systems. The super-puff planets may have low masses for their sizes as part of a selection bias: the planet masses are derived from transit timing variation (TTV) interactions, which are most prominent for planets in or near a resonance chain. HD 191939 d's potential low density, combined with its placement as the outer member of a near 4:3 resonance with planet c (see §2.7 for more detail), draws some comparison to the super-puffs and brings forward questions on its possible formation history.

Two different mechanisms have been proposed for explaining the prevalence of highly inflated plants in or near resonance. [125] showed super-puff planets most easily gain their extended atmospheres in dust-free environments at distances beyond 1 AU before migrating inwards. As part of this migration, they are more likely to form the outer companion of a resonance chain with another interior planet in the system. Under this formation scenario, planet d would likely contain a large fraction of water, a composition which we do not explore in this paper. [156] describes how super-puffs that exist just wide of resonance with another planet are thought to have preferentially high obliquities, which could drive heat dissipation through obliquity tides resulting in inflated planet radii.

HD 191939 d represents a unique opportunity to study a possible low density planet and to

test the above theories for two reasons. The mass measurement we provide comes from the RV method rather than TTVs. The location in the system interior to the Jovian planet e can provide dynamical constraints for any potential migration history. Of the super-puffs listed above, only Kepler-79d has a confirmed planet exterior to its orbit in the system, and this planet is another sub-Neptune.

The relatively small masses, low densities, and high equilibrium temperatures of these planets might combine to drive atmospheric escape on some or all of the three inner planets. By the Jeans escape mechanism, to first order approximation a gas will eventually completely escape if its thermal velocity exceeds one sixth the planet's escape velocity. Planet b's temperature is likely high enough to allow the steady escape of atomic and molecular hydrogen. Fixing each planet's radius to the median values of our photometry model, we calculated whether molecular hydrogen would escape each planet for a grid of every combination of planet mass and equilibrium temperature out to 3σ of each value. We find that molecular hydrogen escapes planet b in 84% of combinations, 52% for planet c, and 94% for planet d. Following the same procedure, planet d's small mass means it may not even be able to retain helium as 47% of combinations allow this gas to escape. If any of these planets are experiencing atmospheric escape, transmission spectroscopy with *JWST* might show evidence.

2.5 Planet f Constraints

What is the nature of the 5th planet in the system? Our RV analysis favors both a trend and curvature in the residuals of the preferred 4-planet model, suggesting a 5th planet with an orbital period much longer than our 415-day observing baseline. The presence of this planet can be further constrained by the change in HD 191939's proper motion over a period of 24 years. Using these independent data sets, we can place constraints on the mass and semi-major axis of planet f.

We derived these constraints using a novel method which compares model orbits using just 3 free parameters. We quantify long-period signals in the RV residuals through trend ($\dot{\gamma}$) and curvature ($\ddot{\gamma}$) terms; and astrometric motion through $\Delta\mu$, the difference in proper motions at two epochs. We generated a set of randomly-sampled orbits and computed these three parameters for each. A high-likelihood orbital model is one that reproduces the true values of $\dot{\gamma}$, $\ddot{\gamma}$, and $\Delta\mu$.

To produce a set of model orbits, we first defined our search range for both mass and semi-major axis. We started with $\tau_{\rm min}$, the lower bound on orbital period. Planet f produced only a small detected curvature over our observing baseline, a feature that we estimate would require an orbital period >4 times the baseline. This yielded a lower semi-major axis limit of 2.6 AU. We limited our search to semi-major axes within 50 AU. We used a similar argument to obtain a lower bound on M_p. We took the maximum ΔRV from the residuals of fitting for planets b-e and set it equal to the semi-amplitude of a planet with a period of $\tau_{\rm min}$, again assuming a circular orbit. From this amplitude, we calculated a minimum mass of 2.05 $M_{\rm J}$. We chose 200 $M_{\rm J}$ as the upper limit of our mass search, reasoning that more massive objects would be luminous enough to detect in high-contrast imaging.

We marginalized over four additional orbital parameters: inclination i, eccentricity e, argument of periastron ω, and mean anomaly M. In total we drew 10^8 random samples from this 6-dimensional parameter space using the following prior distributions:

- $\log\left(\frac{a}{1\ \rm AU}\right) \sim \mathcal{U}(2.62, 50)$
- $\log\left(\frac{M_p}{1\ M_{\rm J}}\right) \sim \mathcal{U}(2.05, 200)$
- $\cos(i) \sim \mathcal{U}(0, 1)$
- $\omega \sim \mathcal{U}(0, 2\pi)$
- $M \sim \mathcal{U}(0, 2\pi)$

- $e \sim \mathcal{B}(0.867, 3.03)$

where $\mathcal{B}$ is the two-parameter [121] beta distribution for e. We used the same samples to generate both the RV curves and the astrometric proper motions.

To impose RV constraints, we computed for each sample the first ($\dot{\gamma}$) and second ($\ddot{\gamma}$) time derivatives of the stellar radial velocity. We began by differentiating the true anomaly ν:

$$\nu = 2\tan^{-1}\left[\sqrt{\frac{1+e}{1-e}}\tan\left(\frac{E}{2}\right)\right] \tag{2.1}$$

$$\dot{\nu} = \frac{2\pi\sqrt{1-e^2}}{\tau\left[1-e\cos(E)\right]^2}, \tag{2.2}$$

where τ is the orbital period calculated from Kepler's Third Law and E is the eccentric anomaly, which we obtained by numerically solving Kepler's equation:

$$M = E - e\sin E. \tag{2.3}$$

The second derivative of ν is also needed to compute $\ddot{\gamma}$:

$$\ddot{\nu} = -\dot{\nu}^2\frac{2e\sin(E)}{\sqrt{1-e^2}} \tag{2.4}$$

With the derivatives of ν, we can write the equations for $\dot{\gamma}$ and $\ddot{\gamma}$. We start with the RV value itself, γ:

$$\gamma = K\left[e\cos(\omega) + \cos(\nu+\omega)\right], \tag{2.5}$$

where

$$K = \sqrt{\frac{G}{1-e^2}}\frac{M_p \sin i}{\sqrt{a(M_p+M_\star)}}. \tag{2.6}$$

The derivatives of γ are:

$$\dot{\gamma} = -K\left[\dot{\nu}\sin(\nu+\omega)\right] \tag{2.7}$$

and

$$\ddot{\gamma} = -K\left[\dot{\nu}^2\cos(\nu+\omega) + \ddot{\nu}\sin(\nu+\omega)\right]. \tag{2.8}$$

We evaluated the sample likelihood according to

$$P(\dot{\gamma}, \ddot{\gamma} | \dot{\gamma}_m, \ddot{\gamma}_m) \propto \exp\left[-\left(\frac{(\dot{\gamma}-\dot{\gamma}_m)^2}{2\sigma_{\dot{\gamma}}^2} + \frac{(\ddot{\gamma}-\ddot{\gamma}_m)^2}{2\sigma_{\ddot{\gamma}}^2}\right)\right]. \tag{2.9}$$

To obtain the 2D a-M_p joint posterior, we marginalized over $\{e, i, \omega, M\}$. The results from the RV only constraints can be seen in Figure 2.7 in green with 1- and 2-σ contours.

We next incorporated astrometry to further constrain the characteristics of the fifth planet. [37] aligned the reference frames of *Hipparcos* [2] and *Gaia EDR3* [128] to produce a self-consistent catalog of stellar proper motions measured at epochs 1991.25 and 2015.5. [37] reported the proper motion based on the difference in position between these epochs. The *Gaia* and position-derived proper motions, $\vec{\mu}_G = (150.19 \pm 0.02, -63.99 \pm 0.02)$ mas/yr and $\vec{\mu}_{HG} = (150.31 \pm 0.03, -63.94 \pm 0.03)$ mas/yr, were the most precise, and indicated a change in proper motion $\Delta\mu = |\vec{\mu}_G - \vec{\mu}_{HG}|$ of 0.13 ± 0.03 mas/yr over the 24 years separating the two epochs.

Using the same orbit models as in the RV analysis, we first computed the average proper motion vector in the *Gaia EDR3* epoch. We also used the change in astrometric position between the *Gaia* and *Hipparcos* epochs to obtain an average proper motion over the 24 year baseline. We then computed the magnitude of the difference vector $\Delta\mu_m$ and evaluated the likelihood via

$$P(\Delta\mu | \Delta\mu_m) \propto \exp\left(-\frac{(\Delta\mu - \Delta\mu_m)^2}{2\sigma_{\Delta\mu}^2}\right). \tag{2.10}$$

The detected proper motion difference rules out high mass models that were permitted by our RV-only analysis. The blue region of Figure 2.7 shows the range of a-M_p values that are

allowed by astrometry at the 1 and 2σ levels.

Because the RV and astrometric data sets are independent, we may evaluate the joint RV-astrometry likelihood by multiplying Equations 2.9 and 2.10. Figure 2.7 shows in red the region of a-M_p space that is allowed by both the RV and astrometric constraints. We find at 95% confidence that planet f has a mass of 2–11 $M_{\rm J}$ and orbits at a distance of 2.6–7.0 AU.

Throughout this paper we refer to this companion as a "planet" because these current mass constraints place it most likely below the generally accepted upper mass limit for planets of $\sim 13\,M_{\rm J}$; but we caution that the high-mass tail of the probability distribution includes objects that would typically be characterized as brown dwarfs. Such high mass objects on the planet-brown dwarf boundary are thought to form by one of two general formation pathways: core accretion [184] or gravitational instability [35]. Core accretion is more successful at producing low mass objects and is the most plausible formation channel for planets b through e. [208] showed a transition point in formation mechanism at $10\,M_{\rm J}$, which may represent a mass upper limit for objects formed via core-accretion. Therefore, more massive objects more likely formed via gravitational instability and are therefore not planets. If planet f is at the upper end of its mass range, gravitational instability becomes a plausible pathway. This raises the possibility that both mechanisms were active in the HD 191939 system. We advocate for continued Doppler/astrometric monitoring of the HD 191939 system to fully resolve this companion's orbit and measure its mass more precisely to identify which formation channel is more likely.

2.6 Planet e is Nearly Coplanar

What is the inclination of planet e? Given the emergence of planet e in our RV data, we searched the *TESS* photometry for evidence of its transit. We would expect this $0.34 \pm$

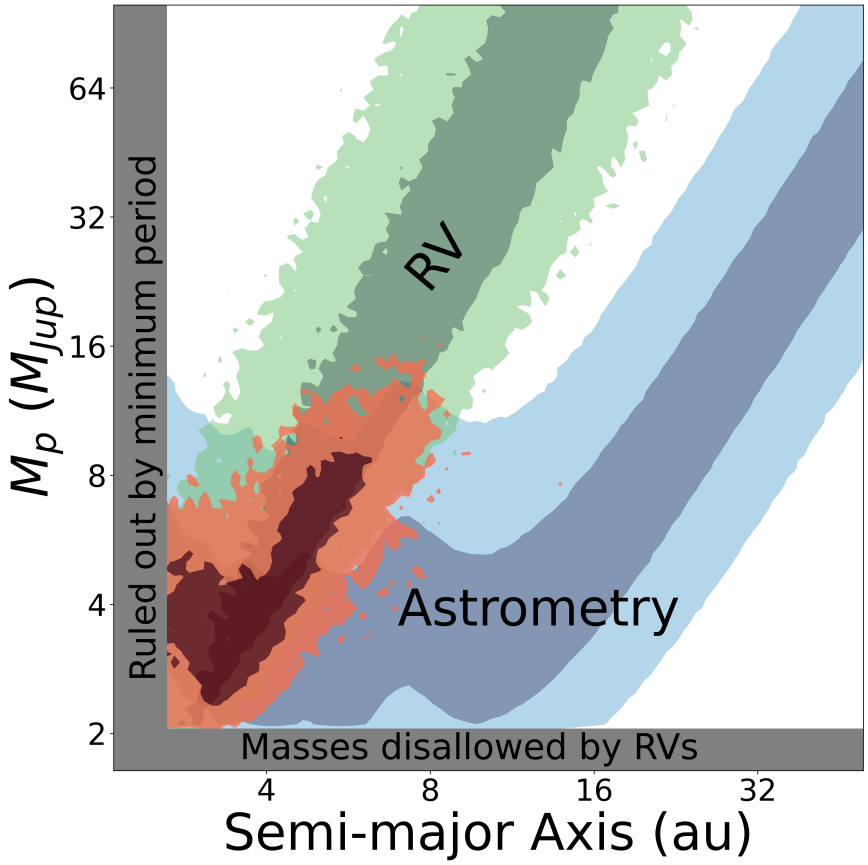

Figure 2.7: Constraints on the mass and semi-major axis of planet f. The green region shows values that are consistent with the measured RV trend and curvature. The blue region shows values that are consistent with the Hipparcos/Gaia astrometry. The red region shows the values consistent with both RV and astrometry. Dark and light regions indicate the 1 and 2σ confidence intervals, respectively. Planet f is likely between 2–11 M_J, orbiting between 2.6–7.0 AU.

$0.01\,M_{\rm J}/\sin i$ Jovian planet to have a radius of $\sim 1\,R_{\rm J}$, implying a transit depth on the order of 1%. At a 101 day orbital period, assuming zero eccentricity and an edge-on orbit, we expect the duration of its transit to be ~ 8 hours. Such a transit event should be obvious in the data by visual inspection. We do not see planet e's transit (see Figure 2.5).

Within the error bars of our period and time of conjunction for planet e, it is possible that *TESS* missed the transits of planet e by unlucky timing. Still, the most likely explanation for the missing transits is that the planet is non-transiting. We did not search for a transit of planet f because its transit event should be a similar depth but even longer than planet

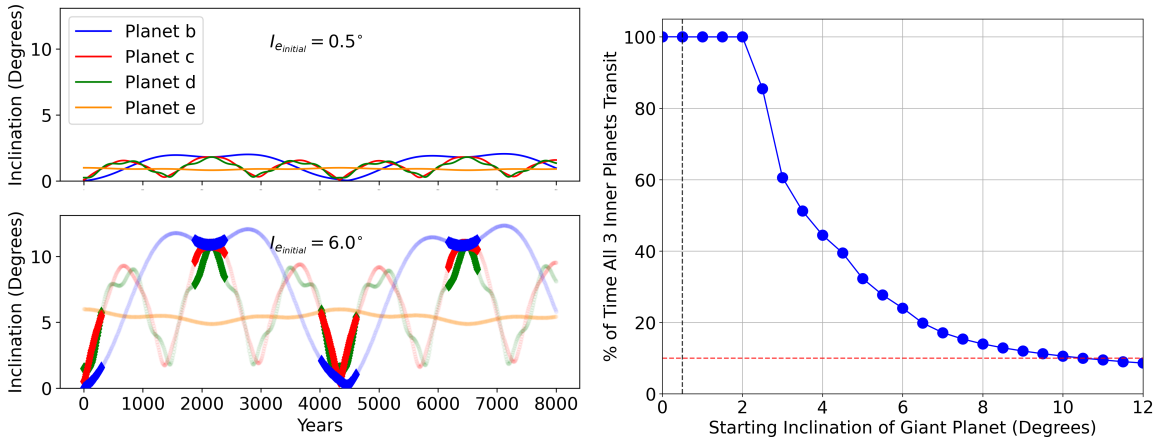

Figure 2.8: Details on the Laplace-Lagrange analysis. **Left:** The inclination curves for each planet when planet e is given a starting value of $I_e = 0.5°$ vs $I_e = 6.0°$. When the mutual inclination of the three is small enough for all three to transit together, the line is opaque. **Right:** The percent of time during which the inner three planets transit depends on the inclination of planet e. The vertical black dashed line indicates the nominal maximum inclination for which we would expect planet e to still transit. The horizontal red dashed indicates the 10% threshold for our conservative estimate on the upper limit to the giant planet's inclination.

e's and it was not near its expected time of conjunction at the time of *TESS*'s observations.

Assuming planet e is non-transiting and has a radius of 1 R_J, we place an upper limit on the inclination at 89.5°. To place a lower limit, we explored the dynamics of the system with Laplace-Lagrange secular perturbation theory [145]. Following the methods in [161], we analytically derived equations for the time dependence of the inclination for each of the planets in the system. We chose to ignore effects from planet f. Due to planet f's large semi-major axis relative to the other 4 planets, the inner 4 will move together under its influence. Additionally, any of effects from planet f will play out over much longer timescales than we are interested in (∼2 orders of magnitude longer). For the four planets in question, we used the median values for mass and semi-major axis from Table 2.1. Within the Laplace-Lagrange framework, eccentricity and inclination become decoupled; for simplicity and consistency with our preferred RV model, we assumed circular orbits.

The Laplace-Lagrange secular perturbation theory is built on the foundation of the disturbing

function, where I is the inclination, j and k are planet indices that run from 0 to N with N being the number of planets in the system:

$$\frac{\partial I_j}{\partial t} = -\frac{1}{n_j a_j^2 I_j} \frac{\partial R_j}{\partial \Omega_j}, \tag{2.11}$$

where R_j is the disturbing function

$$R_j = n_j a_j^2 \left[\frac{1}{2} B_{jj} I_j^2 + B_{jk} I_j I_k \cos(\Omega_j - \Omega_k) \right] \tag{2.12}$$

and

$$B_{jk} = \frac{1}{4} \left[\frac{G(M_* + m_j)}{a_j^3} \right]^{\frac{1}{2}} \frac{m_k}{M_* + m_j} \alpha_{jk} \overline{\alpha}_{jk} b^{(1)}_{\frac{3}{2}}(\alpha_{jk}), \tag{2.13}$$

and

$$n_j = \sqrt{\frac{G(M_* + m_j)}{a_j^3}} \tag{2.14}$$

where $B_{jk} = -B_{jj}$. Terms α_{jk} and $\overline{\alpha}_{jk}$ are constants determined by semi-major axis ratios of the jth and kth planets, $b^{(1)}_{\frac{3}{2}}(\alpha_{jk})$ is a definite integral also dependent on semi-major axes [161], and Ω is the longitude of ascending node. From the disturbing function we constructed

the B matrix. The eigenvalues of the B matrix, f_k, represent the periodicity of the oscillations of the planets' inclination and the eigenvectors (which are unscaled and must be normalized) along with the initial conditions of the system's configuration represent the amplitude of the oscillations.

In the normalization process we calculated both a scaling factor and a phase angle for the oscillation periodicity of each planet, γ_k. This is accomplished by implementing the initial conditions at t = 0 (both I_o and Ω_o) to generate a set of set of $2N$ equations from which we can solve for N scaling factors and N phase angles. With these scaling factors in hand, the final amplitudes of the oscillations, V_{jk}, are determined.

Then we calculated the inclinations of each planet at a given time:

$$I_j = (p_j^2 + q_j^2)^{\frac{1}{2}}, \tag{2.15}$$

where p_j and q_j are parameterized variables:

$$p_j = \sum_{k=0}^{N_{planets}} V_{jk} \sin(f_k t + \gamma_k), \tag{2.16}$$

$$q_j = \sum_{k=0}^{N_{planets}} V_{jk} \cos(f_k t + \gamma_k). \tag{2.17}$$

Within this framework, we derived $I_j(t)$ for each planets j $\in$ {b, c, d, e} for various initial

configurations of the system.

For each configuration, planets b, c, and d were initialized at 0°, corresponding to placing all three on the same plane. Note that the plane from which we are measuring inclinations is 90° transposed from the conventional plane of reference for inclinations, the sky plane. For ease of reference, we call this plane the *LL-Plane*. We also initialized all four planets' longitude of ascending node, Ω, to the same value, arbitrarily 0°. We tested various trials where Ω_e was initialized at different values between 0°-360° and found it had little to no effect on the outcome of our experiment. In each configuration we set the starting inclination for planet e to different values, stepping in 0.5° intervals from 0° to 12.0°.

We computed $I_j(t)$ for an 8,000 year span, roughly double the longest eigenfrequency. For every year in a configuration, we computed the mutual inclination of the three planets [46]:

$$\cos I_{xy} = \cos I_x \cos I_y + \sin I_x \sin I_y \cos(\Omega_x - \Omega_y). \tag{2.18}$$

We determined a maximum limiting angle for mutual transiting of the inner 3 planets by geometric reasoning. We calculated the minimum transiting inclinations for both the innermost and second innermost planets, by $i_{min} \approx R_*/a$. Then the sum of these two angles is the limiting angle. This corresponds to placing the innermost and second innermost planets at the opposite limbs of the star. For a given timestamp, if the mutual inclinations of all pairs of planets are less than the limiting angle, then all planets transit together at that timestamp.

Figure 2.8 shows the $I_j(t)$ curves for two examples from our trials as well as the results of all trials. For each trial of planet e's starting inclination, we computed the percent of timestamps within the 8000 year time span during which all three of the inner planets transited with

respect to an arbitrary line of sight. As expected, the farther from the LL-Plane that we start planet e's inclination, the smaller the percent of the timestamps during which all three inner planets will transit. There is a range of starting inclinations for which we would expect all three inner planets to transit 100% of the timestamps, from 0° to 2.0° in the LL-Plane. We nominally rule out inclinations less than 0.5° based on the absence of a transit for planet e, although this limit does not take into account the uncertainty in planet e's radius and the simplification that all three inner planets start at 0°. In sample tests where we included planet f with mass and semi-major axis values drawn from results in §2.5, we find the results to be similar. Including planet f, the value for the percentage of timestamps where the inner 3 planets are all transiting for any given inclination of planet e is within 5% of the value as when we exclude planet f.

Above 2.0° in the LL-plane, the percentage of timestamps where all three are transiting together falls sharply and then decreases asymptotically towards 0%. From these results, we conservatively place a upper limit on the planet e's mutual inclination at 10°. This angle corresponds to a lower limit for absolute inclination of 80° in the conventional sky-plane frame of reference. For starting inclinations above 10°, the amplitudes of the planets' oscillations in inclination space become large enough that it is rare for all three to transit together from an arbitrary line of sight: $< 10\%$ of the timestamps tested. Mutual inclinations of planet e larger than 10° are viable solutions. However, in those scenarios, the decreasingly short windows in time where all three planets transit make Earth observers increasingly lucky to have caught the system at one of these rare moments in its dynamical periodicity. This investigation suggests that planet e is likely to be nearly coplanar with the three transiting planets.

2.7 TTVs and MMR

Planets c and d have orbital periods very near to 4:3 mean-motion resonance (MMR). But do they indeed reside in MMR? We explored this possibility and the implications which follow.

In general, planets which reside in MMR are characterized by period ratios of

$$\frac{P_2}{P_1} = \frac{j}{j-1}, \tag{2.19}$$

where j is an integer and subscripts 1 and 2 denote the inner and outer planet of the pair, respectively. We quantify the "proximity" to MMR by

$$\Delta_{12} = \frac{P_2}{P_1}\frac{j-1}{j} - 1, \tag{2.20}$$

following [130].

Applying this formula to planets c and d, $\Delta_{cd} = 0.6432 \pm 0.0001\%$. Following [25], the resonant bandwidth can be approximated as:

$$|\chi| \lesssim 5\frac{j-1}{j^{2/3}}\Big(\frac{M_1+M_2}{M_*}\Big)^{2/3}. \tag{2.21}$$

For planets c and d, $\chi_{cd} = 0.662 \pm 0.001\%$. Because $\Delta < |\chi|$, we cannot rule out that the two planets are librating in MMR.

Under the assumption that planets c and d are close to but *not* in MMR, we calculated the period and amplitude of TTV oscillations of the pair following [130]. TTV oscillations will be oppositely-phased sinusoids, each at a period designated as the *super period* (SP):

$$P_{SP} = \frac{P_2}{j\,|\Delta|}, \tag{2.22}$$

with amplitudes

$$TTV_1 = P_1 \frac{\left(\frac{m_2}{M_*}\right)}{\pi j^{2/3}(j-1)^{1/3}\Delta}\left(-f - \frac{3Z}{2\Delta}\right), \tag{2.23}$$

and

$$TTV_2 = P_2 \frac{\left(\frac{m_1}{M_*}\right)}{\pi j \Delta}\left(-g - \frac{3Z}{2\Delta}\right), \tag{2.24}$$

where f and g are constants associated with the MMR ratio, in this case 4:3, and Z is a linear combination of the free eccentricities of the two planets.

We calculated the super period of planets c and d to be 1490 ± 10 days. In the circular orbit limit, $Z = 0$ and the amplitudes of planet c and d's TTV oscillations are 15.5 ± 9.1 minutes and 59.2 ± 13.8 minutes, respectively. If the phase of the oscillations is near an inflection point, Planet d's oscillation would be large enough that it could be detected even though *TESS* has only sampled about a fifth of the super period.

To further investigate, we calculated the TTV associated with each transit event. We generated model transits offset from the expected transit time by between ±60 minutes and calculated the chi-squared (χ^2) fit of these model transits to the light curve. We adopted the offset that minimized the χ^2 statistic as the value of the TTV. The 1σ error bars are calculated from the offset where the χ^2 increased from its minimum value by 1.0. We performed this process for each transit of each planet.

Figure 2.9 as well as Table 2.2 shows all of the TTVs for each planet. Planet d's 5 transits cover ∼230 days of time, or about 15% of the super period. Its TTVs do not show a trend. Planet c's transits similarly span only ∼230d. Due to *TESS*'s observing strategy, planet c transited just hours before sector 24 observations and hours before and after sector 25 observations, at times when the star was not visible to *TESS*. It is noteworthy that the two planets behave similarly in that when one is late, the corresponding transit of the other is similarly late and vice versa for early transits. Planet b's TTVs are consistent with zero, showing no trend or significant sinusoidal variation.

These results can be interpreted in two ways. First, and most likely, *TESS* has not sampled enough of the 1500 day super period to make a conclusive finding. Alternatively, we could be sampling TTVs very near the maximum or minimum of the TTV signal's phase, so the ΔTTV over the baseline is too small for a significant detection. *TESS*'s extended mission cycle 4 will shed more light onto these three possibilities.

2.8 Gap Complexity

Could there be an additional planet hiding in the gap between planets b and c? With planets c and d very near MMR, it is noticeable that there are not more pairs of planets also spaced in near resonant orbits. Following the peas-in-a-pod architecture where multi-planet

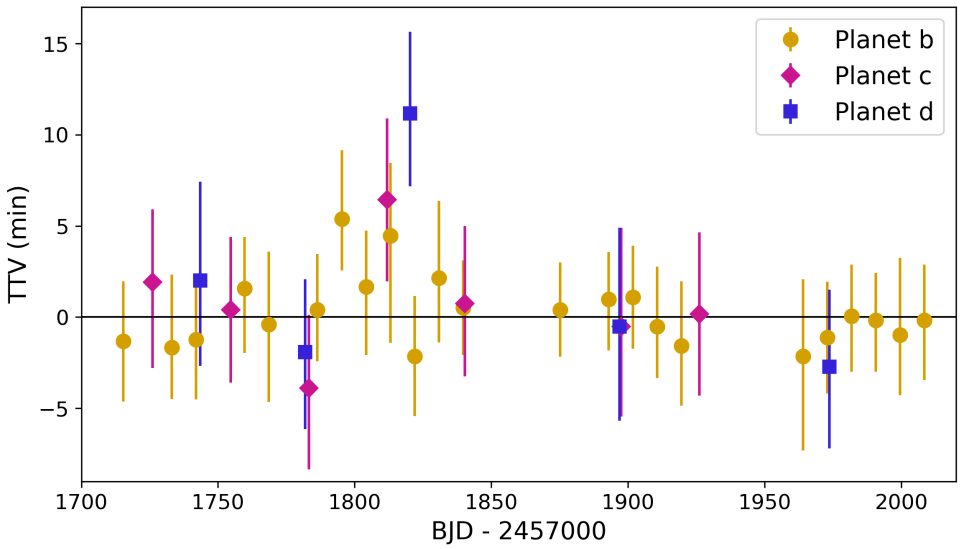

Figure 2.9: TTVs of the transiting planets over the duration of the *TESS* photometry. We do not detect significant TTVs for any of the transiting planets over the observing baseline.

systems show similarly sized planets in regular orbital distance spacing, we might expect more than just one pair in this system to exhibit near-resonance, especially considering that the transiting planets have very similar radii [126].

In the residuals of our GLS periodogram (Figure 2.1), there is a noticeable peak between planets b and c at 17.7 days. A planet at this period would be particularly interesting as it would be near 2:1 resonance with planet b and 8:5 resonance with planet c. A planet at this period would also fill the gap in log Period space of this system well. Given that we have a strong RV detection of planet c, any additional planet in this gap between planets b and c must be less massive than planet c and inclined. When we add a fit for a 17.7d planet in our preferred model, we find a 2σ upper limit to its mass to be 6 $M_{\oplus}$. In order to be non-transiting, its inclination must be at least 2° from the LL plane.

We followed the methods in [93] to calculate the Gap Complexity, $\mathcal{C}$, for the HD 191939 system. $\mathcal{C}$ describes the deviation from uniform planet spacing in a system. $\mathcal{C} = 0$ indicates uniform spacing in log Period space, while as $\mathcal{C} \to 1$ the less uniform the spacing. For Kepler systems, $\mathcal{C}$ peaks at 0 with the majority ($\sim$75%) of systems having $\mathcal{C} < 0.2$. Systems with

larger $\mathcal{C}$ values are more likely to have additional planets hiding in the gaps between known planets. We calculate $\mathcal{C}_{\rm HD\,191939} = 0.846$ considering the transiting planets only, as planet e does not fall into the peas-in-a-pod configuration. We interpret the high value of $\mathcal{C}$ to mean that there is a significant gap, which could be the site of an additional planet. When we include a hypothetical planet on a 17.7 day period with the known transiting planets, we calculate $\mathcal{C}_{\rm HD\,191939} = 0.18$. This value is consistent with the findings of [93] for the general pattern of multi-planet system configurations. Adding a 17.7 day planet to our preferred model does not improve the likelihood enough to justify the extra three parameters. Nevertheless, this planet candidate is interesting and deserves continued attention with additional RV observations.

2.9 Follow Up Prospects

How well suited is this system for further follow up? We identified HD 191939 as a key TKS target for atmospheric follow up with the target selection algorithm described in Scarsdale et al. (in prep). As a bright ($J = 7.6$ mag) multi-planet system, space-based spectroscopic observations offer a unique opportunity for studies in planet formation and evolution.

We use the Transmission Spectroscopy Metric (TSM; [120]) to quantify the expected signal-to-noise ratio of *JWST*-NIRISS observations for the transiting planets:

$$\mathrm{TSM_p} = S \times \frac{R_p^3 T_{eq}}{M_p R_*^2} \times 10^{-0.2 m_J}, \tag{2.25}$$

where S is a dimensionless normalization constant, equal to 1.28 for planets $2.75 < R_p < 4.0\ R_\oplus$. The TSM is a proxy for the expected SNR from a 10-hour observing program with *JWST*-NIRISS assuming a cloud-free, solar-metallicity, H_2-dominated atmosphere. For reference, HD 3167 c, a sub-Neptune orbiting an early-K dwarf with a recent water vapor

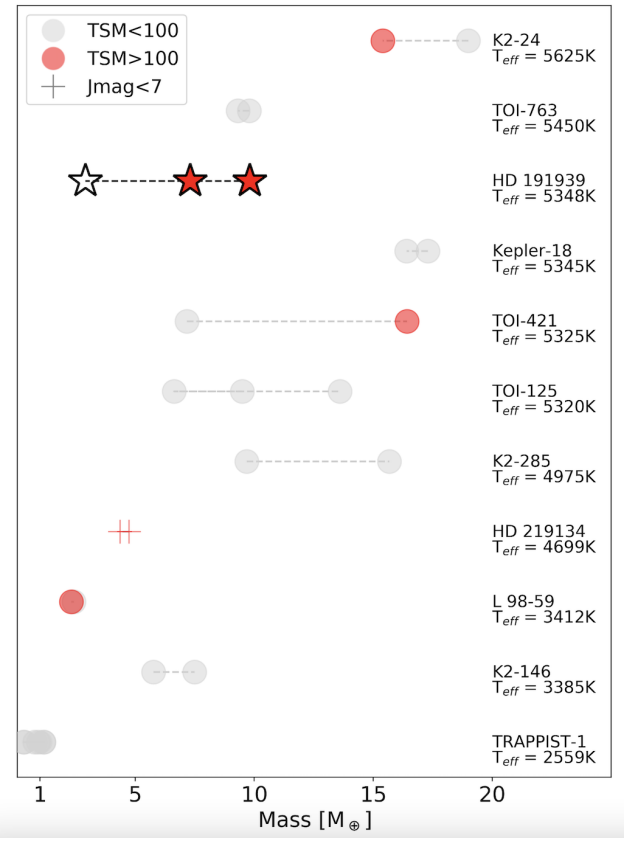

Figure 2.10: All multi-planet systems with 5σ masses and radii for small planets ($R_p < 10R_\oplus, M_p < 100M_\oplus$) with TSMs ¿ 20. Planets are plotted by mass and arranged vertically in order of host star effective temperature (hotter at the top). HD 191939 b and c have TSM values that are individually among the best in the sub-Neptune population, and are unique in having the same host star. Due to Planet d's weak mass measurement, it appears in this plot unfilled. HD 191939 is the only system to date with multiple planets with TSMs greater than 100 that also does not saturate *JWST*.

.

detection from five *HST*-WFC3 transits [153], has a TSM of about 100.

Using the derived planet parameters from Table 2.1, we find HD 191939 b has a TSM of 151 ± 18, which places it in the top quartile of targets in the $2.75 < R_\mathrm{p} < 4.0\ R_\oplus$ range from the statistical sample in [120]. HD 191939 c has a TSM of 106 ± 24, placing it in the third quartile from the top of TSM values for planets between 2.75 and 4.0 $R_\oplus$. We place a lower limit on the TSM of planet d, finding $\mathrm{TSM_d} > 72$ at 2σ confidence. For the transit durations reported in Table 2.1, our TSM values scale to an expected single-transit SNR

with *JWST*-NIRISS of 84 ± 10, 71 ± 16, and >53 for planets b, c, and d respectively, where the lower limit for planet d represents 2σ confidence.

We used `PandExo` [22] to estimate the nominal heights of molecular features in a single-transit *JWST*-NIRISS transmission spectrum for planet b, assuming a cloud-free, solar-metallicity atmosphere. In this ideal case we find feature heights of ∼100-300 ppm between 1 and 5 μm. In reality, clouds and/or enhanced atmospheric metallicity will probably reduce these amplitudes by a factor of three or more [241]. Additionally a sub-Solar C/O ratio, which may be implied from the host star's abundance measurements, also disagrees with the ideal case of a solar-metallicity composition and would produce spectra dominated by CO, H_2O, and CO_2.

A spin-orbit measurement for this system would be particularly informative to planetary formation theories. Only 8 systems with three or more planets have had their sky-projected obliquity angles, λ, measured. In the HD 191939 system, the three inner planets all lie in nearly the same orbital plane, while we have shown that the giant planet should lie close to this plane. If they are misaligned with respect to the stellar spin axis, that could inform the dynamical history of the system and the roles that planets e and f have played in shaping the system. However, the low $v \sin i$ (see Table 2.1) of the host star might be prohibitive to a Rossiter-McLaughlin (RM; [201, 150, 91]) measurement of even the largest expected signal from planet b. A simulation using `arome` [36] finds that for $v \sin i = 1$ km/s and $\lambda = 0°$, planet b's expected RM amplitude is 1.5 m/s.

HD 191939 will be observed again by *TESS* in Cycle 4. Nominal dates for observations include 6 sectors of additional coverage: 41, 48, 49, 51, 52, and 55. These observations will extend the total baseline of photometry observations to 2022-09-01 for a a total of 1142 days, about 76% of the super period between planets c and d.

2.10 Conclusions

The overall architecture of the HD 191939 system − multiple small planets, then a warm Saturn, followed by a high mass planet − seemingly stands alone among known systems. Sub-Neptunes are near ubiquitous [109, 180], but the *a priori* occurrence rate for warm sub-Jovians ($30 - 300\,M_\oplus$ at 0.1−1.0 AU) is much smaller at ∼3%, and similarly at ∼5% for cold super-Jovians ($300 - 6000\,M_\oplus$ at 3−10 AU) [85]. We cannot simply multiply together these occurrence rates to discern how rare it is for such a system like HD 191939 to exist, as [245] found that adjacent planets tend to have similar sizes, and some studies have found a relationship between sub-Neptune occurrence and giant planet occurrence [259, 41]

We searched the literature for analog systems by performing cuts on the known population for systems with 4 planets, with three sub-Neptunes ($M_p < 25M_\oplus$) interior to a warm Saturn ($50M_\oplus < M_p < 300M_\oplus$, with orbital period of 50−360 days) and a long period high mass planet. However, there are a few systems that stand out as notable.

Mills et al. 2019 [158] describe three systems, Kepler-65, Kepler-68, and Kepler-25 with high mass outer planets. Kepler-65 has a tight inner system of three sub-Neptunes and a 0.28 M_J planet with an orbital period of 258 days, similar to the inner system of HD 191939, but there is no evidence for a trend over a ∼2000 day baseline. Kepler-25 is similar in having two inner sub-Neptunes in/near resonance (2:1) and a Saturn mass planet at just over a 100 day orbit; but again, no evidence for a long period companion represented by trend over its ∼3000 day observing baseline. Kepler-68 may represent the most similar system to HD 191939. It has an inner system of of two sub-Neptunes, then a Jovian with an orbital period of 634 days, and then strong evidence for curvature in the residuals. [158] attribute this curvature to an object with a period much longer than the ∼3000 day baseline and place a lower limit of 0.6 M_J, but no upper limit. Lastly, Kepler-129 [257] bears resemblance to HD 191939 in having two inner planets at $< 45\,M_\oplus$ and a high mass Jovian (8.3 M_J) on

$\sim$7 year orbit. [257] also discusses the perturbations of inclinations of the inner transiting planets due to the long period Jovian. Each of these systems has pieces of the HD 191939 system, but none have the full architecture.

Bright, multi-planet systems are invaluable to the exoplanet community due to their enhanced follow up opportunities and comparative planet prospects. With photometry from *TESS* and RV data from both Keck/HIRES and the APF, we have characterized the HD 191939 system: 3 transiting sub-Neptune planets, a fourth Jovian, and 5th high mass planet. We have measured the planets' masses, as well as their radii and densities where applicable. Because of our strong mass measurements of 3 of the 4 inner planets ($> 5\sigma$), we are able to explore and further investigate many aspects of the system to answer more detailed questions about the system. Our main conclusions are as follows:

- The bulk densities of the transiting planets are $\rho_b = 1.5 \pm 0.2$ g/cc, $\rho_c = 1.4 \pm 0.3$ g/cc, and $\rho_d = 0.5 \pm 0.3$ g/cc. We find the compositions of the planets are best explained by extended H/He atmospheres.

- By a new technique for constraining the mass and period of distant companions using both RV and astrometric data sets, we find planet f to be between 2–11 $M_{\rm J}$ on a 1700–7200 day orbital period at 95% confidence.

- Through a dynamical analysis using Laplace-Lagrange secular perturbation theory, we constrain the inclination of the non-transiting planet e. We find it most likely orbits within a plane less than 10° from the plane roughly shared by the three transiting planets.

- By investigation into the potential mean motion resonance of planets c and d, we predict their TTV amplitudes to be 15.5 ± 9.1 minutes and 59.2 ± 13.8 minutes, respectively over a super period of 1490 ± 10 days. However, we find no evidence for

significant TTVs over the short observing baseline (326 days) compared to the super period of the interaction (1500 days).

- We analyze the RV residuals and Gap Complexity of the system to investigate the potential for additional planets in the system, identifying a possible planet candidate at 17.7 days which deserves continued attention.

- We evaluate the transiting planets' prospects for atmospheric characterization through transmission spectroscopy with *JWST*. HD 191939 is the only system that does not saturate JWST-NIRISS where two planets both have TSMs greater than 100, making it an excellent candidate for comparative atmospheric studies.

With its three transiting mini-Neptunes, one non-transiting Jovian planet, and distant high mass planet surrounding a bright, nearby host star, HD 191939 provides a rich natural laboratory for detailed atmospheric characterization and dynamical studies.

2.11 Appendix

Table 2.2: HD 191939 Transit Mid-times

Planet	Epoch #	Mid-time (BJD)	Error (BJD)
b	1	2458715.3552	0.0023
b	3	2458733.1156	0.0028
b	4	2458741.9962	0.0023
b	6	2458759.7587	0.0024
b	7	2458768.6376	0.0029
b	9	2458786.3987	0.0021
b	10	2458795.2825	0.0026
b	11	2458804.1602	0.0026
b	12	2458813.0424	0.0041
b	13	2458821.9181	0.0023
b	14	2458830.8014	0.0029
b	15	2458839.6806	0.0018
b	19	2458875.2017	0.0018
b	21	2458892.9626	0.0020
b	22	2458901.8430	0.0020
b	23	2458910.7222	0.0023
b	24	2458919.6017	0.0024
b	29	2458964.0028	0.0036
b	30	2458972.8837	0.0021
b	31	2458981.7649	0.0021
b	32	2458990.6450	0.0020
b	33	2458999.5248	0.0029
b	34	2459008.4056	0.0023
c	1	2458726.0546	0.0033
c	2	2458754.6340	0.0028
c	3	2458783.2116	0.0031
c	4	2458811.7992	0.0031
c	5	2458840.3758	0.0029
c	7	2458897.5359	0.0038
c	8	2458926.1168	0.0031
d	1	2458743.5531	0.0038
d	2	2458781.9029	0.0029
d	3	2458820.2645	0.0031
d	5	2458896.9613	0.0038
d	6	2458973.6648	0.0031

Table 2.3: HD 191939 RV Time Series

BJD	RV (m/s)	RV err (m/s)	S-Value	S-Value err	Instrument
2458795.832	−20.961	1.225	0.146	0.001	HIRES
2458802.800	−9.760	1.291	0.146	0.001	HIRES
2458815.779	−14.967	1.241	0.142	0.001	HIRES
2458834.647	1.901	3.891	0.141	0.002	APF
2458834.661	8.670	3.813	0.145	0.002	APF
2458837.734	−6.977	4.347	0.176	0.002	APF

The full data set in a machine readable format is available online.

Chapter 3

Stellar Activity Manifesting at a One Year Alias Explains Barnard b as a False Positive - Lubin et al. 2021

3.1 Foreword

In the 105 years since its discovery by E.E. Barnard as the star with the largest proper motion [20], Barnard's star (GJ 699) has become one of the most studied and heavily scrutinized star systems. Adding to its distinguishing characteristics, it is the nearest star to our own Sun in the Northern Celestial Hemisphere, and the second-closest star system overall [86, 15]. This proximity has engendered fascination by astronomers in many sub-fields of astronomy.

All these qualities have made the star attractive to astronomers in exoplanet science for decades. In 1963, Peter van de Kamp believed he had detected an astrometic wobble of Barnard's star using Swarthmore College's 24-inch refractor at Sproul Observatory [233], which he attributed to a planet. He later updated his findings three more times, proposing

a second planet in the system [234] and then revising the orbital parameters of both planets twice, finally concluding the system was comprised of 0.7 M_J and 0.5 M_J planets orbiting with periods of 12 and 20 years, respectively [235, 236].

The 1975 and 1982 revisions were published in spite of two earlier results challenging the validity of those planets' detections. In the first, [105] used van de Kamp's photographic plates to determine that all the stars in the field of Barnard's star appeared to wobble in concert, and the source of this variability could be traced to telescope and instrumentation upgrades at times concurrent with the shifts in the data. Additionally, [89] reported no astrometric wobble of Barnard's star using the Van Vleek and Allegheny Observatories at Wesleyan University and University of Pittsburgh, respectively. More recent studies have confirmed that van de Kamp's planets are not recoverable by instruments which ought to have detected them easily [28, 123, 49, 189].

More recently, Barnard's star is often referred to as a Doppler standard star for its relatively quiet nature, RV stability, high apparent brightness, and equatorial declination. Through this combination of factors, it is widely considered as *the* RV standard for fully convective stars [e.g. 26, 10]. Such standard stars are vital to the exoplanet community for instrument commissioning and calibration. As our instruments become more precise, we may find planets and/or activity signals for *all* stars. It is crucial that we fully understand and characterize the signals associated with whichever stars we designate as standards so that we can continue to have standard stars at all.

The Habitable-zone Planet Finder (HPF) began observing Barnard's star in the Spring of 2018 for engineering purposes. At the time, the star was not known to host a planet. Shortly after, [189] (hereafter R18) announced a super-Earth planet candidate orbiting Barnard's star with a 232.8 $\pm$ 0.4 day orbital period. Metcalf et al. 2019 [152] presented early HPF observations of the star to demonstrate the near-infrared RV precision achievable with HPF and its laser comb, but did not discuss the planet candidate due to the relatively short

observational span compared to the period of the signal. As we continued to observe the star, we still did not find clear evidence of a signal at 233 days. This, combined with the findings from [123] which found a correlation between the RVs and Hα values for Barnard's star, prompted us to revisit the full RV data set and the corresponding activity tracer time series.

After our own analysis of the original discovery data set and the addition of new data from HPF, we find that the signal at 233 days is transitory in nature and is an alias of the 145 $\pm$ 15 day rotation period as reported by [229]: $\left(\frac{1}{145} - \frac{1}{365}\right)^{-1} = 240$. The 233 day proposed period is well within the 1σ uncertainty on the rotation period. We are therefore compelled to conclude that the RV data of Barnard's star is best explained without the planet Barnard b proposed by R18.

3.2 Data

3.2.1 Discovery Data

The claim by R18 of a 233-day planet candidate orbiting Barnard's star was based on a data set that was assembled over a 20 year span using multiple Doppler spectrometers. These instruments included those which employed the iodine-cell (I_2) method [232, 44]: 186 points from the High Resolution Échelle Spectrometer [HIRES; 239] installed on the 10 m Keck I Telescope at Maunakea in Hawaii; 43 points from the Automated Planet Finder [APF; 240] installed on the 2.4 m telescope located at Lick Observatory on Mt. Hamilton outside of San Jose, California; 75 points from the UVES spectrograph installed on the 8.2 m VLT UT2 at Paranal Observatory in Chile [64]; and 39 points from the Planet Finder Spectrometer [PFS; 54] installed on the 6.5m Magellan II located at Las Campanas Observatory in La Silla, Chile. Other instruments used for data collection include 187 points and 40 points

from the HARPS [147] and HARPS-N [53] spectrometers respectively, installed on the ESO 3.6 m at La Silla in Chile and the 3.5 m Telescopio Nazionale Galelio at La Palma, and lastly 201 points from the visible channel of the CARMENES spectrograph [186] installed on the 3.5 m telescope at Calar Alto Observatory in Spain.

In all, 771 RV points were used. Further detailed information on the data sources and reduction methods can be found in R18. For ease of reference herein, we have dubbed this the *discovery* data set.

In addition to RV data, R18 provided time series of Calcium II H&K ($S_{\rm HK}$) and Hα indices for the instruments where either or both of these activity tracers are available. $S_{\rm HK}$ and the Hα index are known tracers of stellar activity which measure the filling in of the photospheric lines from heating in the chromosphere due to increased magnetic flux.

3.2.2 Updates to Data

We made a few updates to the discovery data set. The first concerned the UVES Hα time series. R18 published 21 Hα points alongside 75 RV points, originally from [254]. We noticed a non-uniform offset in time between Hα epochs and seemingly corresponding RV epochs of $\sim$0.5 days. Therefore, we manually changed the Hα timestamps to equal the nearest corresponding RV timestamp for consistency.

Next, we substituted more recent reductions of the RV data for certain instruments for the (now) older reductions used by R18. First, we used the velocities from the reduction of HIRES data provided by [224]. Additionally, we split the HIRES data into "pre" and "post" with respect to the instrument's CCD upgrade in August of 2004. This was motivated by [224], who fit an offset, but we kept this as a free parameter when modelling for completeness. As several nights in this reduction contain multiple observations, we performed a

nightly binning by taking a weighted average with weights $\sigma_{\rm RV}^{-2}$. This binning preserved the sampling used by R18, except the updated time series includes one additional epoch at BJD = 2453301.74204. We excluded the last observation at 2456908.73079 since the associated velocity of 53.319 m/s makes it a $\sim$5.5 σ outlier. We confirmed that this data set had been corrected for secular acceleration.

We similarly used the velocities from the reduction of HARPS data as performed by [230]. We used the RVs which had been corrected for secular acceleration, nightly zero point offsets, and drift. Again, we maintained "pre" and "post" designations with respect to the HARPS fiber upgrade in 2015 for completeness [131]. These data included more observations than were originally included in R18, with 108 observations occurring within an 11 day period in May 2013. These observations were taken as a part of the Cool Tiny Beats (CTB) program [29]. Comparison between the CTB observations and the original HARPS data suggested that R18 performed a nightly averaging to compile their data set, but they do not describe exactly how they performed this binning. We chose to use a nightly weighted average with the same weights as described above.

The last modification to the discovery data set was the addition of the HPF data (§3.2.3). For ease of reference herein, we have dubbed a new data set as the *updated* data set. This updated data set includes the original, unaltered APF, CARMENES, HARPS-N, and PFS data, the UVES data with timestamps adjusted, the new data reductions of HIRES and HARPS (both split into pre and post domains), and the new HPF data, see Figure 3.1.

3.2.3 HPF Data

HPF is a high-resolution ($R \sim$ 55,000) near-infrared (NIR) spectrograph on the 10m Hobby-Eberly Telescope (HET), covering the Doppler information rich z, Y and J bands from 810–1280 nm [142, 143]. To enable precise RVs in the NIR, HPF is temperature stabilized

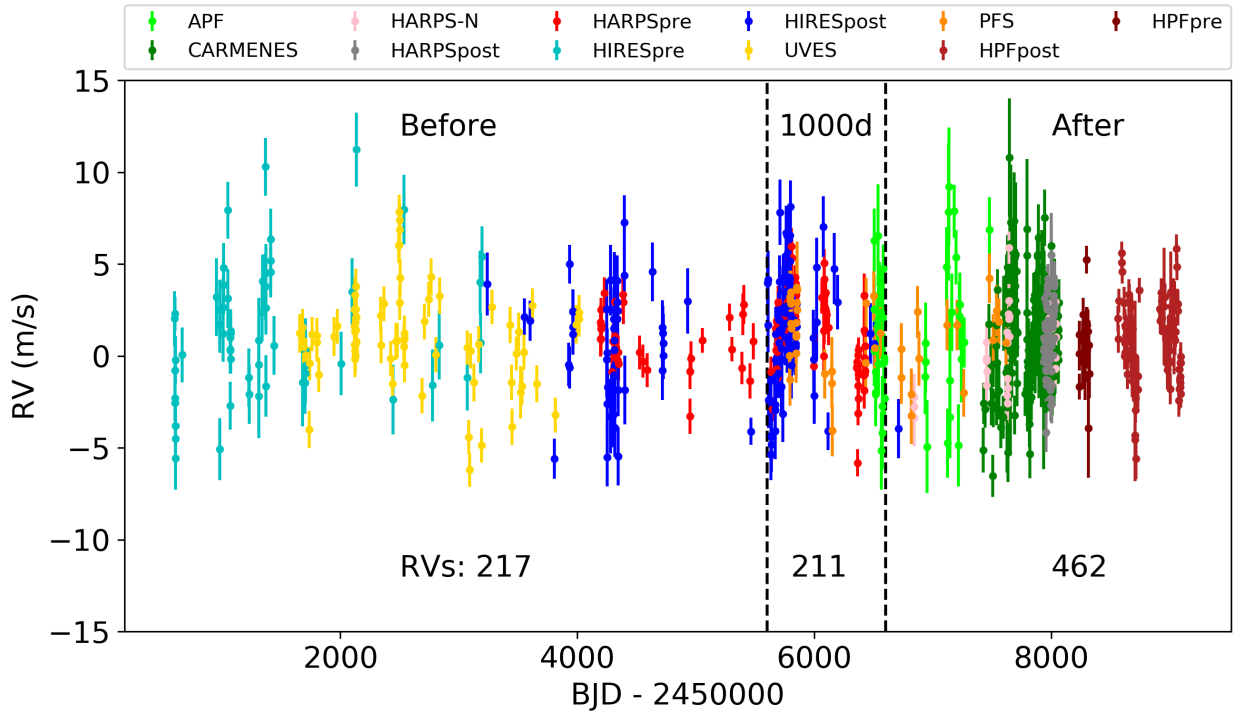

Figure 3.1: The entire Updated RV time series spanning 23 years. Our three time windows of interest are noted along with their number of observations. Excluding HPF, the After window has 343 observations. Instrumental zero point offsets have been applied.

to the sub-milliKelvin level [221]. HET is a fully queue-scheduled telescope [212], and all observations were obtained as part of the HET queue. HPF has a NIR laser-frequency comb (LFC) calibrator which has been shown to enable $\sim$ 20 cm s^{-1} calibration precision in 10 minute bins and 1.53 m s^{-1} RV precision on-sky on Barnard's star [152] over an 3 month baseline. In this paper, we extend this baseline to 856 days. [220] further discusses our drift correction algorithms. To enable maximum RV precision with HPF, we obtained all of our Barnard's star observations using the HPF LFC simultaneously with the on-sky observations.

To test the on-sky RV measurement performance of HPF, we observed Barnard's star as part of HPF Commissioning and ongoing Engineering time due to its brightness, overall known Doppler RV stability, and its rich RV information content in the NIR. Due to the restricted altitude design of the HET, the HET can only observe Barnard's star at certain times of the nights, or "tracks", for approximately 68 minutes at a time. In total, we obtained 1016

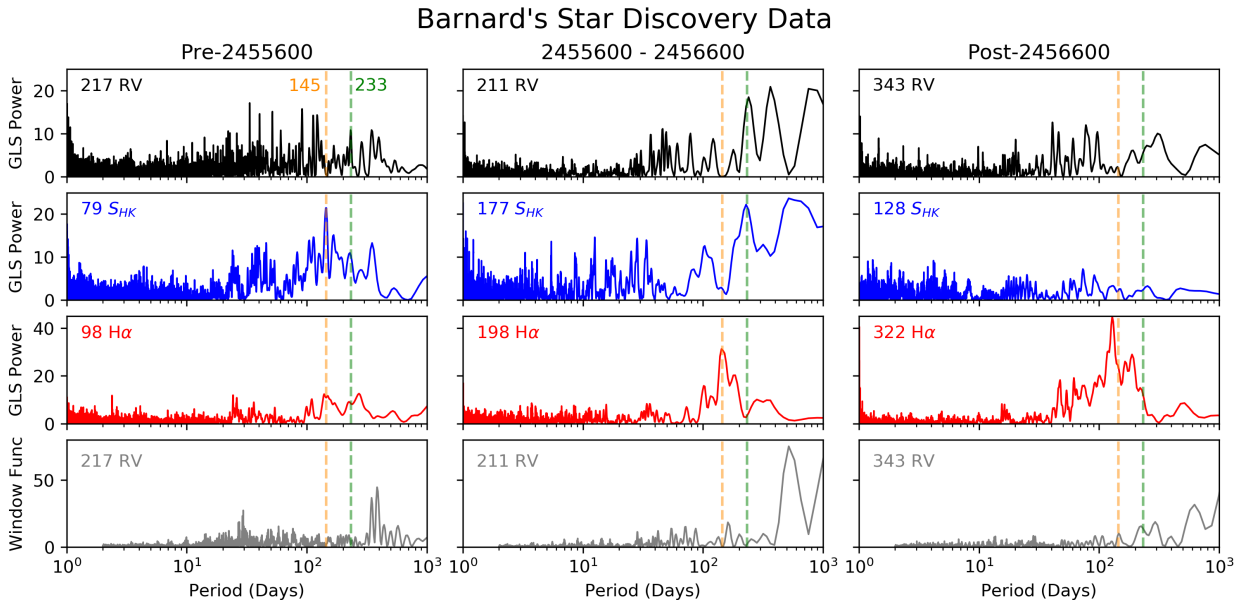

Figure 3.2: GLS periodograms of the discovery data time series broken down in to three time windows. The middle column is the 1000 d window. The 233 day signal is only present at significant power in the 1000 d window in both the RVs (black) and CaHK S-values (blue). The Hα Index (red) traces the rotation period. The Window Function for the RV time series in each window is the last row in gray. The orange line indicates 145 days, the stellar rotation period, and the green line indicates 233 days, the proposed planet period.

high-quality spectra in 118 HET tracks with a median S/N of 479 per extracted 1D pixel evaluated at 1 μm. Due to a planned instrument thermal cycle in August 2018 which led to a minor RV offset before and after the cycling, we place an explicit RV offset before and after this event in our RV modeling. Before the thermal cycle, we generally obtained 6 exposures of Barnard's star with an exposure time of 300 s in each HET track, while we generally obtained 10 exposures with an exposure time of 183 s in each HET track after the thermal cycle. This change was made in order to harmonize the observing strategy of Barnard's star with that employed for the rest of the HPF 5-year blind Doppler survey. This standardized the observing for different targets according to their brightness, minimizing any potential risk of saturation for bright targets such as Barnard's star. The observing setup for Barnard's star has remained the same since the thermal break installation.

Overall, the 1016 high-quality spectra had a median exposure time of 191 s, and a median

photon-limited RV precision of 2.36 ms^{-1}. After performing a weighted average of RV points within a given HET track, we obtain a median RV precision of 0.77 ms^{-1} per binned RV point. We use the binned RV points for subsequent analysis, which can be found in Table 3.1 in the appendix.

The 1D HPF spectra were reduced from the H2RG up-the-ramp data using the algorithms and procedures described in [165], [118], and [152]. Following the 1D spectral reduction, we calculated precise radial velocities of Barnard's star using an adapted version of `SERVAL` (SpEctrum Radial Velocity AnaLyzer) [255], optimized to analyze HPF spectra as further discussed in [152] and [220]. To derive precise RVs, `SERVAL` uses the template-matching algorithm, which has been shown to be particularly effective at producing precise radial velocities for M-dwarfs [10]. To estimate accurate flux-weighted barycentric velocities, we used the `barycorrpy` package [117], which uses the methodology and barycentric-correction algorithms presented in [248]. Following [152] and [220], to derive the RVs we only use the 8 HPF orders cleanest of tellurics, covering the wavelength regions from 8540-8890 Å, and 9940-10760 Å. To minimize the impact of telluric and sky-emission lines on the RV determination, we explicitly mask out such lines as described in [152] and [220]. We subtracted the estimate sky background from the target spectra using the dedicated HPF sky fiber.

3.3 Analysis

We have taken a three-pronged approach to our investigation of the 233-day signal, largely performing the same experiments on both the discovery and updated data sets. First, we model the system's activity and/or potential planet with Gaussian Process (GP) regression models to identify a preferred model. Next, we perform a periodogram analysis to show the transitory nature of the signal. Finally, we analyze subsets of the data to show how the signal power is concentrated in time.

3.3.1 Model Comparison

We began our analysis by modeling the stellar activity and/or planet signals for both the discovery and updated data sets. We chose to model stellar activity signals with GP regression because the GP framework has proven especially adept at modeling quasi-periodic signals associated with stellar rotation [103, 187, 222, 33].

In order to better constrain the stellar rotation signal, we first modeled the activity tracers using GP regression. We used a modified version of `Radvel` [83] which uses logarithmic priors for the GP hyperparameters, setting broad priors as advised by [11]. We used the `Celerite` package [79] for its efficiency. Specifically, we use the celerite-compatible replacement for the quasi-periodic kernel for the covariance between the i^{th} and j^{th} observations:

$$k_{ij} = \frac{B}{2+C} \exp\left(\frac{-|t_i - t_j|}{L}\right) \left[\cos(\frac{2\pi|t_i - t_j|}{P_{rot}}) + (1 + C)\right] + \sigma^2 \delta_{ij},$$

equivalent to Equation 56 in [79]. The hyperparameters of this kernel have similar interpretations to the quasi-periodic kernel function: B is related to the signal amplitude, L is the decay timescale for the exponential term in days, C is a scaling term, σ^2 is the jitter from additional white noise beyond what can be accounted for in the formal measured uncertainties, and $P_{\rm rot}$ is the recurrence timescale of the signal in days; in this case our astrophysical interpretation is closely related to the stellar rotation period. Each instrument received its own B and σ hyperparameters, but all instruments shared global C, L, and $P_{\rm rot}$ hyperparameters.

We first performed a GP regression model to the discovery dataset's Hα values. Table 3.4 shows our priors and subsequent maximal posteriors from this fit. The resulting posterior value for $\log C = -5.85$ indicates that the signal in question, i.e. the stellar rotation, is highly periodic in nature. [229] states a rotation period of 145 $\pm$ 15 days, and from the results of

our GP model of the Hα data we are able to achieve a consistent result at $143.7^{+11.83}_{-10.93}$ days. Performing a GP with the same priors on hyperparameters for the $S_{\rm HK}$ time series yielded similar results.

Using the Hα posteriors of the $\log L$, $\log C$, and $P_{\rm rot}$ terms as the priors in the RV model, we ran a suite of models on the RVs from the discovery data. In all of these RV models, the $\log C$ posterior value continued to prefer negligibly small values. We quickly found a similar behavior with the $\log B$ hyperparameter for APF as we had for the $\log C$ parameter. We believe that, due to the small aperture and iodine calibration on such a faint and red target star, the variability in the APF data is due primarily to photon noise rather than correlated astrophysical variability. We therefore opted to perform all analysis without a GP term for the APF RVs. When modelling activity, APF was allowed only an instrumental jitter and offset term, while when considering a planet, APF data were modelled with a Keplerian and instrumental jitter and offset only.

We computed three models on the discovery data set's RVs: a GP fit only, a 233d planet fit only, and a GP + 233d planet fit. Table 3.2 in the Appendix shows the resulting Bayesian information criteria (BIC) and the number of free parameters in each model. We compare models by their ΔBIC, preferring more complex models to simpler models when $\mathrm{BIC}_{simple} - \mathrm{BIC}_{complex} > 10$ [119]. For the discovery data, this criteria is satisfied for the GP-only model compared to the Planet-only model, but it is not satisfied for the GP+Planet compared to the GP-only. Thus the GP-only model is our preferred model. We then repeated this experiment of model comparisons using the updated data set. We used the same priors as for the discovery data set and we achieved a similar result, as shown in Table 3.3. The GP+233 d model has the smallest BIC, but the ΔBIC between this model and GP only model does not justify the more complex model's additional free parameters, and so therefore the GP-only model is once again our preferred model. The posteriors for all models using the discovery data can be found in Tables 3.4 and 3.5, and using the updated data in

Table 3.6 in the Appendix.

3.3.2 Periodograms

After finding the preferred model to be one which accounts for stellar activity only, we set out to determine how the activity signal might have revealed itself as a planetary signal in the GLS periodogram of the RV time series.

In an attempt to show coherence of the planetary signal, we split the discovery data into roughly equal thirds by observation number (taking care to not cut in the middle of an observing season) and computed the generalized Lomb-Scargle periodogram [GLS; 252] of each block of data. The 233-day signal is strongly present in the middle third, as shown in Figure 3.2. Given some idealized data set which has comparable quality data, sampling, and white noise in all subsets of time, a true planetary signal must persist in all subsets. It will stay in phase across the entire observational time baseline, and the loss of power from removing a fixed number of data should be consistent regardless of which specific data are removed. While this data set is not such a perfect data set, the result of this test was the first indication that the 233 d signal is not planetary in nature.

We then divided the corresponding $S_{\rm HK}$ values in the same manner and, after computing GLS periodograms for each block, we saw similar behavior. Notably, in the time window when the RV signal at 233 d is strongest, there is a matching peak in the $S_{\rm HK}$ periodogram. This result is similar to [101] where it was shown that activity signals changing over seasonal time spans can imprint planet-like periodicity into the RV time series.

From these early results, we performed a season-by-season, instrument-by-instrument analysis of the discovery data in an effort to identify tighter, more scientifically grounded boundaries for splitting the data. We found that for both the Hα and the $S_{\rm HK}$ time series, the

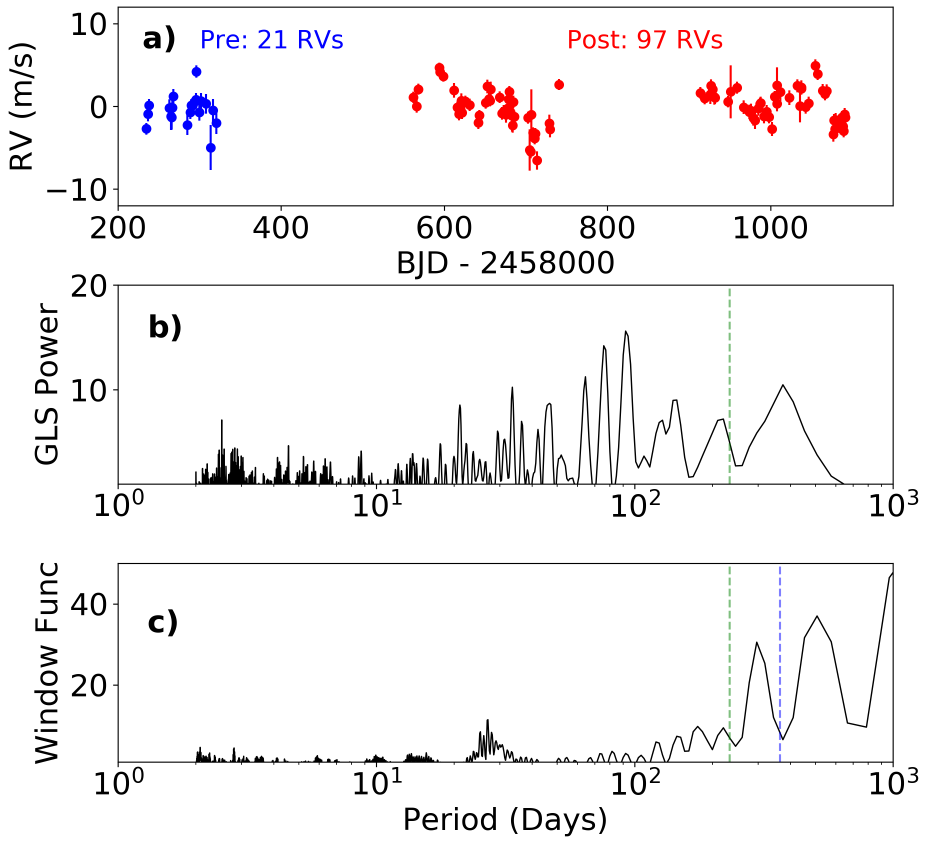

Figure 3.3: **Top:** The HPF RV time series split into "pre" (blue) and "post" (red) with respect to the thermal break. **Middle:** The GLS periodogram for the HPF RVs. The green dashed line is at the proposed planet period. **Bottom:** The accompanying window function periodogram. The blue dashed line denotes 365 days.

rotation period of the star, 145 ± 15d [229], is recoverable in the 2011 season by visual inspection when plotting out the data. Through this, we realized that the 233 day signal persisted with significant power only for a 1000 day stretch of time —from BJD 2455600 to 2456600, 211 observations (see Fig 3.1 — during the observing seasons of 2011, 2012, and 2013). For ease of communication, we have subsequently designated this time span as *the 1000 d window*. From here on, we begin referring to time with respect to the 1000 d window: the before, during, and after epochs. The RV and activity periodograms in Figure 3.2 show the behavior of the 233 d and 145 d signals in each of our three epochs.

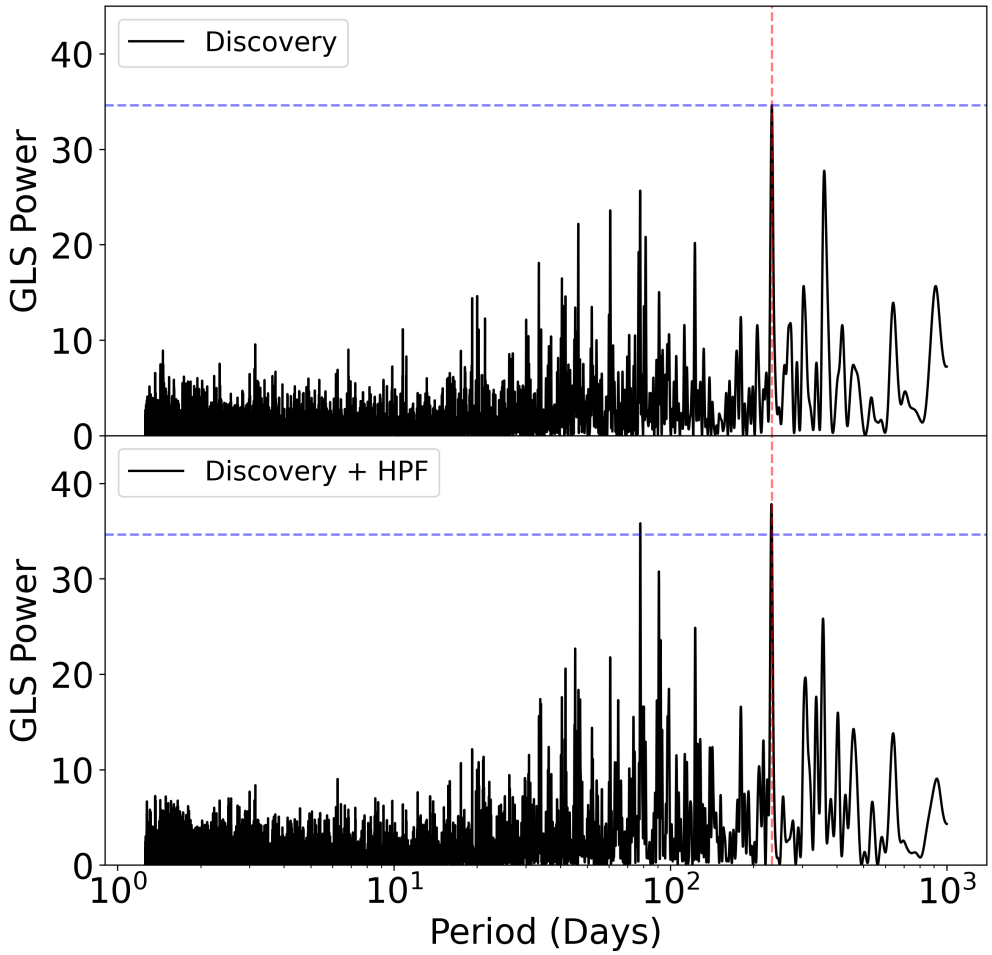

Figure 3.4: A comparison of the GLS periodograms for two different data sets. The addition of HPF data to the original discovery data set only marginally increases the strength of the peak at 233 days, while the peak at 77 days, the first harmonic of the rotation period, greatly increases. The horizontal blue dashed lines are set at the height of the peak at 233 days in the discovery data set, and are intended to guide the eye.

When we stitch back together the Before and After RVs of the discovery data set to create a data set with 560 points, albeit with a noticeable gap in the center, we still do not see any significant power at the 233 day period. In fact, the GLS power of the 233 day signal drops from ~ 31 down to ~ 15. As GLS power scales exponentially with significance, this loss in power corresponds to a large loss in statistical significance. Additionally, the 233 day signal loses its place as the top peak in favor of a 45 day signal.

With this in mind, we turned to the new HPF data. Figure 3.3 shows the time-series HPF

RVs as well as its periodogram and window function. We do not see evidence for a signal at 233 days. This could be due to a combination of the fact that HPF is a NIR spectrograph, which is less susceptible to spot-dominated stellar activity than a visible spectrograph, and/or the star could have been less active in the last few years than it was in 2011-2013. The top peak in the HPF data's GLS periodogram is at 92 days. We believe this peak is part of a comb of aliases of the $\sim$75 day (second peak) first harmonic of the rotation period.

With the addition of 118 new data points, we would have expected the power of the signal at the proposed planet's period to increase. Adding the HPF RVs to the discovery data set (note this is not the same as our *updated* data set since it still includes the original reductions of the HARPS and non-split HIRES data sets), we recover the signal at 233 days in a GLS periodogram at nearly the same power as is found when only considering the discovery data alone (Δ Power $\simeq$ 3) while the signal at 77 days has a large increase in power (Δ Power $\simeq$ 10), see Figure 3.4. As explored in detail in §3.3.3, the HPF RVs do not increase the power at 233 d as much as would be expected for a genuine exoplanet. When we exclude the 1000 d window observations from this combined data set, the 233-day signal again loses significant power and no longer retains its place as the top peak in the periodogram.

Lastly, we have chosen to demonstrate the transitory nature of the 233-day signal with the Lomb-Scargle periodogram due to the broader community's common understanding of the algorithm. Regardless of the periodogram we used (Bayes Factor, Marginalized Likelihood [77]; Compressed Sensing [100]), when we remove the observations in the 1000d window we see the same result. The strength of the 233 day signal is almost entirely contained within the 211 data points which compose the 1000 d window.

3.3.3 Sampling Sensitivity

Such a dramatic reduction in signal significance by the exclusion of certain data prompted us to ask if it was reasonable to remove 27.6% of the data (the percentage of the RV time series which is inside the 1000 d window for the discovery data set) and still expect a signal to persist. In an effort to address this, we created subsets of data where we removed RV points from the time series, and computed the GLS periodogram of the resulting subset.

Random Removal

First, we experimented with an approach of randomly removing data. We created 2000 different subsets of the discovery data where 211 observations–the same number as are found in the 1000 d window–were randomly removed. For the first 1000 subsets, we allowed the randomizer to choose any observations for removal (except for the first and last observation, as we did not want to change the baseline of the time series in any subset). In the second 1000 subsets, we enforced that the randomizer *not* choose any observations that were taken during the 1000 d window (as well as first and last observation again). This is an important distinction because it tests how localized the signal is by keeping the data where we believe all of the signal power lies.

For each subset, after removing the randomly selected observations, we re-calculated and removed zero-point instrumental offsets and then computed the GLS peridogram. In each subset's periodogram, we tracked how the power of the signal at 233 days was affected by the removal of data. Figure 3.5 shows the fractional power (normalized by the true power of the signal when all discovery data is included) of a signal peak nearest to 233 days within a $\pm$ 3 day span (in fact, we see the same results when expanding this as far as $\pm$ 20 days) in each of these two rounds of subsets.

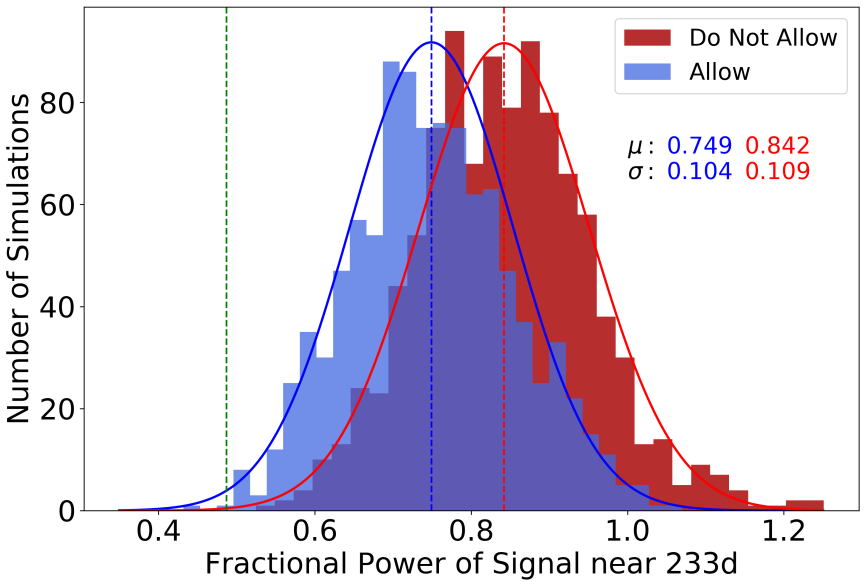

Figure 3.5: Histograms of the GLS Power from randomly removing 211 observations from the discovery data set in 1000 subsets via two different methods: where we allow for observations within the 1000 d window to be part of the random removal (blue) and for when we do not allow those observations to be part of the random removal (red). The green line indicates the subset which corresponds to removing only the 211 observations that make up the 1000 d window. Gaussian best fit parameters are shown in their respective colors.

For the those where we allowed for any observation to be removed, the average loss in power of the 233-day peak is 25%. By fitting a Gaussian distribution to the ensemble of subsets, we see that when we remove the specific 211 observations which make up the 1000d window, the resulting subset constitutes a 2.5σ outlier. For those subsets where we do not allow for removal of any observations from the 1000d window, the average loss of power is less, only 16%. This result is consistent with our hypothesis that the power of the 233 day signal lies mostly in the 1000 d window. A Gaussian fit to this ensemble shows the removal of the specific 1000 d window observations is a 3.25σ outlier. Furthermore, and equally important, for both methods of removal there are subsets of the discovery data where the significance of the 233-day signal actually *increases*, by up to 20%. These increases are notable because they indicate there are subsets where the removal of data significantly strengthens the proposed planet signal.

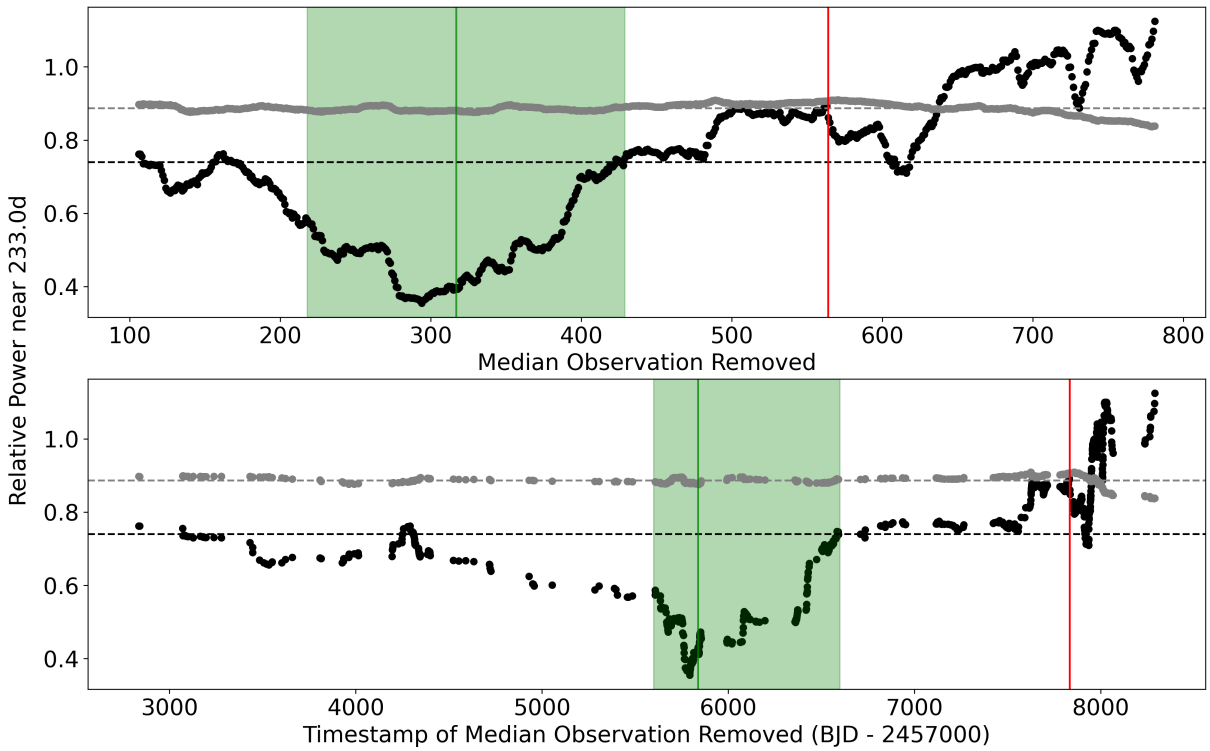

Figure 3.6: **Above:** The results from the rolling omission tests in observation number space. Black points are the true updated data set, gray points are an average of 10 synthetic data sets. The green line is the simulation which matches the removal of the 1000 d window points exactly, with green shading to indicate the duration of the 1000 d window. The red line indicates the simulation where the first observation of the 211 consecutive removed observations corresponds to the first CARMENES observation. **Below:** The same results but in time space.

Consecutive Removal

Next, we performed a similar analysis wherein we removed 211 *consecutive* data points, by a process we call *rolling omission*. First, we fit for instrumental zero point offsets. We created an algorithm to start with an observation, remove the subsequent 211 points, compute the GLS periodogram for the subsequent subset of the data, and track the fractional power of the signal (data subset power at 233 d / full data set power at 233 d). Then increment to the next starting observation and repeat for the next subsequent 211 observations. Since we did not want to create a subset with a different baseline than the full data set, the first iteration began with the removal of the second observation and the last iteration began with

the observation equal to $N - 211 - 1$, where N is the total number of observations in the time series. We performed this test on both the discovery and updated data sets, but the results are more illuminating with the addition of the HPF data in the updated data set, primarily because with more data points, the algorithm is able to run longer before reaching the end.

To show the results' deviation from expectation more clearly, we performed the rolling omission test on synthetic data in which we include a planet signature. We created synthetic data sets where for each timestamp and associated error of the real observations, we calculated the corresponding expected velocity for a planet with the same parameters as published in by R18. Then we added a white noise term to each velocity. Noise was drawn from a Gaussian centered at zero with width equal to the error measurement for the observation at that timestamp. We created 10 of these synthetic data sets and ran the rolling omission test on each one, averaging the results.

Figure 3.6 shows the result of the rolling omission test on the updated data set (black points) and the averaged synthetic data sets (gray points) as function of both observation number and time. The vertical green line indicates the iteration of rolling omission where the subset removed matches exactly the removal of the specific 211 observations of the 1000 d window. The green shading shows the width of the 1000d window in index and timestamp space. The red vertical line shows the iteration of rolling omission where the first point of the consecutive removal is equal to the first observation in the CARMENES time series. Like in the random removal experiments, this experiment shows that the loss in fractional power when we remove the specific 211 observations that make up the 1000 d window is far greater than the average (black dashed line).

In addition, the tests on synthetic data sets track a nearly horizontal line, showing that for a signal which persists throughout the span of the data the loss in power from removing consecutive chunks of data is nearly agnostic to the window that is removed. When the

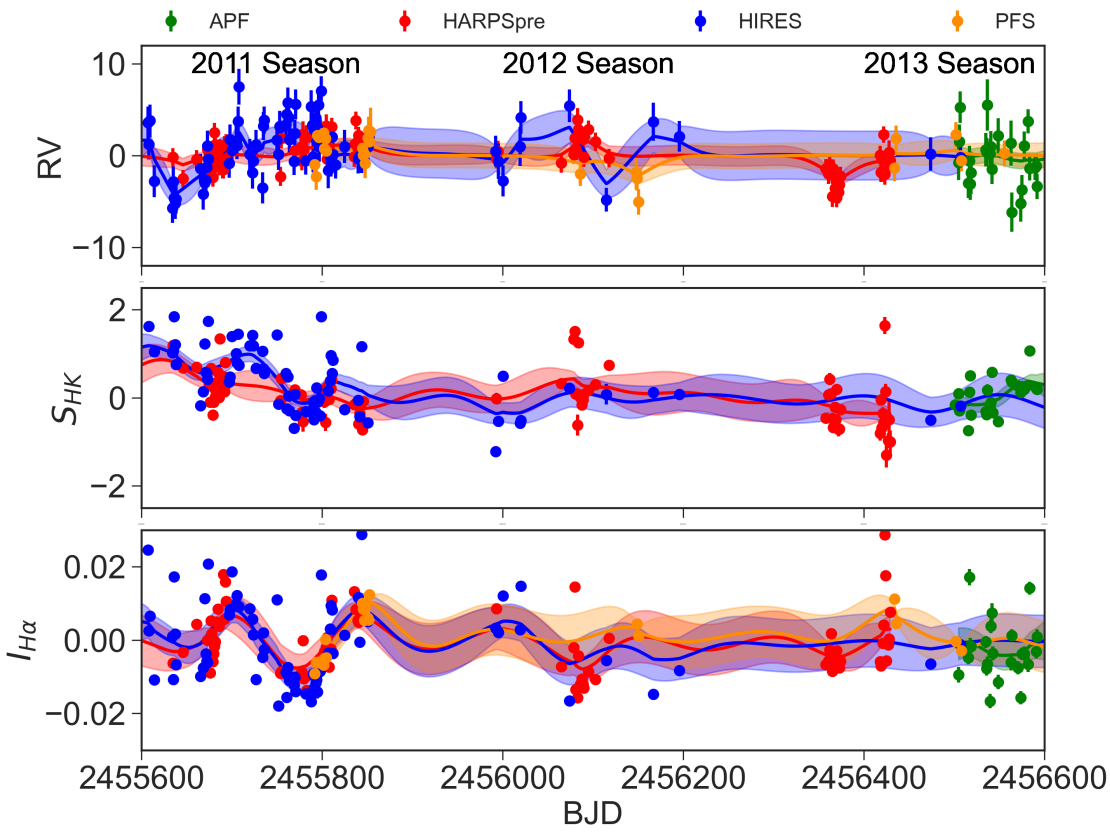

Figure 3.7: The time series of RV, $S_{\rm HK}$, and $I_{\rm H\alpha}$ in the 1000 d window with GP functions overlaid with 1σ uncertainty regions. In the first of these observing seasons, 2011, the rotation period of the star is recoverable by eye in $S_{\rm HK}$ and Hα.

data is dense in time, as it is toward the end of the data set, the fractional power begins to decrease. However, for the real data set, we see just the opposite behavior: the fractional power *increases* dramatically after the red vertical line, even going above 1.0. This means that as we remove some of the best data, in terms of nightly cadence, RV precision, and redder instruments less susceptible to spot-dominated stellar activity in the case of the HPF and CARMENES data, the signal becomes *stronger* and more significant than if we include all of the data. This is because we are removing data which does not actually contain a signal at 233 days, thus concentrating the subset on the observations which truly contain the signal.

Through these tests we became convinced that not only does nearly all of the signal power

of the proposed planet lie in the particular 211 RVs that make up the 1000 d window, but also that if the signal were persistent in time, our analysis suggests that the most recent observations from CARMENES, HARPS, HARPS-N, and HPF should add power to the 233 d signal if it is caused by an exoplanet, when in reality they do not.

3.4 Discussion

This result is both novel and concerning. It is novel in the sense that there are no examples in the literature of a false positive exoplanet detection created by a stellar rotation alias *longer* than the rotation period. [32] showed that confidently disentangling planetary signals from stellar activity induced signals requires a few circumstances, primarily that the period of the planet signal not be near the stellar rotation period or one of its harmonics. Harmonics, by definition being integer multiples of the frequency, are shorter periods. While false positive exoplanet signals have also been identified at rotation period aliases, they too tend to fall towards shorter periods [195], and the same is for true planets where the period is uncertain between two aliases [63, 192]. This result has farther reaching implications for the field of RV exoplanet discovery than just this one system.

Equally, this result is concerning. The exoplanet science community will now have to be as vigilant in scrutinizing the longer aliases of the stellar rotation as it has been for shorter aliases and harmonics. Similarly concerning, this result seems to contradict Extended Data Figure 2 in R18 where they show a stacked periodogram in the fashion of [159]. The figure shows a monotonically rising confidence in the 233 day signal with increased observation. How can we reconcile this figure with our own Figure 3.6 where we see the signal is localized to a relatively small time and observation space window? An alias is, in itself, a signal which can increase in significance monotonically in the same manner as a planetary signal. Additionally, the periodogram of the first X observations should achieve similar results to

the periodogram of the first $X + 1$ observations. A better approach would be to stack periodograms of disjoint time spans of the data, similar to our rolling omission test. Along those lines, our rolling omission test is better suited for tracing the localization of a signal in time, which, when used in concert with a stacked periodogram, can provide a more holistic understanding of the nature and veracity of a signal.

We have described the false positive 233 d exoplanet signal as an "alias" of the 142-day rotation period due to its apparent connection to the stellar rotation and the location of the periodicity near the 1-year alias of said rotation: $\left(\frac{1}{145} - \frac{1}{365}\right)^{-1} = 240$. However, this signal cannot be explained as simply as the result of a pure 142-day sinusoid sampled at the irregular cadence and precision of the RV time series. Instead, we believe several factors explain why the rotation signal manifested as observed in RV, Hα, and $S_{\rm HK}$:

- During the 1000 d window, the sampling between Hα and $S_{\rm HK}$ observations was not identical but also not too different. Yet the resulting periodograms are very different. In the 1000 d window, the Hα values track a decaying and coherent-across-instruments stellar rotation signal, while the $S_{\rm HK}$ values generally do not, see Figure 3.7. The $S_{\rm HK}$ shows the rotation period only in the first season, 2011, and in one instrument, HIRES. This might be explained by the low SNR in the continuum of this very red star near the Ca II H&K doublet [193].

- Hα and $S_{\rm HK}$ often trace different astrophysical phenomena [96]. The activity and periodicity associated with one or the other–or even both–can imprint through to the RVs.

- The decaying aspect of this signal would make aliasing worse. As shown in Figure 3.7, the rotation signal during the critical 1000-day window is prominent in the first season, and then slowly decays. Irregular sampling of this decaying, non-sinusoidal signal, alongside any unknown true low-amplitude planet(s) might have created the

perfect storm resulting in the false positive detection of Barnard's star b.

It is crucial that we have a strong understanding of Barnard's star if we are to continue using it as a standard star for commissioning and monitoring red-optical and NIR RV instruments. The star is often considered to be *the* RV standard for the mid-to-late M dwarf class. As our spectrometers become capable of breaking through ever smaller instrumental noise floors, we will need a thorough understanding of the astrophysical variability of any standard star. Barnard's star has always been considered a quiet star, and this is still largely true for signals on the order of a few meters per second and up. But we now see that the stellar activity of Barnard's star will play a factor at amplitudes near and below 1 m/s. If we do not properly understand this stellar activity, then we may not be able to use the star as a standard for commissioning new, ever more sensitive instruments in the future.

As astronomy enters this new era of highly precise instruments capable of detecting exoplanets with RV amplitudes < 1 m/s, we are excited by the outlook of finding more low amplitude planets, be they low mass or long period or both. However, long period planets with small amplitudes in particular will need extra care when the proposed period is close to, not only the rotation period of the star or its harmonics, but also its longer seasonal aliases. This will be even more important when the period of a proposed signal is nearly as long as the duration of an observing season.

Planetary companions to Barnard's star would be very interesting, not only for their relative proximity to our Sun and therefore enhanced follow-up opportunities, but also because the star belongs to an old stellar population. [95] classified the star as an "Intermediate Population II" star, which places it somewhere between the halo and the thin disk population of the Milky Way. That said, it would be strange if Barnard's star *did not* host a planet. We know from planet occurrence rate studies like [68, 110] that planets are common at short periods in M Dwarf systems, though clustering of planets in multi systems is also seen in both FGK

stars [104] and M dwarfs [16]. Therefore, we might expect Barnard's star to host a planetary system, although, despite ∼850 RVs, we may still not be sensitive enough to detect planets. It is also possible that Barnard's star hosts a nearly face-on planetary system, which would effectively hide any planets from transit or RV searches. Direct imaging with the next generation of large telescopes might help resolve this. R18 states that the separation between the proposed planet and the star would be great enough for Hubble to detect an astrometric signal, which [225] confirms and goes on to include Gaia DR2 as an instrument capable of making this measurement. If such measurements are undertaken, based on the result we have presented in this paper we would not expect a significant signal corresponding to the planet candidate proposed by R18.

With all this in mind, we put effort into searching for a planetary signal in the updated data. We investigated a signal at 45 days, which is seen when removing the 1000d window observations. However, this signal is concernedly close to the second harmonic of the rotation period, it disappears in the residuals of the GP only model, and when treated as a planet it is not favored by the model comparison tests (either with or without a GP).

3.5 Conclusion

The addition of new data from HPF, as well as a suite of tests on the discovery data set, have shown that the 233 day signal is not planetary in origin, rather a transitory one year alias of the stellar rotation period which took place over a 1000-day time span from 2011 to 2013.

In summary:

- The 233 day period of the planet candidate proposed by R18 is a one year alias of the rotation period, $\left(\frac{1}{145} + \frac{1}{365}\right)^{-1} = 240$ days. The claimed period of 233 days is well

within the 1σ error bars of the rotation period found by [229], and consistent with our own analysis of the Hα time series.

- We created various models of the system, taking into account stellar activity and/or a planet. For the updated data set, we have strong evidence (Δ BIC $=\sim$160) to reject the planet only model in favor of an activity only model. Then, while we can never rule out one or more planets in the system, our analysis finds that the updated data favors the activity only model over the activity+planet model (Δ BIC $=\sim$1).

- The RV signal at 233 days does not persist through all the tested time windows. Rather, it appears strongly in the middle window, dubbed *the 1000d window* from JD 2455600 to 2456600, comprising of 211 observations, while statistically insignificant in the the other two windows.

- The coincidence of the 233-day peak in the RVs and $S_{\rm HK}$ values in the 1000 d window while absent otherwise suggests a common stellar activity origin for both signals, aliases of the 145 $\pm$15 day stellar rotation period.

- Hα and $S_{\rm HK}$ clearly trace out the stellar rotation period at the beginning of the 1000 d window during the 2011 observing season. The Hα time series in all windows consistently shows a signal at the stellar rotation period.

- Removing observations from a data set will typically weaken any signal, regardless of its astrophysical origin. We created subsets the data by randomly removing 211 observations and find that in nearly all simulations the loss of power resulting from this removal is much less than when we remove the specific 211 observations that make up the 1000 d window.

- Similarly, we removed 211 consecutive RV observations from the full data set, by a process we call *Rolling Omission* and found that, again, it is the particular 211 RV

observations in the 1000 d window which have the most impact on the strength of the signal. Removing later chunks of data actually increased the power of the signal.

The addition of new data can, and should, change our understanding of any system. Barnard's star is listed in the Guaranteed Time Observations (GTO) lists for the ESPRESSO [177] and NEID [210] exoplanet surveys. The HPF team will also continue to monitor this star. Barnard's star has long fascinated and continually surprised astronomers; we expect this to continue.

3.6 Appendix - HPF RV extractions

We extract precise RVs from the HPF 1D spectra using the `SERVAL` template-matching RV-extraction code [252], which we have tailored to work for HPF data as discussed in [152] and [220]. To test the robustness of our extracted HPF RVs and accompanying estimated RV uncertainties at these high precision levels, we performed an additional RV extraction test. For this test, we performed an RV extraction where we split each HPF spectral order into four separate segments along the four different readout channels on the HPF H2RG detector. We then compared the standard deviation of the RVs derived from the four different segments to the expected standard deviation from our estimated RV uncertainties. In doing so, we noticed that for some observations the standard deviation across the four different segments was slightly higher than than expected from our RV uncertainty estimates derived from the inherent RV information content in the HPF spectra and RV template. We suspect this increased level of scatter is due to additional sources of systematic noise in the HPF H2RG detector. H2RGs are known to have a number of systematic noise sources that affect precision RV extractions including bias-level fluctuations, persistence effects, and cross-hatch patterns [see e.g., 165, for a discussion on some of these effects in the HPF H2RG]. To account for the additional source of systematic noise we see between the different HPF readout channels,

we took the following steps to conservatively increase the estimated RV error bar from the normal SERVAL pipeline.

- First, as the SERVAL pipeline has been demonstrated to be accurate at the 1m/s level in [252], we extract the HPF RVs order by order using the full RV order. This results in an RV value and RV uncertainty estimate per HPF order. We follow [252] and [152] and perform a weighted average per RV order.

- Second, we independently reduce the same spectra by splitting each spectrum into disjoint segments along the four HPF readout channels (512 pixel wide). This yields four independent RV estimates and accompanying RV uncertainties for a given observation after performing a weighted average across all of the orders analyzed (independently for each segment of the spectrum).

- Third, we modeled the four readout channel RVs (v_i) as statistically independent draws from a Gaussian distribution with the mean equal to the full order RV (v_f). The Gaussian model's width was set to what we would expect from the reduced information in the readout channel level spectra if the expected error in the full order RV (σ_f) is multiplied by an unknown *inflation factor* k. i.e,

$$v_i \sim N(v_f, \sigma_i), \quad \text{where} \;\; \sigma_i = C_i \times (k\sigma_f). \tag{3.1}$$

  The reduction in the information-content (C_i) due to reducing the size of the spectra into four chunks is $\sim$2. This Bayesian model was implemented in the `pymc3` package [205] and fitted to each epoch of data. For most of the observations, the inflation factor k was found to be consistent with 1 (implying the scatter in RVs across the four readout channels is consistent with the full order RV and its derived RV uncertainty). For those epochs where the inflation factor k is greater than 1 with a probability of 95%,

we inflated the full order RV uncertainty by the median of the posterior distribution of the inflation factor k.

- Lastly, using the newly derived RVs for all of the epochs we perform a final weighted average of RVs within a given HET track to give a binned RV point and accompanying RV uncertainty per HPF visit.

Using this methodology, of the 1016 unbinned observations, we found that 89 observations have sufficient evidence to increase the RV uncertainty by the inflation factor. Figure 3.8 compares the RVs and the RV uncertainty of the binned HPF RVs before and after applying this correction to the RV uncertainties. In this binned-by-track view, although a few of the observations have their RV uncertainty increased, the median RV uncertainty remains similar before and after applying this correction. As an additional test, we also tried running all of the same analysis presented in this work with the un-inflated RV uncertainties, and achieve the same results.

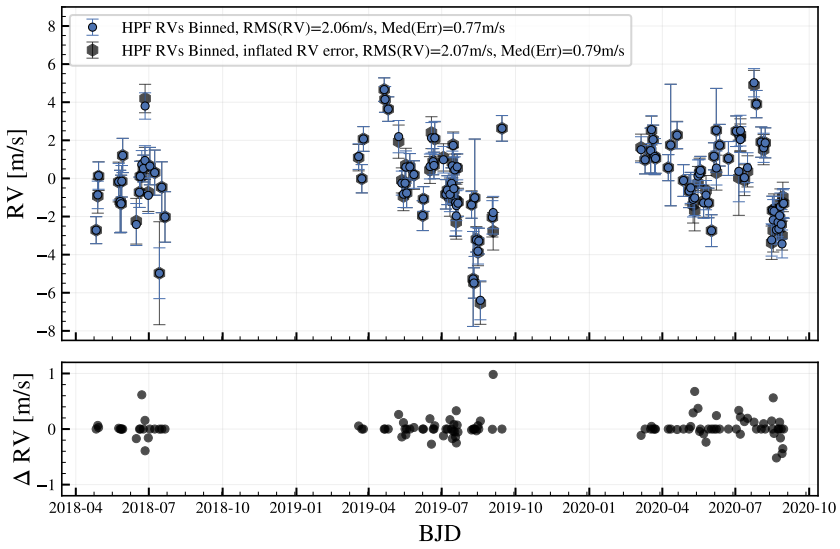

Figure 3.8: HPF RVs of Barnard's Star before and after accounting for additional RV noise between the different HPF readout channels. We use the inflated RV uncertainties for the final RV analysis.

Table 3.1: HPF RV measurements of Barnard's Star

BJD	RV (m/s)	Err (m/s)	Flag[a]
2458234.87812	−3.715	0.709	1
2458236.87809	−1.930	0.893	1
2458237.87424	−0.881	0.755	1
2458262.94194	−1.188	1.043	1
2458264.78751	−2.212	1.640	1
2458265.93688	−2.328	1.498	1
2458266.80097	−1.148	0.826	1
2458267.94149	+0.206	0.898	1
2458284.89214	−3.246	1.199	1
2458288.87073	−1.726	0.796	1
2458289.86962	−0.891	0.792	1
2458291.72340	−0.889	0.804	1
2458293.71806	−0.480	0.704	1
2458295.70498	−0.211	0.839	1
2458295.85022	+3.193	0.747	1
2458299.84260	−1.729	1.002	1
2458301.84403	−0.354	0.982	1
2458307.81476	−0.696	1.184	1
2458313.66578	−5.974	2.702	1
2458316.64416	−1.463	1.335	1
2458320.65702	−3.021	1.325	1
2458561.98905	+0.090	0.693	2
2458565.96692	−1.016	0.743	2
2458567.96441	+1.071	0.648	2
2458593.89213	+3.663	0.616	2

2458594.88889	+3.146	0.676	2
2458598.88624	+2.639	0.643	2
2458611.85165	+0.930	0.871	2
2458615.83819	−1.103	0.658	2
2458617.83549	−1.941	0.752	2
2458619.82476	−1.250	0.655	2
2458620.81519	−0.300	0.882	2
2458621.82486	−1.764	0.770	2
2458625.80795	−0.390	0.696	2
2458630.93991	−0.824	0.750	2
2458641.90046	−2.952	0.784	2
2458642.76256	−2.080	0.649	2
2458650.87920	−0.559	0.703	2
2458652.73437	+1.401	0.837	2
2458654.87231	−0.121	0.687	2
2458655.87345	−0.318	0.697	2
2458656.86163	+1.070	0.898	2
2458667.69533	+0.104	0.716	2
2458670.82515	−1.833	0.773	2
2458672.68754	−1.615	0.758	2
2458675.81356	−2.007	0.977	2
2458677.81057	−1.258	0.814	2
2458678.80473	−0.164	0.803	2
2458679.79854	+0.771	0.668	2
2458680.65540	−1.618	0.802	2
2458681.78999	−0.499	0.782	2
2458682.79255	−2.132	1.912	2

2458683.64977	−3.297	0.891	2
2458683.78730	−2.179	0.877	2
2458684.78188	−0.464	0.745	2
2458685.78554	−2.246	0.730	2
2458702.73098	−2.371	0.721	2
2458704.73015	−6.277	2.492	2
2458705.72662	−6.487	0.797	2
2458706.71574	−2.014	3.080	2
2458708.72053	−4.194	0.665	2
2458710.71091	−4.877	0.704	2
2458711.71354	−4.288	0.675	2
2458713.70287	−7.541	1.115	2
2458728.66701	−3.039	1.034	2
2458729.67255	−3.774	0.985	2
2458740.63395	+1.628	0.673	2
2458914.00923	+0.622	0.704	2
2458919.00205	−0.020	0.743	2
2458925.97803	+0.460	1.178	2
2458926.97803	+1.513	0.755	2
2458928.98375	+1.038	0.761	2
2458930.97168	+0.146	0.947	2
2458931.97305	+0.050	0.780	2
2458947.92495	−0.435	0.684	2
2458950.91341	+0.753	3.190	2
2458958.89271	+1.274	0.724	2
2458966.87951	−1.109	0.832	2
2458973.84711	−1.664	0.866	2

2458975.85009	−1.540	0.849	2
2458978.84716	−2.391	0.95	2
2458980.83324	−2.696	1.056	2
2458984.95797	−1.25	0.880	2
2458986.96208	−0.72	0.784	2
2458987.95142	−0.582	0.739	2
2458991.94310	−2.193	0.844	2
2458994.94212	−1.64	0.794	2
2458997.93706	−2.288	0.777	2
2459001.77769	−3.742	0.836	2
2459004.91390	+0.161	0.710	2
2459007.75067	+1.526	2.199	2
2459007.89829	−0.696	0.918	2
2459011.88773	+0.744	1.094	2
2459022.85758	+0.047	0.890	2
2459032.69635	+1.477	0.802	2
2459035.82506	−0.964	1.973	2
2459037.68397	+1.132	0.726	2
2459037.82959	+1.293	0.837	2
2459042.80748	−1.091	0.809	2
2459046.65818	−0.630	0.818	2
2459054.76850	+3.898	0.773	2
2459057.76746	+2.900	0.717	2
2459063.74665	+0.908	0.795	2
2459066.73442	+0.511	0.792	2
2459068.73500	+0.867	0.788	2
2459076.71518	−4.375	0.875	2

2459077.71313	−2.679	0.748	2
2459078.70214	−3.740	1.122	2
2459079.70819	−2.645	0.834	2
2459082.69876	−3.184	0.792	2
2459084.69172	−3.295	0.769	2
2459085.68536	−3.649	0.732	2
2459086.68122	−3.077	0.695	2
2459087.67943	−2.309	0.760	2
2459088.67738	−3.406	0.773	2
2459089.67546	−3.998	0.762	2
2459090.67292	−1.971	0.773	2
2459091.66643	−2.310	0.778	2

NOTES

[a] 1 indicates Pre and 2 indicates Post split

3.7 Additional Tables

Table 3.2: Discovery Data Model Comparison

	Parameters		ΔBIC		
Model	Free Parameters	BIC	GP only	GP + Planet	Planet only
GP only	**26**	**3485.0785**	–	2.040	99.814
GP + Planet	31	3487.1186		–	97.774
Planet only	21	3584.8938			–

NOTES
Our preferred model, taking into account ΔBIC, is in **bold**

Table 3.3: Updated Data Model Comparison

	Parameters		ΔBIC		
Model	Free Parameters	BIC	GP + Planet	GP only	Planet only
GP + Planet	40	4021.3900	–	1.354	160.970
GP only	**35**	**4022.7433**		–	159.616
Planet only	27	4182.3590			–

NOTES
Our preferred model, taking into account ΔBIC, is in **bold**

Table 3.4: Priors and Posteriors for Discovery Hα Data Sets

Model	Parameter	Prior	Posterior
GP	$\log L$	$\mathcal{U}(0.1, 6)$	$1.91^{+0.19}_{-0.19}$
	$\log C$	$\mathcal{U}(-6, 6)$	$-5.44^{+2.60}_{-0.51}$
	$P_{\rm rot}$	$\mathcal{G}(145, 15)$	$142.96^{+11.65}_{-10.49}$
	$\log B$	$\mathcal{U}(-9, 6)$	$-4.28^{+0.08}_{0.08}$
Instrument	$\sigma_{\rm APF}$	$\mathcal{U}(0.001, 1)$	0.01 ± 0.001
	$\sigma_{\rm CARMENES}$	$\mathcal{U}(0.001, 1)$	0.01 ± 0.001
	$\sigma_{\rm HARPSN}$	$\mathcal{U}(0.001, 1)$	0.01 ± 0.001
	$\sigma_{\rm HARPSpre}$	$\mathcal{U}(0.001, 1)$	0.01 ± 0.001
	$\sigma_{\rm HARPSpost}$	$\mathcal{U}(0.001, 1)$	0.01 ± 0.001
	$\sigma_{\rm HIRES}$	$\mathcal{U}(0.001, 1)$	0.01 ± 0.001
	$\sigma_{\rm PFS}$	$\mathcal{U}(0.001, 1)$	0.01 ± 0.001
	$\sigma_{\rm UVES}$	$\mathcal{U}(0.001, 1)$	0.01 ± 0.001
	$\gamma_{\rm APF}$	$\mathcal{U}(-5, 5)$	-0.51 ± 0.001
	$\gamma_{\rm CARMENES}$	$\mathcal{U}(-5, 5)$	-0.52 ± 0.001
	$\gamma_{\rm HARPSN}$	$\mathcal{U}(-5, 5)$	-0.52 ± 0.001
	$\gamma_{\rm HARPSpre}$	$\mathcal{U}(-5, 5)$	-0.51 ± 0.001
	$\gamma_{\rm HARPSpost}$	$\mathcal{U}(-5, 5)$	-0.52 ± 0.001
	$\gamma_{\rm HIRES}$	$\mathcal{U}(-5, 5)$	-0.51 ± 0.001
	$\gamma_{\rm PFS}$	$\mathcal{U}(-5, 5)$	-0.52 ± 0.001
	$\gamma_{\rm UVES}$	$\mathcal{U}(-5, 5)$	-0.51 ± 0.001

Table 3.5: Priors and Posteriors for Discovery RV Data Sets

Model	Parameter	Prior	GP only	Planet only	GP + Planet
GP	$\log L$	$\mathcal{G}(1.91, 0.19)$	$1.60^{+0.15}_{-0.12}$	–	$1.56^{+0.18}_{-0.13}$
	$\log C$	$\mathcal{U}(-6, 6)$	$-5.85^{+0.57}_{-0.13}$	–	$-5.88^{+0.33}_{-0.10}$
	$\mathrm{P_{rot}}$	$\mathcal{G}(142.96, 11.65)$	$141.18^{+12.95}_{-12.45}$	–	$139.75^{+14.08}_{-13.79}$
	$\log B_{\mathrm{CARMENES}}$	$\mathcal{U}(-2, 2)$	$0.56^{+0.16}_{-0.14}$	–	$0.49^{+0.17}_{-0.15}$
	$\log B_{\mathrm{HARPSN}}$	$\mathcal{U}(-2, 2)$	$0.51^{+0.25}_{-0.20}$	–	$0.56^{+0.23}_{-0.17}$
	$\log B_{\mathrm{HARPSpre}}$	$\mathcal{U}(-2, 2)$	$0.05^{0.14}_{-0.13}$	–	$0.36^{+0.21}_{0.19-}$
	$\log B_{\mathrm{HARPSpost}}$	$\mathcal{U}(-2, 2)$	$0.21^{+0.30}_{-0.22}$	–	$0.27^{+0.28}_{-0.23}$
	$\log B_{\mathrm{HIRES}}$	$\mathcal{U}(-2, 2)$	$0.85^{+0.12}_{-0.12}$	–	$0.74^{+0.15}_{-0.14}$
	$\log B_{\mathrm{PFS}}$	$\mathcal{U}(-2, 2)$	$0.26^{+0.21}_{-0.34}$	–	$-0.01^{+0.23}_{-0.58}$
	$\log B_{\mathrm{UVES}}$	$\mathcal{U}(-2, 2)$	$0.70^{+0.11}_{-0.13}$	–	$0.67^{+0.12}_{-0.13}$
Instrument	σ_{APF}	$\mathcal{U}(0.5, 10)$	$2.95^{+0.55}_{-0.45}$	$2.86^{+0.52}_{-0.44}$	$2.88^{0.60}_{-0.48}$
	$\sigma_{\mathrm{CARMENES}}$	$\mathcal{U}(0.5, 10)$	$1.16^{+0.19}_{-0.20}$	$1.88^{+0.16}_{-0.14}$	$1.17^{+0.20}_{-0.21}$
	σ_{HARPSN}	$\mathcal{U}(0.5, 10)$	$0.90^{+0.29}_{-0.23}$	$2.08^{+0.33}_{-0.28}$	$0.90^{+0.29}_{-0.24}$
	$\sigma_{\mathrm{HARPSpre}}$	$\mathcal{U}(0.5, 10)$	$0.63^{+0.14}_{-0.09}$	$0.95^{+0.15}_{-0.14}$	$0.66^{+0.16}_{-0.11}$
	$\sigma_{\mathrm{HARPSpost}}$	$\mathcal{U}(0.5, 10)$	$0.77^{+0.21}_{-0.17}$	$1.18^{+0.20}_{-0.19}$	$0.75^{+0.23}_{-0.17}$
	σ_{HIRES}	$\mathcal{U}(0.5, 10)$	$1.32^{+0.30}_{-0.32}$	$2.56^{+0.20}_{-0.19}$	$1.38^{+0.31}_{-0.34}$
	σ_{PFS}	$\mathcal{U}(0.5, 10)$	$0.79^{+0.39}_{-0.22}$	$1.17^{+0.34}_{-0.32}$	$0.83^{+0.41}_{-0.25}$
	σ_{UVES}	$\mathcal{U}(0.5, 10)$	$0.75^{+0.28}_{-0.18}$	$2.33^{+0.25}_{-0.22}$	$0.75^{+0.29}_{-0.19}$
	γ_{APF}	$\mathcal{U}(-10, 10)$	$0.47^{+0.51}_{-0.52}$	$0.21^{+0.48}_{-0.47}$	$0.19^{+0.45}_{-0.47}$
	$\gamma_{\mathrm{CARMENES}}$	$\mathcal{U}(-10, 10)$	$2.40^{+0.58}_{-0.62}$	$2.99^{+0.17}_{-0.17}$	$2.36^{+0.54}_{-0.56}$
	γ_{HARPSN}	$\mathcal{U}(-10, 10)$	$1.67^{+0.80}_{-0.85}$	$2.37^{+0.37}_{-0.37}$	$1.88^{+0.86}_{-0.87}$
	$\gamma_{\mathrm{HARPSpre}}$	$\mathcal{U}(-10, 10)$	$-0.75^{+0.28}_{-0.29}$	$-0.43^{+0.13}_{-0.13}$	$-0.61^{+0.21}_{-0.23}$
	$\gamma_{\mathrm{HARPSpost}}$	$\mathcal{U}(-10, 10)$	$2.97^{+0.82}_{-0.83}$	$3.44^{+0.23}_{-0.23}$	$3.30^{+0.88}_{-0.95}$
	γ_{HIRES}	$\mathcal{U}(-10, 10)$	$0.89^{+0.46}_{-0.49}$	$-0.65^{+0.23}_{-0.23}$	$-0.89^{+0.44}_{-0.44}$
	γ_{PFS}	$\mathcal{U}(-10, 10)$	$0.38^{+0.42}_{-0.42}$	$0.36^{+0.29}_{-0.29}$	$0.25^{+0.34}_{-0.33}$
	γ_{UVES}	$\mathcal{U}(-10, 10)$	$1.46^{+0.49}_{-0.50}$	$1.75^{+0.30}_{-0.30}$	$1.45^{+0.49}_{-0.48}$
Planet	Period	$\mathcal{G}(233, 15)$	–	$232.86^{+0.29}_{-0.43}$	$232.64^{+0.32}_{-0.39}$
	T_c	$\mathcal{G}(2454937.92, 20)$	–	$2454934.03^{+4.55}_{-4.01}$	$2454936.11^{+4.24}_{-4.33}$
	K_{amp}	$\mathcal{U}(0.3, 10)$	–	$1.16^{+0.12}_{-0.12}$	$1.16^{+0.22}_{-0.23}$
	$\sqrt{e}\sin\omega$	$\mathcal{U}(-1, 1)$	–	$0.53^{+0.09}_{-0.13}$	$0.59^{+0.12}_{-0.22}$
	$\sqrt{e}\cos\omega$	$\mathcal{U}(-1, 1)$	–	$-0.16^{+0.19}_{-0.18}$	$-0.08^{+0.21}_{-0.20}$

Table 3.6: Priors and Posteriors for Updated RV Data Sets

Model	Parameter	Prior	GP only	Planet only	GP + Planet
GP	$\log L$	$\mathcal{G}(1.91, 0.19)$	$1.56^{+0.13}_{-0.09}$	–	$1.52^{+0.14}_{-0.09}$
	$\log C$	$\mathcal{U}(-6, 6)$	$-5.92^{+0.18}_{-0.06}$	–	$-5.92^{+0.16}_{-0.06}$
	$\mathrm{P_{rot}}$	$\mathcal{G}(142.96, 11.65)$	$142.78^{+13.41}_{-13.93}$	–	$139.36^{+14.56}_{-14.76}$
	$\log B_{\mathrm{CARMENES}}$	$\mathcal{U}(-2, 2)$	$0.54^{+0.15}_{-0.12}$	–	$0.48^{+0.16}_{-0.12}$
	$\log B_{\mathrm{HARPSN}}$	$\mathcal{U}(-2, 2)$	$0.48^{+0.22}_{-0.17}$	–	$0.57^{+0.19}_{-0.14}$
	$\log B_{\mathrm{HARPSpre}}$	$\mathcal{U}(-2, 2)$	$0.25^{+0.13}_{-0.11}$	–	$-0.11^{+0.18}_{-0.13}$
	$\log B_{\mathrm{HARPSpost}}$	$\mathcal{U}(-2, 2)$	$0.52^{+0.26}_{-0.16}$	–	$0.62^{+0.22}_{-0.17}$
	$\log B_{\mathrm{HIRESpre}}$	$\mathcal{U}(-2, 2)$	$0.94^{+0.19}_{-0.17}$	–	$0.85^{+0.19}_{-0.17}$
	$\log B_{\mathrm{HIRESpost}}$	$\mathcal{U}(-2, 2)$	$0.81^{+0.14}_{-0.14}$	–	$0.59^{+0.18}_{-0.15}$
	$\log B_{\mathrm{PFS}}$	$\mathcal{U}(-2, 2)$	$0.28^{+0.16}_{-0.27}$	–	$-0.01^{+0.19}_{-0.31}$
	$\log B_{\mathrm{UVES}}$	$\mathcal{U}(-2, 2)$	$0.71^{+0.11}_{-0.11}$	–	$0.67^{+0.10}_{-0.12}$
	$\log B_{\mathrm{HPFpre}}$	$\mathcal{U}(-2, 2)$	$-1.91^{+0.19}_{-0.07}$	–	$-1.93^{+0.16}_{-0.06}$
	$\log B_{\mathrm{HPFpost}}$	$\mathcal{U}(-2, 2)$	$0.64^{+0.13}_{-0.11}$	–	$0.64^{+0.14}_{-0.11}$
Instrument	σ_{APF}	$\mathcal{U}(0.5, 10)$	$2.97^{+0.61}_{-0.50}$	$2.88^{+0.53}_{-0.46}$	$2.89^{+0.61}_{-0.50}$
	$\sigma_{\mathrm{CARMENES}}$	$\mathcal{U}(0.5, 10)$	$1.15^{+0.20}_{-0.21}$	$1.86^{+0.16}_{-0.15}$	$1.16^{+0.20}_{-0.21}$
	σ_{HARPSN}	$\mathcal{U}(0.5, 10)$	$0.91^{+0.29}_{-0.24}$	$2.07^{+0.33}_{-0.28}$	$0.89^{+0.31}_{-0.23}$
	$\sigma_{\mathrm{HARPSpre}}$	$\mathcal{U}(0.5, 10)$	$0.93^{+0.16}_{-0.15}$	$1.43^{+0.14}_{-0.13}$	$0.96^{+0.17}_{-0.15}$
	$\sigma_{\mathrm{HARPSpost}}$	$\mathcal{U}(0.5, 10)$	$1.04^{+0.23}_{-0.22}$	$1.67^{+0.22}_{-0.19}$	$1.02^{+0.25}_{-0.24}$
	$\sigma_{\mathrm{HIRESpre}}$	$\mathcal{U}(0.5, 10)$	$1.58^{+0.55}_{-0.52}$	$2.82^{+0.40}_{-0.35}$	$1.65^{+0.54}_{-0.53}$
	$\sigma_{\mathrm{HIRESpost}}$	$\mathcal{U}(0.5, 10)$	$1.51^{+0.32}_{-0.33}$	$2.46^{+0.23}_{-0.21}$	$1.61^{+0.32}_{-0.33}$
	σ_{PFS}	$\mathcal{U}(0.5, 10)$	$0.77^{+0.36}_{-0.21}$	$1.30^{+0.36}_{-0.33}$	$0.77^{+0.38}_{-0.21}$
	σ_{UVES}	$\mathcal{U}(0.5, 10)$	$0.74^{+0.29}_{-0.18}$	$2.39^{+0.25}_{-0.22}$	$0.71^{+0.28}_{-0.16}$
	σ_{HPFpre}	$\mathcal{U}(0.5, 10)$	$1.38^{+0.41}_{-0.31}$	$1.31^{+0.38}_{-0.31}$	$1.27^{+0.43}_{-0.32}$
	$\sigma_{\mathrm{HPFpost}}$	$\mathcal{U}(0.5, 10)$	$0.59^{+0.14}_{-0.07}$	$1.87^{+0.19}_{-0.16}$	$0.59^{+0.13}_{-0.07}$
	γ_{APF}	$\mathcal{U}(-10, 10)$	$0.48^{+0.47}_{-0.50}$	$0.23^{+0.46}_{-0.47}$	$0.28^{+0.40}_{-0.42}$
	$\gamma_{\mathrm{CARMENES}}$	$\mathcal{U}(-10, 10)$	$2.43^{+0.57}_{-0.59}$	$2.99^{+0.17}_{-0.17}$	$2.37^{+0.56}_{-0.59}$
	γ_{HARPSN}	$\mathcal{U}(-10, 10)$	$1.68^{+0.75}_{-0.84}$	$2.21^{+0.37}_{-0.38}$	$1.82^{+0.86}_{-0.90}$
	$\gamma_{\mathrm{HARPSpre}}$	$\mathcal{U}(-10, 10)$	$-0.67^{+0.32}_{-0.34}$	$-0.25^{+0.16}_{-0.16}$	$-0.50^{+0.25}_{-0.26}$
	$\gamma_{\mathrm{HARPSpost}}$	$\mathcal{U}(-10, 10)$	$-0.86^{+0.90}_{-1.01}$	$-0.37^{+0.25}_{-0.27}$	$-0.47^{+0.92}_{-0.79}$
	$\gamma_{\mathrm{HIRESpre}}$	$\mathcal{U}(-10, 10)$	$-1.40^{+0.79}_{-0.79}$	$-1.55^{+0.44}_{-0.43}$	$-1.45^{+0.70}_{-0.75}$
	$\gamma_{\mathrm{HIRESpost}}$	$\mathcal{U}(-10, 10)$	$-0.34^{+0.45}_{-0.47}$	$-0.14^{+0.23}_{-0.23}$	$-0.32^{+0.35}_{-0.40}$
	γ_{PFS}	$\mathcal{U}(-10, 10)$	$0.34^{+0.38}_{-0.39}$	$-0.37^{+0.30}_{-0.30}$	$0.26^{+0.33}_{-0.31}$
	γ_{UVES}	$\mathcal{U}(-10, 10)$	$1.46^{+0.50}_{-0.49}$	$1.78^{+0.30}_{-0.30}$	$1.44^{+0.48}_{-0.50}$
	γ_{HPFpre}	$\mathcal{U}(-10, 10)$	$-1.20^{+0.39}_{-0.42}$	$-0.90^{+0.39}_{-0.40}$	$-0.99^{+0.42}_{-0.43}$
	$\gamma_{\mathrm{HPFpost}}$	$\mathcal{U}(-10, 10)$	$0.51^{+0.59}_{-0.59}$	$-1.04^{+0.22}_{-0.22}$	$-0.58^{+0.54}_{-0.62}$
Planet	Period	$\mathcal{G}(233, 15)$	–	$231.93^{+0.49}_{-0.30}$	$232.36^{+0.17}_{-0.22}$
	T_c	$\mathcal{G}(2454937.92, 20)$	–	$2454920.91^{+6.29}_{-7.01}$	$2454935.87^{+2.30}_{-2.96}$
	K_{amp}	$\mathcal{U}(0.3, 10)$	–	$1.19^{+0.13}_{-0.13}$	$1.28^{+0.28}_{-0.28}$
	$\sqrt{e}\sin\omega$	$\mathcal{U}(-1, 1)$	–	$0.10^{+0.20}_{-0.23}$	$0.60^{+0.12}_{-0.21}$
	$\sqrt{e}\cos\omega$	$\mathcal{U}(-1, 1)$	–	$0.28^{+0.16}_{-0.25}$	$-0.24^{+0.21}_{-0.16}$

Chapter 4

`Lia`: Finding a Sparse Representation of an Exoplanet RV Time Series in the Time/Frequency Domain - Lubin et al. (in prep)

4.1 Foreword

The first goal of the exoplanet-searching astronomer is to identify periodic signals in their data sets. This is the foundation upon which all subsequent scientific inquiry is performed, as it is the prime evidence for the very existence of a planet in the first place. When using the RV method to search for planets, the periodic signal in question originates from the Doppler shift of light from the star's motion around the shared center of mass with its planet(s). Through the corresponding change in wavelength of known absorption lines in the stellar spectrum, we compute the RV. Ideally, each absorption line in the spectrum will shift linearly

and equally in wavelength space only due to the physical, radial motion of the star. However, the physical motion of the star is not the only way to induce a shift, or at least an apparent shift, in the stellar spectrum. Stellar activity can also induce real and/or apparent shifts in the stellar spectrum. In turn, this affects the computed RV.

The processes that produce stellar activity induced signals are quasi-periodic; they have a general periodic nature but they come and go in a characteristic timescale, potentially returning with minor period and/or phase changes. Therefore, the resulting computed RVs will be contaminated with quasi-periodic signals. With exception of long, multi-year magnetic cycles, like our Sun's 11 year cycle, all stellar activity signals are transient and exist on a wide variety of timescales. But the signals associated with spots and plage are inherently tied to the rotation period of the star. Therefore, they manifest in the data at periodicities at or near the stellar rotation period (depending on the strength of differential rotation), its harmonics [32], or their associated aliases.

Depending on the length of the time baseline of RV observations, a quasi-periodic stellar activity signal can look a lot like a planetary signal. For example, if a quasi-periodic signal grows and subsequently decays over a two thousand day time span, but observations only sample this signal for 200 days in the middle of its life, the resulting signal in the RVs will appear strictly periodic. This is exacerbated by the way we look and test for periodic signals in RV data sets. Many computational methods have been proposed for identifying periodic signals in a RV time series but they all make the same underlying assumption: periodic signals in the data, regardless of their origin, will be strictly periodic.

Here we introduce a new periodogram, one which is designed to further characterize the properties of candidate signals, *the ℓ_1 Apodized Periodogram*, or `Lia`[1]. By leveraging ℓ_1 minimization techniques [47, 228, 66], which fit for all signals in a time series simultaneously,

[1]For installation instructions, documentation, and tutorials, see the GitHub repository here: https://github.com/jluby127

`Lia` can help distinguish between strictly and quasi periodic signals. In the process of identifying signals, it provides estimates of the signal's periodicity, the decay lifetime, the phase, the apodization window center, and the amplitude, all in astrophysically motivated units. Through this more holistic picture of a candidate signal with `Lia`, we can be more confident in determining a signal's astrophysical origin, which helps us better understand our data before more complex analysis methods and minimize false positive detections.

This work is organized in the following manner. First we outline our methods and describe the theory behind the algorithm in §4.2. Next, we demonstrate the application of `Lia` in three stages: first in synthetic data, §4.3.1, then in well-studied Solar data, §4.3.2, and lastly in the Keck/HIRES archival data set for HD 26965, §4.3.3. Then we discuss use cases and limitations of the software in §4.4 before concluding in §4.5.

4.2 Methods

For all following descriptions, convention will denote a set or array of values with bold text and a single value with standard text. Additionally, we assume a typical RV time series data set consisting of N observations as a set of timestamps, $\mathbf{t}$, with sets of associated velocities, $\mathbf{y}$, and errors, $\mathbf{e}$.

4.2.1 Review of method in 1D

`Lia` is built a upon an ℓ_1 minimization algorithm. This technique has been applied many times in astronomy before [218, 31], but was first brought to the exoplanet community in the ℓ_1 Periodogram from Hara et al. 2017 [100], from which `Lia` draws inspiration and some code. A complete description of the ℓ_1 minimization technique can be found therein, but a short overview is provided here, keeping consistent notation.

Generally, the ℓ_1 minimization technique is a minimization problem. Given a dataset $\mathbf{y(t)}$, we wish to recreate the data using a linear combination of a small number of vectors, $\boldsymbol{\mathcal{A}} = (\boldsymbol{a_j(t)})_{\boldsymbol{j \in I}}$ from a larger set of vectors, I, called the *dictionary*. We find this small solution set of vectors by minimizing the ℓ_1 norm of a set of coefficients, one per vector in the dictionary, to an allowed tolerance, ϵ, with the data:

$$\boldsymbol{x^\star} = \arg\min_{x \in \mathbb{C}^n} \|\boldsymbol{x}\|_{\ell_1} \, s.t. \, \|\boldsymbol{W}(\boldsymbol{A}\boldsymbol{x} - \boldsymbol{y})\|_{\ell_2} \leqslant \epsilon \tag{4.1}$$

The solution set, $\boldsymbol{x^\star}$, is the set of coefficients matching one-to-one the with the vectors in $\mathcal{A}$. One major advantage of this method is the assumption of sparsity. Most elements of $\boldsymbol{x^\star}$ will be zero, leaving a small number of non-zero coefficients whose corresponding vectors linearly combine to approximate the data to within the allowed tolerance.

The ℓ_1 minimization is performed using an implementation of the Least Angle Regression (LARS) algorithm from [73]. LARS sequentially finds the vector most correlated with the data and begins to increase that vector's coefficient, computing residuals to a fit until a new vector is most correlated with the residuals. It then increases both coefficients in their joint least squares direction until a third vector is most correlated and so on until the residuals are smaller than the pre-determined tolerance. `Lia` uses the same LARS implementation from [100] and more information on the method can be found in the source code.

One of the main advantages of the ℓ_1 minimization technique is that it estimates all the amplitudes of a discretized Fourier spectrum at once, as opposed to fitting sines at one frequency at a time like the GLSP. Fitting all signals helps decrease the problem of aliasing. Another advantage of this method over a GLSP is the final coefficients estimate the strength of the signal in the same units as the dataset's y-axis units. This provides a more meaningful

solution to this astrophysical problem of identifying periodic signals in RV data sets.

4.2.2 Grids and Dictionary

No periodogram can test every imaginable parameter. For example, in a 1D periodogram, a grid of frequencies is constructed and then those frequencies are tested in the algorithm. In the 1D case, frequency is the only parameter and therefore the only required grid. In `Lia`, there are 4 parameters, each requiring its own grid: frequency ($\boldsymbol{\omega}$), decay lifetime ($\boldsymbol{\tau}$), apodization window center ($\mathbf{T0}$), and phase ($\boldsymbol{\phi}$).

First, as the problem for creating a well-sampled grid of frequencies is solved, we adopt the conventional logic:

$$\boldsymbol{\omega}_{k_1 \in 0 \ldots n} = k_1 \Delta\omega \tag{4.2}$$

where

$$\Delta\omega = \frac{2\pi}{T_{base} N_\omega} \tag{4.3}$$

Where T_{base} is the baseline of the timestamps and N_ω is the oversampling factor for frequencies. We generally adopt an oversampling factor of 8 for frequencies. Finally, n is the desired length of $\boldsymbol{\omega}$, best determined by:

$$n = \frac{\omega_{min} - \omega_{max}}{\Delta\omega} \tag{4.4}$$

where the parameter ω_{max} is defined as

$$\omega_{max} = \frac{2\pi}{T_{base}} \tag{4.5}$$

and ω_{min} is a user-defined minimum frequency parameter.

Next, the phase grid, $\boldsymbol{\phi}$, is determined by a single oversampling factor, N_ϕ, which sets evenly-spaced phases between 0 and π:

$$\boldsymbol{\phi}_{k_2 \in 0 \ldots N_\phi} = \frac{k_2 \pi}{N_\phi} \tag{4.6}$$

In practice we adopt a standard N_ϕ of 4, as a compromise between grid density and algorithm speed.

Next we create the grid for the decay lifetime parameter, $\boldsymbol{\tau}$. This grid represents the apodization timescales to be tested by the algorithm. Here we adopt a modified version of the logic for an exponential-spaced grid determined by the baseline of the time series from [**?**]:

$$\tau_{k_3 \in 1 \ldots N_\tau} = \alpha^{k_3} \times T_{base} \tag{4.7}$$

where α is the "downscaling of the timescale" and N_τ is the desired number of decay lifetimes in the grid. Note that in all cases, k_3 begins at 1, not 0, because we set

$$\tau_0 = 10 \times T_{base} \tag{4.8}$$

so that the first element in $\boldsymbol{\tau}$ is always a decay lifetime that is much longer than the baseline of the time series. This will represent an "infinite" decay lifetime, analogous to a robust sinusoid. In practice, weighing computational limits and speed with grid density, we suggest a maximum N_τ of 8 but most often work with a value of 5.

Once $\boldsymbol{\tau}$ is chosen, we can then create a grid of apodization window center offsets, **T0**. We want to evenly sample offsets across the time baseline, but simultaneously not oversample offsets. To achieve this, each $\tau \in \boldsymbol{\tau}$ is assigned its own grid of offsets. The spacing, $\Delta T0_{k_3}$, between offsets for a given decay lifetime, τ_{k_3}, is a proportion of the lifetime, determined by a single user-chosen density factor, d:

$$\Delta T0_{k_3} = \frac{\tau_{k_3}}{d}. \tag{4.9}$$

Smaller density factors create more dense T0 grids where the number of offsets within one T0 grid is computed as:

$$N_{T0_{k_3}} = \frac{T_{base}}{\Delta T0_{k_3}}. \tag{4.10}$$

Then the resulting $\boldsymbol{T0}$ for a given $\tau \in \boldsymbol{\tau}$ is computed as:

$$\boldsymbol{T0}_{k_4 \in -1 \ldots N_{T0}+1} = k_4 \Delta T0 \tag{4.11}$$

Note the limits that k_4 runs. This formation is designed in such a way that offsets are evenly spaced throughout the baseline with an additional offset allocated one ΔT0 beyond the baseline at both sides of the baseline. In a practical example, for a decay lifetime $\tau = 100$ across a 1000 day baseline (from day 0 to day 999) and $d = 2$, this prescription would create grid that has offsets every 50 days ranging from -50 to 1050. The advantage of this design is it will allow the solver to include decaying functions that begin or end slightly beyond the bounds of the baseline. This prescription is for all $\tau \in \boldsymbol{\tau}$ except the infinite τ. Since the infinite decay time represents a robust sinusoid which has no beginning or end to the wave packet, we only allow its T0 grid to contain a single offset value, set to the arbitrary value of 0. This ensures that the solver does not have equivalent but competing functions in the dictionary for modeling robust sinusoids.

With all the grids defined, the last step is to apply a customization of the $\boldsymbol{\omega}$ grid for each $\tau \in \boldsymbol{\tau}$. Qualitatively, for a decay lifetime of τ, the practical frequency resolution is $\frac{2\pi}{\tau}$. To eliminate this conundrum, we create sub-grids of $\boldsymbol{\omega}$ for each $\tau \in \boldsymbol{\tau}$. The sub-grids are constructed identically to $\boldsymbol{\omega}$ above, but for a given τ, we choose ω_{min} so that its corresponding period is not longer than a user-defined fraction, f, of the given τ:

$$\omega_{min} = \frac{2\pi}{f \times \tau}. \tag{4.12}$$

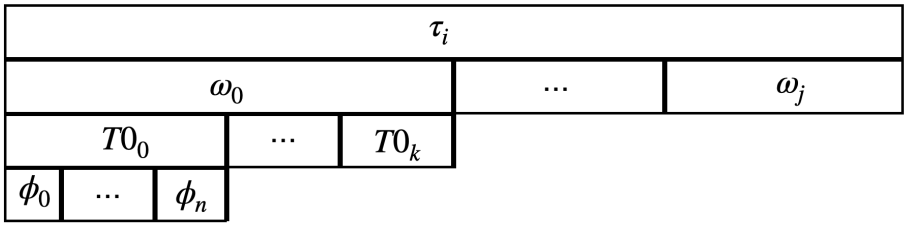

Figure 4.1: A schematic of the organization of the dictionary.

With all grids defined, we can begin constructing the dictionary. The dictionary is a set of functions from which a small number are selected by the solver because their linear combination reproduces the data to within an allowed tolerance, see Equation 4.1. In theory, the dictionary has no size limitations and the functions inside may take on any form. This is an advantage of the `Lia` method as it provides the flexibility necessary to recover quasi-periodic signals. No longer do we assume all periodic signals in the data set will follow a strictly sinusoidal shape. In practice, the dictionary size is limited by computational power for reasonable run-time and the functions included are written and ordered in a logic that allows for easy determination of their key parameters during post-processing. The dictionary exists as an $N \times M$ matrix, where M is the number of vectors included in the dictionary.

As stated earlier, many non-strictly periodic functional forms have been proposed as the best way to model quasi-periodic stellar activity induced signals. We choose to follow [97], who showed Apodized Keplerians are very successful models for stellar activity. This is the framework that `Lia` is built on as well. We employ a similar functional form to [97] for all vectors, $\mathcal{V}$, in the dictionary:

$$\mathcal{V} = \sin(\frac{2\pi t}{\omega} + \phi) \times e^{-\pi(\frac{t+T0}{\tau})} \tag{4.13}$$

The number of entries in the dictionary, M, can be computed from the previously defined grids:

$$M = \sum_{k=0}^{N_\tau} N_{\boldsymbol{\omega_k}} \times N_{T0_k} \times N_\phi \tag{4.14}$$

The dictionary is constructed in a logic that maximizes the ease and efficiency of locating a vector with particular set of parameters. This will assist us later when we wish to connect the solution set's chosen indices within the dictionary with those vectors' signal parameters. In the dictionary, all functions are ordered first by their decay lifetime, then by frequency, then by offset, and lastly by phase, see Figure 4.1 for a schematic of this design.

As the dictionary is constructed, we want to ensure that each vector going into the dictionary has a reasonable chance of being represented in the data. By pre-cleaning the dictionary of vectors that are sufficiently inactive, we can save on compute time later on. For example, imagine a data set with two seasons of dense observations separated by ∼100 days with no observations, as is typical of astronomical observations. For a relatively short decay time of 50 days, there exist a few T0 offsets that bring the wave packet entirely or nearly entirely into the gap between seasons. Thus, the apodized sinusoid function evaluated at the timestamps of the data is essentially a flat line equivalent to y = 0. This vector provides nearly no information in a potential solution set and so we wish to remove it from consideration to save computational time with the solver. We achieve this by computing the norm of each vector and if it is sufficiently small (in practice less than 1), then this vector is completely zeroed out. In the case where a wave packet truly falls entirely in a data gap, the vector will have been completely zeroed out anyway, so this extra check is primarily designed to remove vectors where the wave packet only exists in few timestamps at the edge of a data gap or in a region of time where few observations are recorded and there is no reasonable expectation

of recovering a decaying signal due to lack of sampling, even if one does exist in truth. The norms of all vectors are stored for later use in the post-processing steps, in order to better estimate the amplitudes of vectors that comprise the solution set.

Lastly, to complete its construction, the dictionary is dotted with the covariance noise matrix, $\mathbf{V}$, then all columns are centered, and then normalized by dividing each vector by the sum of its ℓ_2 norm.

4.2.3 Noise Model

While we are interested in recovering real, quasi-periodic signals associated with stellar activity, there will still always be an underlying noise to the velocities, for example, instrumental noise and photon noise. To best model this noise, we construct a covariance matrix, $\mathbf{V}$, for all observations in the time series.

We assume this noise is Gaussian and that each instrument will have its own white noise value. Constructing the covariance matrix follows [100] and [17], where the diagonals of the matrix are equal to the white noise term for that observation's instrument squared, and off-diagonals are all zero.

In order to best choose the white noise term for each instrument, we run a cross-validation analysis. The `Lia` algorithm is computed for a variety of covariance matrices, each differing only in the value of their white noise term. To effectively sample, we construct a grid of white noise values and test each. Then, following [99], the cross validation score is computed. The white noise value with the smallest likelihood is selected as the best value and `Lia` is run in full.

This approaches an interesting question on its own. What does it mean to create a sparse representation of something, in this case white noise, that is inherently not sparse? If we

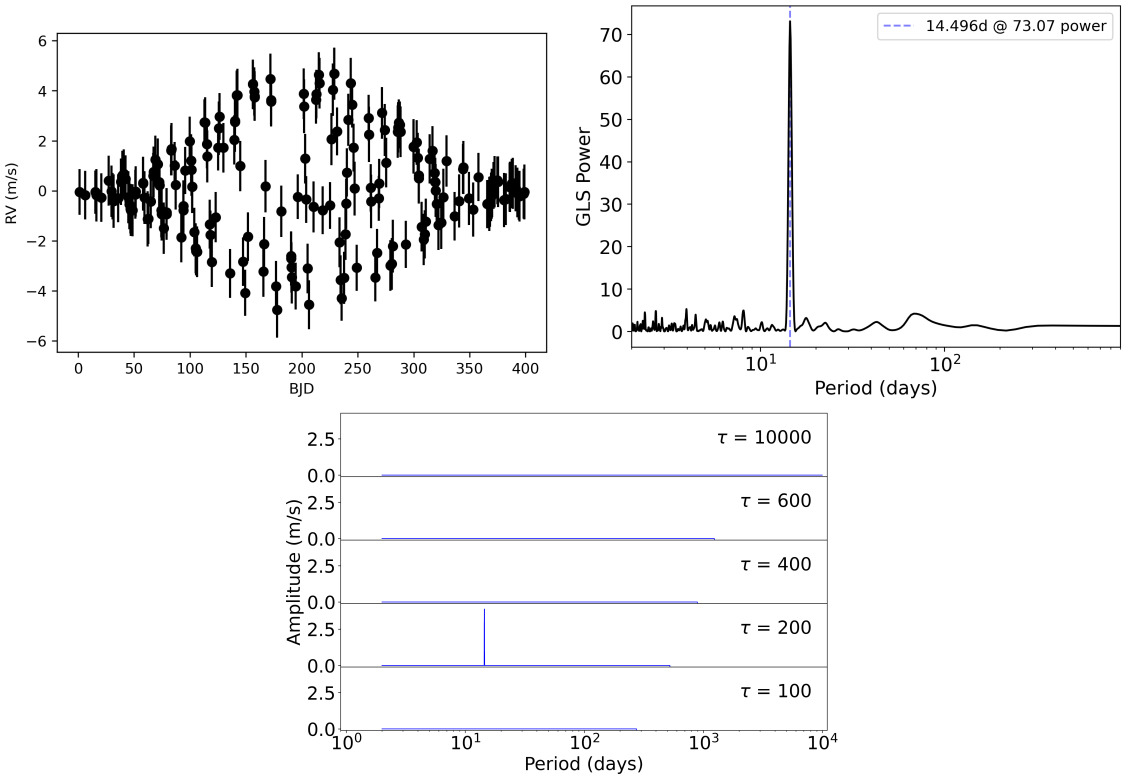

Figure 4.2: **Top**: A simple synthetic data set consisting of a single decaying signal, well-sampled across the baseline and without added noise. **Middle**: The GLSP for the above data set. It identifies as strong periodicity at the true period, but says nothing of its decaying nature. **Bottom**: `Lia` output on the same data. The red region indicates the *a priori* expected solution. The periodicity is recovered and also identified to be decaying. In one quick-look, `Lia` provides a more holistic picture of the signal in question.

were not to enforce sparsity, then we would expect `Lia` to always include a forest of peaks at high frequency with the shortest decay time allowed. This is a result of trying to fit noise as if it has a true functional form. However, we leverage this idea with the cross-validation analysis as a way to better understand the noise in our data set. Through cross-validation, as the white noise term is tuned up through trial and error to minimize the likelihood, peaks associated with noise will fall in height as larger white noise terms in the covariance matrix suppress these spurious peaks.

4.2.4 Post Processing

After the LARS algorithm returns the set of coefficients, we must process and clean it into a state where it can be meaningfully displayed. The primary output plot of `Lia` displays 1D slices of amplitude vs period stacked atop one another to create the second dimension of decay lifetime. To properly display this, for all vectors in the dictionary, we group by pair of period and decay lifetime. Then all vectors which have different T0 offsets and phases, fall within a group and all coefficients associated with these vectors are summed to create a single amplitude value for each period/decay lifetime pair. Note that it is a choice to group by period/decay lifetime. We could instead reformulate this sum and group any two parameters (period and T0 offset, decay and T0 offset, etc), but the most information is gained from period/decay lifetime groupings. This summation is then plotted as the amplitude, in m/s, as seen on the primary output plot, see Figure 4.2. This process may have the unintended consequence of inflating the amplitude of a signal that appears at multiple, distinct offsets, as would be the case the scenario where the same signal lives and fades in the beginning of the data set but then returns again later in the data set. Information about all the exact functions selected by the solver, including offset time and phase, are still saved and outputted separately from the plot.

4.3 Application

We demonstrate the application of `Lia` in four stages. First, we demonstrate basic level injection/recovery of a single quasi-periodic signal through simulated data where signal parameters are known *a priori*. Second, we show `Lia`'s analysis of the solar RV data sets from HARPS-N. Lastly, we apply the algorithm to an archival Keck/HIRES data set of RVs of HD 26965.

4.3.1 Simulated Data

The easiest way to demonstrate the basic ability of any new software is to test it on data where we know the solution. In this spirit, we designed multiple tests using synthetic data sets. Figure 4.2 shows the most basic demonstration of `Lia`'s abilities. Generating a simple decaying signal over a well-sampled time series, we see that `Lia` easily and clearly recovers the periodicity *and* identifies the decaying nature. Meanwhile, a traditional GLSP also recovers the periodicity, but without further information about the signal's lifetime, which can lead to misinterpretation of the signal's astrophysical origin.

Next, we scale this test up and generate 1000 synthetic data sets. For each, we create a time series where 200 timestamps uniformly sample the entire 400 day baseline at nearly one observation every two days (a small jitter in time, <0.1 days, was added to each timestamp to ensure that simulated observations were not taken in uniform spacing). We then inject an apodized sinusoidal signal where the five parameters of period, decay lifetime, T0 offset, phase, and amplitude are each randomly drawn from a distribution, given in Table 4.1. For each data set, we add noise to each observation drawn from $\mathcal{G}(0, 1)$ which means we assign a standard 1 m/s error bar. We generate 1000 of these synthetic data sets and run each through `Lia`. Each run has the same parameters (including a 1 m/s white noise component in the covariance matrix) and grid settings.

After completing the test, for each trial we take all of the recovered signals and assign a score to each one. The score, S, for each signal is determined according to a bitwise-style mask:

$$S = (A \cdot 2^3) + (B \cdot 2^2) + (C \cdot 2^1) + (D \cdot 2^0) \tag{4.15}$$

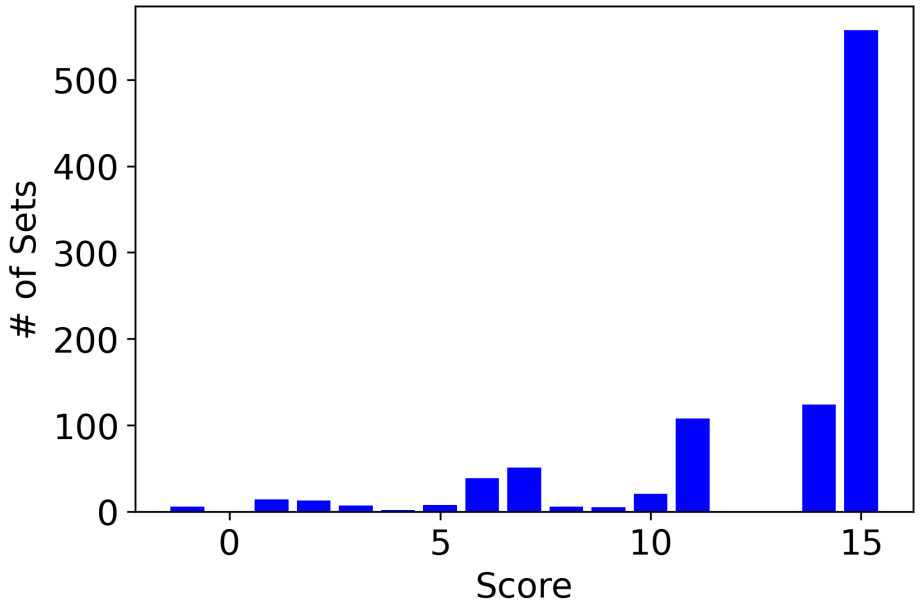

Figure 4.3: A histogram of the scoring for 1000 data sets of random signals generated from distributions in Table 4.1. Scores above 12 indicate both period and decay lifetime as well as one additional parameter are correctly recovered. Such a score deems a trial successful and there are 682 such successful trials. Additionally, there are 151 trials that scored below 10, of which for 6 trials no signals were recovered at all.

where

- A = 1 if solution period is within 10% of the true value, 0 otherwise. This accounts for the fact that longer periods are more sparsely sampled in the grids than shorter periods.
- B = 1 if solution τ is in the closest τ bin to true value, 0 otherwise. Close is defined as the element of the decay grid which minimizes of the difference between the true τ and the element within the decay grid, as compared to all other elements within the decay grid
- C = 1 if solution T0 is within 2 T0 grid steps from true value, 0 otherwise
- D = 1 if solution phase is equal to true value, 0 otherwise

In this system, a perfect score is S = 16, and all scores have a unique sum which can be directly traced back to which parameters are recovered correctly or not. This system also weights the parameters in order of importance, with period, decay, and T0 taking precedent in that order over phase. Amplitude is an important metric which is recoverable by `Lia`, but ℓ_1 minimization methods are known to under-predict true amplitudes [100] and therefore we have chosen to exclude it from this scoring scheme. We then take the best scoring signal for a trial and assign its score to the be the score of the trial. We accept successful trials as scores of greater than 12, which in effect requires period and decay lifetime to be correct, as well as one additional parameter. In this logic, 682 of 1000 runs are successful. All this said, in the bigger picture it is not vitally important that `Lia` recover the exact correct parameters as much as it is important that `Lia` helps prevent us from mislabelling time-localized signals as planetary and robust signals as activity.

Figure 4.4 shows the results along three axes of recovery (period, decay lifetime, T0 offset), comparing injected and recovered solutions against a one-to-one line. We confirm in panel a) the strong recovery of the injected periodicity, as would be expected for any functional periodogram. In our test, any trial that did not recover any solution signal (43 trials) returned a solution period equal to zero by default.

Next, in the decay lifetime, Figure 4.4 panel b), we see very good agreement with expectations. Because we cannot sample decay lifetimes in anywhere near as fine a grid as frequencies, a given injected τ will rarely be equal to any of the allowed τ's in the decay lifetime grid. Therefore, it is common, and expected, for `Lia` to recover a decay lifetime close to the injected value. Close is a relative term, and sometimes the recovered value is not necessarily the closest grid value, as is seen in the one-to-one plot. We still deem this a success because `Lia` is still recognizing the decaying nature of the signal in question with high confidence. As for the period parameter, when no signal is recovered in a trial, the solution τ is set to zero by default.

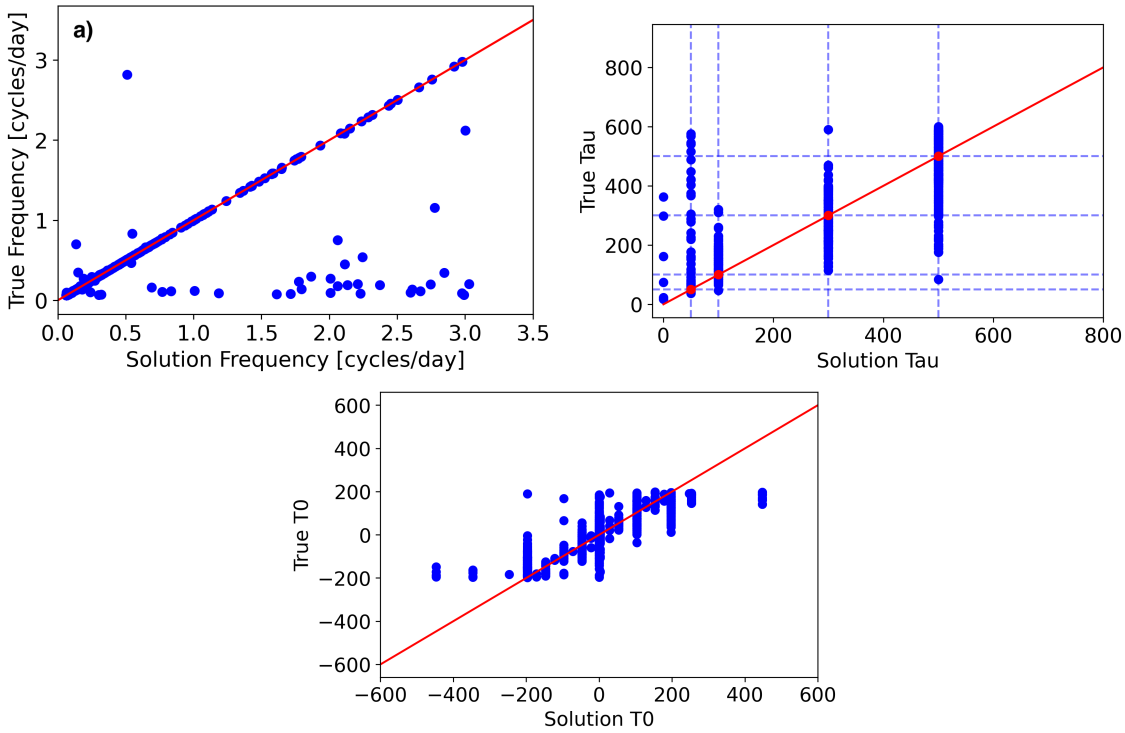

Figure 4.4: Injection/Recovery results for 1000 trial data sets with randomized signal parameters as drawn from distributions in Table 4.1. One to One lines are shown for frequency (Top), decay lifetime (Middle), and T0 offset (Bottom).

Finally, we see in panel c) of Figure 4.4 that T0 offsets are also being recovered well. The T0 grids are a medium level of sparseness, in between the levels of the frequency and decay lifetime grids. Therefore we see a one-to-one trend but with pockets where the same T0 offset is recovered for many different injected values. Primarily, this is a result of the grid construction logic. For long decay lifetime signals, very few T0 offsets are allowed, as few as three (left and right edges, and middle of time series). Therefore, we see a large pileup in recovered T0 offsets at the zero value, because the middle of the time series is often the best fit of these three options for long decay signals.

Next we perform the same experiment again, but with more realistic time series sampling. We curate a list of stars with archival RV data sets containing at least 100 observations in an observing baseline of between 365 and 2000 days. In total, twelve stars were selected for meeting these criteria as well as visual inspection for a representative sampling of RVs

across the baseline. We collect these archival data sets entirely from the published HARPS archive [230], see Table 4.2 for the list as well as a few simple statistics about each data set. Some of these targets have additional observations from other instruments but those were not included. For this test, 1000 times we randomly choose one of the twelve sample data sets, taking the timestamps and the true error bar values for each timestamp. We apply a 2 sigma clip on error to remove outlier timestamps. We then re-center the timestamps around MBJD = 0, and we inject a signal using the same distributions in Table 4.1 (except now T0 offset is uniform across the baseline of the selected time-series), and add noise to the velocities from $\mathcal{G}(0, 1)$. We then run `Lia` on each set with the same parameters, grid settings, and scoring criteria as before. We see that only 375 of 1000 are successful. Many more are nearly successful, off by slightly beyond the period recovery restriction or with decay lifetime recovered in the wrong rung of the grid. This rate is understandably lower because of the nature of these timeseries. True astronomical observations are never sampled ideally. When it comes to time-localized signals, if the density of observations within the signal wave packet is not sufficient, then `Lia` will not be able to recover those signals. Similarly, less dense data within a wave packet will lead to greater uncertainty in the true values of the signal parameters, meaning many signals will score below the accepted value for success, but still provide useful information. See §4.4.2 for a more in-depth discussion.

4.3.2 Solar Data

Next we demonstrate the power of `Lia` on a real and well-studied data set where we know the true variability structure with high confidence: our Sun. The HARPS-N team provided a large, public data set of disk-integrated solar RVs [71, 70]. This data set has been the subject of multiple studies (see below for the relevant findings from each) and furthermore our Sun is well understood in terms of its rotation period and activity cycles.

In [52], the authors report strong periodicities at both the rotation period and its first harmonic in both their RV reduction time series and in their Bisection Inverse Slope (BIS) time series. But they find no correlation between these two data sets. Additionally, in the RVs there is a small peak near 150 days and in the BIS there is a long period signal centered around 500 days.

In [155], the authors find that the HARPS-N Solar RVs do not correlate with activity measurements from the Solar $\log R'_{HK}$ measurements, the Solar Dynamics Observatory's (SDO) Helioseismic and Magnetic Imager (HMI) filling factors, or the Solar Radiation and Climate Experiment Total Irradiance Monitor's (SORCE/TIM) total solar irradiance (TSI) factor, which all correlate with each other. They state that at timescales shorter than the rotation period, we expect RVs to be "modulated to some degree by magnetic region growth and decay", but that while their more sophisticated model is not designed to capture this information, they find both the rotation period and its first harmonic as strong signals in a periodogram. They further note an unaccounted 1 m/s variation remains after their reconstructed RVs are subtracted.

In [144], the authors perform extensive periodogram analyses on a variety of activity indicators. They find each indicator provides a slightly different rotation period estimate, ranging from 26.3 to 31.2 days. They also find, through a Pooled Variance technique, evidence for a 300 day, or 10 rotation periods, lifetime for the typical plage and faculae complex. They also perform a sliding periodogram analysis and recover the rotation period strongly in all windows, and the first harmonic occasionally in a temporally localized window.

In [154], the authors perform a line-by-line RV extraction using a custom line list. They primarily use lines that exhibit a non-linear relationship of convective blueshift with line depth, known as third signature lines. Later, they run a GLSP on their reduced timeseries and find strong signals at both the rotation period and its first harmonic, which they state is "consistent with some significant RV_{conv} contribution", where RV_{conv} is convective blueshift

due to photospheric plage.

In [227], the authors construct relative spectra of the HARPS-N Solar spectra by dividing high activity spectra by low activity spectra. This reveals "pseudo-emission" features that trace activity. When investigating how these pseudo-emission features behave when a specific, large spot/plage traverses the solar disc, they find a positive slant. This indicates a move from blueshift to redshift over the course of a half rotation of the sun. They find strong periodicities at this harmonic when associated with specific solar events, otherwise they find strong periodicity at the full rotation period.

Finally, in [**?**], the authors construct a new framework to test if a RV signal is strictly periodic. Their technique makes use of MCMC simulations and the computation of relative likelihoods. They analyze the HARPS-N solar RVs, finding the dominant signal is at the first harmonic of the rotation period, at 13.39 days. Furthermore, they find this signal to be strictly periodic, although with amplitude variations. Additionally, they find signals at the rotation period of 26 days, a signal at 160 days, and another very long period signal. On top of this, they find that a phase offset between the RVs and the log R'_{HK} measurements.

Running `Lia` with the same curated data set of HARPS-N solar RVs from [70], we choose to adopt the same decay lifetime grid as used in [**?**] for this data set. We recover many of the same signals as seen in other works, but in much shorter time and less computation power. Figure 4.5 shows the results, which ran in 140 seconds on a standard laptop. Primarily, we recover the rotation period and first harmonic signals that so many other studies report. We find that the rotation period signal decays between 120 and 360 days, corresponding to between 4 and 12 full rotations. We also find that the first harmonic signal is both consistent throughout the time series, as reported by many studies, but also we find a decaying component at a lifetime of 120 days, as also found by [**?**]. `Lia` also recovers the same 160 day signal that has been widely reported, we find it decays over a 360 day lifetime. We also find a long period signal, between 400 and 600 days that is split across the strictly

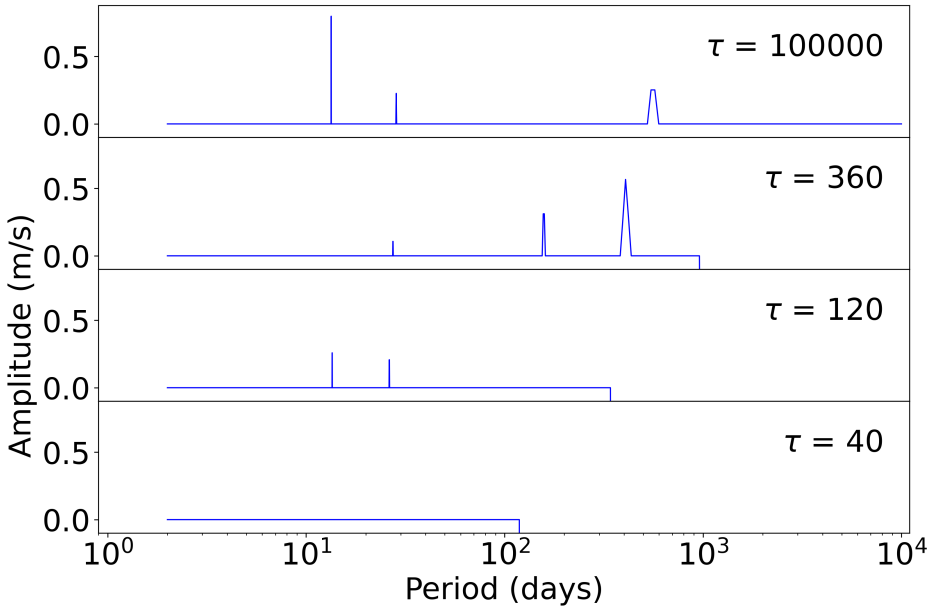

Figure 4.5: The results of running `Lia` on the HARPS-N Solar RV data set from [70]. We recover similar signals as prior analyses.

periodic and the 360 day lifetime grids. See Table 4.3 for a full list of the recovered signal parameters.

Overall, the performance of `Lia` on this seminal data set is very encouraging. It is recovering the same signals as seen in previous studies of this unique and valuable data set, but it is finding these same results in a much quicker and easier way. For this data set, `Lia` runs in ∼1 minute on a laptop. In line with other studies, `Lia` finds that the signals associated with the rotation period, ∼27 days and ∼13 days, are found in both decaying and non-decaying bins. We interpret this to mean that the rotation period signal for the Sun in this time frame was consistent but additionally there were times where the signal grew stronger than and then decayed back down to its average value.

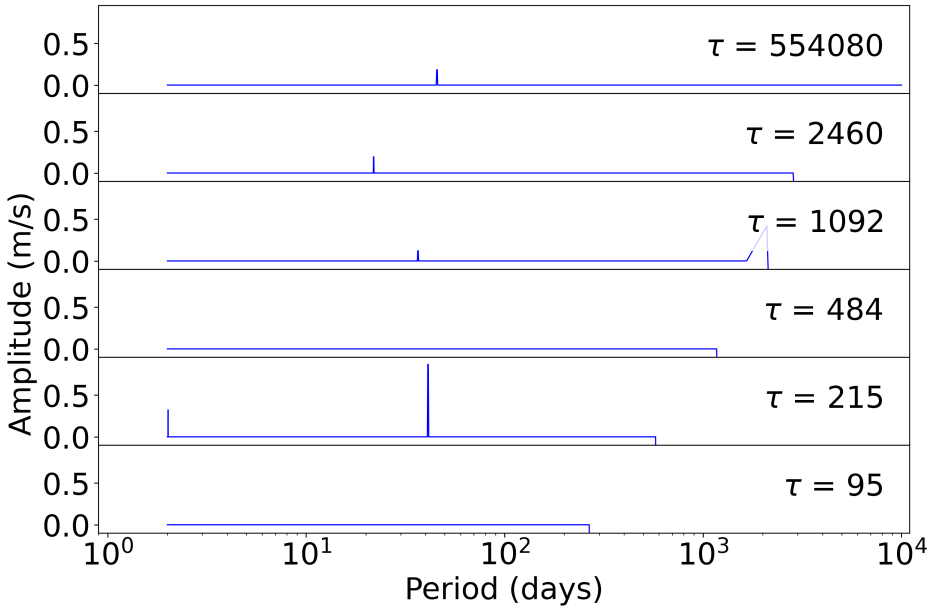

Figure 4.6: Applying `Lia` to the HIRES data set for HD 26965.

4.3.3 Example Stellar Data

Finally, we demonstrate the power of `Lia` on a real stellar data set. We looked for a system that was well studied by the community and has a signal in the RV timeseries that has a disputed origin. We choose to apply `Lia` to the HD 26965 system.

HD 26965 (40 Eridani A) is a K dwarf that has long been observed by RV surveys due to its brightness at V=4.4. A super-Earth planet was first announced in the system in [65] where they report a candidate signal at 42.36 days using a combined data set from HIRES, HARPS, CHIRON, and PFS. The authors note that the periodicity is uncomfortably close to a measurement of the rotation period. That same year, [139] also report a signal at 42.38 days using the same data set plus the addition of RVs from TOU. They similarly conclude the signal to be most likely planetary in origin despite the similarity to the stellar rotation period.

Then, [199] found the 42d signal to be most likely originating from stellar activity. In the community data challenge summarized in [258], the results from the many participants vary

and therefore the planetary designation varies. It is worth noting here again that the authors of [258] describe how 5 of the 6 lowest RMS results, the primary metric of comparison, find the 42d signal to be activity related. Finally, in [124], the authors further conclude that the 42d signal originates from stellar activity.

Running `Lia` with standard parameters and a hand-chosen decay lifetime grid, we recover the main signals in question. Primarily of interest, we see a 45.79d signal recovered in the longest decay lifetime grid. This is a noticeably different period than previously reported by the planet candidate papers (¿20 frequency grid steps away) but within the window of the known rotation period (38-45d) from earlier analyses. Also worth noting, the amplitude of this signal is small at 24 cm/s. `Lia` is undoubtedly under-reporting the amplitude due to well understood underestimation of the ℓ_1 minimization technique, but ratios of amplitudes are still important. Then another similar signal, found at 41.27 days and decaying over 180 days ($\sim$4 cycles of the period), with an amplitude ¿3x at 86 cm/s is noted. This signal is well consistent with the rotation period, and its decay lifetime is consistent with a spot dominated signal that lives and decays away over a timescale that is expected for this stellar type. Next there is a $\sim$3000d periodicity which decays over 1100 days. This is consistent with the 10 year magnetic cycle also found by earlier analyses. This analysis favors the interpretation of the RV signal as originating from stellar activity.

4.4 Discussion

4.4.1 Use Cases

`Lia` is best used as a quick-look tool in the same way that any other periodogram is a quick-look tool. It gives a completely new look on the data which can be helpful to diagnose unanticipated effects. The difference between `Lia` and other periodograms is the added

information it provides in that first look. By characterizing all signals in the data further than just a periodicity, `Lia` can provide a new perspective to a data set.

Despite providing a holistic picture in a quick-look tool, `Lia` is not designed to be the only tool applied to the data. `Lia` does not replace more complex analyses, like a Gaussian Process (GP) with MCMC sampling, for example. Rather, `Lia` compliments these tools by providing a more informed look at the underlying data set and its noise structure. With a better understanding of the data, one can set better priors and more complex tools can search more detailed parameter spaces and/or eliminate other spaces to hasten runtime.

4.4.2 Limitations

`Lia` does have limitations. Two most notable limits are worth mentioning.

First, the algorithm's run time is very sensitive to the baseline of observations. By far, the largest contributor to the size of the dictionary is T_{base}. The longer the baseline of observations, the more offsets go into each T0 grid, which is in turn applied to each $\omega \in \boldsymbol{\omega_k}$ within each $\tau \in \boldsymbol{\tau}$. Depending on the desired $\boldsymbol{\tau}$ for a given T_{base}, total dictionary sizes can exceed multiple millions of entries, which severely slows down the algorithm from seconds to minutes or even hours. It is recommended that in practice, total dictionary size be kept under 3 million entries. Trimming down long dictionaries can be accomplished in multiple ways:

- Eliminate small decay lifetimes from $\boldsymbol{\tau}$. The dictionary is naturally bottom heavy in that smaller τ are assigned disproportionally more T0 offsets at every tested frequency than larger τ.
- Split the data set into smaller time spans to be run independently. This is generally ok in that we do not expect spot/plage/faculae-driven stellar activity signals to persist

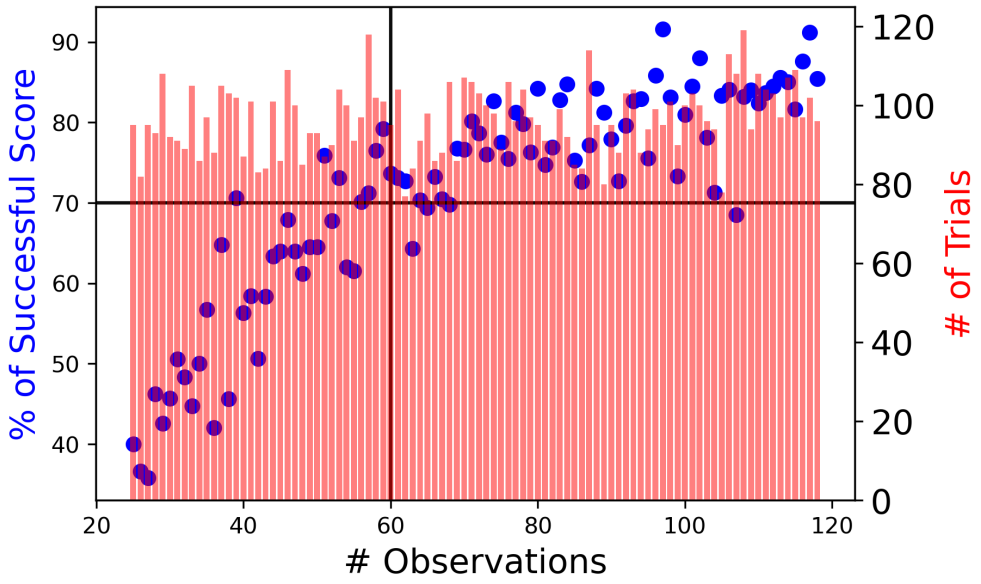

Figure 4.7: The successful (score > 12) recovery rate as a function of the number of observations in the fixed baseline, a proxy for density of observations (blue). A histogram of how many trials occurred with each number of observations is over-plotted in red. A minimum sampling of 60 observations in 400 days (black vertical line) is needed to achieve the standard 70% successful recovery (black horizontal line) as set by the simulated data trial of idealized data sets.

longer than ~ 1000 days (as was the seen in the extreme case of Barnard's star, see §3), and robust sinusoids should be recoverable in all bins, assuming similar data quality and quantity.

- Increase the density factor, d, that determines $\Delta T0$. This will create a sparser $\boldsymbol{T0}$ grid for each $\boldsymbol{\omega}$ in each $\boldsymbol{\tau}$ grid.

- Decrease N_ϕ. For example, decreasing from 4 to 2 will halve the dictionary size without much loss in the solution.

- Decrease the oversampling factor for frequency, N_ω, for a sparser frequency grid.

The second limitation of `Lia` is data driven. When the number of observations within a given wave packet is not sufficiently dense, the algorithm has trouble recovering the signal. This is a unique problem to `Lia` that other periodograms do not share because when searching

for robust sinusoids, the signal is sampled in every observation. But with decaying wave packets, many observations do not sample the signal at all. Therefore, a minimum density of observations that do sample the wave packet are required in order to distinguish the signal from noise. While recovering a signal of any kind depends on many factors such as cadence, SNR, sampling coverage, etc, we attempt to quantify the limit of `Lia`'s ability with a simple test. We generate 10,000 data sets where the number of observations is randomly chosen from $\mathcal{U}(20, 120)$ and those observations are randomly sampled across a 400 day baseline. We then inject each timeseries with the same signal: a 21.5 day period that decays over 200 days with an offset 0 days from the center of the baseline, a phase of 0 degrees, and an amplitude of 2 m/s. We also add white noise drawn from $\mathcal{G}(0, 1)$ to each observation. This test simulates different sampling densities of the same signal and demonstrates a lower limit in how often we should expect successful recovery for a decaying signal. The results can be seen in Figure 4.7.

In this test, to achieve a 70% success rate (black horizontal line), on par with results from our earlier test on uniformly sampled signals, for a 200 day decaying signal, the density of observations must exceed 60 observations in the 400 day baseline (black vertical line). Therefore, the minimum sampling is $\frac{60}{400} = 0.15$ observations per day, or $\sim$1 observation per week, consistently throughout the baseline. Repeating this test for the same signal parameters except halving the decay lifetime to 100 days, reveals a similar pattern. However, the minimum sampling to achieve a 70% success rate is now higher, at $\sim$110 observations. This equates to a cadence of about two observations per week.

4.5 Conclusion

We introduce and describe `Lia`, a new, first-look tool for identifying and characterizing decaying signals in RV data sets.

In the emerging EPRV era, understanding the origin of signals in our data sets will be crucial in the search for smaller and longer period planets. To do so, we must be able to identify and characterized true signals originating from activity in our data sets. `Lia` will assist us in this endeavor and help us better understand stellar activity cycles.

`Lia` provides a new way to look at RV time series data by estimating more than just the periodicity of a signal in question. Through an ℓ_1 minimization technique and a flexible dictionary, `Lia` can estimate a signal's period, decay lifetime, offset in time, phase, and amplitude. This holistic picture of a signal provides a more robust insight into the astrophysical origin of the signal.

`Lia` is designed to be a first-look tool. It is easy to run, requiring as little input as the time series itself, but it provides a wealth of insight into the data set. `Lia` bridges the gap between uninformed periodograms and over-flexible noise models, occupying a unique niche in astrophysical software space.

Table 4.1: Randomized Injection/Recovery Distributions

Parameter	**Distribution**
Period (days)	$\mathcal{U}$(2, 100)
Decay Lifetime (days)	$\mathcal{U}(1.5 \times \text{Period}, 600)$
T0 Offset (days)	$\mathcal{U}$(-200, 200)
Phase (radians)	Equal odds choosing [0, $\frac{\pi}{4}$, π, $\frac{3\pi}{4}$]
Amplitude (m/s)	$\mathcal{U}$(3,5)

Table 4.2: Sample Timestamps from Archival Sets

Star Name	**N Obs**	**Baseline (days)**	**Mean Error (m/s)**	**StDev Error (m/s)**
GJ 1132	128	745	2.07	0.94
GJ 3341	137	1456	2.17	0.96
GJ 361	101	1919	0.97	0.20
GJ 688	102	1675	0.67	0.90
GJ 436	169	1532	1.13	0.39
GJ 279	195	1949	0.76	0.13
K2-32	115	363	3.22	1.44
HD 38677	148	763	0.70	0.17
BD-156276	153	389	1.86	1.20
HD 43834B	219	1308	0.38	0.21
GJ 205	102	1400	0.54	0.29
GJ 3053	208	780	4.37	0.57

All data used was sourced from the [230] reduction of public HARPS RVs. We take only the timestamps and error bars for the observations. For any target where data from additional instruments and/or where newer HARPS data exist, those data were not included.

Table 4.3: Signals Recovered in HARPS-N Solar RVs

Decay Lifetime (days)	**Period (days)**	**T0 Offset (days)**	**Phase (radians)**	**Amplitude (m/s)**
10000	571.65	0	$\pi/2$	0.25
10000	28.53	0	$\pi/2$	0.09
10000	28.47	0	$\pi/2$	0.13
10000	13.39	0	$\pi/2$	0.80
360	420.58	-186	0	0.30
360	407.13	-186	0	0.27
360	158.61	534	0	0.31
360	27.42	714	0	0.11
120	26.29	-246	$\pi/2$	0.21
120	13.54	-246	0	0.26

Chapter 5

Conclusion

The beginning of the EPRV era has brought with it new, exciting discoveries and increased challenges when it comes to exoplanet detection. We currently stand on the cusp of two new eras in exoplanet science.

First is the pipeline to advanced and detailed characterization of planetary systems. When it comes to formation, evolution, and habitability of planetary systems, so many scientific questions are laid out in front of us. But for the first time, it seems like all the tools needed to set out for meaningful answers are available to us. TESS is delivering the targets for EPRV instruments to measure masses for JWST to characterize atmospheres. This pipeline will build up the collection of stamps required to reveal fundamental truths about planet atmospheres and how they form and evolve. Furthermore, the pipeline initiated by TESS will continue to grow into the future as the next generation of Great Observatories, with goals of directly imaging Earth-like planets, takes flight. The target lists for these missions will be set ahead of time, by the discoveries and successful characterizations of today.

A prime example of this pipeline in action is the HD 191939 system which I describe in §2. As a bright star hosting a mini solar system with a wide variety of planet diversity, HD 191939

will be a touchstone system for a long time to come. The detailed characterization that we perform sets this target up for further atmospheric studies and beyond. At play are multiple case studies probing formation, evolution, and dynamics. The system's long-period super-Jupiter is massive enough to be on the border of formation mechanisms. If found to have formed through gravitational instability, unlike the inner planets which mostly likely formed through core accretion, that would mean two formation mechanisms were at play in the same system, something not yet explored at large. Next, because the interior sub-Neptunes in this system have a variety of planet densities, there is a unique chance to perform the first intra-system atmospheric study which can constrain two planetary evolutions within the same formation environment. Finally, the interior sub-Neptunes (and possible additional planets) are shepherded by a warm Jovian, providing an interesting window in system dynamics. The HD 191939 system will continue to be studied by many researchers whose scientific interests will span many sub-fields, as this system has something for everyone. Until now, out of instrumentation and target limits, the field has so long focused on characterization of whole systems against one another. But I believe HD 191939 will set the standard for future efforts to characterize all planets within the same system and explore the relationships between them all. This will open a new era of exoplanetary and bring us closer to studying exoplanet systems in the same way we study our own Solar System.

Second comes the heart of my graduate research work. The one sentence summary of this dissertation is as follows. Quasi-periodic signals are real signals; with sophisticated analysis techniques, we can distinguish them from strictly periodic signals in RV data. This statement comes after many years of studying stellar activity in RV data sets and through the lessons learned in the projects described in §3 and §4.

The exploration of stellar activity of Barnard's star opened my interest in trying to quantify quasi-periodic signals in RV data sets. In this work, we show how the 233-day signal attributed to a planet is instead a one year alias of the 145-day stellar rotation period. In

particular, we were able to show how the planetary signal in question was localized in time to within a 1000-day window of observations in the middle of the baseline. This kind of behavior is not consistent with a planet but is consistent with spot-driven, decaying stellar activity. We showed this localization of the signal through a series of tests, each building off of the last, and building towards new ideas in how to identify time-restricted signals.

My work concerning Barnard's star as a test subject to identify localized signals began by breaking down the time series into different chunks of time. Planetary signals should be robust across all time chunks (assuming similar cadence, instrument precision, etc), but stellar activity signals should be transient. Therefore, we split the time series into roughly equal thirds (in terms of number of RVs in each third). In this view, we demonstrated how the planet signal is strong in the middle third, and essentially absent from the last third, despite the last third having higher cadence and better precision RVs. This was the first hint at the transient nature of this signal. Next, in this same format, we showed how in the middle third, the Ca H&K S-value time-series peaks at the same 233-day periodicity. Given that the S-values trace the chromospheric heating which in turn tracks the rotation period, this was the smoking gun that showed how the sampling contributed to generating an alias. That same alias then appearing in the RVs and in the same time window, led us to conclude the planet was a false positive. Ultimately, we used this simple test as a foundation for developing more sophisticated tests for identifying the locality of a signal. We constructed an algorithm, which we call Rolling Omission, to identify the exact RVs which contribute the most to the proposed planet signal. This test isolates the locality of the quasi-periodic signal at the most granular level. The lessons learned through these tests got me thinking more about ways to find and recognize quasi-periodic signals in RV data sets.

In §4, I describe a new software package, `Lia`, that I developed based off the ideas first conceived in my work on Barnard's star. The work in §3 was wholly bespoke to the system at hand. It was arduous work, requiring many weeks of trials and tests in attempt to reveal

the hidden signals in the data set. Through this work, I thought there should be a way to make this kind of work more homogeneous and applicable across any time series. This idea was the inception of `Lia`, which was designed to provide new insights into the signals in a time series by quantifying each signal's decay lifetime. Run by the user in the same way as a traditional periodogram, `Lia` uses an ℓ_1 minimization framework to model the quasi-periodic signals of stellar activity as apodized sinusoids. Signals with decay times longer than the baseline of observations are most likely to be planetary in origin and those with shorter decay lifetimes are more likely to be stellar activity in origin. Through identifying and characterizing decaying signals alongside strictly periodic signals quickly and easily, `Lia` will help disentangle activity and planets in RV data sets, paving the way for more confident detections and fewer false positives.

The problem of stellar activity is far from solved. I see the current and future efforts to understand stellar activity as split into two categories: understanding signals in RV data sets better, and learning to calculate activity-free RVs. I believe both will be vital in working towards solving this problem as best as we can. Advancing the first effort was largely the topic of this dissertation. This work relies on understanding our data better and finding novel software and analysis techniques to get the very most out of the data we currently have and currently produce. In this regard, certain data sets are more valuable than others, namely, ones where we believe we understand the stellar activity of the system well. These systems act as rulers and guides to testing new methods. `Lia` is a large benefactor of these data sets. In particular, perhaps the most valuable, is the growing solar RV data sets of the newest EPRV instruments. The Sun will be one of our greatest tools for studying and understanding stellar activity. The Sun's cycles and timescales are generally well understood, and we have the added benefit of observing from many facilities with many unique instruments. For this reason, all upcoming and seemingly any future RV dedicated facility has or will have a solar feed to produce solar RVs each day. When we are able to analyze the Sun-as-a-Star RV data sets and confidently remove stellar activity signals, then we will be ready to apply techniques

wholesale to stellar data sets, in the same way I have demonstrated with `Lia`.

And then there is the effort to produce better RVs themselves, ideally RVs without the contamination from stellar activity in the first place. This effort is predicated on the fundamental idea of computing an RV: that gravitationally induced Doppler shifts should move all the absorption features equally and linearly. Meanwhile, activity should only change the shape of individual absorption lines, and change each line differently. This is the basis for Line-by-Line and "shape vs. shift" studies. In this regard, the newer spectrographs with higher resolving powers mounted on larger mirrors to gather exceptionally high SNR will be the prime data sets. Leading these efforts will be KPF once it is commissioned as well as the upcoming iLocator instrument [55]. These efforts go hand in hand with the efforts above as minimizing activity contamination will only enhance and complement the abilities of our software.

Only when we understand the physics of stellar activity better, along with the ways in which we analyze stellar activity from a software perspective will we be able to get the most out of our RV data sets. Through identifying, characterizing, and removing stellar activity, we will not only discover new populations of smaller and longer period planets, but also measure masses of all planets, especially small ones, ever more precisely to set up detailed intra-system characterizations. In all, I plan to continue my research on both of these paths. I will set out towards finding new and exciting systems that can be detailed through continued follow up. I will continue to work towards more ways to disentangle stellar activity from planetary signals. And I will continue to work in wonder of the Universe and the many wonderful worlds out there.

Bibliography

[1] *The HIPPARCOS and TYCHO catalogues. Astrometric and photometric star catalogues derived from the ESA HIPPARCOS Space Astrometry Mission*, volume 1200 of *ESA Special Publication*, Jan. 1997.

[2] *The HIPPARCOS and TYCHO catalogues. Astrometric and photometric star catalogues derived from the ESA HIPPARCOS Space Astrometry Mission*, volume 1200 of *ESA Special Publication*, Jan. 1997.

[3] E. Agol, J. Steffen, R. Sari, and W. Clarkson. On detecting terrestrial planets with timing of giant planet transits. *Monthly Notices of the Royal Astronomical Society*, 359(2):567–579, May 2005.

[4] E.-M. Ahrer, K. B. Stevenson, M. Mansfield, S. E. Moran, J. Brande, G. Morello, C. A. Murray, N. K. Nikolov, D. J. M. Petit dit de la Roche, E. Schlawin, P. J. Wheatley, S. Zieba, N. E. Batalha, M. Damiano, J. M. Goyal, M. Lendl, J. D. Lothringer, S. Mukherjee, K. Ohno, N. M. Batalha, M. P. Battley, J. L. Bean, T. G. Beatty, B. Benneke, Z. K. Berta-Thompson, A. L. Carter, P. E. Cubillos, T. Daylan, N. Espinoza, P. Gao, N. P. Gibson, S. Gill, J. Harrington, R. Hu, L. Kreidberg, N. K. Lewis, M. R. Line, M. López-Morales, V. Parmentier, D. K. Powell, D. K. Sing, S.-M. Tsai, H. R. Wakeford, L. Welbanks, M. K. Alam, L. Alderson, N. H. Allen, D. R. Anderson, J. K. Barstow, D. Bayliss, T. J. Bell, J. Blecic, E. M. Bryant, M. R. Burleigh, L. Carone, S. L. Casewell, Q. Changeat, K. L. Chubb, I. J. M. Crossfield, N. Crouzet, L. Decin, J.-M. Désert, A. D. Feinstein, L. Flagg, J. J. Fortney, J. E. Gizis, K. Heng, N. Iro, E. M. R. Kempton, S. Kendrew, J. Kirk, H. A. Knutson, T. D. Komacek, P.-O. Lagage, J. Leconte, J. Lustig-Yaeger, R. J. MacDonald, L. Mancini, E. M. May, N. J. Mayne, Y. Miguel, T. Mikal-Evans, K. Molaverdikhani, E. Palle, C. Piaulet, B. V. Rackham, S. Redfield, L. K. Rogers, P.-A. Roy, Z. Rustamkulov, E. L. Shkolnik, K. S. Sotzen, J. Taylor, P. Tremblin, G. S. Tucker, J. D. Turner, M. de Val-Borro, O. Venot, and X. Zhang. Early Release Science of the exoplanet WASP-39b with JWST NIRCam. *Nature*, 614(7949):653–658, Feb. 2023.

[5] S. Aigrain, F. Pont, and S. Zucker. A simple method to estimate radial velocity variations due to stellar activity using photometry. *Monthly Notices of the Royal Astronomical Society*, 419(4):3147–3158, Feb. 2012.

[6] H. Akaike. A new look at the statistical model identification. *IEEE Transactions on Automatic Control*, 19(6):716–723, 1974.

[7] R. Akeson, L. Armus, E. Bachelet, V. Bailey, L. Bartusek, A. Bellini, D. Benford, D. Bennett, A. Bhattacharya, R. Bohlin, M. Boyer, V. Bozza, G. Bryden, S. Calchi Novati, K. Carpenter, S. Casertano, A. Choi, D. Content, P. Dayal, A. Dressler, O. Doré, S. M. Fall, X. Fan, X. Fang, A. Filippenko, S. Finkelstein, R. Foley, S. Furlanetto, J. Kalirai, B. S. Gaudi, K. Gilbert, J. Girard, K. Grady, J. Greene, P. Guhathakurta, C. Heinrich, S. Hemmati, D. Hendel, C. Henderson, T. Henning, C. Hirata, S. Ho, E. Huff, A. Hutter, R. Jansen, S. Jha, S. Johnson, D. Jones, J. Kasdin, P. Kelly, R. Kirshner, A. Koekemoer, J. Kruk, N. Lewis, B. Macintosh, P. Madau, S. Malhotra, K. Mandel, E. Massara, D. Masters, J. McEnery, K. McQuinn, P. Melchior, M. Melton, B. Mennesson, M. Peeples, M. Penny, S. Perlmutter, A. Pisani, A. Plazas, R. Poleski, M. Postman, C. Ranc, B. Rauscher, A. Rest, A. Roberge, B. Robertson, S. Rodney, J. Rhoads, J. Rhodes, J. Ryan, Russell, K. Sahu, D. Sand, D. Scolnic, A. Seth, Y. Shvartzvald, K. Siellez, A. Smith, D. Spergel, K. Stassun, R. Street, L.-G. Strolger, A. Szalay, J. Trauger, M. A. Troxel, M. Turnbull, R. van der Marel, A. von der Linden, Y. Wang, D. Weinberg, B. Williams, R. Windhorst, E. Wollack, H.-Y. Wu, J. Yee, and N. Zimmerman. The Wide Field Infrared Survey Telescope: 100 Hubbles for the 2020s. *arXiv e-prints*, page arXiv:1902.05569, Feb. 2019.

[8] S. Albrecht, J. N. Winn, J. A. Johnson, A. W. Howard, G. W. Marcy, R. P. Butler, P. Arriagada, J. D. Crane, S. A. Shectman, I. B. Thompson, T. Hirano, G. Bakos, and J. D. Hartman. Obliquities of Hot Jupiter Host Stars: Evidence for Tidal Interactions and Primordial Misalignments. *The Astrophysical Journal*, 757(1):18, Sept. 2012.

[9] L. Alderson, H. R. Wakeford, M. K. Alam, N. E. Batalha, J. D. Lothringer, J. Adams Redai, S. Barat, J. Brande, M. Damiano, T. Daylan, N. Espinoza, L. Flagg, J. M. Goyal, D. Grant, R. Hu, J. Inglis, E. K. H. Lee, T. Mikal-Evans, L. Ramos-Rosado, P.-A. Roy, N. L. Wallack, N. M. Batalha, J. L. Bean, B. Benneke, Z. K. Berta-Thompson, A. L. Carter, Q. Changeat, K. D. Colón, I. J. M. Crossfield, J.-M. Désert, D. Foreman-Mackey, N. P. Gibson, L. Kreidberg, M. R. Line, M. López-Morales, K. Molaverdikhani, S. E. Moran, G. Morello, J. I. Moses, S. Mukherjee, E. Schlawin, D. K. Sing, K. B. Stevenson, J. Taylor, K. Aggarwal, E.-M. Ahrer, N. H. Allen, J. K. Barstow, T. J. Bell, J. Blecic, S. L. Casewell, K. L. Chubb, N. Crouzet, P. E. Cubillos, L. Decin, A. D. Feinstein, J. J. Fortney, J. Harrington, K. Heng, N. Iro, E. M. R. Kempton, J. Kirk, H. A. Knutson, J. Krick, J. Leconte, M. Lendl, R. J. MacDonald, L. Mancini, M. Mansfield, E. M. May, N. J. Mayne, Y. Miguel, N. K. Nikolov, K. Ohno, E. Palle, V. Parmentier, D. J. M. Petit dit de la Roche, C. Piaulet, D. Powell, B. V. Rackham, S. Redfield, L. K. Rogers, Z. Rustamkulov, X. Tan, P. Tremblin, S.-M. Tsai, J. D. Turner, M. de Val-Borro, O. Venot, L. Welbanks, P. J. Wheatley, and X. Zhang. Early Release Science of the exoplanet WASP-39b with JWST NIRSpec G395H. *Nature*, 614(7949):664–669, Feb. 2023.

[10] G. Anglada-Escudé and R. P. Butler. The HARPS-TERRA Project. I. Description of the Algorithms, Performance, and New Measurements on a Few Remarkable Stars Observed by HARPS. *The Astrophysical Journal, Supplement*, 200:15, June 2012.

[11] R. Angus, T. Morton, S. Aigrain, D. Foreman-Mackey, and V. Rajpaul. Inferring

probabilistic stellar rotation periods using Gaussian processes. *Monthly Notices of the Royal Astronomical Society*, 474(2):2094–2108, Feb. 2018.

[12] J. Arcangeli, J.-M. Désert, V. Parmentier, K. B. Stevenson, J. L. Bean, M. R. Line, L. Kreidberg, J. J. Fortney, and A. P. Showman. Climate of an ultra hot Jupiter. Spectroscopic phase curve of WASP-18b with HST/WFC3. *Astronomy and Astrophysics*, 625:A136, May 2019.

[13] É. Artigau, C. Cadieux, N. J. Cook, R. Doyon, T. Vandal, J.-F. Donati, C. Moutou, X. Delfosse, P. Fouqué, E. Martioli, F. Bouchy, J. Parsons, A. Carmona, X. Dumusque, N. Astudillo-Defru, X. Bonfils, and L. Mignon. Line-by-line Velocity Measurements: an Outlier-resistant Method for Precision Velocimetry. *The Astronomical Journal*, 164(3):84, Sept. 2022.

[14] M. Badenas-Agusti, M. N. Günther, T. Daylan, T. Mikal-Evans, A. Vanderburg, C. X. Huang, E. Matthews, B. V. Rackham, A. Bieryla, K. G. Stassun, S. R. Kane, A. Shporer, B. J. Fulton, M. L. Hill, G. Nowak, I. Ribas, E. Pallé, J. M. Jenkins, D. W. Latham, S. Seager, G. R. Ricker, R. K. Vanderspek, J. N. Winn, O. Abril-Pla, K. A. Collins, P. Guerra Serra, P. Niraula, Z. Rustamkulov, T. Barclay, I. J. M. Crossfield, S. B. Howell, D. R. Ciardi, E. J. Gonzales, J. E. Schlieder, D. A. Caldwell, M. Fausnaugh, S. McDermott, M. Paegert, J. Pepper, M. E. Rose, and J. D. Twicken. HD 191939: Three Sub-Neptunes Transiting a Sun-like Star Only 54 pc Away. *arXiv e-prints*, page arXiv:2002.03958, Feb. 2020.

[15] C. A. L. Bailer-Jones, J. Rybizki, M. Fouesneau, G. Mantelet, and R. Andrae. Estimating Distance from Parallaxes. IV. Distances to 1.33 Billion Stars in Gaia Data Release 2. *The Astronomical Journal*, 156(2):58, Aug. 2018.

[16] S. Ballard and J. A. Johnson. The Kepler Dichotomy among the M Dwarfs: Half of Systems Contain Five or More Coplanar Planets. *The Astrophysical Journal*, 816(2):66, Jan. 2016.

[17] R. V. Baluev. Orbital structure of the GJ876 extrasolar planetary system based on the latest Keck and HARPS radial velocity data. *Celestial Mechanics and Dynamical Astronomy*, 111(1-2):235–266, Oct. 2011.

[18] A. Baranne, D. Queloz, M. Mayor, G. Adrianzyk, G. Knispel, D. Kohler, D. Lacroix, J. P. Meunier, G. Rimbaud, and A. Vin. ELODIE: A spectrograph for accurate radial velocity measurements. *Astrophysics and Space Science*, 119:373–390, Oct. 1996.

[19] T. Barclay, J. F. Rowe, J. J. Lissauer, D. Huber, F. Fressin, S. B. Howell, S. T. Bryson, W. J. Chaplin, J.-M. Désert, E. D. Lopez, G. Marcy, F. Mullally, D. Ragozzine, G. Torres, E. R. Adams, E. Agol, D. Barrado, S. Basu, T. R. Bedding, L. A. Buchhave, D. Charbonneau, J. L. Christiansen, J. Christensen-Dalsgaard, D. Ciardi, W. D. Cochran, A. K. Dupree, Y. Elsworth, M. Everett, D. A. Fischer, E. B. Ford, J. J. Fortney, J. C. Geary, M. R. Haas, R. Handberg, S. Hekker, C. E. Henze, E. Horch, A. W. Howard, R. C. Hunter, H. Isaacson, J. M. Jenkins, C. Karoff, S. D. Kawaler, H. Kjeldsen, T. C. Klaus, D. W. Latham, J. Li, J. Lillo-Box, M. N. Lund, M. Lundkvist, T. S.

Metcalfe, A. Miglio, R. L. Morris, E. V. Quintana, D. Stello, J. C. Smith, M. Still, and S. E. Thompson. A sub-Mercury-sized exoplanet. *Nature*, 494(7438):452–454, Feb. 2013.

[20] E. E. Barnard. A small star with large proper-motion. *The Astronomical Journal*, 29:181–183, Sep 1916.

[21] N. E. Batalha, T. Lewis, J. J. Fortney, N. M. Batalha, E. Kempton, N. K. Lewis, and M. R. Line. The Precision of Mass Measurements Required for Robust Atmospheric Characterization of Transiting Exoplanets. *The Astrophysical Journal Letters*, 885(1):L25, Nov. 2019.

[22] N. E. Batalha, A. Mandell, K. Pontoppidan, K. B. Stevenson, N. K. Lewis, J. Kalirai, N. Earl, T. Greene, L. Albert, and L. D. Nielsen. PandExo: A Community Tool for Transiting Exoplanet Science with JWST & HST. *Publications of the Astronomical Society of the Pacific*, 129(976):064501, June 2017.

[23] N. M. Batalha, W. J. Borucki, S. T. Bryson, L. A. Buchhave, D. A. Caldwell, J. Christensen-Dalsgaard, D. Ciardi, E. W. Dunham, F. Fressin, I. Gautier, Thomas N., R. L. Gilliland, M. R. Haas, S. B. Howell, J. M. Jenkins, H. Kjeldsen, D. G. Koch, D. W. Latham, J. J. Lissauer, G. Marcy, J. F. Rowe, D. D. Sasselov, S. Seager, J. H. Steffen, G. Torres, G. S. Basri, T. M. Brown, D. Charbonneau, J. Christiansen, B. Clarke, W. D. Cochran, A. Dupree, D. C. Fabrycky, D. Fischer, E. B. Ford, J. Fortney, F. R. Girouard, M. J. Holman, J. Johnson, H. Isaacson, T. C. Klaus, P. Machalek, A. V. Moorehead, R. C. Morehead, D. Ragozzine, P. Tenenbaum, J. Twicken, S. Quinn, J. VanCleve, L. M. Walkowicz, W. F. Welsh, E. Devore, and A. Gould. Kepler's First Rocky Planet: Kepler-10b. *The Astrophysical Journal*, 729(1):27, Mar. 2011.

[24] N. M. Batalha, J. F. Rowe, S. T. Bryson, T. Barclay, C. J. Burke, D. A. Caldwell, J. L. Christiansen, F. Mullally, S. E. Thompson, T. M. Brown, A. K. Dupree, D. C. Fabrycky, E. B. Ford, J. J. Fortney, R. L. Gilliland, H. Isaacson, D. W. Latham, G. Marcy, S. N. Quinn, D. Ragozzine, A. Shporer, W. J. Borucki, D. R. Ciardi, I. Gautier, Thomas N., M. R. Haas, J. M. Jenkins, D. G. Koch, J. J. Lissauer, W. Rapin, G. S. Basri, A. P. Boss, L. A. Buchhave, J. A. Carter, D. Charbonneau, J. Christensen-Dalsgaard, B. D. Clarke, W. D. Cochran, B.-O. Demory, J.-M. Desert, E. Devore, L. R. Doyle, G. A. Esquerdo, M. Everett, F. Fressin, J. C. Geary, F. R. Girouard, A. Gould, J. R. Hall, M. J. Holman, A. W. Howard, S. B. Howell, K. A. Ibrahim, K. Kinemuchi, H. Kjeldsen, T. C. Klaus, J. Li, P. W. Lucas, S. Meibom, R. L. Morris, A. Prša, E. Quintana, D. T. Sanderfer, D. Sasselov, S. E. Seader, J. C. Smith, J. H. Steffen, M. Still, M. C. Stumpe, J. C. Tarter, P. Tenenbaum, G. Torres, J. D. Twicken, K. Uddin, J. Van Cleve, L. Walkowicz, and W. F. Welsh. Planetary Candidates Observed by Kepler. III. Analysis of the First 16 Months of Data. *The Astrophysical Journal, Supplement*, 204(2):24, Feb. 2013.

[25] K. Batygin and F. C. Adams. An Analytic Criterion for Turbulent Disruption of Planetary Resonances. *The Astronomical Journal*, 153(3):120, Mar. 2017.

[26] J. L. Bean, A. Seifahrt, H. Hartman, H. Nilsson, G. Wiedemann, A. Reiners, S. Dreizler, and T. J. Henry. The CRIRES Search for Planets Around the Lowest-mass Stars. I. High-precision Near-infrared Radial Velocities with an Ammonia Gas Cell. *The Astrophysical Journal*, 713(1):410–422, Apr. 2010.

[27] S. Bellotti, P. Petit, J. Morin, G. A. J. Hussain, C. P. Folsom, A. Carmona, X. Delfosse, and C. Moutou. Mitigating stellar activity jitter with different line lists for least-squares deconvolution. Analysis of a parametric and a randomised line selection. *Astronomy and Astrophysics*, 657:A107, Jan. 2022.

[28] G. F. Benedict, B. McArthur, D. W. Chappell, E. Nelan, W. H. Jefferys, W. van Altena, J. Lee, D. Cornell, P. J. Shelus, P. D. Hemenway, O. G. Franz, L. H. Wasserman, R. L. Duncombe, D. Story, A. L. Whipple, and L. W. Fredrick. Interferometric Astrometry of Proxima Centauri and Barnard's Star Using HUBBLE SPACE TELESCOPE Fine Guidance Sensor 3: Detection Limits for Substellar Companions. *The Astronomical Journal*, 118(2):1086–1100, Aug. 1999.

[29] Z. M. Berdinas, P. J. Amado, and G. Anglada-Escude. The Cool Tiny Beats Project - A High-cadence HARPS Survey Searching for Short-period Planets, Pulsations and Activity Signatures in M stars. In *18th Cambridge Workshop on Cool Stars, Stellar Systems, and the Sun*, volume 18 of *Cambridge Workshop on Cool Stars, Stellar Systems, and the Sun*, pages 723–732, Jan. 2015.

[30] T. A. Berger, D. Huber, J. L. van Saders, E. Gaidos, J. Tayar, and A. L. Kraus. The Gaia-Kepler Stellar Properties Catalog. I. Homogeneous Fundamental Properties for 186,301 Kepler Stars. *The Astronomical Journal*, 159(6):280, June 2020.

[31] J. Bobin, J.-L. Starck, and R. Ottensamer. Compressed Sensing in Astronomy. *IEEE Journal of Selected Topics in Signal Processing*, 2(5):718–726, Nov. 2008.

[32] I. Boisse, F. Bouchy, G. Hébrard, X. Bonfils, N. Santos, and S. Vauclair. Disentangling between stellar activity and planetary signals. In D. Prasad Choudhary and K. G. Strassmeier, editors, *Physics of Sun and Star Spots*, volume 273 of *IAU Symposium*, pages 281–285, Aug. 2011.

[33] A. Bortle, H. Fausey, J. Ji, S. Dodson-Robinson, V. Ramirez Delgado, and J. Gizis. A Gaussian Process Regression Reveals No Evidence for Planets Orbiting Kapteyn's Star. *The Astronomical Journal*, 161(5):230, May 2021.

[34] W. J. Borucki, D. Koch, G. Basri, N. Batalha, T. Brown, D. Caldwell, J. Caldwell, J. Christensen-Dalsgaard, W. D. Cochran, E. DeVore, E. W. Dunham, A. K. Dupree, T. N. Gautier, J. C. Geary, R. Gilliland, A. Gould, S. B. Howell, J. M. Jenkins, Y. Kondo, D. W. Latham, G. Marcy, S. Meibom, H. Kjeldsen, J. J. Lissauer, D. G. Monet, D. Morrison, D. Sasselov, J. Tarter, A. Boss, D. Brownlee, T. Owen, D. Buzasi, D. Charbonneau, L. Doyle, J. Fortney, E. B. Ford, M. J. Holman, S. Seager, J. H. Steffen, W. F. Welsh, J. Rowe, H. Anderson, L. Buchhave, D. Ciardi, L. Walkowicz, W. Sherry, E. Horch, H. Isaacson, M. E. Everett, D. Fischer, G. Torres, J. A. Johnson,

M. Endl, P. MacQueen, S. T. Bryson, J. Dotson, M. Haas, J. Kolodziejczak, J. Van Cleve, H. Chandrasekaran, J. D. Twicken, E. V. Quintana, B. D. Clarke, C. Allen, J. Li, H. Wu, P. Tenenbaum, E. Verner, F. Bruhweiler, J. Barnes, and A. Prsa. Kepler Planet-Detection Mission: Introduction and First Results. *Science*, 327(5968):977, Feb. 2010.

[35] A. P. Boss. Giant planet formation by gravitational instability. *Science*, 276:1836–1839, Jan. 1997.

[36] G. Boué, M. Montalto, I. Boisse, M. Oshagh, and N. C. Santos. New analytical expressions of the Rossiter-McLaughlin effect adapted to different observation techniques. *Astronomy and Astrophysics*, 550:A53, Feb. 2013.

[37] T. D. Brandt. The Hipparcos-Gaia Catalog of Accelerations: Gaia EDR3 Edition. *arXiv e-prints*, page arXiv:2105.11662, May 2021.

[38] G. L. Bretthorst. Generalizing the Lomb-Scargle periodogram. In A. Mohammad-Djafari, editor, *Bayesian Inference and Maximum Entropy Methods in Science and Engineering*, volume 568 of *American Institute of Physics Conference Series*, pages 241–245, May 2001.

[39] J. M. Brewer and D. A. Fischer. Erratum: "C/O and Mg/Si Ratios of Stars in the Solar Neighborhood" (¡A href="http://doi.org/10.3847/0004-637x/831/1/20"¿2016, ApJ, 831, 20¡/A¿). *The Astrophysical Journal*, 840(2):121, May 2017.

[40] J. M. Brewer, D. A. Fischer, R. T. Blackman, S. H. C. Cabot, A. B. Davis, G. Laughlin, C. Leet, J. M. J. Ong, R. R. Petersburg, A. E. Szymkowiak, L. L. Zhao, G. W. Henry, and J. Llama. EXPRES. I. HD 3651 as an Ideal RV Benchmark. *The Astronomical Journal*, 160(2):67, Aug. 2020.

[41] M. L. Bryan, H. A. Knutson, E. J. Lee, B. J. Fulton, K. Batygin, H. Ngo, and T. Meshkat. An Excess of Jupiter Analogs in Super-Earth Systems. *The Astronomical Journal*, 157(2):52, Feb. 2019.

[42] L. A. Buchhave, D. W. Latham, A. Johansen, M. Bizzarro, G. Torres, J. F. Rowe, N. M. Batalha, W. J. Borucki, E. Brugamyer, C. Caldwell, S. T. Bryson, D. R. Ciardi, W. D. Cochran, M. Endl, G. A. Esquerdo, E. B. Ford, J. C. Geary, R. L. Gilliland, T. Hansen, H. Isaacson, J. B. Laird, P. W. Lucas, G. Marcy, J. A. Morse, P. Robertson, A. Shporer, R. P. Stefanik, M. Still, and S. N. Quinn. An abundance of small exoplanets around stars with a wide range of metallicities. *Nature*, 486(7403):375–377, June 2012.

[43] R. P. Butler and G. Marcy. A planet orbiting 47 ursae majoris*. *The Astrophysical Journal*, 464(2):L153, jun 1996.

[44] R. P. Butler, G. Marcy, E. Williams, C. McCarthy, P. Dosanjh, and S. S. Vogt. Attaining Doppler Precision of 3 M s-1. *Publications of the Astronomical Society of the Pacific*, 108:500, June 1996.

[45] R. P. Butler, J. T. Wright, G. Marcy, D. A. Fischer, S. S. Vogt, C. G. Tinney, H. R. A. Jones, B. D. Carter, J. A. Johnson, C. McCarthy, and A. J. Penny. Catalog of Nearby Exoplanets. *The Astrophysical Journal*, 646(1):505–522, July 2006.

[46] J. A. Carter, E. Agol, W. J. Chaplin, S. Basu, T. R. Bedding, L. A. Buchhave, J. Christensen-Dalsgaard, K. M. Deck, Y. Elsworth, D. C. Fabrycky, E. B. Ford, J. J. Fortney, S. J. Hale, R. Handberg, S. Hekker, M. J. Holman, D. Huber, C. Karoff, S. D. Kawaler, H. Kjeldsen, J. J. Lissauer, E. D. Lopez, M. N. Lund, M. Lundkvist, T. S. Metcalfe, A. Miglio, L. A. Rogers, D. Stello, W. J. Borucki, S. Bryson, J. L. Christiansen, W. D. Cochran, J. C. Geary, R. L. Gilliland, M. R. Haas, J. Hall, A. W. Howard, J. M. Jenkins, T. Klaus, D. G. Koch, D. W. Latham, P. J. MacQueen, D. Sasselov, J. H. Steffen, J. D. Twicken, and J. N. Winn. Kepler-36: A Pair of Planets with Neighboring Orbits and Dissimilar Densities. *Science*, 337(6094):556, Aug. 2012.

[47] S. S. Chen, D. L. Donoho, and M. A. Saunders. Atomic decomposition by basis pursuit. *SIAM Journal on Scientific Computing*, 20(1):33–61, 1998.

[48] J. Choi, A. Dotter, C. Conroy, M. Cantiello, B. Paxton, and B. D. Johnson. Mesa Isochrones and Stellar Tracks (MIST). I. Solar-scaled Models. *The Astrophysical Journal*, 823(2):102, June 2016.

[49] J. Choi, C. McCarthy, G. Marcy, A. W. Howard, D. A. Fischer, J. A. Johnson, H. Isaacson, and J. T. Wright. Precise Doppler Monitoring of Barnard's Star. *The Astrophysical Journal*, 764(2):131, Feb. 2013.

[50] A. Chontos, J. M. Akana Murphy, M. G. MacDougall, T. Fetherolf, J. Van Zandt, R. A. Rubenzahl, C. Beard, D. Huber, N. M. Batalha, I. J. M. Crossfield, C. D. Dressing, B. Fulton, A. W. Howard, H. Isaacson, S. R. Kane, E. A. Petigura, P. Robertson, A. Roy, L. M. Weiss, A. Behmard, F. Dai, P. A. Dalba, S. Giacalone, M. L. Hill, J. Lubin, A. Mayo, T. Mocnik, A. S. Polanski, L. J. Rosenthal, N. Scarsdale, and E. V. Turtelboom. The TESS-Keck Survey: Science Goals and Target Selection. *arXiv e-prints*, page arXiv:2106.06156, June 2021.

[51] R. Cloutier, J. E. Rodriguez, J. Irwin, D. Charbonneau, K. G. Stassun, A. Mortier, D. W. Latham, H. Isaacson, A. W. Howard, S. Udry, T. G. Wilson, C. A. Watson, M. Pinamonti, F. Lienhard, P. Giacobbe, P. Guerra, K. A. Collins, A. Beiryla, G. A. Esquerdo, E. Matthews, R. A. Matson, S. B. Howell, E. Furlan, I. J. M. Crossfield, J. G. Winters, C. Nava, K. Ment, E. D. Lopez, G. Ricker, R. Vanderspek, S. Seager, J. M. Jenkins, E. B. Ting, P. Tenenbaum, A. Sozzetti, L. Sha, D. Ségransan, J. E. Schlieder, D. Sasselov, A. Roy, P. Robertson, K. Rice, E. Poretti, G. Piotto, D. Phillips, J. Pepper, F. Pepe, E. Molinari, T. Mocnik, G. Micela, M. Mayor, A. F. Martinez Fiorenzano, F. Mallia, J. Lubin, C. Lovis, M. López-Morales, M. R. Kosiarek, J. F. Kielkopf, S. R. Kane, E. L. N. Jensen, G. Isopi, D. Huber, M. L. Hill, A. Harutyunyan, E. Gonzales, S. Giacalone, A. Ghedina, A. Ercolino, X. Dumusque, C. D. Dressing, M. Damasso, P. A. Dalba, R. Cosentino, D. M. Conti, K. D. Colón, K. I. Collins, A. C. Cameron, D. Ciardi, J. Christiansen, A. Chontos, M. Cecconi, D. A. Caldwell, C. Burke, L. Buchhave, C. Beichman, A. Behmard, C. Beard, and J. M. Akana Murphy.

TOI-1235 b: A Keystone Super-Earth for Testing Radius Valley Emergence Models around Early M Dwarfs. *The Astronomical Journal*, 160(1):22, July 2020.

[52] A. Collier Cameron, A. Mortier, D. Phillips, X. Dumusque, R. D. Haywood, N. Langellier, C. A. Watson, H. M. Cegla, J. Costes, D. Charbonneau, A. Coffinet, D. W. Latham, M. Lopez-Morales, L. Malavolta, J. Maldonado, G. Micela, T. Milbourne, E. Molinari, S. H. Saar, S. Thompson, N. Buchschacher, M. Cecconi, R. Cosentino, A. Ghedina, A. Glenday, M. Gonzalez, C. H. Li, M. Lodi, C. Lovis, F. Pepe, E. Poretti, K. Rice, D. Sasselov, A. Sozzetti, A. Szentgyorgyi, S. Udry, and R. Walsworth. Three years of Sun-as-a-star radial-velocity observations on the approach to solar minimum. *Monthly Notices of the Royal Astronomical Society*, 487(1):1082–1100, July 2019.

[53] R. Cosentino, C. Lovis, F. Pepe, A. C. Cameron, D. W. Latham, E. Molinari, S. Udry, N. Bezawada, M. Black, A. Born, N. Buchschacher, D. Charbonneau, P. Figueira, M. Fleury, A. Galli, A. Gallie, X. Gao, A. Ghedina, C. Gonzalez, M. Gonzalez, J. Guerra, D. Henry, K. Horne, I. Hughes, D. Kelly, M. Lodi, D. Lunney, C. Maire, M. Mayor, G. Micela, M. P. Ordway, J. Peacock, D. Phillips, G. Piotto, D. Pollacco, D. Queloz, K. Rice, C. Riverol, L. Riverol, J. S. Juan, D. Sasselov, D. Segransan, A. Sozzetti, D. Sosnowska, B. Stobie, A. Szentgyorgyi, A. Vick, and L. Weber. Harps-N: the new planet hunter at TNG. In I. S. McLean, S. K. Ramsay, and H. Takami, editors, *Ground-based and Airborne Instrumentation for Astronomy IV*, volume 8446, pages 657 – 676. International Society for Optics and Photonics, SPIE, 2012.

[54] J. D. Crane, S. A. Shectman, R. P. Butler, I. B. Thompson, C. Birk, P. Jones, and G. S. Burley. The Carnegie Planet Finder Spectrograph: integration and commissioning. In I. S. McLean, S. K. Ramsay, and H. Takami, editors, *Ground-based and Airborne Instrumentation for Astronomy III*, volume 7735, pages 1909 – 1923. International Society for Optics and Photonics, SPIE, 2010.

[55] J. Crass, D. Aikens, J. Mason, D. King, J. R. Crepp, A. Bechter, E. Bechter, M. Farsad, C. Schwab, and M. VanSickle. The final design of the iLocater spectrograph: an optimized architecture for diffraction-limited EPRV instruments. In C. J. Evans, J. J. Bryant, and K. Motohara, editors, *Ground-based and Airborne Instrumentation for Astronomy IX*, volume 12184 of *Society of Photo-Optical Instrumentation Engineers (SPIE) Conference Series*, page 121841P, Aug. 2022.

[56] M. Cretignier, X. Dumusque, R. Allart, F. Pepe, and C. Lovis. Measuring precise radial velocities on individual spectral lines. II. Dependance of stellar activity signal on line depth. *Astronomy and Astrophysics*, 633:A76, Jan. 2020.

[57] A. Cumming, G. Marcy, and R. P. Butler. The Lick Planet Search: Detectability and Mass Thresholds. *The Astrophysical Journal*, 526(2):890–915, Dec. 1999.

[58] F. Dai, A. W. Howard, N. M. Batalha, C. Beard, A. Behmard, S. Blunt, C. L. Brinkman, A. Chontos, I. J. M. Crossfield, P. A. Dalba, C. Dressing, B. Fulton, S. Giacalone, M. L. Hill, D. Huber, H. Isaacson, S. R. Kane, J. Lubin, A. Mayo, T. Močnik, J. M. Akana Murphy, E. A. Petigura, M. Rice, P. Robertson, L. Rosenthal, A. Roy,

R. A. Rubenzahl, L. M. Weiss, J. V. Zandt, C. Beichman, D. Ciardi, K. A. Collins, E. Gonzales, S. B. Howell, R. A. Matson, E. C. Matthews, J. E. Schlieder, R. P. Schwarz, G. R. Ricker, R. Vanderspek, D. W. Latham, S. Seager, J. N. Winn, J. M. Jenkins, D. A. Caldwell, K. D. Colon, D. Dragomir, M. B. Lund, B. McLean, A. Rudat, and A. Shporer. TKS X: Confirmation of TOI-1444b and a Comparative Analysis of the Ultra-short-period Planets with Hot Neptunes. *The Astronomical Journal*, 162(2):62, Aug. 2021.

[59] F. Dai, A. Roy, B. Fulton, P. Robertson, L. Hirsch, H. Isaacson, S. Albrecht, A. W. Mann, M. H. Kristiansen, N. M. Batalha, C. Beard, A. Behmard, A. Chontos, I. J. M. Crossfield, P. A. Dalba, C. Dressing, S. Giacalone, M. Hill, A. W. Howard, D. Huber, S. R. Kane, M. Kosiarek, J. Lubin, A. Mayo, T. Mocnik, J. M. Akana Murphy, E. A. Petigura, L. Rosenthal, R. A. Rubenzahl, N. Scarsdale, L. M. Weiss, J. Van Zandt, G. R. Ricker, R. Vanderspek, D. W. Latham, S. Seager, J. N. Winn, J. M. Jenkins, D. A. Caldwell, D. Charbonneau, T. Daylan, M. N. Günther, E. Morgan, S. N. Quinn, M. E. Rose, and J. C. Smith. The TESS-Keck Survey. III. A Stellar Obliquity Measurement of TOI-1726 c. *The Astronomical Journal*, 160(4):193, Oct. 2020.

[60] P. A. Dalba, A. F. Gupta, J. E. Rodriguez, D. Dragomir, C. X. Huang, S. R. Kane, S. N. Quinn, A. Bieryla, G. A. Esquerdo, B. J. Fulton, N. Scarsdale, N. M. Batalha, C. Beard, A. Behmard, A. Chontos, I. J. M. Crossfield, C. D. Dressing, S. Giacalone, M. L. Hill, L. A. Hirsch, A. W. Howard, D. Huber, H. Isaacson, M. Kosiarek, J. Lubin, A. W. Mayo, T. Mocnik, J. M. Akana Murphy, E. A. Petigura, P. Robertson, L. J. Rosenthal, A. Roy, R. A. Rubenzahl, J. Van Zandt, L. M. Weiss, E. Knudstrup, M. F. Andersen, F. Grundahl, X. Yao, J. Pepper, J. Villanueva, Steven, D. R. Ciardi, R. Cloutier, T. L. Jacobs, M. H. Kristiansen, D. M. LaCourse, M. Lendl, H. P. Osborn, E. Palle, K. G. Stassun, D. J. Stevens, G. R. Ricker, R. Vanderspek, D. W. Latham, S. Seager, J. N. Winn, J. M. Jenkins, D. A. Caldwell, T. Daylan, W. Fong, R. F. Goeke, M. E. Rose, P. Rowden, J. E. Schlieder, J. C. Smith, and A. Vanderburg. The TESS-Keck Survey. I. A Warm Sub-Saturn-mass Planet and a Caution about Stray Light in TESS Cameras. *The Astronomical Journal*, 159(5):241, May 2020.

[61] P. A. Dalba, S. R. Kane, D. Dragomir, S. Villanueva, K. A. Collins, T. L. Jacobs, D. M. LaCourse, R. Gagliano, M. H. Kristiansen, M. Omohundro, H. M. Schwengeler, I. A. Terentev, A. Vanderburg, B. Fulton, H. Isaacson, J. Van Zandt, A. W. Howard, D. P. Thorngren, S. B. Howell, N. M. Batalha, A. Chontos, I. J. M. Crossfield, C. D. Dressing, D. Huber, E. A. Petigura, P. Robertson, A. Roy, L. M. Weiss, A. Behmard, C. Beard, C. L. Brinkman, S. Giacalone, M. L. Hill, J. Lubin, A. W. Mayo, T. Močnik, J. M. Akana Murphy, A. S. Polanski, M. Rice, L. J. Rosenthal, R. A. Rubenzahl, N. Scarsdale, E. V. Turtelboom, D. Tyler, P. Benni, P. Boyce, T. M. Esposito, E. Girardin, D. Laloum, P. Lewin, C. R. Mann, F. Marchis, R. P. Schwarz, G. Srdoc, J. Steuer, T. Sivarani, A. Unni, N. L. Eisner, T. Fetherolf, Z. Li, X. Yao, J. Pepper, G. R. Ricker, R. Vanderspek, D. W. Latham, S. Seager, J. N. Winn, J. M. Jenkins, C. J. Burke, J. D. Eastman, M. B. Lund, D. R. Rodriguez, P. Rowden, E. B. Ting, and J. N. Villaseñor. The TESS-Keck Survey. VIII. Confirmation of a Transit-

ing Giant Planet on an Eccentric 261 Day Orbit with the Automated Planet Finder Telescope. *The Astronomical Journal*, 163(2):61, Feb. 2022.

[62] J. R. A. Davenport, G. T. Mendoza, and S. L. Hawley. 10 Years of Stellar Activity for GJ 1243. *The Astronomical Journal*, 160(1):36, July 2020.

[63] R. I. Dawson and D. C. Fabrycky. Radial Velocity Planets De-aliased: A New, Short Period for Super-Earth 55 Cnc e. *The Astrophysical Journal*, 722(1):937–953, Oct. 2010.

[64] H. Dekker, S. D'Odorico, A. Kaufer, B. Delabre, and H. Kotzlowski. Design, construction, and performance of UVES, the echelle spectrograph for the UT2 Kueyen Telescope at the ESO Paranal Observatory. In M. Iye and A. F. Moorwood, editors, *Optical and IR Telescope Instrumentation and Detectors*, volume 4008 of *Society of Photo-Optical Instrumentation Engineers (SPIE) Conference Series*, pages 534–545, Aug. 2000.

[65] M. R. Díaz, J. S. Jenkins, M. Tuomi, R. P. Butler, M. G. Soto, J. K. Teske, F. Feng, S. A. Shectman, P. Arriagada, J. D. Crane, I. B. Thompson, and S. S. Vogt. The Test Case of HD 26965: Difficulties Disentangling Weak Doppler Signals from Stellar Activity. *The Astronomical Journal*, 155(3):126, Mar. 2018.

[66] D. Donoho. Compressed sensing. *IEEE Transactions on Information Theory*, 52(4):1289–1306, 2006.

[67] L. R. Doyle, J. A. Carter, D. C. Fabrycky, R. W. Slawson, S. B. Howell, J. N. Winn, J. A. Orosz, A. Přsa, W. F. Welsh, S. N. Quinn, D. Latham, G. Torres, L. A. Buchhave, G. Marcy, J. J. Fortney, A. Shporer, E. B. Ford, J. J. Lissauer, D. Ragozzine, M. Rucker, N. Batalha, J. M. Jenkins, W. J. Borucki, D. Koch, C. K. Middour, J. R. Hall, S. McCauliff, M. N. Fanelli, E. V. Quintana, M. J. Holman, D. A. Caldwell, M. Still, R. P. Stefanik, W. R. Brown, G. A. Esquerdo, S. Tang, G. Furesz, J. C. Geary, P. Berlind, M. L. Calkins, D. R. Short, J. H. Steffen, D. Sasselov, E. W. Dunham, W. D. Cochran, A. Boss, M. R. Haas, D. Buzasi, and D. Fischer. Kepler-16: A Transiting Circumbinary Planet. *Science*, 333(6049):1602, Sept. 2011.

[68] C. D. Dressing and D. Charbonneau. The Occurrence of Potentially Habitable Planets Orbiting M Dwarfs Estimated from the Full Kepler Dataset and an Empirical Measurement of the Detection Sensitivity. *The Astrophysical Journal*, 807(1):45, July 2015.

[69] X. Dumusque. Measuring precise radial velocities on individual spectral lines. I. Validation of the method and application to mitigate stellar activity. *Astronomy and Astrophysics*, 620:A47, Nov. 2018.

[70] X. Dumusque, M. Cretignier, D. Sosnowska, N. Buchschacher, C. Lovis, D. F. Phillips, F. Pepe, F. Alesina, L. A. Buchhave, J. Burnier, M. Cecconi, H. M. Cegla, R. Cloutier, A. Collier Cameron, R. Cosentino, A. Ghedina, M. González, R. D. Haywood, D. W.

Latham, M. Lodi, M. López-Morales, J. Maldonado, L. Malavolta, G. Micela, E. Molinari, A. Mortier, H. Pérez Ventura, M. Pinamonti, E. Poretti, K. Rice, L. Riverol, C. Riverol, J. San Juan, D. Ségransan, A. Sozzetti, S. J. Thompson, S. Udry, and T. G. Wilson. Three years of HARPS-N high-resolution spectroscopy and precise radial velocity data for the Sun. *Astronomy and Astrophysics*, 648:A103, Apr. 2021.

[71] X. Dumusque, A. Glenday, D. F. Phillips, N. Buchschacher, A. Collier Cameron, M. Cecconi, D. Charbonneau, R. Cosentino, A. Ghedina, D. W. Latham, C.-H. Li, M. Lodi, C. Lovis, E. Molinari, F. Pepe, S. Udry, D. Sasselov, A. Szentgyorgyi, and R. Walsworth. HARPS-N Observes the Sun as a Star. *The Astrophysical Journal Letters*, 814(2):L21, Dec. 2015.

[72] X. Dumusque, F. Pepe, C. Lovis, D. Ségransan, J. Sahlmann, W. Benz, F. Bouchy, M. Mayor, D. Queloz, N. Santos, and S. Udry. An Earth-mass planet orbiting α Centauri B. *Nature*, 491(7423):207–211, Nov. 2012.

[73] B. Efron, T. Hastie, I. Johnstone, and R. Tibshirani. Least Angle Regression. *arXiv Mathematics e-prints*, page math/0406456, June 2004.

[74] R. Egeland, W. Soon, S. Baliunas, J. C. Hall, A. A. Pevtsov, and L. Bertello. The Mount Wilson Observatory S-index of the Sun. *The Astrophysical Journal*, 835(1):25, Jan. 2017.

[75] D. Fabrycky and S. Tremaine. Shrinking Binary and Planetary Orbits by Kozai Cycles with Tidal Friction. *The Astrophysical Journal*, 669(2):1298–1315, Nov. 2007.

[76] A. D. Feinstein, M. Radica, L. Welbanks, C. A. Murray, K. Ohno, L.-P. Coulombe, N. Espinoza, J. L. Bean, J. K. Teske, B. Benneke, M. R. Line, Z. Rustamkulov, A. Saba, A. Tsiaras, J. K. Barstow, J. J. Fortney, P. Gao, H. A. Knutson, R. J. MacDonald, T. Mikal-Evans, B. V. Rackham, J. Taylor, V. Parmentier, N. M. Batalha, Z. K. Berta-Thompson, A. L. Carter, Q. Changeat, L. A. dos Santos, N. P. Gibson, J. M. Goyal, L. Kreidberg, M. López-Morales, J. D. Lothringer, Y. Miguel, K. Molaverdikhani, S. E. Moran, G. Morello, S. Mukherjee, D. K. Sing, K. B. Stevenson, H. R. Wakeford, E.-M. Ahrer, M. K. Alam, L. Alderson, N. H. Allen, N. E. Batalha, T. J. Bell, J. Blecic, J. Brande, C. Caceres, S. L. Casewell, K. L. Chubb, I. J. M. Crossfield, N. Crouzet, P. E. Cubillos, L. Decin, J.-M. Désert, J. Harrington, K. Heng, T. Henning, N. Iro, E. M. R. Kempton, S. Kendrew, J. Kirk, J. Krick, P.-O. Lagage, M. Lendl, L. Mancini, M. Mansfield, E. M. May, N. J. Mayne, N. K. Nikolov, E. Palle, D. J. M. Petit dit de la Roche, C. Piaulet, D. Powell, S. Redfield, L. K. Rogers, M. T. Roman, P.-A. Roy, M. C. Nixon, E. Schlawin, X. Tan, P. Tremblin, J. D. Turner, O. Venot, W. C. Waalkes, P. J. Wheatley, and X. Zhang. Early Release Science of the exoplanet WASP-39b with JWST NIRISS. *Nature*, 614(7949):670–675, Feb. 2023.

[77] F. Feng, M. Tuomi, and H. R. A. Jones. Agatha: disentangling periodic signals from correlated noise in a periodogram framework. *Monthly Notices of the Royal Astronomical Society*, 470(4):4794–4814, Oct. 2017.

[78] D. Foreman-Mackey, E. Agol, S. Ambikasaran, and R. Angus. Fast and Scalable Gaussian Process Modeling with Applications to Astronomical Time Series. *The Astronomical Journal*, 154(6):220, Dec. 2017.

[79] D. Foreman-Mackey, E. Agol, R. Angus, and S. Ambikasaran. Fast and scalable gaussian process modeling with applications to astronomical time series. *AJ*, 154:220, 2017.

[80] D. Foreman-Mackey, R. Luger, I. Czekala, E. Agol, A. Price-Whelan, E. Gilbert, T. D. Brandt, T. Barclay, and L. Bouma. exoplanet-dev/exoplanet v0.4.1, Nov. 2020.

[81] B. J. Fulton and E. A. Petigura. The California-Kepler Survey. VII. Precise Planet Radii Leveraging Gaia DR2 Reveal the Stellar Mass Dependence of the Planet Radius Gap. *The Astronomical Journal*, 156(6):264, Dec. 2018.

[82] B. J. Fulton, E. A. Petigura, S. Blunt, and E. Sinukoff. RadVel: The Radial Velocity Modeling Toolkit. *Publications of the Astronomical Society of the Pacific*, 130(986):044504, Apr. 2018.

[83] B. J. Fulton, E. A. Petigura, S. Blunt, and E. Sinukoff. RadVel: The Radial Velocity Modeling Toolkit. *Publications of the Astronomical Society of the Pacific*, 130(986):044504, Apr 2018.

[84] B. J. Fulton, E. A. Petigura, A. W. Howard, H. Isaacson, G. Marcy, P. A. Cargile, L. Hebb, L. M. Weiss, J. A. Johnson, T. D. Morton, E. Sinukoff, I. J. M. Crossfield, and L. A. Hirsch. The California-Kepler Survey. III. A Gap in the Radius Distribution of Small Planets. *The Astronomical Journal*, 154(3):109, Sept. 2017.

[85] B. J. Fulton, L. J. Rosenthal, L. A. Hirsch, H. Isaacson, A. W. Howard, C. M. Dedrick, I. A. Sherstyuk, S. C. Blunt, E. A. Petigura, H. A. Knutson, A. Behmard, A. Chontos, J. R. Crepp, I. J. M. Crossfield, P. A. Dalba, D. A. Fischer, G. W. Henry, S. R. Kane, M. Kosiarek, G. W. Marcy, R. A. Rubenzahl, L. M. Weiss, and J. T. Wright. The California Legacy Survey II. Occurrence of Giant Planets Beyond the Ice line. *arXiv e-prints*, page arXiv:2105.11584, May 2021.

[86] Gaia Collaboration. VizieR Online Data Catalog: Gaia DR2 (Gaia Collaboration, 2018). *VizieR Online Data Catalog*, page I/345, Apr. 2018.

[87] Gaia Collaboration, A. G. A. Brown, A. Vallenari, T. Prusti, J. H. J. de Bruijne, C. Babusiaux, C. A. L. Bailer-Jones, M. Biermann, D. W. Evans, L. Eyer, F. Jansen, C. Jordi, S. A. Klioner, U. Lammers, L. Lindegren, X. Luri, F. Mignard, C. Panem, D. Pourbaix, S. Randich, P. Sartoretti, H. I. Siddiqui, C. Soubiran, F. van Leeuwen, N. A. Walton, F. Arenou, U. Bastian, M. Cropper, R. Drimmel, D. Katz, M. G. Lattanzi, J. Bakker, C. Cacciari, J. Castañeda, L. Chaoul, N. Cheek, F. De Angeli, C. Fabricius, R. Guerra, B. Holl, E. Masana, R. Messineo, N. Mowlavi, K. Nienartowicz, P. Panuzzo, J. Portell, M. Riello, G. M. Seabroke, P. Tanga, F. Thévenin, G. Gracia-Abril, G. Comoretto, M. Garcia-Reinaldos, D. Teyssier, M. Altmann, R. Andrae, M. Audard, I. Bellas-Velidis, K. Benson, J. Berthier, R. Blomme, P. Burgess, G. Busso, B. Carry, A. Cellino, G. Clementini, M. Clotet, O. Creevey, M. Davidson,

J. De Ridder, L. Delchambre, A. Dell'Oro, C. Ducourant, J. Fernández-Hernández, M. Fouesneau, Y. Frémat, L. Galluccio, M. García-Torres, J. González-Núñez, J. J. González-Vidal, E. Gosset, L. P. Guy, J. L. Halbwachs, N. C. Hambly, D. L. Harrison, J. Hernández, D. Hestroffer, S. T. Hodgkin, A. Hutton, G. Jasniewicz, A. Jean-Antoine-Piccolo, S. Jordan, A. J. Korn, A. Krone-Martins, A. C. Lanzafame, T. Lebzelter, W. Löffler, M. Manteiga, P. M. Marrese, J. M. Martín-Fleitas, A. Moitinho, A. Mora, K. Muinonen, J. Osinde, E. Pancino, T. Pauwels, J. M. Petit, A. Recio-Blanco, P. J. Richards, L. Rimoldini, A. C. Robin, L. M. Sarro, C. Siopis, M. Smith, A. Sozzetti, M. Süveges, J. Torra, W. van Reeven, U. Abbas, A. Abreu Aramburu, S. Accart, C. Aerts, G. Altavilla, M. A. Álvarez, R. Alvarez, J. Alves, R. I. Anderson, A. H. Andrei, E. Anglada Varela, E. Antiche, T. Antoja, B. Arcay, T. L. Astraatmadja, N. Bach, S. G. Baker, L. Balaguer-Núñez, P. Balm, C. Barache, C. Barata, D. Barbato, F. Barblan, P. S. Barklem, D. Barrado, M. Barros, M. A. Barstow, S. Bartholomé Muñoz, J. L. Bassilana, U. Becciani, M. Bellazzini, A. Berihuete, S. Bertone, L. Bianchi, O. Bienaymé, S. Blanco-Cuaresma, T. Boch, C. Boeche, A. Bombrun, R. Borrachero, D. Bossini, S. Bouquillon, G. Bourda, A. Bragaglia, L. Bramante, M. A. Breddels, A. Bressan, N. Brouillet, T. Brüsemeister, E. Brugaletta, B. Bucciarelli, A. Burlacu, D. Busonero, A. G. Butkevich, R. Buzzi, E. Caffau, R. Cancelliere, G. Cannizzaro, T. Cantat-Gaudin, R. Carballo, T. Carlucci, J. M. Carrasco, L. Casamiquela, M. Castellani, A. Castro-Ginard, P. Charlot, L. Chemin, A. Chiavassa, G. Cocozza, G. Costigan, S. Cowell, F. Crifo, M. Crosta, C. Crowley, J. Cuypers, C. Dafonte, Y. Damerdji, A. Dapergolas, P. David, M. David, P. de Laverny, F. De Luise, R. De March, D. de Martino, R. de Souza, A. de Torres, J. Debosscher, E. del Pozo, M. Delbo, A. Delgado, H. E. Delgado, P. Di Matteo, S. Diakite, C. Diener, E. Distefano, C. Dolding, P. Drazinos, J. Durán, B. Edvardsson, H. Enke, K. Eriksson, P. Esquej, G. Eynard Bontemps, C. Fabre, M. Fabrizio, S. Faigler, A. J. Falcão, M. Farràs Casas, L. Federici, G. Fedorets, P. Fernique, F. Figueras, F. Filippi, K. Findeisen, A. Fonti, E. Fraile, M. Fraser, B. Frézouls, M. Gai, S. Galleti, D. Garabato, F. García-Sedano, A. Garofalo, N. Garralda, A. Gavel, P. Gavras, J. Gerssen, R. Geyer, P. Giacobbe, G. Gilmore, S. Girona, G. Giuffrida, F. Glass, M. Gomes, M. Granvik, A. Gueguen, A. Guerrier, J. Guiraud, R. Gutiérrez-Sánchez, R. Haigron, D. Hatzidimitriou, M. Hauser, M. Haywood, U. Heiter, A. Helmi, J. Heu, T. Hilger, D. Hobbs, W. Hofmann, G. Holland, H. E. Huckle, A. Hypki, V. Icardi, K. Janßen, G. Jevardat de Fombelle, P. G. Jonker, Á. L. Juhász, F. Julbe, A. Karampelas, A. Kewley, J. Klar, A. Kochoska, R. Kohley, K. Kolenberg, M. Kontizas, E. Kontizas, S. E. Koposov, G. Kordopatis, Z. Kostrzewa-Rutkowska, P. Koubsky, S. Lambert, A. F. Lanza, Y. Lasne, J. B. Lavigne, Y. Le Fustec, C. Le Poncin-Lafitte, Y. Lebreton, S. Leccia, N. Leclerc, I. Lecoeur-Taibi, H. Lenhardt, F. Leroux, S. Liao, E. Licata, H. E. P. Lindstrøm, T. A. Lister, E. Livanou, A. Lobel, M. López, S. Managau, R. G. Mann, G. Mantelet, O. Marchal, J. M. Marchant, M. Marconi, S. Marinoni, G. Marschalkó, D. J. Marshall, M. Martino, G. Marton, N. Mary, D. Massari, G. Matijevič, T. Mazeh, P. J. McMillan, S. Messina, D. Michalik, N. R. Millar, D. Molina, R. Molinaro, L. Molnár, P. Montegriffo, R. Mor, R. Morbidelli, T. Morel, D. Morris, A. F. Mulone, T. Muraveva, I. Musella, G. Nelemans, L. Nicastro, L. Noval, W. O'Mullane, C. Ordénovic, D. Ordóñez-Blanco, P. Osborne, C. Pagani, I. Pagano, F. Pailler, H. Palacin, L. Palaversa, A. Panahi, M. Pawlak,

A. M. Piersimoni, F. X. Pineau, E. Plachy, G. Plum, E. Poggio, E. Poujoulet, A. Prša, L. Pulone, E. Racero, S. Ragaini, N. Rambaux, M. Ramos-Lerate, S. Regibo, C. Reylé, F. Riclet, V. Ripepi, A. Riva, A. Rivard, G. Rixon, T. Roegiers, M. Roelens, M. Romero-Gómez, N. Rowell, F. Royer, L. Ruiz-Dern, G. Sadowski, T. Sagristà Sellés, J. Sahlmann, J. Salgado, E. Salguero, N. Sanna, T. Santana-Ros, M. Sarasso, H. Savietto, M. Schultheis, E. Sciacca, M. Segol, J. C. Segovia, D. Ségransan, I. C. Shih, L. Siltala, A. F. Silva, R. L. Smart, K. W. Smith, E. Solano, F. Solitro, R. Sordo, S. Soria Nieto, J. Souchay, A. Spagna, F. Spoto, U. Stampa, I. A. Steele, H. Steidelmüller, C. A. Stephenson, H. Stoev, F. F. Suess, J. Surdej, L. Szabados, E. Szegedi-Elek, D. Tapiador, F. Taris, G. Tauran, M. B. Taylor, R. Teixeira, D. Terrett, P. Teyssand ier, W. Thuillot, A. Titarenko, F. Torra Clotet, C. Turon, A. Ulla, E. Utrilla, S. Uzzi, M. Vaillant, G. Valentini, V. Valette, A. van Elteren, E. Van Hemelryck, M. van Leeuwen, M. Vaschetto, A. Vecchiato, J. Veljanoski, Y. Viala, D. Vicente, S. Vogt, C. von Essen, H. Voss, V. Votruba, S. Voutsinas, G. Walmsley, M. Weiler, O. Wertz, T. Wevers, Ł. Wyrzykowski, A. Yoldas, M. Žerjal, H. Ziaeepour, J. Zorec, S. Zschocke, S. Zucker, C. Zurbach, and T. Zwitter. Gaia Data Release 2. Summary of the contents and survey properties. *Astronomy and Astrophysics*, 616:A1, Aug. 2018.

[88] Gaia Collaboration, T. Prusti, J. H. J. de Bruijne, A. G. A. Brown, A. Vallenari, C. Babusiaux, C. A. L. Bailer-Jones, U. Bastian, M. Biermann, D. W. Evans, L. Eyer, F. Jansen, C. Jordi, S. A. Klioner, U. Lammers, L. Lindegren, X. Luri, F. Mignard, D. J. Milligan, C. Panem, V. Poinsignon, D. Pourbaix, S. Randich, G. Sarri, P. Sartoretti, H. I. Siddiqui, C. Soubiran, V. Valette, F. van Leeuwen, N. A. Walton, C. Aerts, F. Arenou, M. Cropper, R. Drimmel, E. Høg, D. Katz, M. G. Lattanzi, W. O'Mullane, E. K. Grebel, A. D. Holland, C. Huc, X. Passot, L. Bramante, C. Cacciari, J. Castañeda, L. Chaoul, N. Cheek, F. De Angeli, C. Fabricius, R. Guerra, J. Hernández, A. Jean-Antoine-Piccolo, E. Masana, R. Messineo, N. Mowlavi, K. Nienartowicz, D. Ordóñez-Blanco, P. Panuzzo, J. Portell, P. J. Richards, M. Riello, G. M. Seabroke, P. Tanga, F. Thévenin, J. Torra, S. G. Els, G. Gracia-Abril, G. Comoretto, M. Garcia-Reinaldos, T. Lock, E. Mercier, M. Altmann, R. Andrae, T. L. Astraatmadja, I. Bellas-Velidis, K. Benson, J. Berthier, R. Blomme, G. Busso, B. Carry, A. Cellino, G. Clementini, S. Cowell, O. Creevey, J. Cuypers, M. Davidson, J. De Ridder, A. de Torres, L. Delchambre, A. Dell'Oro, C. Ducourant, Y. Frémat, M. García-Torres, E. Gosset, J. L. Halbwachs, N. C. Hambly, D. L. Harrison, M. Hauser, D. Hestroffer, S. T. Hodgkin, H. E. Huckle, A. Hutton, G. Jasniewicz, S. Jordan, M. Kontizas, A. J. Korn, A. C. Lanzafame, M. Manteiga, A. Moitinho, K. Muinonen, J. Osinde, E. Pancino, T. Pauwels, J. M. Petit, A. Recio-Blanco, A. C. Robin, L. M. Sarro, C. Siopis, M. Smith, K. W. Smith, A. Sozzetti, W. Thuillot, W. van Reeven, Y. Viala, U. Abbas, A. Abreu Aramburu, S. Accart, J. J. Aguado, P. M. Allan, W. Allasia, G. Altavilla, M. A. Álvarez, J. Alves, R. I. Anderson, A. H. Andrei, E. Anglada Varela, E. Antiche, T. Antoja, S. Antón, B. Arcay, A. Atzei, L. Ayache, N. Bach, S. G. Baker, L. Balaguer-Núñez, C. Barache, C. Barata, A. Barbier, F. Barblan, M. Baroni, D. Barrado y Navascués, M. Barros, M. A. Barstow, U. Becciani, M. Bellazzini, G. Bellei, A. Bello García, V. Belokurov, P. Bendjoya, A. Berihuete, L. Bianchi, O. Bienaymé, F. Billebaud, N. Blagorodnova, S. Blanco-Cuaresma, T. Boch, A. Bombrun, R. Bor-

rachero, S. Bouquillon, G. Bourda, H. Bouy, A. Bragaglia, M. A. Breddels, N. Brouillet, T. Brüsemeister, B. Bucciarelli, F. Budnik, P. Burgess, R. Burgon, A. Burlacu, D. Busonero, R. Buzzi, E. Caffau, J. Cambras, H. Campbell, R. Cancelliere, T. Cantat-Gaudin, T. Carlucci, J. M. Carrasco, M. Castellani, P. Charlot, J. Charnas, P. Charvet, F. Chassat, A. Chiavassa, M. Clotet, G. Cocozza, R. S. Collins, P. Collins, G. Costigan, F. Crifo, N. J. G. Cross, M. Crosta, C. Crowley, C. Dafonte, Y. Damerdji, A. Dapergolas, P. David, M. David, P. De Cat, F. de Felice, P. de Laverny, F. De Luise, R. De March, D. de Martino, R. de Souza, J. Debosscher, E. del Pozo, M. Delbo, A. Delgado, H. E. Delgado, F. di Marco, P. Di Matteo, S. Diakite, E. Distefano, C. Dolding, S. Dos Anjos, P. Drazinos, J. Durán, Y. Dzigan, E. Ecale, B. Edvardsson, H. Enke, M. Erdmann, D. Escolar, M. Espina, N. W. Evans, G. Eynard Bontemps, C. Fabre, M. Fabrizio, S. Faigler, A. J. Falcão, M. Farràs Casas, F. Faye, L. Federici, G. Fedorets, J. Fernández-Hernández, P. Fernique, A. Fienga, F. Figueras, F. Filippi, K. Findeisen, A. Fonti, M. Fouesneau, E. Fraile, M. Fraser, J. Fuchs, R. Furnell, M. Gai, S. Galleti, L. Galluccio, D. Garabato, F. García-Sedano, P. Garé, A. Garofalo, N. Garralda, P. Gavras, J. Gerssen, R. Geyer, G. Gilmore, S. Girona, G. Giuffrida, M. Gomes, A. González-Marcos, J. González-Núñez, J. J. González-Vidal, M. Granvik, A. Guerrier, P. Guillout, J. Guiraud, A. Gúrpide, R. Gutiérrez-Sánchez, L. P. Guy, R. Haigron, D. Hatzidimitriou, M. Haywood, U. Heiter, A. Helmi, D. Hobbs, W. Hofmann, B. Holl, G. Holland, J. A. S. Hunt, A. Hypki, V. Icardi, M. Irwin, G. Jevardat de Fombelle, P. Jofré, P. G. Jonker, A. Jorissen, F. Julbe, A. Karampelas, A. Kochoska, R. Kohley, K. Kolenberg, E. Kontizas, S. E. Koposov, G. Kordopatis, P. Koubsky, A. Kowalczyk, A. Krone-Martins, M. Kudryashova, I. Kull, R. K. Bachchan, F. Lacoste-Seris, A. F. Lanza, J. B. Lavigne, C. Le Poncin-Lafitte, Y. Lebreton, T. Lebzelter, S. Leccia, N. Leclerc, I. Lecoeur-Taibi, V. Lemaitre, H. Lenhardt, F. Leroux, S. Liao, E. Licata, H. E. P. Lindstrøm, T. A. Lister, E. Livanou, A. Lobel, W. Löffler, M. López, A. Lopez-Lozano, D. Lorenz, T. Loureiro, I. MacDonald, T. Magalhães Fernandes, S. Managau, R. G. Mann, G. Mantelet, O. Marchal, J. M. Marchant, M. Marconi, J. Marie, S. Marinoni, P. M. Marrese, G. Marschalkó, D. J. Marshall, J. M. Martín-Fleitas, M. Martino, N. Mary, G. Matijevič, T. Mazeh, P. J. McMillan, S. Messina, A. Mestre, D. Michalik, N. R. Millar, B. M. H. Miranda, D. Molina, R. Molinaro, M. Molinaro, L. Molnár, M. Moniez, P. Montegriffo, D. Monteiro, R. Mor, A. Mora, R. Morbidelli, T. Morel, S. Morgenthaler, T. Morley, D. Morris, A. F. Mulone, T. Muraveva, I. Musella, J. Narbonne, G. Nelemans, L. Nicastro, L. Noval, C. Ordénovic, J. Ordieres-Meré, P. Osborne, C. Pagani, I. Pagano, F. Pailler, H. Palacin, L. Palaversa, P. Parsons, T. Paulsen, M. Pecoraro, R. Pedrosa, H. Pentikäinen, J. Pereira, B. Pichon, A. M. Piersimoni, F. X. Pineau, E. Plachy, G. Plum, E. Poujoulet, A. Prša, L. Pulone, S. Ragaini, S. Rago, N. Rambaux, M. Ramos-Lerate, P. Ranalli, G. Rauw, A. Read, S. Regibo, F. Renk, C. Reylé, R. A. Ribeiro, L. Rimoldini, V. Ripepi, A. Riva, G. Rixon, M. Roelens, M. Romero-Gómez, N. Rowell, F. Royer, A. Rudolph, L. Ruiz-Dern, G. Sadowski, T. Sagristà Sellés, J. Sahlmann, J. Salgado, E. Salguero, M. Sarasso, H. Savietto, A. Schnorhk, M. Schultheis, E. Sciacca, M. Segol, J. C. Segovia, D. Segransan, E. Serpell, I. C. Shih, R. Smareglia, R. L. Smart, C. Smith, E. Solano, F. Solitro, R. Sordo, S. Soria Nieto, J. Souchay, A. Spagna, F. Spoto, U. Stampa, I. A. Steele, H. Steidelmüller, C. A. Stephenson, H. Stoev, F. F. Suess, M. Süveges, J. Surdej, L. Sz-

abados, E. Szegedi-Elek, D. Tapiador, F. Taris, G. Tauran, M. B. Taylor, R. Teixeira, D. Terrett, B. Tingley, S. C. Trager, C. Turon, A. Ulla, E. Utrilla, G. Valentini, A. van Elteren, E. Van Hemelryck, M. van Leeuwen, M. Varadi, A. Vecchiato, J. Veljanoski, T. Via, D. Vicente, S. Vogt, H. Voss, V. Votruba, S. Voutsinas, G. Walmsley, M. Weiler, K. Weingrill, D. Werner, T. Wevers, G. Whitehead, Ł. Wyrzykowski, A. Yoldas, M. Žerjal, S. Zucker, C. Zurbach, T. Zwitter, A. Alecu, M. Allen, C. Allende Prieto, A. Amorim, G. Anglada-Escudé, V. Arsenijevic, S. Azaz, P. Balm, M. Beck, H. H. Bernstein, L. Bigot, A. Bijaoui, C. Blasco, M. Bonfigli, G. Bono, S. Boudreault, A. Bressan, S. Brown, P. M. Brunet, P. Bunclark, R. Buonanno, A. G. Butkevich, C. Carret, C. Carrion, L. Chemin, F. Chéreau, L. Corcione, E. Darmigny, K. S. de Boer, P. de Teodoro, P. T. de Zeeuw, C. Delle Luche, C. D. Domingues, P. Dubath, F. Fodor, B. Frézouls, A. Fries, D. Fustes, D. Fyfe, E. Gallardo, J. Gallegos, D. Gardiol, M. Gebran, A. Gomboc, A. Gómez, E. Grux, A. Gueguen, A. Heyrovsky, J. Hoar, G. Iannicola, Y. Isasi Parache, A. M. Janotto, E. Joliet, A. Jonckheere, R. Keil, D. W. Kim, P. Klagyivik, J. Klar, J. Knude, O. Kochukhov, I. Kolka, J. Kos, A. Kutka, V. Lainey, D. LeBouquin, C. Liu, D. Loreggia, V. V. Makarov, M. G. Marseille, C. Martayan, O. Martinez-Rubi, B. Massart, F. Meynadier, S. Mignot, U. Munari, A. T. Nguyen, T. Nordlander, P. Ocvirk, K. S. O'Flaherty, A. Olias Sanz, P. Ortiz, J. Osorio, D. Oszkiewicz, A. Ouzounis, M. Palmer, P. Park, E. Pasquato, C. Peltzer, J. Peralta, F. Péturaud, T. Pieniluoma, E. Pigozzi, J. Poels, G. Prat, T. Prod'homme, F. Raison, J. M. Rebordao, D. Risquez, B. Rocca-Volmerange, S. Rosen, M. I. Ruiz-Fuertes, F. Russo, S. Sembay, I. Serraller Vizcaino, A. Short, A. Siebert, H. Silva, D. Sinachopoulos, E. Slezak, M. Soffel, D. Sosnowska, V. Straižys, M. ter Linden, D. Terrell, S. Theil, C. Tiede, L. Troisi, P. Tsalmantza, D. Tur, M. Vaccari, F. Vachier, P. Valles, W. Van Hamme, L. Veltz, J. Virtanen, J. M. Wallut, R. Wichmann, M. I. Wilkinson, H. Ziaeepour, and S. Zschocke. The Gaia mission. *Astronomy and Astrophysics*, 595:A1, Nov. 2016.

[89] G. Gatewood and H. Eichhorn. An unsuccessful search for a planetary companion of Barnard's star BD +4 3561. *The Astronomical Journal*, 78:769–776, Oct 1973.

[90] B. S. Gaudi, K. G. Stassun, K. A. Collins, T. G. Beatty, G. Zhou, D. W. Latham, A. Bieryla, J. D. Eastman, R. J. Siverd, J. R. Crepp, E. J. Gonzales, D. J. Stevens, L. A. Buchhave, J. Pepper, M. C. Johnson, K. D. Colon, E. L. N. Jensen, J. E. Rodriguez, V. Bozza, S. C. Novati, G. D'Ago, M. T. Dumont, T. Ellis, C. Gaillard, H. Jang-Condell, D. H. Kasper, A. Fukui, J. Gregorio, A. Ito, J. F. Kielkopf, M. Manner, K. Matt, N. Narita, T. E. Oberst, P. A. Reed, G. Scarpetta, D. C. Stephens, R. R. Yeigh, R. Zambelli, B. J. Fulton, A. W. Howard, D. J. James, M. Penny, D. Bayliss, I. A. Curtis, D. L. Depoy, G. A. Esquerdo, A. Gould, M. D. Joner, R. B. Kuhn, J. Labadie-Bartz, M. B. Lund, J. L. Marshall, K. K. McLeod, R. W. Pogge, H. Relles, C. Stockdale, T. G. Tan, M. Trueblood, and P. Trueblood. A giant planet undergoing extreme-ultraviolet irradiation by its hot massive-star host. *Nature*, 546(7659):514–518, June 2017.

[91] B. S. Gaudi and J. N. Winn. Prospects for the Characterization and Confirmation of

Transiting Exoplanets via the Rossiter-McLaughlin Effect. *The Astrophysical Journal*, 655(1):550–563, Jan. 2007.

[92] S. R. Gibson, A. W. Howard, G. Marcy, J. Edelstein, E. H. Wishnow, and C. L. Poppett. KPF: Keck Planet Finder. In C. J. Evans, L. Simard, and H. Takami, editors, *Ground-based and Airborne Instrumentation for Astronomy VI*, volume 9908 of *Society of Photo-Optical Instrumentation Engineers (SPIE) Conference Series*, page 990870, Aug. 2016.

[93] G. J. Gilbert and D. C. Fabrycky. An Information Theoretic Framework for Classifying Exoplanetary System Architectures. *The Astronomical Journal*, 159(6):281, June 2020.

[94] H. A. C. Giles, A. Collier Cameron, and R. D. Haywood. A Kepler study of starspot lifetimes with respect to light-curve amplitude and spectral type. *Monthly Notices of the Royal Astronomical Society*, 472(2):1618–1627, Dec. 2017.

[95] J. E. Gizis. M-Subdwarfs: Spectroscopic Classification and the Metallicity Scale. *The Astronomical Journal*, 113:806–822, Feb. 1997.

[96] J. Gomes da Silva, N. C. Santos, I. Boisse, X. Dumusque, and C. Lovis. On the long-term correlation between the flux in the Ca ii H & K and Hα lines for FGK stars. *Astronomy and Astrophysics*, 566:A66, June 2014.

[97] P. C. Gregory. An apodized Kepler periodogram for separating planetary and stellar activity signals. *Monthly Notices of the Royal Astronomical Society*, 458(3):2604–2633, May 2016.

[98] K. Griest and N. Safizadeh. The Use of High-Magnification Microlensing Events in Discovering Extrasolar Planets. *The Astrophysical Journal*, 500(1):37–50, June 1998.

[99] N. C. Hara, F. Bouchy, M. Stalport, I. Boisse, J. Rodrigues, J. B. Delisle, A. Santerne, G. W. Henry, L. Arnold, N. Astudillo-Defru, S. Borgniet, X. Bonfils, V. Bourrier, B. Brugger, B. Courcol, S. Dalal, M. Deleuil, X. Delfosse, O. Demangeon, R. F. Díaz, X. Dumusque, T. Forveille, G. Hébrard, M. J. Hobson, F. Kiefer, T. Lopez, L. Mignon, O. Mousis, C. Moutou, F. Pepe, J. Rey, N. C. Santos, D. Ségransan, S. Udry, and P. A. Wilson. The SOPHIE search for northern extrasolar planets. XVI. HD 158259: A compact planetary system in a near-3:2 mean motion resonance chain. *Astronomy and Astrophysics*, 636:L6, Apr. 2020.

[100] N. C. Hara, G. Boué, J. Laskar, and A. C. M. Correia. Radial velocity data analysis with compressed sensing techniques. *Monthly Notices of the Royal Astronomical Society*, 464(1):1220–1246, Jan. 2017.

[101] A. P. Hatzes. The Radial Velocity Detection of Earth-mass Planets in the Presence of Activity Noise: The Case of α Centauri Bb. *The Astrophysical Journal*, 770(2):133, June 2013.

[102] A. P. Hatzes, R. Dvorak, G. Wuchterl, P. Guterman, M. Hartmann, M. Fridlund, D. Gandolfi, E. Guenther, and M. Pätzold. An investigation into the radial velocity variations of CoRoT-7. *Astronomy and Astrophysics*, 520:A93, Sept. 2010.

[103] R. D. Haywood, A. Collier Cameron, D. Queloz, S. C. C. Barros, M. Deleuil, R. Fares, M. Gillon, A. F. Lanza, C. Lovis, C. Moutou, F. Pepe, D. Pollacco, A. Santerne, D. Ségransan, and Y. C. Unruh. Planets and stellar activity: hide and seek in the CoRoT-7 system. *Monthly Notices of the Royal Astronomical Society*, 443(3):2517–2531, Sept. 2014.

[104] M. Y. He, E. B. Ford, and D. Ragozzine. Architectures of Exoplanetary Systems. II. An Increase in Inner Planetary System Occurrence toward Later Spectral Types for Kepler's FGK Dwarfs. *The Astronomical Journal*, 161(1):16, Jan. 2021.

[105] J. L. Hershey. Astrometric analysis of the field of AC +65 6955 from plates taken with the Sproul 24-inch refractor. *The Astronomical Journal*, 78:421–425, Jun 1973.

[106] M. Hippke and R. Heller. Optimized transit detection algorithm to search for periodic transits of small planets. *Astronomy and Astrophysics*, 623:A39, Mar. 2019.

[107] R. J. Holcomb, P. Robertson, P. Hartigan, R. J. Oelkers, and C. Robinson. SpinSpotter: Stellar rotation periods from high-cadence photometry calculator. Astrophysics Source Code Library, record ascl:2206.014, June 2022.

[108] A. W. Howard, J. A. Johnson, G. W. Marcy, D. A. Fischer, J. T. Wright, D. Bernat, G. W. Henry, K. M. G. Peek, H. Isaacson, K. Apps, M. Endl, W. D. Cochran, J. A. Valenti, J. Anderson, and N. E. Piskunov. The California Planet Survey. I. Four New Giant Exoplanets. *The Astrophysical Journal*, 721:1467–1481, Oct. 2010.

[109] A. W. Howard, G. Marcy, S. T. Bryson, J. M. Jenkins, J. F. Rowe, N. M. Batalha, W. J. Borucki, D. G. Koch, E. W. Dunham, I. Gautier, Thomas N., J. Van Cleve, W. D. Cochran, D. W. Latham, J. J. Lissauer, G. Torres, T. M. Brown, R. L. Gilliland, L. A. Buchhave, D. A. Caldwell, J. Christensen-Dalsgaard, D. Ciardi, F. Fressin, M. R. Haas, S. B. Howell, H. Kjeldsen, S. Seager, L. Rogers, D. D. Sasselov, J. H. Steffen, G. S. Basri, D. Charbonneau, J. Christiansen, B. Clarke, A. Dupree, D. C. Fabrycky, D. A. Fischer, E. B. Ford, J. J. Fortney, J. Tarter, F. R. Girouard, M. J. Holman, J. A. Johnson, T. C. Klaus, P. Machalek, A. V. Moorhead, R. C. Morehead, D. Ragozzine, P. Tenenbaum, J. D. Twicken, S. N. Quinn, H. Isaacson, A. Shporer, P. W. Lucas, L. M. Walkowicz, W. F. Welsh, A. Boss, E. Devore, A. Gould, J. C. Smith, R. L. Morris, A. Prsa, T. D. Morton, M. Still, S. E. Thompson, F. Mullally, M. Endl, and P. J. MacQueen. Planet Occurrence within 0.25 AU of Solar-type Stars from Kepler. *The Astrophysical Journal, Supplement*, 201(2):15, Aug. 2012.

[110] D. C. Hsu, E. B. Ford, and R. Terrien. Occurrence Rates of Planets Orbiting M Stars: Applying ABC to Kepler DR25, Gaia DR2, and 2MASS Data. *arXiv e-prints*, page arXiv:2002.02573, Feb. 2020.

[111] D. Huber, J. Zinn, M. Bojsen-Hansen, M. Pinsonneault, C. Sahlholdt, A. Serenelli, V. Silva Aguirre, K. Stassun, D. Stello, J. Tayar, F. Bastien, T. R. Bedding, L. A. Buchhave, W. J. Chaplin, G. R. Davies, R. A. García, D. W. Latham, S. Mathur, B. Mosser, and S. Sharma. Asteroseismology and Gaia: Testing Scaling Relations Using 2200 Kepler Stars with TGAS Parallaxes. *The Astrophysical Journal*, 844(2):102, Aug. 2017.

[112] H. Isaacson and D. Fischer. Chromospheric Activity and Jitter Measurements for 2630 Stars on the California Planet Search. *The Astrophysical Journal*, 725(1):875–885, Dec. 2010.

[113] H. Isaacson and D. Fischer. Chromospheric Activity and Jitter Measurements for 2630 Stars on the California Planet Search. *The Astrophysical Journal*, 725(1):875–885, Dec. 2010.

[114] J. M. Jenkins, J. D. Twicken, S. McCauliff, J. Campbell, D. Sanderfer, D. Lung, M. Mansouri-Samani, F. Girouard, P. Tenenbaum, T. Klaus, J. C. Smith, D. A. Caldwell, A. D. Chacon, C. Henze, C. Heiges, D. W. Latham, E. Morgan, D. Swade, S. Rinehart, and R. Vanderspek. The TESS science processing operations center. In G. Chiozzi and J. C. Guzman, editors, *Software and Cyberinfrastructure for Astronomy IV*, volume 9913 of *Society of Photo-Optical Instrumentation Engineers (SPIE) Conference Series*, page 99133E, Aug. 2016.

[115] D. Jontof-Hutter, J. J. Lissauer, J. F. Rowe, and D. C. Fabrycky. Kepler-79's Low Density Planets. *The Astrophysical Journal*, 785(1):15, Apr. 2014.

[116] C. Jurgenson, D. Fischer, T. McCracken, D. Sawyer, A. Szymkowiak, A. Davis, G. Muller, and F. Santoro. EXPRES: a next generation RV spectrograph in the search for earth-like worlds. In C. J. Evans, L. Simard, and H. Takami, editors, *Ground-based and Airborne Instrumentation for Astronomy VI*, volume 9908 of *Society of Photo-Optical Instrumentation Engineers (SPIE) Conference Series*, page 99086T, Aug. 2016.

[117] S. Kanodia and J. Wright. Python Leap Second Management and Implementation of Precise Barycentric Correction (barycorrpy). *Research Notes of the American Astronomical Society*, 2:4, Jan 2018.

[118] K. F. Kaplan, C. F. Bender, R. Terrien, J. P. Ninan, A. Roy, and S. Mahadevan. The algorithms behind the HPF and NEID pipeline. The 28th International Astronomical Data Analysis Software & Systems, Nov. 2018.

[119] R. E. Kass and A. E. Raftery. Bayes factors. *Journal of the American Statistical Association*, 90(430):773–795, 1995.

[120] E. M. R. Kempton, J. L. Bean, D. R. Louie, D. Deming, D. D. B. Koll, M. Mansfield, J. L. Christiansen, M. López-Morales, M. R. Swain, R. T. Zellem, S. Ballard, T. Barclay, J. K. Barstow, N. E. Batalha, T. G. Beatty, Z. Berta-Thompson, J. Birkby, L. A. Buchhave, D. Charbonneau, N. B. Cowan, I. Crossfield, M. de Val-Borro, R. Doyon, D. Dragomir, E. Gaidos, K. Heng, R. Hu, S. R. Kane, L. Kreidberg, M. Mallonn, C. V.

Morley, N. Narita, V. Nascimbeni, E. Pallé, E. V. Quintana, E. Rauscher, S. Seager, E. L. Shkolnik, D. K. Sing, A. Sozzetti, K. G. Stassun, J. A. Valenti, and C. von Essen. A Framework for Prioritizing the TESS Planetary Candidates Most Amenable to Atmospheric Characterization. *Publications of the Astronomical Society of the Pacific*, 130(993):114401, Nov. 2018.

[121] D. M. Kipping. Parametrizing the exoplanet eccentricity distribution with the beta distribution. *Monthly Notices of the Royal Astronomical Society*, 434:L51–L55, July 2013.

[122] Y. Kozai. Secular perturbations of asteroids with high inclination and eccentricity. *The Astronomical Journal*, 67:591–598, Nov. 1962.

[123] M. Kürster, M. Endl, F. Rouesnel, S. Els, A. Kaufer, S. Brillant, A. P. Hatzes, S. H. Saar, and W. D. Cochran. The low-level radial velocity variability in Barnard's star (= GJ 699). Secular acceleration, indications for convective redshift, and planet mass limits. *Astronomy and Astrophysics*, 403:1077–1087, June 2003.

[124] K. Laliotis, J. A. Burt, E. E. Mamajek, Z. Li, V. Perdelwitz, J. Zhao, R. P. Butler, B. Holden, L. Rosenthal, B. J. Fulton, F. Feng, S. R. Kane, J. Bailey, B. Carter, J. D. Crane, E. Furlan, C. L. Gnilka, S. B. Howell, G. Laughlin, S. A. Shectman, J. K. Teske, C. G. Tinney, S. S. Vogt, S. Xuesong Wang, and R. A. Wittenmyer. Doppler Constraints on Planetary Companions to Nearby Sun-like Stars: An Archival Radial Velocity Survey of Southern Targets for Proposed NASA Direct Imaging Missions. *arXiv e-prints*, page arXiv:2302.10310, Feb. 2023.

[125] E. J. Lee and E. Chiang. Breeding Super-Earths and Birthing Super-puffs in Transitional Disks. *The Astrophysical Journal*, 817(2):90, Feb. 2016.

[126] A. Leleu, Y. Alibert, N. C. Hara, M. J. Hooton, T. G. Wilson, P. Robutel, J. B. Delisle, J. Laskar, S. Hoyer, C. Lovis, E. M. Bryant, E. Ducrot, J. Cabrera, L. Delrez, J. S. Acton, V. Adibekyan, R. Allart, C. Allende Prieto, R. Alonso, D. Alves, D. R. Anderson, D. Angerhausen, G. Anglada Escudé, J. Asquier, D. Barrado, S. C. C. Barros, W. Baumjohann, D. Bayliss, M. Beck, T. Beck, A. Bekkelien, W. Benz, N. Billot, A. Bonfanti, X. Bonfils, F. Bouchy, V. Bourrier, G. Boué, A. Brandeker, C. Broeg, M. Buder, A. Burdanov, M. R. Burleigh, T. Bárczy, A. C. Cameron, S. Chamberlain, S. Charnoz, B. F. Cooke, C. Corral Van Damme, A. C. M. Correia, S. Cristiani, M. Damasso, M. B. Davies, M. Deleuil, O. D. S. Demangeon, B. O. Demory, P. Di Marcantonio, G. Di Persio, X. Dumusque, D. Ehrenreich, A. Erikson, P. Figueira, A. Fortier, L. Fossati, M. Fridlund, D. Futyan, D. Gandolfi, A. García Muñoz, L. J. Garcia, S. Gill, E. Gillen, M. Gillon, M. R. Goad, J. I. González Hernández, M. Guedel, M. N. Günther, J. Haldemann, B. Henderson, K. Heng, A. E. Hogan, K. Isaak, E. Jehin, J. S. Jenkins, A. Jordán, L. Kiss, M. H. Kristiansen, K. Lam, B. Lavie, A. Lecavelier des Etangs, M. Lendl, J. Lillo-Box, G. Lo Curto, D. Magrin, C. J. A. P. Martins, P. F. L. Maxted, J. McCormac, A. Mehner, G. Micela, P. Molaro, M. Moyano, C. A. Murray, V. Nascimbeni, N. J. Nunes, G. Olofsson, H. P. Osborn, M. Oshagh, R. Ottensamer, I. Pagano, E. Pallé, P. P. Pedersen, F. A. Pepe, C. M. Persson, G. Peter,

G. Piotto, G. Polenta, D. Pollacco, E. Poretti, F. J. Pozuelos, D. Queloz, R. Ragazzoni, N. Rando, F. Ratti, H. Rauer, L. Raynard, R. Rebolo, C. Reimers, I. Ribas, N. C. Santos, G. Scandariato, J. Schneider, D. Sebastian, M. Sestovic, A. E. Simon, A. M. S. Smith, S. G. Sousa, A. Sozzetti, M. Steller, A. Suárez Mascareño, G. M. Szabó, D. Ségransan, N. Thomas, S. Thompson, R. H. Tilbrook, A. Triaud, O. Turner, S. Udry, V. Van Grootel, H. Venus, F. Verrecchia, J. I. Vines, N. A. Walton, R. G. West, P. J. Wheatley, D. Wolter, and M. R. Zapatero Osorio. Six transiting planets and a chain of Laplace resonances in TOI-178. *arXiv e-prints*, page arXiv:2101.09260, Jan. 2021.

[127] A. S. J. Lin, A. Monson, S. Mahadevan, J. P. Ninan, S. Halverson, C. Nitroy, C. F. Bender, S. E. Logsdon, S. Kanodia, R. C. Terrien, A. Roy, J. K. Luhn, A. F. Gupta, E. B. Ford, F. Hearty, R. R. Laher, E. Hunting, W. R. McBride, N. I. Salazar Rivera, J. Rajagopal, M. J. Wolf, P. Robertson, J. T. Wright, C. H. Blake, C. I. Cañas, E. Lubar, M. W. McElwain, L. W. Ramsey, C. Schwab, and G. Stefansson. Observing the Sun as a Star: Design and Early Results from the NEID Solar Feed. *The Astronomical Journal*, 163(4):184, Apr. 2022.

[128] L. Lindegren, S. A. Klioner, J. Hernández, A. Bombrun, M. Ramos-Lerate, H. Steidelmüller, U. Bastian, M. Biermann, A. de Torres, E. Gerlach, R. Geyer, T. Hilger, D. Hobbs, U. Lammers, P. J. McMillan, C. A. Stephenson, J. Castañeda, M. Davidson, C. Fabricius, G. Gracia-Abril, J. Portell, N. Rowell, D. Teyssier, F. Torra, S. Bartolomé, M. Clotet, N. Garralda, J. J. González-Vidal, J. Torra, U. Abbas, M. Altmann, E. Anglada Varela, L. Balaguer-Núñez, Z. Balog, C. Barache, U. Becciani, M. Bernet, S. Bertone, L. Bianchi, S. Bouquillon, A. G. A. Brown, B. Bucciarelli, D. Busonero, A. G. Butkevich, R. Buzzi, R. Cancelliere, T. Carlucci, P. Charlot, M. R. L. Cioni, M. Crosta, C. Crowley, E. F. del Peloso, E. del Pozo, R. Drimmel, P. Esquej, A. Fienga, E. Fraile, M. Gai, M. Garcia-Reinaldos, R. Guerra, N. C. Hambly, M. Hauser, K. Janßen, S. Jordan, Z. Kostrzewa-Rutkowska, M. G. Lattanzi, S. Liao, E. Licata, T. A. Lister, W. Löffler, J. M. Marchant, A. Masip, F. Mignard, A. Mints, D. Molina, A. Mora, R. Morbidelli, C. P. Murphy, C. Pagani, P. Panuzzo, X. Peñalosa Esteller, E. Poggio, P. Re Fiorentin, A. Riva, A. Sagristà Sellés, V. Sanchez Gimenez, M. Sarasso, E. Sciacca, H. I. Siddiqui, R. L. Smart, D. Souami, A. Spagna, I. A. Steele, F. Taris, E. Utrilla, W. van Reeven, and A. Vecchiato. Gaia Early Data Release 3: The astrometric solution. *arXiv e-prints*, page arXiv:2012.03380, Dec. 2020.

[129] Y. Lithwick and S. Naoz. The Eccentric Kozai Mechanism for a Test Particle. *The Astrophysical Journal*, 742(2):94, Dec. 2011.

[130] Y. Lithwick, J. Xie, and Y. Wu. Extracting Planet Mass and Eccentricity from TTV Data. *The Astrophysical Journal*, 761(2):122, Dec. 2012.

[131] G. Lo Curto, F. Pepe, G. Avila, H. Boffin, S. Bovay, B. Chazelas, A. Coffinet, M. Fleury, I. Hughes, C. Lovis, C. Maire, A. Manescau, L. Pasquini, S. Rihs, P. Sinclaire, and S. Udry. HARPS Gets New Fibres After 12 Years of Operations. *The Messenger*, 162:9–15, Dec. 2015.

[132] N. R. Lomb. Least-Squares Frequency Analysis of Unequally Spaced Data. , 39(2):447–462, Feb. 1976.

[133] E. D. Lopez and J. J. Fortney. Understanding the Mass-Radius Relation for Sub-neptunes: Radius as a Proxy for Composition. *The Astrophysical Journal*, 792(1):1, Sept. 2014.

[134] J. Lubin, P. Robertson, G. Stefansson, J. Ninan, S. Mahadevan, M. Endl, E. Ford, J. T. Wright, C. Beard, C. Bender, W. D. Cochran, S. A. Diddams, C. Fredrick, S. Halverson, S. Kanodia, A. J. Metcalf, L. Ramsey, A. Roy, C. Schwab, and R. Terrien. Stellar Activity Manifesting at a One-year Alias Explains Barnard b as a False Positive. *The Astronomical Journal*, 162(2):61, Aug. 2021.

[135] J. Lubin, J. Van Zandt, R. Holcomb, L. M. Weiss, E. A. Petigura, P. Robertson, J. M. Akana Murphy, N. Scarsdale, K. Batygin, A. S. Polanski, N. M. Batalha, I. J. M. Crossfield, C. Dressing, B. Fulton, A. W. Howard, D. Huber, H. Isaacson, S. R. Kane, A. Roy, C. Beard, S. Blunt, A. Chontos, F. Dai, P. A. Dalba, K. Gary, S. Giacalone, M. L. Hill, A. Mayo, T. Močnik, M. R. Kosiarek, M. Rice, R. A. Rubenzahl, D. W. Latham, S. Seager, J. N. Winn, and K. Gary. TESS-Keck Survey. IX. Masses of Three Sub-Neptunes Orbiting HD 191939 and the Discovery of a Warm Jovian plus a Distant Substellar Companion. *The Astronomical Journal*, 163(2):101, Feb. 2022.

[136] J. Lubin, J. Van Zandt, R. Holcomb, L. M. Weiss, E. A. Petigura, P. Robertson, J. M. Akana Murphy, N. Scarsdale, K. Batygin, A. S. Polanski, N. M. Batalha, I. J. M. Crossfield, C. Dressing, B. Fulton, A. W. Howard, D. Huber, H. Isaacson, S. R. Kane, A. Roy, C. Beard, S. Blunt, A. Chontos, F. Dai, P. A. Dalba, K. Gary, S. Giacalone, M. L. Hill, A. Mayo, T. Močnik, M. R. Kosiarek, M. Rice, R. A. Rubenzahl, D. W. Latham, S. Seager, J. N. Winn, and K. Gary. TESS-Keck Survey. IX. Masses of Three Sub-Neptunes Orbiting HD 191939 and the Discovery of a Warm Jovian plus a Distant Substellar Companion. *The Astronomical Journal*, 163(2):101, Feb. 2022.

[137] R. Luque and E. Pallé. Density, not radius, separates rocky and water-rich small planets orbiting M dwarf stars. *Science*, 377(6611):1211–1214, Sept. 2022.

[138] J. Lustig-Yaeger, G. Fu, E. M. May, K. N. Ortiz Ceballos, S. E. Moran, S. Peacock, K. B. Stevenson, M. López-Morales, R. J. MacDonald, L. C. Mayorga, D. K. Sing, K. S. Sotzen, J. A. Valenti, J. Adams, M. K. Alam, N. E. Batalha, K. A. Bennett, J. Gonzalez-Quiles, J. Kirk, E. Kruse, J. D. Lothringer, Z. Rustamkulov, and H. R. Wakeford. A JWST transmission spectrum of a nearby Earth-sized exoplanet. *arXiv e-prints*, page arXiv:2301.04191, Jan. 2023.

[139] B. Ma, J. Ge, M. Muterspaugh, M. A. Singer, G. W. Henry, J. I. González Hernández, S. Sithajan, S. Jeram, M. Williamson, K. Stassun, B. Kimock, F. Varosi, S. Schofield, J. Liu, S. Powell, A. Cassette, H. Jakeman, L. Avner, N. Grieves, R. Barnes, B. Zhao, S. Gilda, J. Grantham, G. Stafford, D. Savage, S. Bland, and B. Ealey. The first super-Earth detection from the high cadence and high radial velocity precision Dharma Planet Survey. *Monthly Notices of the Royal Astronomical Society*, 480(2):2411–2422, Oct. 2018.

[140] M. G. MacDougall, E. A. Petigura, I. Angelo, J. Lubin, N. M. Batalha, C. Beard, A. Behmard, S. Blunt, C. Brinkman, A. Chontos, I. J. M. Crossfield, F. Dai, P. A. Dalba, C. Dressing, B. Fulton, S. Giacalone, M. L. Hill, A. W. Howard, D. Huber, H. Isaacson, S. R. Kane, A. Mayo, T. Močnik, J. M. Akana Murphy, A. Polanski, M. Rice, P. Robertson, L. J. Rosenthal, A. Roy, R. A. Rubenzahl, N. Scarsdale, E. Turtelboom, J. V. Zandt, L. M. Weiss, E. Matthews, J. M. Jenkins, D. W. Latham, G. R. Ricker, S. Seager, R. K. Vanderspek, J. N. Winn, C. E. Brasseur, J. Doty, M. Fausnaugh, N. Guerrero, C. Henze, M. B. Lund, and A. Shporer. The TESS-Keck Survey. VI. Two Eccentric Sub-Neptunes Orbiting HIP-97166. *The Astronomical Journal*, 162(6):265, Dec. 2021.

[141] M. G. MacDougall, E. A. Petigura, T. Fetherolf, C. Beard, J. Lubin, I. Angelo, N. M. Batalha, A. Behmard, S. Blunt, C. Brinkman, A. Chontos, I. J. M. Crossfield, F. Dai, P. A. Dalba, C. Dressing, B. Fulton, S. Giacalone, M. L. Hill, A. W. Howard, D. Huber, H. Isaacson, S. R. Kane, M. Kosiarek, A. Mayo, T. Močnik, J. M. Akana Murphy, D. Pidhorodetska, A. Polanski, M. Rice, P. Robertson, L. J. Rosenthal, A. Roy, R. A. Rubenzahl, N. Scarsdale, E. V. Turtelboom, D. Tyler, J. Van Zandt, L. M. Weiss, E. Esparza-Borges, A. Fukui, K. Isogai, K. Kawauchi, M. Mori, F. Murgas, N. Narita, T. Nishiumi, E. Palle, H. Parviainen, N. Watanabe, J. M. Jenkins, D. W. Latham, G. R. Ricker, S. Seager, R. K. Vanderspek, J. N. Winn, A. Bieryla, D. A. Caldwell, D. Dragomir, M. M. Fausnaugh, I. Mireles, and D. R. Rodriguez. The TESS-Keck Survey. XIII. An Eccentric Hot Neptune with a Similar-mass Outer Companion around TOI-1272. *The Astronomical Journal*, 164(3):97, Sept. 2022.

[142] S. Mahadevan, L. Ramsey, C. Bender, R. Terrien, J. T. Wright, S. Halverson, F. Hearty, M. Nelson, A. Burton, S. Redman, S. Osterman, S. Diddams, J. Kasting, M. Endl, and R. Deshpande. *The habitable-zone planet finder: a stabilized fiber-fed NIR spectrograph for the Hobby-Eberly Telescope*, volume 8446 of *Society of Photo-Optical Instrumentation Engineers (SPIE) Conference Series*, page 84461S. 2012.

[143] S. Mahadevan, L. W. Ramsey, R. Terrien, S. Halverson, A. Roy, F. Hearty, E. Levi, G. K. Stefansson, P. Robertson, C. Bender, C. Schwab, and M. Nelson. The Habitable-zone Planet Finder: A status update on the development of a stabilized fiber-fed near-infrared spectrograph for the for the Hobby-Eberly telescope. In *Ground-based and Airborne Instrumentation for Astronomy V*, volume 9147 of *Society of Photo-Optical Instrumentation Engineers (SPIE) Conference Series*, page 91471G, Jul 2014.

[144] J. Maldonado, D. F. Phillips, X. Dumusque, A. Collier Cameron, R. D. Haywood, A. F. Lanza, G. Micela, A. Mortier, S. H. Saar, A. Sozzetti, K. Rice, T. Milbourne, M. Cecconi, H. M. Cegla, R. Cosentino, J. Costes, A. Ghedina, M. Gonzalez, J. Guerra, N. Hernández, C. H. Li, M. Lodi, L. Malavolta, E. Molinari, F. Pepe, G. Piotto, E. Poretti, D. Sasselov, J. San Juan, S. Thompson, S. Udry, and C. Watson. Temporal evolution and correlations of optical activity indicators measured in Sun-as-a-star observations. *Astronomy and Astrophysics*, 627:A118, July 2019.

[145] P.-S. Marquis de Laplace. Traite de mecanique celeste. *"Traite de Mecanique Celeste"*, Ch. VII:569–634, 1825.

[146] K. Masuda. Very Low Density Planets around Kepler-51 Revealed with Transit Timing Variations and an Anomaly Similar to a Planet-Planet Eclipse Event. *The Astrophysical Journal*, 783(1):53, Mar. 2014.

[147] M. Mayor, F. Pepe, D. Queloz, F. Bouchy, G. Rupprecht, G. Lo Curto, G. Avila, W. Benz, J. L. Bertaux, X. Bonfils, T. Dall, H. Dekker, B. Delabre, W. Eckert, M. Fleury, A. Gilliotte, D. Gojak, J. C. Guzman, D. Kohler, J. L. Lizon, A. Longinotti, C. Lovis, D. Megevand, L. Pasquini, J. Reyes, J. P. Sivan, D. Sosnowska, R. Soto, S. Udry, A. van Kesteren, L. Weber, and U. Weilenmann. Setting New Standards with HARPS. *The Messenger*, 114:20–24, Dec. 2003.

[148] M. Mayor and D. Queloz. A Jupiter-mass companion to a solar-type star. *Nature*, 378(6555):355–359, Nov 1995.

[149] T. Mazeh, T. Holczer, and S. Faigler. Dearth of short-period Neptunian exoplanets: A desert in period-mass and period-radius planes. *Astronomy and Astrophysics*, 589:A75, May 2016.

[150] D. B. McLaughlin. Some results of a spectrographic study of the Algol system. *The Astrophysical Journal*, 60:22–31, July 1924.

[151] A. McQuillan, T. Mazeh, and S. Aigrain. Rotation Periods of 34,030 Kepler Main-sequence Stars: The Full Autocorrelation Sample. *The Astrophysical Journal, Supplement*, 211(2):24, Apr 2014.

[152] A. J. Metcalf, T. Anderson, C. F. Bender, S. Blakeslee, W. Brand, D. R. Carlson, W. D. Cochran, S. A. Diddams, M. Endl, C. Fredrick, S. Halverson, D. D. Hickstein, F. Hearty, J. Jennings, S. Kanodia, K. F. Kaplan, E. Levi, E. Lubar, S. Mahadevan, A. Monson, J. P. Ninan, C. Nitroy, S. Osterman, S. B. Papp, F. Quinlan, L. Ramsey, P. Robertson, A. Roy, C. Schwab, S. Sigurdsson, K. Srinivasan, G. Stefansson, D. A. Sterner, R. Terrien, A. Wolszczan, J. T. Wright, and G. Ycas. Stellar spectroscopy in the near-infrared with a laser frequency comb. *Optica*, 6(2):233, Feb 2019.

[153] T. Mikal-Evans, I. J. M. Crossfield, B. Benneke, L. Kreidberg, J. Moses, C. V. Morley, D. Thorngren, P. Mollière, K. K. Hardegree-Ullman, J. Brewer, J. L. Christiansen, D. R. Ciardi, D. Dragomir, C. Dressing, J. J. Fortney, V. Gorjian, T. P. Greene, L. A. Hirsch, A. W. Howard, S. B. Howell, H. Isaacson, M. R. Kosiarek, J. Krick, J. H. Livingston, J. D. Lothringer, F. Y. Morales, E. A. Petigura, J. E. Schlieder, and M. Werner. Transmission Spectroscopy for the Warm Sub-Neptune HD 3167c: Evidence for Molecular Absorption and a Possible High-metallicity Atmosphere. *The Astronomical Journal*, 161(1):18, Jan. 2021.

[154] M. Miklos, T. W. Milbourne, R. D. Haywood, D. F. Phillips, S. H. Saar, N. Meunier, H. M. Cegla, X. Dumusque, N. Langellier, J. Maldonado, L. Malavolta, A. Mortier, S. Thompson, C. A. Watson, M. Cecconi, R. Cosentino, A. Ghedina, C. H. Li, M. López-Morales, E. Molinari, E. Poretti, D. Sasselov, A. Sozzetti, and R. L. Walsworth. Testing the Spectroscopic Extraction of Suppression of Convective Blueshift. *The Astrophysical Journal*, 888(2):117, Jan. 2020.

[155] T. W. Milbourne, R. D. Haywood, D. F. Phillips, S. H. Saar, H. M. Cegla, A. C. Cameron, J. Costes, X. Dumusque, N. Langellier, D. W. Latham, J. Maldonado, L. Malavolta, A. Mortier, I. Palumbo, M. L., S. Thompson, C. A. Watson, F. Bouchy, N. Buchschacher, M. Cecconi, D. Charbonneau, R. Cosentino, A. Ghedina, A. G. Glenday, M. Gonzalez, C. H. Li, M. Lodi, M. López-Morales, C. Lovis, M. Mayor, G. Micela, E. Molinari, F. Pepe, G. Piotto, K. Rice, D. Sasselov, D. Ségransan, A. Sozzetti, A. Szentgyorgyi, S. Udry, and R. L. Walsworth. HARPS-N Solar RVs Are Dominated by Large, Bright Magnetic Regions. *The Astrophysical Journal*, 874(1):107, Mar. 2019.

[156] S. Millholland. Tidally Induced Radius Inflation of Sub-Neptunes. *The Astrophysical Journal*, 886(1):72, Nov. 2019.

[157] S. Millholland, S. Wang, and G. Laughlin. Kepler multi-planet systems exhibit unexpected intra-system uniformity in mass and radius. *The Astrophysical Journal*, 849(2):L33, nov 2017.

[158] S. M. Mills, A. W. Howard, L. M. Weiss, J. H. Steffen, H. Isaacson, B. J. Fulton, E. A. Petigura, M. R. Kosiarek, L. A. Hirsch, and J. H. Boisvert. Long-period Giant Companions to Three Compact, Multiplanet Systems. *The Astronomical Journal*, 157(4):145, Apr. 2019.

[159] A. Mortier and A. Collier Cameron. Stacked Bayesian general Lomb-Scargle periodogram: Identifying stellar activity signals. *Astronomy and Astrophysics*, 601:A110, May 2017.

[160] A. Mortier, J. P. Faria, C. M. Correia, A. Santerne, and N. C. Santos. BGLS: A Bayesian formalism for the generalised Lomb-Scargle periodogram. *Astronomy and Astrophysics*, 573:A101, Jan. 2015.

[161] C. D. Murray and S. F. Dermott. *Solar system dynamics*. Cambridge Univ. Press, 2010.

[162] E. R. Newton, J. Irwin, D. Charbonneau, Z. K. Berta-Thompson, J. A. Dittmann, and A. A. West. The Rotation and Galactic Kinematics of Mid M Dwarfs in the Solar Neighborhood. *The Astrophysical Journal*, 821(2):93, Apr 2016.

[163] I. Newton. *Philosophiae Naturalis Principia Mathematica*. 1687.

[164] M. B. Nielsen, L. Gizon, H. Schunker, and C. Karoff. Rotation periods of 12 000 main-sequence Kepler stars: Dependence on stellar spectral type and comparison with v sin i observations. *Astronomy and Astrophysics*, 557:L10, Sep 2013.

[165] J. P. Ninan, C. F. Bender, S. Mahadevan, E. B. Ford, A. J. Monson, K. F. Kaplan, R. C. Terrien, A. Roy, P. M. Robertson, S. Kanodia, and G. K. Stefansson. The Habitable-Zone Planet Finder: improved flux image generation algorithms for H2RG up-the-ramp data. In *High Energy, Optical, and Infrared Detectors for Astronomy VIII*, volume 10709 of *Society of Photo-Optical Instrumentation Engineers (SPIE) Conference Series*, page 107092U, Aug. 2018.

[166] P. E. Nissen, J. Christensen-Dalsgaard, J. R. Mosumgaard, V. Silva Aguirre, E. Spitoni, and K. Verma. High-precision abundances of elements in solar-type stars. Evidence of two distinct sequences in abundance-age relations. *Astronomy and Astrophysics*, 640:A81, Aug. 2020.

[167] R. W. Noyes, L. W. Hartmann, S. L. Baliunas, D. K. Duncan, and A. H. Vaughan. Rotation, convection, and magnetic activity in lower main-sequence stars. *The Astrophysical Journal*, 279:763–777, Apr. 1984.

[168] R. W. Noyes, S. Jha, S. G. Korzennik, M. Krockenberger, P. Nisenson, T. M. Brown, E. J. Kennelly, and S. D. Horner. A Planet Orbiting the Star ρ Coronae Borealis. *The Astrophysical Journal Letters*, 483(2):L111–L114, July 1997.

[169] N. A. of Sciences Engineering and Medicine. Pathways to Discovery in Astronomy and Astrophysics for the 2020s. *The National Academies Press*, 2021.

[170] A. Ofir, S. Dreizler, M. Zechmeister, and T.-O. Husser. An independent planet search in the Kepler dataset. II. An extremely low-density super-Earth mass planet around Kepler-87. *Astronomy and Astrophysics*, 561:A103, Jan. 2014.

[171] J. E. Owen and Y. Wu. Kepler Planets: A Tale of Evaporation. *The Astrophysical Journal*, 775(2):105, Oct. 2013.

[172] J. E. Owen and Y. Wu. The Evaporation Valley in the Kepler Planets. *The Astrophysical Journal*, 847(1):29, Sept. 2017.

[173] H. Parviainen and S. Aigrain. ldtk: Limb Darkening Toolkit. *Monthly Notices of the Royal Astronomical Society*, 453(4):3821–3826, 09 2015.

[174] K. C. Patra, J. N. Winn, M. J. Holman, L. Yu, D. Deming, and F. Dai. The Apparently Decaying Orbit of WASP-12b. *The Astronomical Journal*, 154(1):4, July 2017.

[175] M. J. Pecaut and E. E. Mamajek. Intrinsic Colors, Temperatures, and Bolometric Corrections of Pre-main-sequence Stars. *The Astrophysical Journal, Supplement*, 208(1):9, Sept. 2013.

[176] M. T. Penny, B. S. Gaudi, E. Kerins, N. J. Rattenbury, S. Mao, A. C. Robin, and S. Calchi Novati. Predictions of the WFIRST Microlensing Survey. I. Bound Planet Detection Rates. *The Astrophysical Journal, Supplement*, 241(1):3, Mar. 2019.

[177] F. A. Pepe, S. Cristiani, R. Rebolo Lopez, N. C. Santos, A. Amorim, G. Avila, W. Benz, P. Bonifacio, A. Cabral, P. Carvas, R. Cirami, J. Coelho, M. Comari, I. Coretti, V. De Caprio, H. Dekker, B. Delabre, P. Di Marcantonio, V. D'Odorico, M. Fleury, R. García, J. M. Herreros Linares, I. Hughes, O. Iwert, J. Lima, J.-L. Lizon, G. Lo Curto, C. Lovis, A. Manescau, C. Martins, D. Mégevand, A. Moitinho, P. Molaro, M. Monteiro, M. Monteiro, L. Pasquini, C. Mordasini, D. Queloz, J. L. Rasilla, J. M. Rebordão, S. Santana Tschudi, P. Santin, D. Sosnowska, P. Spanò, F. Tenegi, S. Udry, E. Vanzella, M. Viel, M. R. Zapatero Osorio, and F. Zerbi. ESPRESSO: the Echelle

spectrograph for rocky exoplanets and stable spectroscopic observations. In *Proceedings of the SPIE*, volume 7735 of *Society of Photo-Optical Instrumentation Engineers (SPIE) Conference Series*, page 77350F, July 2010.

[178] J. Pepper, R. W. Pogge, D. L. DePoy, J. L. Marshall, K. Z. Stanek, A. M. Stutz, S. Poindexter, R. Siverd, T. P. O'Brien, M. Trueblood, and P. Trueblood. The Kilodegree Extremely Little Telescope (KELT): A Small Robotic Telescope for Large-Area Synoptic Surveys. *Publications of the Astronomical Society of the Pacific*, 119(858):923–935, Aug. 2007.

[179] W. D. Pesnell, B. J. Thompson, and P. C. Chamberlin. The Solar Dynamics Observatory (SDO). , 275(1-2):3–15, Jan. 2012.

[180] E. A. Petigura, A. W. Howard, and G. Marcy. Prevalence of Earth-size planets orbiting Sun-like stars. *Proceedings of the National Academy of Science*, 110(48):19273–19278, Nov. 2013.

[181] E. A. Petigura, A. W. Howard, G. W. Marcy, J. A. Johnson, H. Isaacson, P. A. Cargile, L. Hebb, B. J. Fulton, L. M. Weiss, T. D. Morton, J. N. Winn, L. A. Rogers, E. Sinukoff, L. A. Hirsch, and I. J. M. Crossfield. The California-Kepler Survey. I. High-resolution Spectroscopy of 1305 Stars Hosting Kepler Transiting Planets. *The Astronomical Journal*, 154(3):107, Sept. 2017.

[182] C. Piaulet. *Smint*, 2020. `https://github.com/cpiaulet/smint`.

[183] A. G. M. Pietrow, D. Kiselman, J. de la Cruz Rodríguez, C. J. Díaz Baso, A. Pastor Yabar, and R. Yadav. Inference of the chromospheric magnetic field configuration of solar plage using the Ca II 8542 Å line. *Astronomy and Astrophysics*, 644:A43, Dec. 2020.

[184] J. B. Pollack, O. Hubickyj, P. Bodenheimer, J. J. Lissauer, M. Podolak, and Y. Greenzweig. Formation of the Giant Planets by Concurrent Accretion of Solids and Gas. *Icarus*, 124(1):62–85, Nov. 1996.

[185] D. Queloz, G. W. Henry, J. P. Sivan, S. L. Baliunas, J. L. Beuzit, R. A. Donahue, M. Mayor, D. Naef, C. Perrier, and S. Udry. No planet for HD 166435. *Astronomy and Astrophysics*, 379:279–287, Nov. 2001.

[186] A. Quirrenbach, P. J. Amado, J. A. Caballero, R. Mundt, A. Reiners, I. Ribas, W. Seifert, M. Abril, J. Aceituno, F. J. Alonso-Floriano, H. Anwand-Heerwart, M. Azzaro, F. Bauer, D. Barrado, S. Becerril, V. J. S. Bejar, D. Benitez, Z. M. Berdinas, M. Brinkmöller, M. C. Cardenas, E. Casal, A. Claret, J. Colomé, M. Cortes-Contreras, S. Czesla, M. Doellinger, S. Dreizler, C. Feiz, M. Fernandez, I. M. Ferro, B. Fuhrmeister, D. Galadi, I. Gallardo, M. C. Gálvez-Ortiz, A. Garcia-Piquer, R. Garrido, L. Gesa, V. G. Galera, J. I. G. Hernández, R. G. Peinado, U. Grözinger, J. Guàrdia, E. W. Guenther, E. de Guindos, H.-J. Hagen, A. P. Hatzes, P. H. Hauschildt, J. Helmling, T. Henning, D. Hermann, R. H. Arabi, L. H. Castaño, F. H. Hernando, E. Herrero, A. Huber, K. F. Huber, P. Huke, S. V. Jeffers, E. de Juan, A. Kaminski, M. Kehr,

M. Kim, R. Klein, J. Klüter, M. Kürster, M. Lafarga, L. M. Lara, A. Lamert, W. Laun, R. Launhardt, U. Lemke, R. Lenzen, M. Llamas, M. L. del Fresno, M. López-Puertas, J. López-Santiago, J. F. L. Salas, H. M. Madinabeitia, U. Mall, H. Mandel, L. Mancini, J. A. M. Molina, D. M. Fernández, E. L. Martín, S. Martín-Ruiz, C. Marvin, R. J. Mathar, E. Mirabet, D. Montes, J. C. Morales, R. M. Muñoz, E. Nagel, V. Naranjo, G. Nowak, E. Palle, J. Panduro, V. M. Passegger, A. Pavlov, S. Pedraz, E. Perez, D. Pérez-Medialdea, M. Perger, M. Pluto, A. Ramón, R. Rebolo, P. Redondo, S. Reffert, S. Reinhart, P. Rhode, H.-W. Rix, F. Rodler, E. Rodríguez, C. R. López, R. R. Rohloff, A. Rosich, M. A. S. Carrasco, J. Sanz-Forcada, P. Sarkis, L. F. Sarmiento, S. Schäfer, J. Schiller, C. Schmidt, J. H. M. M. Schmitt, P. Schöfer, A. Schweitzer, D. Shulyak, E. Solano, O. Stahl, C. Storz, H. M. Tabernero, M. Tala, L. Tal-Or, R.-G. Ulbrich, G. Veredas, J. I. V. Linares, F. Vilardell, K. Wagner, J. Winkler, M.-R. Z. Osorio, M. Zechmeister, M. A. von Eiff, G. Anglada-Escudé, C. del Burgo, M. L. Garcia-Vargas, A. Klutsch, J.-L. Lizon, M. Lopez-Morales, A. Ofir, A. Pérez-Calpena, M. A. C. Perryman, E. Sánchez-Blanco, J. B. P. Strachan, J. Stürmer, J. C. Suárez, T. Trifonov, S. M. Tulloch, and W. Xu. CARMENES: an overview six months after first light. In C. J. Evans, L. Simard, and H. Takami, editors, *Ground-based and Airborne Instrumentation for Astronomy VI*, volume 9908, pages 296 – 309. International Society for Optics and Photonics, SPIE, 2016.

[187] V. Rajpaul, S. Aigrain, M. A. Osborne, S. Reece, and S. Roberts. A Gaussian process framework for modelling stellar activity signals in radial velocity data. *Monthly Notices of the Royal Astronomical Society*, 452(3):2269–2291, Sept. 2015.

[188] A. Reiners, N. Joshi, and B. Goldman. A Catalog of Rotation and Activity in Early-M Stars. *The Astronomical Journal*, 143(4):93, Apr. 2012.

[189] I. Ribas, M. Tuomi, A. Reiners, R. P. Butler, J. C. Morales, M. Perger, S. Dreizler, C. Rodríguez-López, J. I. González Hernández, A. Rosich, F. Feng, T. Trifonov, S. S. Vogt, J. A. Caballero, A. Hatzes, E. Herrero, S. V. Jeffers, M. Lafarga, F. Murgas, R. P. Nelson, E. Rodríguez, J. B. P. Strachan, L. Tal-Or, J. Teske, B. Toledo-Padrón, M. Zechmeister, A. Quirrenbach, P. J. Amado, M. Azzaro, V. J. S. Béjar, J. R. Barnes, Z. M. Berdiñas, J. Burt, G. Coleman, M. Cortés-Contreras, J. Crane, S. G. Engle, E. F. Guinan, C. A. Haswell, T. Henning, B. Holden, J. Jenkins, H. R. A. Jones, A. Kaminski, M. Kiraga, M. Kürster, M. H. Lee, M. J. López-González, D. Montes, J. Morin, A. Ofir, E. Pallé, R. Rebolo, S. Reffert, A. Schweitzer, W. Seifert, S. A. Shectman, D. Staab, R. A. Street, A. Suárez Mascareño, Y. Tsapras, S. X. Wang, and G. Anglada-Escudé. A candidate super-Earth planet orbiting near the snow line of Barnard's star. *Nature*, 563(7731):365–368, Nov 2018.

[190] M. Rice and J. M. Brewer. Stellar Characterization of Keck HIRES Spectra with The Cannon. *The Astrophysical Journal*, 898(2):119, Aug. 2020.

[191] G. R. Ricker, J. N. Winn, R. Vanderspek, D. W. Latham, G. Á. Bakos, J. L. Bean, Z. K. Berta-Thompson, T. M. Brown, L. Buchhave, N. R. Butler, R. P. Butler, W. J. Chaplin, D. Charbonneau, J. Christensen-Dalsgaard, M. Clampin, D. Deming, J. Doty,

N. De Lee, C. Dressing, E. W. Dunham, M. Endl, F. Fressin, J. Ge, T. Henning, M. J. Holman, A. W. Howard, S. Ida, J. M. Jenkins, G. Jernigan, J. A. Johnson, L. Kaltenegger, N. Kawai, H. Kjeldsen, G. Laughlin, A. M. Levine, D. Lin, J. J. Lissauer, P. MacQueen, G. Marcy, P. R. McCullough, T. D. Morton, N. Narita, M. Paegert, E. Palle, F. Pepe, J. Pepper, A. Quirrenbach, S. A. Rinehart, D. Sasselov, B. Sato, S. Seager, A. Sozzetti, K. G. Stassun, P. Sullivan, A. Szentgyorgyi, G. Torres, S. Udry, and J. Villasenor. Transiting Exoplanet Survey Satellite (TESS). *Journal of Astronomical Telescopes, Instruments, and Systems*, 1:014003, Jan. 2015.

[192] P. Robertson. Aliasing in the Radial Velocities of YZ Ceti: An Ultra-short Period for YZ Ceti c? *The Astrophysical Journal Letters*, 864(2):L28, Sept. 2018.

[193] P. Robertson, C. Bender, S. Mahadevan, A. Roy, and L. W. Ramsey. Proxima Centauri as a Benchmark for Stellar Activity Indicators in the Near-infrared. *The Astrophysical Journal*, 832(2):112, Dec. 2016.

[194] P. Robertson, M. Endl, W. D. Cochran, and S. E. Dodson-Robinson. Hα Activity of Old M Dwarfs: Stellar Cycles and Mean Activity Levels for 93 Low-mass Stars in the Solar Neighborhood. *The Astrophysical Journal*, 764(1):3, Feb. 2013.

[195] P. Robertson and S. Mahadevan. Disentangling Planets and Stellar Activity for Gliese 667C. *The Astrophysical Journal Letters*, 793(2):L24, Oct 2014.

[196] P. Robertson, A. Roy, and S. Mahadevan. Stellar Activity Mimics a Habitable-zone Planet around Kapteyn's Star. *The Astrophysical Journal Letters*, 805(2):L22, June 2015.

[197] P. Robertson, G. Stefansson, S. Mahadevan, M. Endl, W. D. Cochran, C. Beard, C. F. Bender, S. A. Diddams, N. Duong, E. B. Ford, C. Fredrick, S. Halverson, F. Hearty, R. Holcomb, L. Juan, S. Kanodia, J. Lubin, A. J. Metcalf, A. Monson, J. P. Ninan, J. Palafoutas, L. W. Ramsey, A. Roy, C. Schwab, R. C. Terrien, and J. T. Wright. Persistent starspot signals on M dwarfs: multi-wavelength Doppler observations with the Habitable-zone Planet Finder and Keck/HIRES. *arXiv e-prints*, page arXiv:2005.09657, May 2020.

[198] L. A. Rogers. Most 1.6 Earth-radius Planets are Not Rocky. *The Astrophysical Journal*, 801(1):41, Mar. 2015.

[199] L. J. Rosenthal, B. J. Fulton, L. A. Hirsch, H. T. Isaacson, A. W. Howard, C. M. Dedrick, I. A. Sherstyuk, S. C. Blunt, E. A. Petigura, H. A. Knutson, A. Behmard, A. Chontos, J. R. Crepp, I. J. M. Crossfield, P. A. Dalba, D. A. Fischer, G. W. Henry, S. R. Kane, M. Kosiarek, G. W. Marcy, R. A. Rubenzahl, L. M. Weiss, and J. T. Wright. The California Legacy Survey. I. A Catalog of 178 Planets from Precision Radial Velocity Monitoring of 719 Nearby Stars over Three Decades. *The Astrophysical Journal, Supplement*, 255(1):8, July 2021.

[200] L. J. Rosenthal, H. A. Knutson, Y. Chachan, F. Dai, A. W. Howard, B. J. Fulton, A. Chontos, J. R. Crepp, P. A. Dalba, G. W. Henry, S. R. Kane, E. A. Petigura,

L. M. Weiss, and J. T. Wright. The California Legacy Survey. III. On the Shoulders of (Some) Giants: The Relationship between Inner Small Planets and Outer Massive Planets. *The Astrophysical Journal, Supplement*, 262(1):1, Sept. 2022.

[201] R. A. Rossiter. On the detection of an effect of rotation during eclipse in the velocity of the brigher component of beta Lyrae, and on the constancy of velocity of this system. *The Astrophysical Journal*, 60:15–21, July 1924.

[202] D. Rowan, S. Meschiari, G. Laughlin, S. S. Vogt, R. P. Butler, J. Burt, S. Wang, B. Holden, R. Hanson, P. Arriagada, S. Keiser, J. Teske, and M. Diaz. The Lick-Carnegie Exoplanet Survey: HD 32963—A New Jupiter Analog Orbiting a Sun-like Star. *The Astrophysical Journal*, 817(2):104, Feb. 2016.

[203] R. A. Rubenzahl, F. Dai, A. W. Howard, A. Chontos, S. Giacalone, J. Lubin, L. J. Rosenthal, H. Isaacson, N. M. Batalha, I. J. M. Crossfield, C. Dressing, B. Fulton, D. Huber, S. R. Kane, E. A. Petigura, P. Robertson, A. Roy, L. M. Weiss, C. Beard, M. L. Hill, A. Mayo, T. Močnik, J. M. Akana Murphy, and N. Scarsdale. The TESS-Keck Survey IV: A Retrograde, Polar Orbit for the Ultra-Low-Density, Hot Super-Neptune WASP-107b. *arXiv e-prints*, page arXiv:2101.09371, Jan. 2021.

[204] Z. Rustamkulov, D. Sing, S. Mukherjee, E. May, M. Line, E. Schlawin, K. Stevenson, C. Piaulet, S. Moran, A. Carter, J. Kirk, N. Batalha, J. Lothringer, M. Lopez-Morales, J. Bean, N. Espinoza, N. Batalha, and JWST Transiting Exoplanet Community ERS Team. JWST Transiting Exoplanet Early Release Science: A Transmission Spectrum of WASP-39b with NIRSpec PRISM. In *American Astronomical Society Meeting Abstracts*, volume 55 of *American Astronomical Society Meeting Abstracts*, page 124.01, Jan. 2023.

[205] J. Salvatier, T. V. Wiecki, and C. Fonnesbeck. Probabilistic programming in python using pymc3. *PeerJ Computer Science*, 2:e55, 2016.

[206] J. D. Scargle. Studies in astronomical time series analysis. II. Statistical aspects of spectral analysis of unevenly spaced data. *The Astrophysical Journal*, 263:835–853, Dec. 1982.

[207] N. Scarsdale, J. M. A. Murphy, N. M. Batalha, I. J. M. Crossfield, C. D. Dressing, B. Fulton, A. W. Howard, D. Huber, H. Isaacson, S. R. Kane, E. A. Petigura, P. Robertson, A. Roy, L. M. Weiss, C. Beard, A. Behmard, A. Chontos, J. L. Christiansen, D. R. Ciardi, Z. R. Claytor, K. A. Collins, K. I. Collins, F. Dai, P. A. Dalba, D. Dragomir, T. Fetherolf, A. Fukui, S. Giacalone, E. J. Gonzales, M. L. Hill, L. A. Hirsch, E. L. N. Jensen, M. R. Kosiarek, J. P. de Leon, J. Lubin, M. B. Lund, R. Luque, A. W. Mayo, T. Močnik, M. Mori, N. Narita, G. Nowak, E. Pallé, M. Rabus, L. J. Rosenthal, R. A. Rubenzahl, J. E. Schlieder, A. Shporer, K. G. Stassun, J. Twicken, G. Wang, D. A. Yahalomi, J. Jenkins, D. W. Latham, G. R. Ricker, S. Seager, R. Vanderspek, and J. N. Winn. TESS-Keck Survey. V. Twin Sub-Neptunes Transiting the Nearby G Star HD 63935. *The Astronomical Journal*, 162(5):215, Nov. 2021.

[208] K. C. Schlaufman. Evidence of an Upper Bound on the Masses of Planets and Its Implications for Giant Planet Formation. *The Astrophysical Journal*, 853(1):37, Jan. 2018.

[209] A. Schuster. On the investigation of hidden periodicities with application to a supposed 26 day period of meteorological phenomena. *Terrestrial Magnetism (Journal of Geophysical Research)*, 3(1):13, Jan. 1898.

[210] C. Schwab, A. Rakich, Q. Gong, S. Mahadevan, S. P. Halverson, A. Roy, R. C. Terrien, P. M. Robertson, F. R. Hearty, E. I. Levi, A. J. Monson, J. T. Wright, M. W. McElwain, C. F. Bender, C. H. Blake, J. Stürmer, Y. V. Gurevich, A. Chakraborty, and L. W. Ramsey. Design of NEID, an extreme precision Doppler spectrograph for WIYN. In *Proceedings of the SPIE*, volume 9908 of *Society of Photo-Optical Instrumentation Engineers (SPIE) Conference Series*, page 99087H, Aug. 2016.

[211] A. Seifahrt, J. L. Bean, J. Stürmer, D. Kasper, L. Gers, C. Schwab, M. Zechmeister, G. Stefánsson, B. Montet, L. A. Dos Santos, A. Peck, J. White, and E. Tapia. On-sky commissioning of MAROON-X: a new precision radial velocity spectrograph for Gemini North. In C. J. Evans, J. J. Bryant, and K. Motohara, editors, *Ground-based and Airborne Instrumentation for Astronomy VIII*, volume 11447 of *Society of Photo-Optical Instrumentation Engineers (SPIE) Conference Series*, page 114471F, Dec. 2020.

[212] M. Shetrone, M. E. Cornell, J. R. Fowler, N. Gaffney, B. Laws, J. Mader, C. Mason, S. Odewahn, B. Roman, S. Rostopchin, D. P. Schneider, J. Umbarger, and A. Westfall. Ten Year Review of Queue Scheduling of the Hobby-Eberly Telescope. *Publications of the Astronomical Society of the Pacific*, 119(855):556–566, May 2007.

[213] A. M. Silva, J. P. Faria, N. C. Santos, S. G. Sousa, P. T. P. Viana, J. H. C. Martins, P. Figueira, C. Lovis, F. Pepe, S. Cristiani, R. Rebolo, R. Allart, A. Cabral, A. Mehner, A. Sozzetti, A. Suárez Mascareño, C. J. A. P. Martins, D. Ehrenreich, D. Mégevand, E. Palle, G. Lo Curto, H. M. Tabernero, J. Lillo-Box, J. I. González Hernández, M. R. Zapatero Osorio, N. C. Hara, N. J. Nunes, P. Di Marcantonio, S. Udry, V. Adibekyan, and X. Dumusque. A novel framework for semi-Bayesian radial velocities through template matching. *Astronomy and Astrophysics*, 663:A143, July 2022.

[214] D. K. Sing, A. Lecavelier des Etangs, J. J. Fortney, A. S. Burrows, F. Pont, H. R. Wakeford, G. E. Ballester, N. Nikolov, G. W. Henry, S. Aigrain, D. Deming, T. M. Evans, N. P. Gibson, C. M. Huitson, H. Knutson, A. P. Showman, A. Vidal-Madjar, P. A. Wilson, M. H. Williamson, and K. Zahnle. HST hot-Jupiter transmission spectral survey: evidence for aerosols and lack of TiO in the atmosphere of WASP-12b. *Monthly Notices of the Royal Astronomical Society*, 436(4):2956–2973, Dec. 2013.

[215] A. Skumanich, C. Smythe, and E. N. Frazier. On the statistical desription of inhomogeneities in the quiet solar atmosphere. I. Linear regression analysis and absolute calibration of multichannel observations of the Ca^+ emission network. *The Astrophysical Journal*, 200:747–764, Sept. 1975.

[216] S. K. Solanki. Sunspots: An overview. *Astronomy and Astrophysics Reviews*, 11(2-3):153–286, Jan. 2003.

[217] D. Spergel, N. Gehrels, C. Baltay, D. Bennett, J. Breckinridge, M. Donahue, A. Dressler, B. S. Gaudi, T. Greene, O. Guyon, C. Hirata, J. Kalirai, N. J. Kasdin, B. Macintosh, W. Moos, S. Perlmutter, M. Postman, B. Rauscher, J. Rhodes, Y. Wang, D. Weinberg, D. Benford, M. Hudson, W. S. Jeong, Y. Mellier, W. Traub, T. Yamada, P. Capak, J. Colbert, D. Masters, M. Penny, D. Savransky, D. Stern, N. Zimmerman, R. Barry, L. Bartusek, K. Carpenter, E. Cheng, D. Content, F. Dekens, R. Demers, K. Grady, C. Jackson, G. Kuan, J. Kruk, M. Melton, B. Nemati, B. Parvin, I. Poberezhskiy, C. Peddie, J. Ruffa, J. K. Wallace, A. Whipple, E. Wollack, and F. Zhao. Wide-Field InfrarRed Survey Telescope-Astrophysics Focused Telescope Assets WFIRST-AFTA 2015 Report. *arXiv e-prints*, page arXiv:1503.03757, Mar. 2015.

[218] J. L. Starck, M. Elad, and D. L. Donoho. Image decomposition via the combination of sparse representations and a variational approach. *IEEE Transactions on Image Processing*, 14(10):1570–1582, Oct. 2005.

[219] K. G. Stassun, R. J. Oelkers, J. Pepper, M. Paegert, N. De Lee, G. Torres, D. W. Latham, S. Charpinet, C. D. Dressing, D. Huber, S. R. Kane, S. Lépine, A. Mann, P. S. Muirhead, B. Rojas-Ayala, R. Silvotti, S. W. Fleming, A. Levine, and P. Plavchan. The TESS Input Catalog and Candidate Target List. *The Astronomical Journal*, 156(3):102, Sept. 2018.

[220] G. Stefansson, C. Cañas, J. Wisniewski, P. Robertson, S. Mahadevan, M. Maney, S. Kanodia, C. Beard, C. F. Bender, P. Brunt, J. C. Clemens, W. Cochran, S. A. Diddams, M. Endl, E. B. Ford, C. Fredrick, S. Halverson, F. Hearty, L. Hebb, J. Huehnerhoff, J. Jennings, K. Kaplan, E. Levi, E. Lubar, A. J. Metcalf, A. Monson, B. Morris, J. P. Ninan, C. Nitroy, L. Ramsey, A. Roy, C. Schwab, S. Sigurdsson, R. Terrien, and J. T. Wright. A Sub-Neptune-sized Planet Transiting the M2.5 Dwarf G 9-40: Validation with the Habitable-zone Planet Finder. *The Astronomical Journal*, 159(3):100, Mar. 2020.

[221] G. Stefansson, F. Hearty, P. Robertson, S. Mahadevan, T. Anderson, E. Levi, C. Bender, M. Nelson, A. Monson, B. Blank, S. Halverson, C. Henderson, L. Ramsey, A. Roy, C. Schwab, and R. Terrien. A Versatile Technique to Enable Sub-milli-Kelvin Instrument Stability for Precise Radial Velocity Measurements: Tests with the Habitable-zone Planet Finder. *The Astrophysical Journal*, 833(2):175, Dec 2016.

[222] A. Suárez Mascareño, J. P. Faria, P. Figueira, C. Lovis, M. Damasso, J. I. González Hernández, R. Rebolo, S. Cristiano, F. Pepe, N. C. Santos, M. R. Zapatero Osorio, V. Adibekyan, S. Hojjatpanah, A. Sozzetti, F. Murgas, M. Abreo, M. Affolter, Y. Alibert, M. Aliverti, R. Allart, C. Allende Prieto, D. Alves, M. Amate, G. Avila, V. Baldini, T. Bandi, S. C. C. Barros, A. Bianco, W. Benz, F. Bouchy, C. Broeng, A. Cabral, G. Calderone, R. Cirami, J. Coelho, P. Conconi, I. Coretti, C. Cumani, G. Cupani, V. D'Odorico, S. Deiries, B. Delabre, P. Di Marcantonio, X. Dumusque, D. Ehrenreich, A. Fragoso, L. Genolet, M. Genoni, R. Génova Santos, I. Hughes, O. Iwert, K. Ferber,

J. Knusdrtrup, M. Landoni, B. Lavie, J. Lillo-Box, J. Lizon, G. Lo Curto, C. Maire, A. Manescau, C. J. A. P. Martins, D. Mégevand, A. Mehner, G. Micela, A. Modigliani, P. Molaro, M. A. Monteiro, M. J. P. F. G. Monteiro, M. Moschetti, E. Mueller, N. J. Nunes, L. Oggioni, A. Oliveira, E. Pallé, G. Pariani, L. Pasquini, E. Poretti, J. L. Rasilla, E. Redaelli, M. Riva, S. Santana Tschudi, P. Santin, P. Santos, A. Segovia, D. Sosnoswska, S. Sousa, P. Spanò, F. Tenegi, S. Udry, A. Zanutta, and F. Zerbi. Revisiting Proxima with ESPRESSO. *arXiv e-prints*, page arXiv:2005.12114, May 2020.

[223] A. Suárez Mascareño, R. Rebolo, J. I. González Hernández, B. Toledo-Padrón, M. Perger, I. Ribas, L. Affer, G. Micela, M. Damasso, J. Maldonado, E. González-Alvarez, G. Leto, I. Pagano, G. Scandariato, A. Sozzetti, A. F. Lanza, L. Malavolta, R. Claudi, R. Cosentino, S. Desidera, P. Giacobbe, A. Maggio, M. Rainer, M. Esposito, S. Benatti, M. Pedani, J. C. Morales, E. Herrero, M. Lafarga, A. Rosich, and M. Pinamonti. HADES RV programme with HARPS-N at TNG. VII. Rotation and activity of M-dwarfs from time-series high-resolution spectroscopy of chromospheric indicators. *Astronomy and Astrophysics*, 612:A89, Apr. 2018.

[224] L. Tal-Or, T. Trifonov, S. Zucker, T. Mazeh, and M. Zechmeister. Correcting HIRES/Keck radial velocities for small systematic errors. *Monthly Notices of the Royal Astronomical Society*, 484(1):L8–L13, Mar. 2019.

[225] L. Tal-Or, S. Zucker, I. Ribas, G. Anglada-Escudé, and A. Reiners. Prospects for detecting the astrometric signature of Barnard's Star b. *Astronomy and Astrophysics*, 623:A10, Mar. 2019.

[226] J. Tayar, Z. R. Claytor, D. Huber, and J. van Saders. A Guide to Realistic Uncertainties on Fundamental Properties of Solar-Type Exoplanet Host Stars. *arXiv e-prints*, page arXiv:2012.07957, Dec. 2020.

[227] A. P. G. Thompson, C. A. Watson, R. D. Haywood, J. C. Costes, E. de Mooij, A. Collier Cameron, X. Dumusque, D. F. Phillips, S. H. Saar, A. Mortier, T. W. Milbourne, S. Aigrain, H. M. Cegla, D. Charbonneau, R. Cosentino, A. Ghedina, D. W. Latham, M. López-Morales, G. Micela, E. Molinari, E. Poretti, A. Sozzetti, S. Thompson, and R. Walsworth. The spectral impact of magnetic activity on disc-integrated HARPS-N solar observations: exploring new activity indicators. *Monthly Notices of the Royal Astronomical Society*, 494(3):4279–4290, May 2020.

[228] R. Tibshirani. Regression shrinkage and selection via the lasso. *Journal of the Royal Statistical Society. Series B (Methodological)*, 58(1):267–288, 1996.

[229] B. Toledo-Padrón, J. I. González Hernández, C. Rodríguez-López, A. Suárez Mascareño, R. Rebolo, R. P. Butler, I. Ribas, G. Anglada-Escudé, E. N. Johnson, A. Reiners, J. A. Caballero, A. Quirrenbach, P. J. Amado, V. J. S. Béjar, J. C. Morales, M. Perger, S. V. Jeffers, S. Vogt, J. Teske, S. Shectman, J. Crane, M. Díaz, P. Arriagada, B. Holden, J. Burt, E. Rodríguez, E. Herrero, F. Murgas, E. Pallé, N. Morales, M. J. López-González, E. Díez Alonso, M. Tuomi, M. Kiraga, S. G. Engle, E. F.

Guinan, J. B. P. Strachan, F. J. Aceituno, J. Aceituno, V. M. Casanova, S. Martín-Ruiz, D. Montes, J. L. Ortiz, A. Sota, J. Briol, L. Barbieri, I. Cervini, M. Deldem, F. Dubois, F. J. Hambsch, B. Harris, C. Kotnik, L. Logie, J. Lopez, M. McNeely, Y. Ogmen, L. Pérez, S. Rau, D. Rodríguez, F. S. Urquijo, and S. Vanaverbeke. Stellar activity analysis of Barnard's Star: very slow rotation and evidence for long-term activity cycle. *Monthly Notices of the Royal Astronomical Society*, 488(4):5145–5161, Oct 2019.

[230] T. Trifonov, L. Tal-Or, M. Zechmeister, A. Kaminski, S. Zucker, and T. Mazeh. Public HARPS radial velocity database corrected for systematic errors. *Astronomy and Astrophysics*, 636:A74, Apr. 2020.

[231] E. V. Turtelboom, L. M. Weiss, C. D. Dressing, G. Nowak, E. Pallé, C. Beard, S. Blunt, C. Brinkman, A. Chontos, Z. R. Claytor, F. Dai, P. A. Dalba, S. Giacalone, E. Gonzales, C. K. Harada, M. L. Hill, R. Holcomb, J. Korth, J. Lubin, T. Masseron, M. MacDougall, A. W. Mayo, T. Močnik, J. M. Akana Murphy, A. S. Polanski, M. Rice, R. A. Rubenzahl, N. Scarsdale, K. G. Stassun, D. B. Tyler, J. V. Zandt, I. J. M. Crossfield, H. J. Deeg, B. Fulton, D. Gandolfi, A. W. Howard, D. Huber, H. Isaacson, S. R. Kane, K. W. F. Lam, R. Luque, E. L. Martín, G. Morello, J. Orell-Miquel, E. A. Petigura, P. Robertson, A. Roy, V. Van Eylen, D. Baker, A. A. Belinski, A. Bieryla, D. R. Ciardi, K. A. Collins, N. Cutting, D. J. Della-Rose, T. B. Ellingsen, E. Furlan, T. Gan, C. L. Gnilka, P. Guerra, S. B. Howell, M. Jimenez, D. W. Latham, M. Larivière, K. V. Lester, J. Lillo-Box, L. Luker, C. R. Mann, P. P. Plavchan, B. Safonov, B. Skinner, I. A. Strakhov, J. M. Wittrock, D. A. Caldwell, Z. Essack, J. M. Jenkins, E. V. Quintana, G. R. Ricker, R. Vanderspek, S. Seager, and J. N. Winn. The TESS-Keck Survey. XI. Mass Measurements for Four Transiting Sub-Neptunes Orbiting K Dwarf TOI-1246. *The Astronomical Journal*, 163(6):293, June 2022.

[232] J. A. Valenti, R. P. Butler, and G. Marcy. Determining Spectrometer Instrumental Profiles Using FTS Reference Spectra. *Publications of the Astronomical Society of the Pacific*, 107:966, Oct. 1995.

[233] P. van de Kamp. Astrometric study of Barnard's star from plates taken with the 24-inch Sproul refractor. *The Astronomical Journal*, 68:515–521, Sep 1963.

[234] P. van de Kamp. Alternate dynamical analysis of Barnard's star. *The Astronomical Journal*, 74:757–759, Aug 1969.

[235] P. van de Kamp. Astrometric study of Barnard's star from plates taken with the Sproul 61-cm refractor. *The Astronomical Journal*, 80:658, Aug 1975.

[236] P. van de Kamp. The planetary system of Barnard's star. *Vistas in Astronomy*, 26(2):141–157, Jan 1982.

[237] V. Van Eylen, C. Agentoft, M. S. Lundkvist, H. Kjeldsen, J. E. Owen, B. J. Fulton, E. Petigura, and I. Snellen. An asteroseismic view of the radius valley: stripped cores, not born rocky. *Monthly Notices of the Royal Astronomical Society*, 479(4):4786–4795, Oct. 2018.

[238] J. E. Van Zandt, E. A. Petigura, M. MacDougall, G. J. Gilbert, J. Lubin, T. Barclay, N. M. Batalha, I. J. M. Crossfield, C. Dressing, B. Fulton, A. W. Howard, D. Huber, H. Isaacson, S. R. Kane, P. Robertson, A. Roy, L. M. Weiss, A. Behmard, C. Beard, A. Chontos, F. Dai, P. A. Dalba, T. Fetherolf, S. Giacalone, C. E. Henze, M. L. Hill, L. A. Hirsch, R. Holcomb, S. B. Howell, J. M. Jenkins, D. W. Latham, A. Mayo, I. Mireles, T. Mocnik, J. M. Akana Murphy, D. Pidhorodetska, A. S. Polanski, G. R. Ricker, L. J. Rosenthal, R. A. Rubenzahl, S. Seager, N. Scarsdale, E. V. Turtleboom, R. Vanderspek, and J. N. Winn. TESS-Keck Survey XIV: Two giant exoplanets from the Distant Giants Survey. *arXiv e-prints*, page arXiv:2209.06958, Sept. 2022.

[239] S. S. Vogt, S. L. Allen, B. C. Bigelow, L. Bresee, B. Brown, T. Cantrall, A. Conrad, M. Couture, C. Delaney, H. W. Epps, D. Hilyard, D. F. Hilyard, E. Horn, N. Jern, D. Kanto, M. J. Keane, R. I. Kibrick, J. W. Lewis, J. Osborne, G. H. Pardeilhan, T. Pfister, T. Ricketts, L. B. Robinson, R. J. Stover, D. Tucker, J. Ward, and M. Z. Wei. HIRES: the high-resolution echelle spectrometer on the Keck 10-m Telescope. In D. L. Crawford and E. R. Craine, editors, *Proceedings of the SPIE*, volume 2198 of *Society of Photo-Optical Instrumentation Engineers (SPIE) Conference Series*, page 362, June 1994.

[240] S. S. Vogt, M. Radovan, R. Kibrick, R. P. Butler, B. Alcott, S. Allen, P. Arriagada, M. Bolte, J. Burt, J. Cabak, K. Chloros, D. Cowley, W. Deich, B. Dupraw, W. Earthman, H. Epps, S. Faber, D. Fischer, E. Gates, D. Hilyard, B. Holden, K. Johnston, S. Keiser, D. Kanto, M. Katsuki, L. Laiterman, K. Lanclos, G. Laughlin, J. Lewis, C. Lockwood, P. Lynam, G. Marcy, M. McLean, J. Miller, T. Misch, M. Peck, T. Pfister, A. Phillips, E. Rivera, D. Sandford, M. Saylor, R. Stover, M. Thompson, B. Walp, J. Ward, J. Wareham, M. Wei, and C. Wright. APF—The Lick Observatory Automated Planet Finder. *Publications of the Astronomical Society of the Pacific*, 126(938):359, Apr. 2014.

[241] H. R. Wakeford, T. J. Wilson, K. B. Stevenson, and N. K. Lewis. Exoplanet Atmosphere Forecast: Observers Should Expect Spectroscopic Transmission Features to be Muted to 33%. *Research Notes of the American Astronomical Society*, 3(1):7, Jan. 2019.

[242] J. Wang, D. Mawet, G. Ruane, R. Hu, and B. Benneke. Observing Exoplanets with High Dispersion Coronagraphy. I. The Scientific Potential of Current and Next-generation Large Ground and Space Telescopes. *The Astronomical Journal*, 153(4):183, Apr. 2017.

[243] L. M. Weiss, F. Dai, D. Huber, J. M. Brewer, K. A. Collins, D. R. Ciardi, E. C. Matthews, C. Ziegler, S. B. Howell, N. M. Batalha, I. J. M. Crossfield, C. Dressing, B. Fulton, A. W. Howard, H. Isaacson, S. R. Kane, E. A. Petigura, P. Robertson, A. Roy, R. A. Rubenzahl, J. D. Twicken, Z. R. Claytor, K. G. Stassun, M. G. MacDougall, A. Chontos, S. Giacalone, P. A. Dalba, T. Mocnik, M. L. Hill, C. Beard, J. M. Akana Murphy, L. J. Rosenthal, A. Behmard, J. Van Zandt, J. Lubin, M. R. Kosiarek, M. B. Lund, J. L. Christiansen, R. A. Matson, C. A. Beichman, J. E. Schlieder, E. J.

Gonzales, C. Briceño, N. Law, A. W. Mann, K. I. Collins, P. Evans, A. Fukui, E. L. N. Jensen, F. Murgas, N. Narita, E. Palle, H. Parviainen, R. P. Schwarz, T.-G. Tan, J. S. Acton, E. M. Bryant, A. Chaushev, S. Gill, P. Eigmüller, J. Jenkins, G. Ricker, S. Seager, and J. N. Winn. The TESS-Keck Survey. II. An Ultra-short-period Rocky Planet and Its Siblings Transiting the Galactic Thick-disk Star TOI-561. *The Astronomical Journal*, 161(2):56, Feb. 2021.

[244] L. M. Weiss and G. W. Marcy. The Mass-Radius Relation for 65 Exoplanets Smaller than 4 Earth Radii. *The Astrophysical Journal Letters*, 783(1):L6, Mar. 2014.

[245] L. M. Weiss, G. W. Marcy, E. A. Petigura, B. J. Fulton, A. W. Howard, J. N. Winn, H. T. Isaacson, T. D. Morton, L. A. Hirsch, E. J. Sinukoff, A. Cumming, L. Hebb, and P. A. Cargile. The California-Kepler Survey. V. Peas in a Pod: Planets in a Kepler Multi-planet System Are Similar in Size and Regularly Spaced. *The Astronomical Journal*, 155(1):48, Jan. 2018.

[246] O. C. Wilson. Flux Measurements at the Centers of Stellar H- and K-Lines. *The Astrophysical Journal*, 153:221, July 1968.

[247] R. A. Wittenmyer, R. P. Butler, C. G. Tinney, J. Horner, B. D. Carter, D. J. Wright, H. R. A. Jones, J. Bailey, and S. J. O'Toole. The Anglo-Australian Planet Search XXIV: The Frequency of Jupiter Analogs. *The Astrophysical Journal*, 819(1):28, Mar. 2016.

[248] J. T. Wright and J. D. Eastman. Barycentric Corrections at 1 cm s^{-1} for Precise Doppler Velocities. *Publications of the Astronomical Society of the Pacific*, 126:838, Sep 2014.

[249] J. T. Wright, G. Marcy, A. W. Howard, J. A. Johnson, T. D. Morton, and D. A. Fischer. The Frequency of Hot Jupiters Orbiting nearby Solar-type Stars. *The Astrophysical Journal*, 753(2):160, July 2012.

[250] D.-H. Wu, M. Rice, and S. Wang. Evidence for Hidden Nearby Companions to Hot Jupiters. *The Astronomical Journal*, 165(4):171, Apr. 2023.

[251] Y. Wu and N. Murray. Planet Migration and Binary Companions: The Case of HD 80606b. *The Astrophysical Journal*, 589(1):605–614, May 2003.

[252] M. Zechmeister and M. Kürster. The generalised Lomb-Scargle periodogram. A new formalism for the floating-mean and Keplerian periodograms. *Astronomy and Astrophysics*, 496(2):577–584, Mar. 2009.

[253] M. Zechmeister and M. Kürster. The generalised Lomb-Scargle periodogram. A new formalism for the floating-mean and Keplerian periodograms. *Astronomy and Astrophysics*, 496(2):577–584, Mar. 2009.

[254] M. Zechmeister, M. Kürster, and M. Endl. The M dwarf planet search programme at the ESO VLT + UVES. A search for terrestrial planets in the habitable zone of M dwarfs. *Astronomy and Astrophysics*, 505(2):859–871, Oct. 2009.

[255] M. Zechmeister, A. Reiners, P. J. Amado, M. Azzaro, F. F. Bauer, V. J. S. Béjar, J. A. Caballero, E. W. Guenther, H.-J. Hagen, S. V. Jeffers, A. Kaminski, M. Kürster, R. Launhardt, D. Montes, J. C. Morales, A. Quirrenbach, S. Reffert, I. Ribas, W. Seifert, L. Tal-Or, and V. Wolthoff. Spectrum radial velocity analyser (SERVAL). High-precision radial velocities and two alternative spectral indicators. *Astronomy and Astrophysics*, 609:A12, Jan. 2018.

[256] L. Zeng, D. D. Sasselov, and S. B. Jacobsen. Mass-Radius Relation for Rocky Planets Based on PREM. *The Astrophysical Journal*, 819(2):127, Mar. 2016.

[257] J. Zhang, L. M. Weiss, D. Huber, S. Blunt, A. Chontos, B. J. Fulton, S. Grunblatt, A. W. Howard, H. Isaacson, M. R. Kosiarek, E. A. Petigura, L. J. Rosenthal, and R. A. Rubenzahl. Long Period Jovian Tilts the Orbits of Two sub-Neptunes Relative to Stellar Spin Axis in Kepler-129. *arXiv e-prints*, page arXiv:2105.03446, May 2021.

[258] L. L. Zhao, D. A. Fischer, E. B. Ford, A. Wise, M. Cretignier, S. Aigrain, O. Barragan, M. Bedell, L. A. Buchhave, J. D. Camacho, H. M. Cegla, J. Cisewski-Kehe, A. Collier Cameron, Z. L. de Beurs, S. Dodson-Robinson, X. Dumusque, J. P. Faria, C. Gilbertson, C. Haley, J. Harrell, D. W. Hogg, P. Holzer, A. A. John, B. Klein, M. Lafarga, F. Lienhard, V. Maguire-Rajpaul, A. Mortier, B. Nicholson, M. L. Palumbo, V. Ramirez Delgado, C. J. Shallue, A. Vanderburg, P. T. P. Viana, J. Zhao, N. Zicher, S. H. C. Cabot, G. W. Henry, R. M. Roettenbacher, J. M. Brewer, J. Llama, R. R. Petersburg, and A. E. Szymkowiak. The EXPRES Stellar Signals Project II. State of the Field in Disentangling Photospheric Velocities. *The Astronomical Journal*, 163(4):171, Apr. 2022.

[259] W. Zhu and Y. Wu. The Super Earth-Cold Jupiter Relations. *The Astronomical Journal*, 156(3):92, Sept. 2018.

[260] C. Zwaan. Elements and patterns in the solar magnetic field. *Annual Review of Astronomy and Astrophysics*, 25:83–111, Jan. 1987.

[261] C. Zwaan. The Evolution of Sunspots. In J. H. Thomas and N. O. Weiss, editors, *Sunspots. Theory and Observations*, volume 375 of *NATO Advanced Study Institute (ASI) Series C*, page 75, Jan. 1992.